THE UNIVERSITY *of* EDINBURGH

Demographics of dark-matter haloes in standard and non-standard cosmologies

Alexander James Mead

Institute for Astronomy
School of Physics and Astronomy

The University of Edinburgh
Doctor of Philosophy

2014

Lay Summary

On large scales Universe is constructed from galaxies, many of which are similar to our own, and almost all of which are moving away from us – the entire Universe is expanding. Observations of the rate of recession of galaxies have shown unambiguously that the expansion of the Universe is currently *accelerating*, whereas it was decelerating in the past. This is very strange because gravitational forces between massive objects are attractive and thus the presence of matter in the Universe can only decelerate the expansion. Either a previously unknown form of invisible energy must be present in the Universe that is causing the accelerated expansion; so-called 'dark energy', or the laws of gravity used to interpret the expansion are incorrect, and the accelerated expansion arises naturally in the context of the correct theory; so-called modified gravity theories.

The simplest possible explanation for accelerated expansion is that empty space contains a small amount of vacuum energy and that this pushes objects apart. The Universe contains a lot of empty space the cumulative effect of the small vacuum energy ends up being important. A model based on this concept, known as ΛCDM, requires the Universe of today to consist $\simeq 70\%$ of this vacuum energy (Λ), which leaves $\simeq 30\%$ of the Universe to be made of matter. Of this matter $\simeq 80\%$ of this is cold, dark matter (CDM) while the remaining $\simeq 20\%$ is familiar atomic matter. Regardless of the slightly unfamiliar ingredients that go into ΛCDM it has been able to explain all large scale cosmological observations that have ever been made with good accuracy. However, there many competing dark energy and modified gravity theories that aim to explain the accelerated expansion and all need to be tested, which involves theoretical calculations of the consequences of each model.

It is generally believed that the distribution of dark matter and galaxies observed in the Universe today is the result of the gravitational amplification of initially small perturbations to the density that were seeded in a homogeneous early Universe around 14 billion years ago. It is thought that the early Universe underwent a period of rapid inflation and that at this time quantum mechanical noise, generated by the inflationary process, was imprinted onto the smooth distribution of matter, thus producing the re-

quired perturbations. Once seeded, these perturbations evolve under their own gravity and eventually collapse into dense structures with the final result being the distribution of galaxies, and all they contain, observed in the Universe today. Remarkably the distribution, and rate of growth, of cosmic large-scale structure depends on the contents of the Universe and therefore on the particulars of any dark energy or modified gravity model. It therefore follows that by measuring large-scale structure one can hope to constrain the plethora of models for the accelerating expansion of the cosmos. As an example, it is perfectly possible for a theory to correctly model the acceleration of the cosmos, but not to predict the correct distribution of galaxies. The study of structure growth, at all epochs, represents one of the frontiers of modern cosmology. The evolution of structure allows the predictions of the ΛCDM model to be tested outside the arena of the bulk expansion of the homogeneous Universe and thus to test the theory to greater accuracy and compare against competing theories.

This thesis concerns itself with the theory of the distribution of structure in the Universe and particularly with improving the modelling of how structure develops in order that future galaxy surveys might better constrain theories of the accelerated expansion of the cosmos. The main tool employed to this end is a phenomenological model, known as the 'halo model', which is an approximate model of how matter is distributed from large scales down to the scales of individual dark matter haloes, thought to be the sites of galaxy formation. The halo model takes its inspiration from exact theoretical treatments of small perturbations and also from the results of large cosmological N-body simulations in which the exact evolution of structure in the cosmos is computed in a brute force manner.

This thesis begins with three chapters of introductory material, necessary for a full understanding of the research chapters. The research itself is then split into three parts: the first improves the accuracy of the halo model prediction for the matter distribution so that it can be used as a tool for constraining the cosmological parameters of our Universe from current and future large-scale surveys. The second part develops a technique to rescale cosmological N-body simulations, once they have been run, so as to approximate the simulation output that would have been produced had a different cosmological model been simulated. This is done both at the level of the large-scale distribution of structure in the simulation and also at the level of the individual dark matter haloes within the simulation. The final part of this thesis applies the techniques developed in the previous two chapters to modified theories of gravity, trying to keep the approach as general as possible, while focussing tests on a particular class of models, known as $f(R)$ models.

Abstract

This thesis explores topics related to the formation and development of the large-scale structure in the Universe, with the focus being to compute properties of the evolved non-linear density field in an approximate way. The first three chapters form an introduction: Chapter 1 contains the theoretical basis of modern cosmology, Chapter 2 discusses the role of N-body simulations in the study of structure formation and Chapter 3 considers the phenomenological halo model.

In Chapter 4 a novel method of computing the matter power spectrum is developed. This method uses the halo model directly to make accurate predictions for the matter spectrum. This is achieved by fitting parameters of the model to spectra from accurate simulations. The final predictions are good to 5% up to $k = 10\,h\,\mathrm{Mpc}^{-1}$ across a range of cosmological models at $z = 0$, however accuracy degrades at higher redshift and at quasi-linear scales.

Chapter 5 is dedicated to a new method of rescaling a halo catalogue that has previously been generated from a simulation of a specific cosmological model to a different model; a gross rescaling of the simulation box size and redshift label takes place, then individual halo positions are modified in accord with the large scale displacement field and their internal structure is altered. The final power spectrum of haloes can be matched at the 5% level up to $k = 1\,h\,\mathrm{Mpc}^{-1}$, as can the spectrum of particles within haloes reconstituted directly from the rescaled catalogues.

Chapter 6 applies the methods of the previous two chapters to modified gravity models. This is done in as general a way possible but tests are restricted to $f(R)$ type models, which have a scale-dependent linear growth rate as well as having 'chameleon screening' – by which modifications to gravity are screened within *some* haloes. Taking these effects into account leads to predictions of the matter spectrum at the 5% level and rescaled halo distributions that are accurate to 5% in both real and redshift space. For the spectrum of halo particles it is demonstrated that accurate results may be obtained by taking the enhanced gravity in some haloes into account.

Declaration

Except where otherwise stated, the research undertaken in this thesis was the unaided work of the author. Where the work was done in collaboration with others, a significant contribution was made by the author. The work presented here has not been submitted for any other degree or professional qualification.

The majority of work in Chapter 5 has been published in Monthly Notices of the Royal Astronomical Society as Mead & Peacock (2014); and can be found at – `http://arxiv.org/abs/1308.5183`.

Alexander James Mead
September 2014

Acknowledgements

I acknowledge only my own genius.

Contents

List of Figures

List of Tables

Chapter 1

Cosmology

Cosmology: *the science relating to the origin and development of the Universe on large scales*

Cosmology has been the subject of intense speculation for millennia, but the subject of serious academic thought for only a century. However, it is only within the last 20 years that truly precision measurements of the properties of our Universe have been made and these have only been made possible due to improved technology deployed within the latest generation of telescopes. This has transformed cosmology from being quite a speculative subject to a high precision science.

This introductory chapter aims to provide a general introduction to cosmology and contains concepts, equations and derivations necessary for a full understanding of rest of the thesis. Attempts are made to make the discussion of possible cosmological models as general as possible, before honing in on the specifics of the parameter space surrounding the currently accepted model of the Universe. This author believes that a general introduction is necessary because the currently accepted paradigm is strange in a number of ways that can only be appreciated when one has a full understanding of cosmology in the wider sense.

Throughout this chapter units are set such that the speed of light $c = 1$. Fundamental constants, and combinations of constants, in units relevant for large-scale structure cosmology are given in Table 1.2.

1.1 Basics

On peering out into the cosmos one observes it to be approximately homogeneous and isotropic, smooth and featureless. Clearly this statement is not true at the level of the room you are in. The fact that this thesis exists is proof that homogeneity breaks down on small scales. However, on viewing the Universe at larger and larger scales the amplitude of features diminishes and if viewed in sufficiently large patches (several hundreds of Mpc) it can be thought of as being perfectly smooth.

On such large scales in the Universe the only force that is relevant is that of gravity, both the strong and weak nuclear forces have short ranges and the overall charge neutrality of the Universe ensures that electromagnetism is also irrelevant when discussing the evolution of the gross structure of the Universe, except at early times.

A mathematical understanding of the evolution of an infinite, homogeneous, isotropic distribution of matter can be formulated within the framework of Newtonian physics (although one has to ignore certain divergences). In doing this one arrives at the strange conclusion that if an infinite smooth matter distribution is set up at rest and allowed to evolve it will collapse due to gravity. This collapse happens at all points in the matter distribution, not about a single point and due to the initial symmetry all points remain equivalent. Although any one observer will see the universe collapsing about them, any other observer will see the same thing. This strange conclusion makes sense when one realises that all points of reference can all be reached with Galilean transformations. It was only after the publication of the General Theory of Relativity Einstein (1916) that a more sound theoretical understanding of the evolution of homogeneous matter distributions became possible, which takes into account the finite speed of light. Relativity allows an understanding of the propagation of light in such a universe and explains how this relates to the observed redshifts of distant galaxies. Einstein also showed that the geometry of a universe could be curved in a non-trivial way, determined by the total energy density. The Gravitational Field Equations of Einstein relate the curvature of space-time to the contained energy density

$$R_{ab} - \frac{1}{2} R g_{ab} = -8\pi G T_{ab} \ , \tag{1.1}$$

the equations are tensorial and are invariant in form under any general coordinate transformations. The Ricci tensor R_{ab}, and Ricci scalar R, contain various combinations of first- and second-order derivatives of the metric tensor g_{ab} with respect to coordinates. The metric is a central quantity in general relativity and allows one to compute 'distances' between events in a curved space-time. The field equations are differential equations which determine the metric from the stress-energy contents, encoded in the tensor T_{ab}, which contains all the information about the distribution of energy density. The equations are highly non-linear and couple together various components of the metric in an unpleasant manner. Equation (1.1) can be considered the relativistic analogue of the Poisson equation. In a general case one would write down the energy-density distribution in T_{ab} for a system under consideration (equivalent to, for example, first writing down the density distribution when solving the Poisson equation)

and then solve equation (1.1) to find the metric tensor. However, this is extremely difficult in practice and analytic solutions only exist for a small number of symmetric cases, a general solution has never been found.

In the approximation that a universe is spatially homogeneous and isotropic the form of the metric can be constrained on symmetry grounds:

$$g_{ab}dx^a dx^b = dt^2 - R(t)^2[dr^2 + S_k^2(r)(d\theta^2 + \sin^2\theta d\phi^2)] \ . \tag{1.2}$$

Here $R(t)$ is the scale factor which evolves only with time and gives a measure of how far different points in the smooth Universe have moved from each other in time, t, measured by an observer who is at rest with respect to the matter in their vicinity, which is therefore the special relativity time for these observers. Expansion (or contraction) of the Universe is expected in such symmetric models, based on the previous discussion about Newtonian mechanics. The coordinates r, θ and ϕ are the standard spherical polar coordinates with the subtlety that r is a dimensionless comoving coordinate in the sense that it is tied to the expansion of the cosmos – observers moving with the expansion do not change r coordinate. The physical distance between events at time t is $R(t)r$. The function S_k depends on the curvature of the universe and is given by

$$S_k = \begin{cases} \sin r, & k = 1 \\ r, & k = 0 \\ \sinh r, & k = -1 \end{cases}$$

with k and R related via the Friedmann Equation:

$$\left(\frac{\dot{R}}{R}\right)^2 \equiv H^2 = \frac{8\pi G}{3}\sum_i \rho_i(R) - \frac{k}{R^2} \ , \tag{1.3}$$

where the sum over i takes place over all energy densities, ρ, of all of the components of the universe. This is simply the solution of the Einstein Field Equation (1.1) with the Friedmann metric, given in equation (1.2) and a perfect fluid (diagonal) stress-energy tensor. In this way k is not a free parameter, but instead is determined by the energy density of the universe. Equation (1.3) can be viewed as an energy equation: the left hand side is the kinetic energy of the expansion while the first term on the right is the potential energy and the second term (curvature) is the constant total energy. With this in mind it is easy to see that total energy term (related to the curvature) cannot be set independently of the other terms – once an expansion speed and matter content has been specified for a particular universe the energy content is also set. This is in exact analogy with the fact that the total energy of a ball is set, and unchanging, once it has been thrown in the air. That k can only take the specific values 0, 1 or -1 does not mean that the energy of the expansion can only take specific values, the ability of the energy term to vary continuously is allowed by changing the value of R_0 (R evaluated today) which relates to the curvature via

$$k = R_0^2\left(\frac{8\pi G\rho_0}{3} - H_0^2\right) \ , \tag{1.4}$$

where H_0 and ρ_0 are the present day values of these parameters. A universe is called flat if $k = 0$, which occurs only if the two terms on the right hand side exactly equal each other. R_0 can be seen to define a curvature scale – a physical scale beyond which effects due to the non-trivial geometry of space-time become important. If $k = 0$ the value of R_0 becomes undefined and it is common practice to remove the ambiguity by using a dimensionless scale factor:

$$a \equiv \frac{R}{R_0} \ , \tag{1.5}$$

such that $a = 1$ today. Even if $k \neq 0$ a is still a useful quantity and it will be used throughout the rest of this thesis.

As a universe expands or contracts different contributions to the energy density will behave in different ways. How a species behaves is determined via stress-energy conservation, which can be derived by thermodynamic arguments or via the covariant conservation of stress energy, $\nabla_a T^{ab} = 0$, for the smooth universe this gives the continuity equation,

$$\dot{\rho}_i + 3H(\rho_i + p_i) = 0 \ , \tag{1.6}$$

for each component. To solve equation (1.6) for a given component, an equation of state is required that relates the energy density ρ to the pressure p. The three components most commonly considered are cold matter ($p = 0$), radiation ($p = \rho/3$) and vacuum energy ($p = -\rho$). The pressure of vacuum energy (Λ) allows this to maintain a constant energy density as the universe expands ($\rho_\Lambda = \text{const}$) while for matter $\rho_m \propto a^{-3}$ and for radiation $\rho_r \propto a^{-4}$. Pressure plays a different role in cosmology to that normally considered in physics; since a homogeneous universe is being considered the 'pressure' of a species does not contribute to the expansion via a force due to a gradient in pressure but rather because with pressure comes some momentum energy which contributes to the effective energy density of the fluid due to the equivalence of mass and energy. Thus radiation, which has a pressure, is diluted more quickly than matter as the universe expands because its momentum is diluted as well as the physical density.

Given these three components, the Friedmann equation (1.3) can be written as

$$\left(\frac{\dot{a}}{a}\right)^2 \equiv H^2 = \frac{8\pi G}{3}\left(\frac{\rho_{\rm m}}{a^3} + \frac{\rho_r}{a^4} + \rho_\Lambda\right) - \frac{k}{R_0^2 a^2} \ . \tag{1.7}$$

By defining dimensionless parameters

$$\Omega_i(a) = \frac{8\pi G}{3H^2}\rho_i(a) \ , \tag{1.8}$$

and the value of these Ω parameters today as

$$\Omega_i = \frac{8\pi G}{3H_0^2}\rho_{0i} \ , \tag{1.9}$$

equation (1.7) can be written in the convenient form

$$\left(\frac{\dot{a}}{a}\right)^2 = H_0^2\left(\frac{\Omega_{\rm m}}{a^3} + \frac{\Omega_{\rm r}}{a^4} + \Omega_\Lambda + \frac{1-\Omega}{a^2}\right) \ , \tag{1.10}$$

where $\Omega = \Omega_{\rm m} + \Omega_{\rm r} + \Omega_\Lambda$ (added to this sum should be any other component under consideration). For any model under consideration this equation can be solved to give $a(t)$, the expansion history for the model. Throughout this thesis Ω_i is taken to be the value of this parameter 'today' ($a = 1$) and time dependence will be explicitly included, *e.g.* $\Omega_i(a)$, if this is being used. A lack of a consistent system of notation for the Ω parameters in cosmology is the source of many nights of tears for students of cosmology.

By differentiating equation (1.10) a force equation can also be derived:

$$\frac{\ddot{a}}{a} \equiv A = -\frac{H_0^2}{2}\left(\frac{\Omega_{\rm m}}{a^3} + 2\frac{\Omega_{\rm r}}{a^4} - 2\Omega_\Lambda\right) . \tag{1.11}$$

It is possible to construct a universe which is static by a careful balancing done to ensure that $\ddot{a} = 0$ and $\dot{a} = 0$ for all times but this requires very specific values of $\Omega_{\rm m}$ and Ω_Λ (some form of vacuum or dark energy is necessary to stabilise such a universe, and perfect fine tuning is necessary) and it can be shown that such a universe is unstable to small perturbations – structure would grow, so the present state of such a universe would be a mystery considering it had to be much smoother in the infinite past: therefore such a universe is not really static.

By solving equation (1.10) the relationship between time and the scale factor can be found for any given model of the universe – if it is flat ($\Omega = 0$) and contains only matter then $a \propto t^{2/3}$, if only radiation $a \propto t^{1/2}$, and if only vacuum energy then expansion proceeds exponentially $a \propto e^{H_0 t}$ and the Universe has no beginning. If multiple components of the universe are important in the evolution then analytic solutions are more difficult to obtain, however the Friedmann equation (1.3) can always be integrated numerically in these cases.

When solving any second order differential equation in physics, boundary conditions must be imposed. One of these has already been imposed on equation (1.10) which fixes the curvature (last) term to be governed by all of the other terms. This is essentially fixing the total energy of the expansion. The second boundary condition that must be imposed when solving this equation is that today $a = 1$.

In general, equations (1.10) and (1.11) predict that a universe should be either expanding or contracting. For certain universes, with certain combinations of Ω_i, a point is reached in the past when $a = 0$, these cosmologies have a set beginning, known as a big bang. Other sets of cosmological parameters have $a = 0$ at some point in the future which signifies an end point for these models, a so-called big crunch scenario. However, one should bear in mind that formally the equations describing the evolution of the universe breakdown when a is (very close to) zero with certain key quantities, such as dimensions, vanishing from the metric and others, such as the density, becoming infinite. This breakdown is discussed more fully in the context of inflation in Section 1.9 and probably reflects the fact that General Relativity breaks down at high energies and that some other theory is required to describe the Universe at these points. In a given model if an 'age' (t_0) for the universe is quoted this simply refers to the time since $a = 0$ in the past, although some models have no $a = 0$ point and thus no age. If a Universe

has an age this can be simply calculated from equation (1.10) as

$$t_0 = \int_0^1 \frac{\mathrm{d}a}{aH(a)} \ . \tag{1.12}$$

1.2 Redshift

Galaxies in a homogeneous universe are fixed in comoving coordinates – they have fixed positions r. This coordinate can be calculated via

$$r = \int_{t_1}^{t_2} \frac{\mathrm{d}t}{R} \ , \tag{1.13}$$

where t_1 is the emission time of the light and t_2 is the observed time. However, because the comoving coordinate of the galaxy does not change this expression is valid always, including a short time later:

$$r = \int_{t_1+\delta t_1}^{t_2+\delta t_2} \frac{\mathrm{d}t}{R} \ , \tag{1.14}$$

by equating these two expressions one can show

$$\delta t_1 R(t_1) = \delta t_2 R(t_2) \ . \tag{1.15}$$

The cosmological redshift z is defined by how much the wavelength of light has stretched, this means that $1+z \equiv \delta t_2/\delta t_1$ and therefore that $1+z$ is equal to the ratio of scale factors between the time of emission and the time of observation of the light. If light is observed 'today' then

$$\frac{R_0}{R(t)} \equiv \frac{1}{a} = 1 + z \ , \tag{1.16}$$

where R_0 denotes the present day value of the scale factor and $R(t)$ is the scale factor at the time that an object producing a redshift, z, is being observed. In cosmology it is often most convenient to use a or z as a measurement of distance rather than a comoving coordinate from the metric because z is directly observable and model independent.

1.3 Distance in cosmology

The metric defined in equation (1.2) can be used to compute distances to cosmological events (a set of coordinates). For light rays travelling along radial paths (to and from the observer at $r = 0$) $ds = 0$, and one can write

$$r = \int \frac{dt}{R(t)} = \frac{1}{R_0} \int \frac{da}{a^2 H(a)} = \frac{1}{R_0} \int \frac{dz}{H(z)} \ , \tag{1.17}$$

the limits of the integral must be chosen depending on the quantity of interest. For example, to calculate the r coordinate of an event observed at redshift z_0 one would compute

$$R_0 r(z_0) = \int_0^{z_0} \frac{\mathrm{d}z}{H(z)} \ , \tag{1.18}$$

given that the light left the object at $z = z_0$ and reaches us at $z = 0$. In cosmology there exist horizons, which are finite distances that light can have travelled, or that light will be able to travel. If a big bang exists then light can only have travelled a fixed amount of r up to the present because there has only been a finite amount of time. Additionally light may only be able to travel to a fixed r value infinitely far into the future even if time extends to infinity, depending on exactly how the Universe expands. If there is a crunch then light can obviously only travel until the crunch occurs. The particle horizon is defined as the distance particles can have travelled since $R = 0$ and is only defined for models in which $R = 0$ in the past (big bang cosmologies) it can be computed via

$$R_0 r_{\rm p}(z) = R_{\rm p}(z) = \int_0^t \frac{{\rm d}t}{R(t)} = \int_z^\infty \frac{{\rm d}z}{H(z)} \ , \tag{1.19}$$

where the conversion to the integral over z is only valid if $R(t)$ is monotonic. Similarly the event horizon, the maximum comoving distance light can travel, can be computed via

$$R_0 r_{\rm p}(z) = R_{\rm p}(z) = \int_{t_0}^\infty \frac{{\rm d}t}{R(t)} = \int_{-1}^0 \frac{{\rm d}z}{H(z)} \ , \tag{1.20}$$

and may or may not be finite depending on the cosmological model, again the second integral is only valid if $R(t)$ is monotonic. In big-crunch models the $t = \infty$ limit should be replaced by $t = t_{\rm crunch}$ because there is only a finite time in such models.

The quantity $R_0 r$ is commonly referred to the 'physical distance' to an object. However, one must be aware that in General Relativity one must be very careful when talking about something that sounds like an 'absolute' like a physical distance. There are many ways to measure distance; for example one could bounce light off an object and use the fact that the speed of light is a constant to compute a distance based on the travel time of the light. One could also travel at a certain speed to a point and calculate the distance based on the time taken. One could also lay measuring sticks of a fixed length between two points. All of the above methods would be equivalent in our human experience but all give different answers in a curved universe. The way out of such troubles is to be extremely specific when discussing quantities such as distance and time in General Relativity. For example rather than talking about distance talk about r coordinates.

In cosmology two other distance measures, other than $R_0 r$ are commonly used,the angular diameter distance and the luminosity distance. The angular diameter distance is defined as the quantity $D_{\rm A}$ for an object of known physical extent ℓ which subtends an angle on the sky $\delta\theta$, which satisfies

$$D_{\rm A} = \frac{\ell}{\delta\theta} \ , \tag{1.21}$$

in flat space $D_{\rm A}$ would be the distance to the object. $D_{\rm A}$ can be computed using the metric in equation (1.2) and it is given by

$$D_{\rm A} = \frac{R_0 S_k(r)}{1+z} \ . \tag{1.22}$$

In a similar spirit, the luminosity distance $D_{\rm L}$ is defined as the distance which satisfies the flat space relation between bolometric flux F, bolometric luminosity L, and distance:

$$F = \frac{L}{4\pi D_{\rm L}^2} \ , \tag{1.23}$$

$D_{\rm L}$ can be computed from the metric:

$$D_{\rm L} = (1+z) R_0 S_k(r) \ . \tag{1.24}$$

Generally, for an object at fixed r the luminosity distance will be greater than the angular diameter distance; $D_{\rm L}/D_{\rm A} = (1+z)^2$ independent of cosmological model. This means that objects are dimmer than they would be were the universe not expanding but also that they appear larger on the sky than they would were the universe not expanding, this would be reversed if a universe were contracting. The dimness can be understood because photons from the source are released with their time dilated and also that they are spread over a larger area as the universe expands. The boosted angular size of an object compared to Euclidian can be understood as an effect of gravitational lensing due to space-time curvature. Fig. 1.1 shows the evolution of the various distances for an example cosmological model with $\Omega_{\rm m} = 0.3$ and $\Omega_\Lambda = 0.7$, but the trend shown in this plot is quite general.

Both $D_{\rm A}$ and $D_{\rm L}$ are useful quantities to consider in cosmology because they are directly measured by observations. The attention of the reader is now turned to a brief discussion of some of the observational probes used to constrain the type of Universe that we live in compared to the plethora of universes which are available theoretically.

1.4 Observations and ΛCDM

So far the discussion has been completely general, and the mathematics discussed can be used to describe the evolution of any homogeneous universe, with any combination of parameters. However, we find ourselves in a specific Universe and so now observations of this Universe, and how one is able to infer cosmological parameters from these observations, are discussed. This leads to the famous ΛCDM model, which is able to successfully explain all cosmological observations to date.

It appears that our Universe is expanding, and thus that $a(t)$ is currently an increasing function with time. The recession speed of distant galaxies was first noticed by Slipher (1917) but Hubble (1929) was the first to postulate a linear relation between the recession speed v and distance x. This is exactly what one would expect from a universe conforming to the assumptions behind the Friedmann Metric which for nearby objects the metric predicts that

$$v = H_0 x \ , \tag{1.25}$$

so that the constant of proportionality between recession velocity v and distance x is the present day value of the Hubble parameter – the Hubble constant – a misnomer given that it changes will

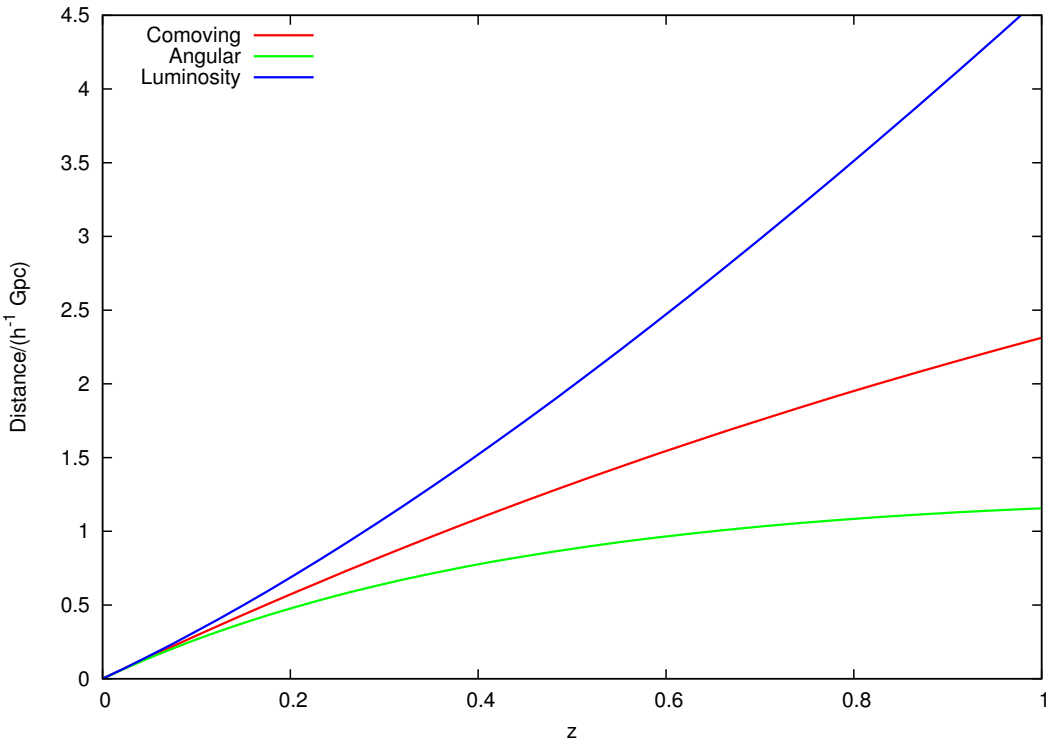

Figure 1.1: For an object with a given redshift z this figure shows the values of the comoving distance, the angular diameter distance and the luminosity distance that would be inferred for such an object assuming a cosmological model with $\Omega_{\rm m} = 0.3$ and $\Omega_\Lambda = 0.7$. Note that the rapid increase of $D_{\rm L}$ means that objects get dim quickly in a cosmological setting and the relatively slow increase of $D_{\rm A}$ means that objects look bigger than one would naively expect at higher z.

time (albeit slowly when compared with human timescales). For very local objects the distance (any measure, physical, comoving, luminosity and angular all converge for small distances) is related to the redshift by

$$z = H_0 x \ , \tag{1.26}$$

so H_0 can be inferred by measuring distances, the typical recession speed of nearby galaxies is several hundred kms^{-1}. The units of H_0 set the typical time and length scales for the Universe, within factors of c, which are often useful when computing physical quantities in cosmology:

$$\frac{1}{H_0} \approx 2997.9\, h^{-1}\,\mathrm{Mpc} \approx 9.7776\, h^{-1}\,\mathrm{Gyr} \ , \tag{1.27}$$

Due to uncertainties in the measurement of the exact value of H_0 it is typical to write H_0 in terms of a small constant h, of order one. So that $H_0 = 100h\,\mathrm{km\,s^{-1}\,Mpc^{-1}}$.

By looking at equations (1.25) and (1.26) one could be forgiven for thinking that the distance and recession velocity of a single galaxy would be sufficient to measure H_0. However, galaxies have peculiar velocities in addition to that from the Hubble flow and so measurements of the recession velocities of a census of galaxies over a representative volume of the Universe is necessary (*e.g.* Ben-Dayan et al. 2014) in order not to be biased by local flows. Some very close galaxies, such as Andromeda (0.8 Mpc) and some satellite and dwarf galaxies have negative redshifts – they are moving towards us. In some sense our position in the Universe is lucky, in that local peculiar velocities seem to be low (the local Hubble flow is quite cold), which is probably due to the fact that we do not live near a massive galaxy cluster (Governato et al. 1997; Macciò et al. 2005; Karachentsev et al. 2009) and so the Hubble law is easier to measure locally. By attempting to measure absolute distance and velocity in this way a number of local H_0 have been made which rely on being able to accurately determine the distance to galaxies.

Distances can be measured by a variety of methods including using the known angular extent of an object. This can be done for objects like SN1987a where the angular extent of the supernova ejecta can be measured along with the expansion velocity of the ejecta. Together this allows the distance to the supernova to be accurately measured and thus provides an accurate distance to the large magellanic cloud (LMC) galaxy (Panagia 1998). The LMC contains a large population of stars called Cepheid Variables for which a tight relationship exists between the period of their luminosity oscillations (these are post main sequence stars with unstable outer layers) and the luminosity itself. It follows that by measuring the period the luminosity can be inferred and thus a distance inferred by measuring the received flux (*e.g.* Feast et al. 2008; Majaess et al. 2009). Hubble (1929) used Cepheids to determine distances in the original work that showed the Universe to be expanding. Another method of measuring astrophysical distances is to use the angular size of accretion disks in active galactic nuclei (AGN). The angular extent of a disk can be measured together with the velocity and acceleration of material in the outer edge of the disk, this then allows the physical size to be estimated using the laws of orbital motion ($\ddot{r} = v^2/r$). The velocity of material can be measured using spectroscopy and the change in radial velocity with time can also be measured which measures the acceleration.

In this way accurate distance to a number of galaxies, most famously NGC 4258 (Herrnstein et al. 1999), have been determined. Cepheids or AGN disks can be used to calibrate accurate distances to galaxies that are quite far away.

If one wishes to measure the Hubble flow further away, then thermonuclear supernovae can be used as a standard candle – an object that has a known intrinsic luminosity. By measuring the received flux from a standard candle one can then infer the distance. Thermonuclear supernovae are known to be such a population and have the advantage that they are extremely luminous and can thus be seen over great distances. They are exclusively the observational type 1A classification – no hydrogen in the spectrum but prevalent silicon lines. The standardness of the explosions is probably due to the fact that they are Carbon-Oxygen white dwarf stars, which explains the lack of hydrogen lines in the spectra because these stars have lost their hydrogen envelope during the planetary nebula phase of stellar evolution. Such stars are supported by electron degeneracy pressure and are pushed over a critical (Chandrasekhar) mass $\sim 1.4M_\odot$ and thus all explode at a similar mass, which then gives similar explosions (*e.g.* Wang et al. 2012). However, such an argument ignores differences in the progenitors such as spin and metallicity which must have an effect on the explosion properties. Additionally it is not clear if the most common progenitor scenario is a single white dwarf being pushed over the Chandrasekhar limit by accretion, or two white dwarfs being driven into contact by gravitational wave emission, with the merger being over the Chandrasekhar limit (*e.g.* Ji et al. 2013). This all leads to the fact that rather than being perfect standard candles, thermonuclear supernova are standardisable in that a relationship can be calibrated (Phillips et al. 1992) between the peak flux and duration of the light curve. This can then be related to the total luminosity which can be used to standardise an individual supernova. In this way the total bolometric luminosity of each supernova can be inferred and this can be related to the luminosity distance, given in equation (1.24). The scaling relations of Phillips et al. (1992) are good to about 5% in distance so large numbers of supernovae are required to beat down the errors. To anchor the distance scale, the distance to a galaxy containing one needs to be calibrated independently using either Cepheids or AGN disk measurements discussed above.

If a supernova is observed at low redshift ($z \ll 1$) then the luminosity distance to them can be approximated as

$$D_{\rm L} = \frac{z}{H_0}\left[1 - \frac{z}{4}(\Omega_{\rm m} - 2\Omega_\Lambda - 2)\right] \ , \tag{1.28}$$

which shows that by measuring low redshift supernovae only the combination $\Omega_{\rm m} - 2\Omega_\Lambda$ will be measured and this combination forms a degenerate direction in the $\Omega_{\rm m}$–Ω_Λ plane, although higher redshift observations break the degeneracy to some degree. Current constraints from supernovae cosmology, shown in Fig. 1.2 (from Suzuki et al. 2012), show the Universe to have a cosmological constant term with the current energy densities in vacuum energy and matter are approximately $\Omega_\Lambda \simeq 0.7$ and $\Omega_{\rm m} \simeq 0.3$ with $h \simeq 0.7$. The presence of a cosmological constant, and thus an accelerating cosmos was first measured from supernova data by Schmidt et al. (1998) and Perlmutter et al. (1999). These constraints require additional information

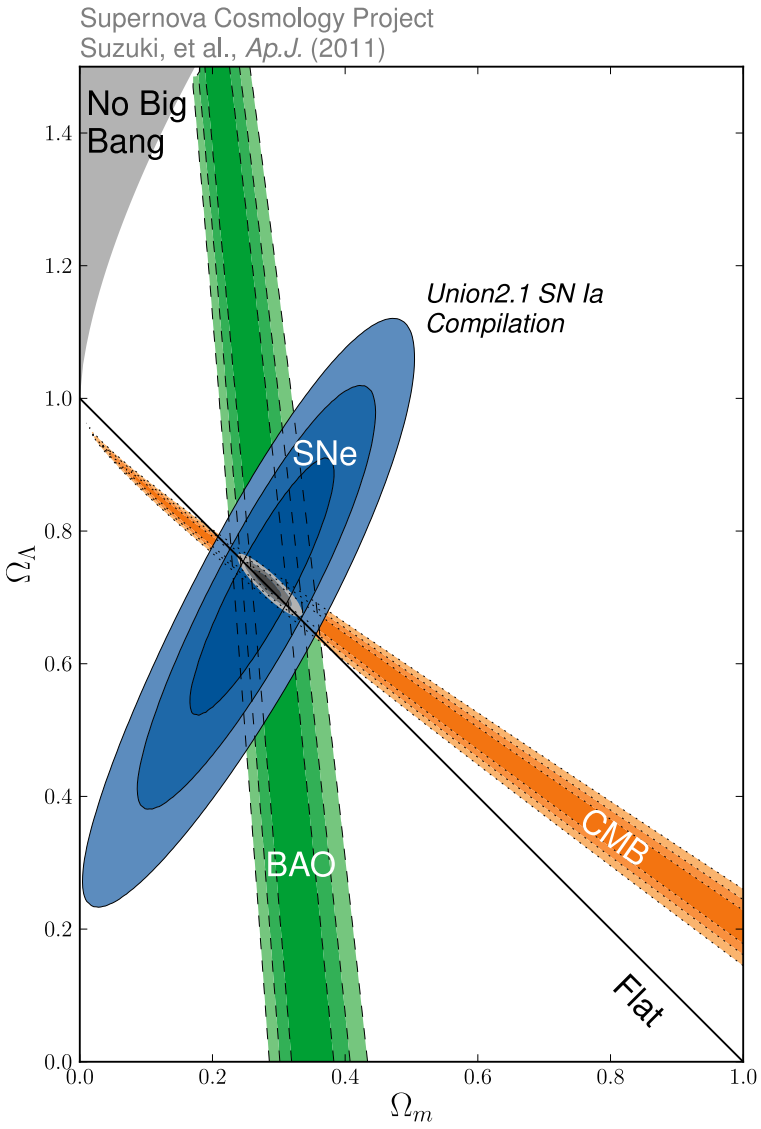

Figure 1.2: Contours of probability in the $\Omega_{\rm m}$–Ω_Λ plane for supernova data combined with CMB and BAO measurements. This shows that a flat model with $\Omega_{\rm m} = 0.3$ and $\Omega_\Lambda = 0.7$ fits all current data sets well.

from the cosmic microwave background (CMB) and baryon-acoustic oscillations (BAO) which are discussed in Section 1.11 and Section 1.12.4 later.

As an aside, the approximations above to $D_{\rm L}$ rely on the Taylor expansion to second order in z of the general expression

$$D_{\rm L} = (1+z)R_0 S_k\left(\frac{1}{R_0}\int_0^z \frac{{\rm d}z}{H(z)}\right) \tag{1.29}$$

if R_0 was extremely small (implying high curvature) then this Taylor expansion is not valid. Essentially by making R_0 smaller and smaller the regime in which the Taylor expansion is valid can be made ever smaller to the point where it avoids any region in which there is data. In this way it is possible to fit *any* measurement of $D_{\rm A}$ or $D_{\rm L}$ with a highly curved Universe, although the necessary form of $H(z)$ and the implied equation of state of the constituents would be odd.

A flat universe with substantial densities only in matter and vacuum is known as a ΛCDM universe and this is the currently accepted standard cosmological model. Interesting features of such a universe are the existence of a big bang ($a \to 0$ in the past), the existence of an infinite span of time into the future ($a \to \infty$ as $t \to \infty$) and the property that it will initially decelerate and then accelerate. The Friedmann equation for such a universe is:

$$H^2 = H_0^2\left(\frac{\Omega_{\rm m}}{a^3} + 1 - \Omega_{\rm m}\right)\ , \tag{1.30}$$

which can be solved to find $a(t)$:

$$a(t) = \left[\left(\frac{\Omega_{\rm m}}{1-\Omega_{\rm m}}\right)\sinh^2\left(\frac{3}{2}\sqrt{1-\Omega_{\rm m}}H_0 t\right)\right]^{1/3}\ . \tag{1.31}$$

The age of the universe can be found by inverting the above relation

$$t_0 \approx 6.52\frac{1}{\sqrt{1-\Omega_{\rm m}}}{\rm arcsinh}\left(\sqrt{\frac{1-\Omega_{\rm m}}{\Omega_{\rm m}}}\right)h^{-1}\,{\rm Gyr}\ . \tag{1.32}$$

Under the assumptions of conventional physics the observation of an accelerated expansion for the universe is strange and this is discussed in Section 1.7.

Another strange feature of these observations of the Universe is that the total energy density $\Omega \simeq 1$. In a Newtonian context this can be seen as the kinetic energy of the expansion exactly balances the potential energy, which in the context of General Relativity means that the Universe would be geometrically exactly flat. This seems very strange given that there are essentially an infinite number of ways the Universe could be open or closed but only a single way that it could be flat. The theory of inflation, discussed in Section 1.9, provides an explanation for the observed flatness. Fig. 1.3 shows the variation of the energy densities in a ΛCDM Universe as a function of scale factor a. This shows the various epochs of our Universe: initially radiation dominated the expansion, then matter and finally vacuum energy takes over and acceleration begins. This thesis concerns itself mainly with the 'late Universe' defined as when radiation is no longer important to the evolution and particularly when dark energy comes to dominate.

Based on this quick round up of observational evidence the rest of this introduction will be biased towards a discussion of models with late time acceleration and a big bang.

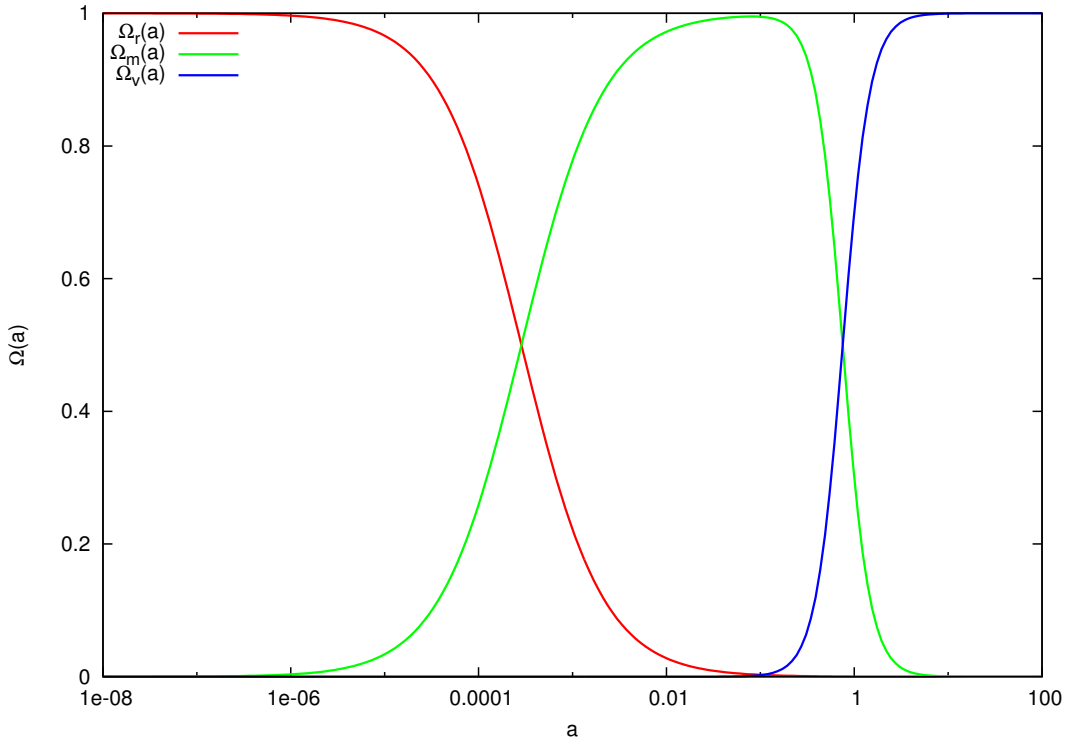

Figure 1.3: The value of the energy densities in a vanilla ΛCDM universe. This shows the different epochs in which different energy densities are important for the evolution of the universe. Of particular interest is the rather gradual shift between radiation domination and matter domination in the early universe and the rapid shift to dark energy domination in the late universe. Initially radiation energy dominates the dynamics of the expansion, then matter and finally vacuum energy and acceleration begins.

1.5 The early Universe

If the Universe contains any radiation at all then this will come to dominate the energy budget when the Universe is smaller due to the a^{-4} scaling of radiation energy density. Following the Universe back into the past and given that theory predicts that $a = 0$ at some point means that there would have been an epoch in which radiation dominated the energy budget. A generic prediction of any model with a big bang is that there would be a hot early epoch and that there should be some light left over from this, which would be observed in all directions – the cosmic microwave background (CMB) radiation. This should come from the time when the Universe transitioned from being an opaque plasma to being neutral, thus releasing the photons. The CMB was first observed (accidently) by Penzias & Wilson (1965) as a perfect black-body with a temperature of $\simeq 2.73$ K that emanates from all directions in space. This temperature of radiation today can be converted into a prediction for the total energy density in radiation:

$$\rho_{\rm r} = \frac{4\sigma T_0^4}{c^3} \ , \tag{1.33}$$

where σ is the Steffan-Boltzmann constant ($\sigma = 5.67 \times 10^{-8}\,\mathrm{W\,m^2\,K^{-4}}$) which in turn can be converted into a value of $\Omega_\gamma \approx 2.5 \times 10^{-5} h^{-2}$. One should note that the total cosmological radiation density is boosted due to the theorised contribution from neutrinos, which should also have a thermal distribution but with a slightly lower temperature of 1.94 K. Cosmological neutrinos have never been observed directly but since the contribution from photons is known accurately from the CMB temperature (equation 1.33) by attempting to measure Ω_r independently one can place constraints on the number of neutrinos (or other relativistic species). The full expression for the radiation density in terms of the effective number of neutrino species (n_eff) is

$$\Omega_\mathrm{r} = 2.5 \times 10^{-5}(1 + 0.227 n_\mathrm{eff}) \ . \tag{1.34}$$

Ω_r can be measured independently via large-scale structure measurements, discussed in Section 1.12.1, and is consistent with 3 neutrino species, as expected from particle physics (*e.g.* Riemer-Sørensen et al. 2013b; Riemer-Sørensen et al. 2013a; Beutler et al. 2014).

The fact that the radiation currently has a black body spectrum might seem strange given that the radiation is no longer in thermal equilibrium but one can show that an initial black body distribution when redshifted remains a black body distribution, but with an effective temperature redshifting according to

$$T(z) = T_0(1 + z) \ . \tag{1.35}$$

In the early Universe, when only matter and radiation are important, the Friedmann equation becomes

$$\left(\frac{\dot{a}}{a}\right)^2 = H_0^2 \left(\frac{\Omega_\mathrm{r}}{a^4} + \frac{\Omega_\mathrm{m}}{a^3}\right) \ . \tag{1.36}$$

At very early times when the energy density of matter is unimportant the universe will grow as $a \propto t^{1/2}$. As matter becomes more important the relation between t and a becomes

$$H_0 t = \frac{2}{3}\frac{\Omega_\mathrm{r}^{3/2}}{\Omega_\mathrm{m}^2}\left[\left(\frac{\Omega_\mathrm{m}}{\Omega_\mathrm{r}}a - 2\right)\sqrt{1 + \frac{\Omega_\mathrm{m}}{\Omega_\mathrm{r}}a} + 2\right] \ , \tag{1.37}$$

which unfortunately cannot be neatly inverted to obtain $a(t)$. From this the time of matter-radiation equality ($\Omega_\mathrm{m} a_\mathrm{eq}^{-3} = \Omega_\mathrm{r} a_\mathrm{eq}^{-4}$ so that $a_\mathrm{eq} = \Omega_\mathrm{r}/\Omega_\mathrm{m}$) can be calculated

$$t_\mathrm{eq} = 13.04 \frac{\Omega_\mathrm{r}^{3/2}}{\Omega_\mathrm{m}^2}\, h^{-1}\,\mathrm{Gyr} \ . \tag{1.38}$$

At sufficiently early times densities are such that thermal equilibrium will occur between the photons and matter, however only in regions that are in causal contact. In this context the isothermal CMB seems odd since one can calculate the size of the particle horizon in a flat universe in which only matter and radiation contribute:

$$R_\mathrm{p}(a) = \frac{2\sqrt{\Omega_\mathrm{r}}}{H_0 \Omega_\mathrm{m}}\left(\sqrt{1 + \frac{\Omega_\mathrm{m}}{\Omega_\mathrm{r}}a} - 1\right) \ . \tag{1.39}$$

The comoving size of the horizon at matter–radiation equality can then be calculated as

$$R_{\rm eq} = \frac{2\sqrt{\Omega_{\rm r}}}{H_0\Omega_{\rm m}}\left(\sqrt{2}-1\right) \ , \tag{1.40}$$

at the time of the release of the CMB the angle on the sky subtended by such a distance is only $\sim 1^\circ$. How the entire sky came to be in thermal equilibrium is a mystery that is dealt with by inflation, discussed in Section 1.9.

As the Universe expands the density will decrease and there will be an epoch when thermal equilibrium is no longer possible and the photons and baryon plasma will decouple. This epoch is known as the 'recombination' of atoms, a misnomer and it should really be called 'combination' since the atoms have never been combined prior to this point. This is the epoch at which the CMB is 'released' and before this the Universe is opaque to radiation. To calculate the recombination epoch as a first guess one might try to equate the decoupling time with the time at which the average photon has enough energy to ionise hydrogen atoms. However, this calculation fails because there is an overwhelming abundance of photons compared to baryonic matter particles ($\approx 10^{10} : 1$), and thus even when the average photon is unable to ionise Hydrogen the small fraction of photons in the high energy tail of the Boltzmann distribution is still able to carry out ionisation. Taking this into account as well as the fact that neutral atoms can only form by emitting pairs of photons (any single photon emitted immediately ionises a nearby atom leaving the ionisation fraction unaffected) allows one to calculate the decoupling redshift as $z_{\rm dec} \sim 1,100$. This is in the era of matter domination, but only a few expansion factors away from matter-radiation equality which can be calculated to be

$$z_{\rm eq} \simeq 24,000\Omega_{\rm m}h^2 \ , \tag{1.41}$$

with $\Omega_{\rm m} = 0.3$ and $h = 0.7$ this becomes

$$z_{\rm eq} \approx 3,500 \ . \tag{1.42}$$

As one follows the Universe back towards $t = 0$ various other interesting epochs occur as the Universe becomes hotter, but a lengthy discussion of these is beyond the scope of this thesis. However, of particular interest is the epoch of big bang nucleosynthesis (BBN). At early times the Universe is comprised of just fundamental particles at early enough times it is hot enough for nuclear reactions to take place. This will convert some fraction of protons and neutrons into Deuterium (D) and Helium (He) and even some heavier nuclei (Li and Be). There are several processes at play here that determine the eventual nuclear abundance; temperature and density dependent reaction rates convert protons and neutrons into heavier nuclei but also unbound neutrons have a short decay time. Surprisingly it turns out that the decay time for free neutrons, and the time that the Universe is hot enough for nuclear reactions to take place are both around 20 minutes. By observing the abundance of D, He and Li nuclei in uncontaminated, pristine gas left over from the big bang, constraints can be put on the rate of nuclear reactions in the early Universe and these depend on the density of Baryons. BBN constrains $\Omega_{\rm b} \sim 0.05$ (*e.g.* Burles

et al. 2001), which is only around one sixth of the total matter content required to be consistent with other observations. This is one of many pieces of observational evidence for missing matter in the Universe, referred to as dark matter. This is discussed in the next section.

1.6 Dark matter

Various cosmological measurements suggest that $\Omega_{\rm m} \sim 0.3$ whilst $\Omega_{\rm b} \sim 0.05$. This leads to the unavoidable conclusion that there is mass in the Universe which is not baryonic. Historically this was first noticed in the 1930s by Fritz Zwicky who noticed that the velocity dispersion of galaxies in clusters was too high if all the mass in the cluster was provided by the stellar content. It was subsequently realised that clusters contain large amounts of hot gas, much more mass in this than in stars, but even this still fails to make up enough mass to provide the observed velocity dispersion of galaxies, which indicates missing dark matter. Additional evidence is provided by the rotation speed of stars and gas in the outer reaches of individual galaxies – these are orbiting much faster than the baryonic content of the galaxy would allow, again suggesting some missing 'dark' mass.

Initially there were two ideas for what dark matter could be, both with rather dubious acronyms: MACHOs (MAssive Compact Halo Objects) a generic name given to dense clumps of matter, such as planets, low mass stars or black holes which could have made up the missing mass. If objects like low mass planets or dark stars existed in abundance then it is plausible that they could make up the missing mass while remaining undetected. However, when it became clear that both BBN and CMB observations (see Section 1.11) required that baryons *not* make up the missing material the idea of baryonic dark matter lost weight. It is possible to conjure up ways of making dense blobs of matter which evade such constraints, such as by having black holes that form early enough in the history of the Universe for baryons in them to not contribute to BBN or the baryon content observable in the CMB (Frampton et al. 2010; Hawkins 2011). To test the MACHO hypothesis microlensing events were looked for in which MACHOs in the halo of the Milky Way would have briefly magnified star light from the LMC as they passed between the observer and the distant stars (Griest 1991). However a signal consistent with zero MACHO contribution to the total matter density was observed (Alcock et al. 1996).

In light of the above it therefore seems likely that the dark matter is comprised of some fundamental particle(s) which has no electromagnetic interactions, thus allowing it to be dark; there are a bewildering array of particle physics theories that introduce the necessary particle(s). Some of these go by the acronym WIMPs (Weakly Interacting Massive Particles) particles that have a weak interaction but no electromagnetic interaction. The 'weakly interacting' hypothesis here is due to the so-called 'WIMP miracle' (*e.g.* Peacock 1999; Roos 2010) by which a massive particle with a standard weak-interaction cross section would produce a contribution to the cosmological mass density of ~ 0.25 because of the number density of such particles that would be left after the particle decoupled from thermal equilibrium in the early Universe. Observations

of the current matter density do not constrain the individual mass of such particles because the same relic density can be produced by fewer high mass particles with a high cross section or more low mass particles with a small cross section. However, if the particle indeed has a cross-section consistent with a weak interaction then the mass of such particles would $\simeq$ 10 GeV, ten times heavier than a proton or neutron.

Another potential candidate for dark matter is the axion – a particle hypothesised to resolve the strong charge-parity (CP) problem in quantum chromodynamics (QCD). Briefly there is no reason for CP symmetry to be respected in QCD but yet experimental evidence shows no CP violation – it seems that a term in the standard model that is not disallowed for symmetry reasons is either zero or very close to zero. Axions are a solution to this problem proposed by Peccei & Quinn (1977) where the CP violating term is promoted to a field and the axions are the oscillations of the new field, which should naturally drive themselves to 0. Such axions would have mass and are thus a reasonable candidate as a dark-matter particle. They are predicted to be very light ($<$ 1 eV) but would be a cold dark-matter particle because they form a Bose-Einstein condensate and were never in thermal equilibrium with the rest of the Universe.

From the perspective of large-scale structure theory (the subject of this thesis) it matters very little what dark matter actually is as long as it can be considered to only interact via gravity. The results presented in this thesis would be as valid for dark matter comprising of 10 GeV WIMPs as for that comprising of $10M_{\odot}$ black holes. The only exception to this is that low particle masses, that have their number densities determined by thermal physics in the early Universe, actually matters from a cosmological perspective because particles of lower mass remain relativistic for more of the history of the cosmos. This has two main effects: First the epoch of matter domination is delayed compared to a model with heavier matter particles. Second, whilst relativistic the particles erase perturbations in themselves on scales corresponding to the length scale that they were able to travel relativistically. This is discussed in more detail in Section 1.12.1 but the fact that the Universe contains structures below certain scales (such as dwarf galaxies) puts limits on how massive the dark particle(s) can be and can be used to rule out models of 'warm' or 'hot' dark matter. For these reasons it is known that neutrinos cannot make up all of the dark matter density because they are light enough that if they did make up all dark matter then the density distribution in the Universe would be much smoother than it is observed to be (see Section 1.12.1). However, neutrinos are known to have some mass (Ahmad et al. 2001) so they must make up some fraction of the dark matter. However, if the dark particle is the canonical $\sim$ 10 GeV WIMP then it is very much 'cold' and such a particle would spend a negligible time travelling relativistically in the early Universe and thus is a good dark-matter candidate.

1.7 Dark energy

The late time acceleration of the Universe is mysterious for a number of reasons: mathematically acceleration can be produced by adding a new fundamental (cosmological) constant of nature into the Einstein Field Equations

$$R_{ab} - \frac{1}{2}Rg_{ab} + \Lambda g_{ab} = -8\pi G T_{ab} \ . \tag{1.43}$$

where the Λ term gives rise to a term in the Friedmann equation that causes accelerated expansion. This would modify the equation (1.3) to be

$$\left(\frac{\dot{a}}{a}\right)^2 = \frac{8\pi G}{3}\rho(a) + \frac{\Lambda}{3} - \frac{kR_0^2}{a^2} \ . \tag{1.44}$$

Adding a constant like this into equation (1.43) constitutes a modification to the gravity law and therefore will also modify other aspects of gravity including planetary orbits, galaxy dynamics and stellar structure. However, the magnitude of Λ required to explain the observed cosmological acceleration is many orders of magnitude smaller than could ever be observed in the Solar System, or that would affect star or galaxy structure in any significant way. The constant factor of $\Lambda/3$ can be related to the energy density term $\Omega_\Lambda = \Lambda/3H_0^2$ defined in equation (1.10). This term can explain the observations of late time acceleration in the Universe in a way that agrees with all current data sets. However, it involves adding a second constant of nature into the action (see later) of gravity arbitrarily, which may seem to be an inelegant way of dealing with the problem.

This exact same accelerating behaviour can be reproduced by adding a homogeneous vacuum energy with negative pressure, $p = -\rho$, which then satisfies $\dot{\rho}_\Lambda = 0$. This is slightly different to the above as it is in effect modifying the stress energy tensor T_{ab} in equation (1.43) by adding a new fluid into the universe. Conversely, adding a Λ term is adding to the G_{ab} part of the equations, on the left hand side of equation (1.43). These two models of accelerated expansion are indistinguishable. However, one benefit of the vacuum energy approach is that just such a constant vacuum energy is predicted in quantum field theory (QFT), although the field theoretic calculation for the vacuum energy is formally infinite and only takes a finite value when the integral used to compute the vacuum contribution is cut off at some energy scale. The motive for this being that QFT is only valid up to this energy and beyond it some other theory would take over, hopefully cutting off the integral quickly.

The field theory expression for the vacuum energy density is given by summing the zero-point energy of oscillators over all mode frequencies

$$\rho_{\rm v} = \frac{\hbar}{2\pi^2 c^5}\int_0^{\omega_0} \omega^3 {\rm d}\omega \ , \tag{1.45}$$

where ω_0 is the cut-off imposed on the integral. This expression can be evaluated as

$$\rho_{\rm v} = \frac{\hbar\omega_0^4}{8\pi^2 c^5} \ , \tag{1.46}$$

or written in terms of an energy cut off E_0

$$\rho_{\rm v} = \frac{E_0^4}{8\pi^2\hbar^3c^5} \ . \tag{1.47}$$

In order for this to match the vacuum energy necessary in cosmology, E_0 would be an energy scale of ∼meV. But this is an absurdly low scale: the first energy scale where one may conceivably cut off the integral would be the energy scale of the Large Hadron Collider (TeV) because particle physics has only been experimentally tested up to this energy. This cutoff gives an error in ρ_v of a factor 10^{64} . Other energy scales where the cutoff may conceivably be imposed would be the energy of grand unification $\sim 10^{16}$ GeV and the Planck energy $\sim 10^{18}$ GeV and these give errors in $\rho_{\rm v}$ of $\sim 10^{112}$ and $\sim 10^{120}$ respectively. This all seems rather bleak for the prospect of explaining the accelerated expansion of the Universe with quantum vacuum energy but one must bear in mind that the energy scale raised to the fourth power exaggerates the magnitude of the problem. In terms of energy scale the above errors are factors of 10^{16}, 10^{28} and 10^{30} respectively. This then generates a new problem, the cosmological constant problem (Weinberg 1989): one is forced to ask why the very high value of $\rho_{\rm v}$ that is predicted is *not* observed. There must be some mechanism either for screening gravity from the effects of the vacuum energy or for cancelling the contribution from vacuum energy either almost entirely, such that the tiny remainder accounts for the accelerated expansion, or leaving another physical mechanism to provide the accelerating component.

It has also been suggested recently by Koksma & Prokopec (2011) that the vacuum energy terms in the equations above are not Lorentz invariant and would not yield $w = -1$. Applying a relativistic cutoff procedure converts the naive $\rho_{\rm v} \sim M^4$, where M is the cutoff scale, to $\rho_{\rm v} \sim m^4 \ln(M/m)$ where m is the particle rest mass. Based on known particles this is several 100 GeV, so the problem remains.

Although the discovery of a cosmological constant and an accelerated expansion to the Universe came as a surprise to most, it should be noted that it was in fact *predicted* before being measured, by Weinberg (1987). Although it should be noted that inflation predicted the Universe to be flat and this leads to a tension with the ages of astronomical systems if $\Omega_{\rm m} = 1$, so there was some early motivation for Λ. The logic Weinberg (1987) used was anthropic in nature – Weinberg reasoned that if the cosmological constant took its bare value, $\sim 10^{120}$ times larger than the observed value, then the acceleration of the Universe would have prevented structure from growing, so no observers would be in that Universe to observe it (see Section 1.10.1 for how vacuum energy stops perturbations from growing). If one then assumes that there is a distribution in values of $\rho_{\rm v}$ then one is led to conclude that one would expect to observe a cosmological constant that is as large as possible without preventing structure growth; essentially this is what is observed. This logic has been investigated by Efstathiou (1995), Martel et al. (1998) and Peacock (2007) who conclude that a value of $\Omega_\Lambda \sim 0.7$ is expected in such an anthropic picture. Such anthropic arguments cause fierce debate amongst cosmologists, mainly because they require the existence of a large ensemble of universes each of which have different values of $\rho_{\rm v}$, an idea that could be potentially forever untestable. Although the existence of a

multiverse of universes is actually a generic prediction of some inflationary theories (*e.g.* Linde 1986), but whether or not they are able to have differing values of fundamental constants is less obvious.

It is also possible that the accelerated expansion is caused by something other than a cosmological constant or a vacuum energy. Some of these ideas are called 'dark energy'; these aim to reproduce the accelerated expansion in a more 'natural' way than by adding in a vacuum energy or by modifying the field equations. The general ethos behind these models is that some symmetry mechanism will set the value of the quantum vacuum energy to exactly zero and they then aim to make up the 'small' residual dark energy necessary for late time acceleration. It is convenient to talk about a dark energy model in terms of the 'equation of state parameter' w which relates pressure to energy density: $p = w\rho$. For matter $w = 0$, for radiation $w = 1/3$ and for the cosmological constant model or pure vacuum energy $w = -1$. Dark energy models can produce different values of w or values that vary over time. If one allows w to be a constant free parameter then one can show from equation (1.6) that the energy density of that species varies with a according to

$$\rho(a) = \rho_0 a^{-3(1+w)} \ , \tag{1.48}$$

which gives a late time Friedmann equation for a flat Universe, containing only matter and dark energy, of

$$H^2 = \left(\frac{\Omega_{\rm m}}{a^3} + \Omega_w a^{-3(1+w)} \right) \ , \tag{1.49}$$

and acceleration equation

$$A = -\frac{H_0^2}{2} \left[\Omega_{\rm m} a^{-3} + (1+3w)\Omega_w a^{-3(1+w)} \right] \ . \tag{1.50}$$

If the Universe is dominated by the dark energy ($\Omega_{\rm m} = 0$, $\Omega_w = 1$) the universe will undergo accelerated expansion if $w < -1/3$. For a multi-component universe containing matter together with dark energy with a constant equation of state, acceleration occurs if $(1+3w)\Omega_w a^{-3w} < -\Omega_{\rm m}$.

Since the value of w affects the rate at which the Universe will expand, it can be constrained by measuring the expansion. The luminosity distance, given in equation (1.24), as measured by low redshift supernovae can be approximated as

$$D_{\rm L} = \frac{z}{H_0} \left\{ 1 - \frac{z}{4} [\Omega_{\rm m} + (1+3w)\Omega_w - 2] \right\} \ , \tag{1.51}$$

or if flatness is assumed then $\Omega_{\rm m} + \Omega_w = 1$ and

$$D_{\rm L} = \frac{z}{H_0} \left\{ 1 - \frac{z}{4} [3w(1-\Omega_{\rm m}) - 1] \right\} \ . \tag{1.52}$$

Current constraints on a constant w show it to be within $5-10\%$ of -1, entirely consistent with dark energy being a cosmological constant or vacuum energy; these constraints are shown in the upper panel of Fig. 1.4 from Suzuki et al. (2012).

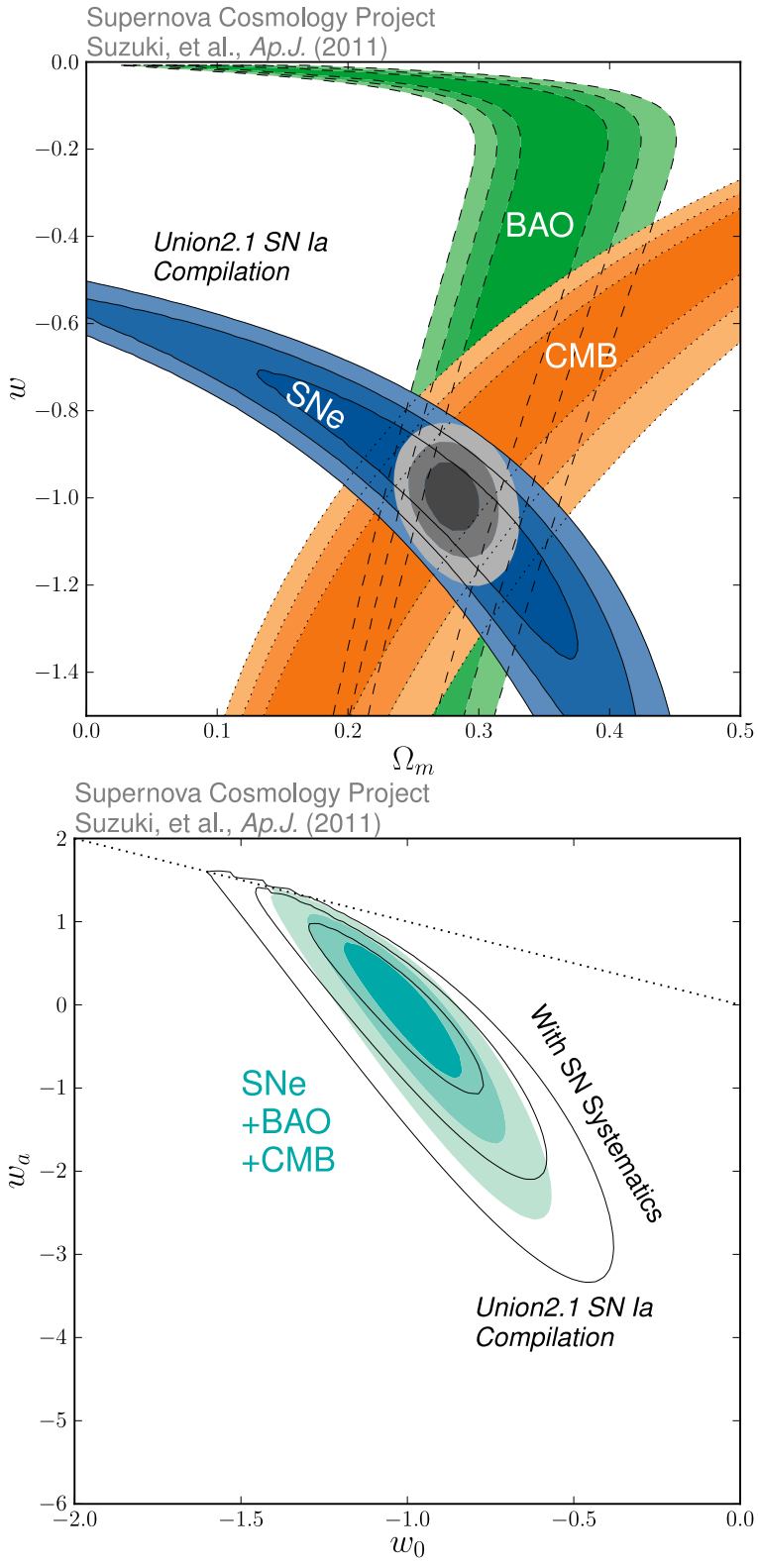

Figure 1.4: Current constrains on dark energy with constant equation of state w. Measurements are entirely consistent with $w = -1$ vacuum energy or Λ type models.

Additionally, in phenomenological dark energy models, w can be allowed to be any function of a. In this case the above expressions are not valid, the energy density in dark energy is calculated via

$$\rho(a) = \rho_0 \exp \int_a^1 \frac{1 + w(a)}{a} \, \mathrm{d}a \ . \tag{1.53}$$

In the case of a general $w(a)$ it is quite difficult to set constraints on the form of $w(a)$ because it can be allowed to mimic the observations for values of a where data exist and to behave quite differently for other values of a. Constraints are shown for the particular parametrisation of Chevallier & Polarski (2001) and Linder (2003), $w(a) = w_0 + (1 - a)w_\mathrm{a}$, in the lower panel of Fig. 1.4 from Suzuki et al. 2012. Note that this form of $w(a)$ can be considered as a Taylor expansion at $a = 1$ and thus might not be a good description of the equation of state at earlier epochs.

Dark energy with arbitrary w or $w(a)$ can be difficult to explain in the context of a physical theory of what the dark energy actually is. Therefore some effort has gone into considering how adding new components to the Universe that have a theoretical underpinning would affect the evolution of the cosmos. The most popular models are scalar field models where an additional scalar degree (or degrees) of freedom is added to the universe and minimally coupled to gravity – known as quintessence theories. These models have received additional impetus lately due to the discovery of the Higgs Boson (Higgs 1964) which is the first discovery of a (possibly) fundamental scalar field in nature. Scalar fields can be invoked at the level of the action from which they are derived. The gravitational field equations in equation (1.1) can be derived from an action principle via the Einstein-Hilbert action

$$S = \int \mathrm{d}^4x \, \sqrt{|g|} \left(\frac{R}{16\pi G} + \mathcal{L}_\mathrm{m}(\psi_i, g_{ab}) \right) \ , \tag{1.54}$$

where g is the determinant of the metric, $R = R^a_a$ is the Ricci scalar and $\mathcal{L}_\mathrm{m}$ is the Lagrangian of matter fields ψ_i, which follow geodesics of the metric g_{ab}. Minimisation of the above action with respect to g_{ab} results in equation (1.1). For a scalar field ϕ that is minimally coupled to gravity, a possible action is

$$S = \int \mathrm{d}^4x \, \sqrt{|g|} \left\{ \frac{1}{16\pi G} \left[R + \partial_a\phi \, \partial^a\phi - 2V(\phi) \right] + \mathcal{L}_m(\psi_i, g_{ab}) \right\} \ . \tag{1.55}$$

Applying the principle of least action with respect to the field ϕ, the following Klein-Gordon equation of motion is obtained:

$$\Box\phi + V'(\phi) = 0 \ , \tag{1.56}$$

where $\Box = \nabla_a\nabla^a$. For a spatially homogeneous ϕ in an expanding background the Klein-Gordon equation simplifies to

$$\ddot{\phi} + 3H\dot{\phi} + V'(\phi) = 0 \ . \tag{1.57}$$

The gravitational field equation can also be derived by applying the principle of least action to the metric, which necessarily receives a ϕ contribution due to the $\sqrt{|g|}$ term minimally coupling

gravity to the scalar:

$$R_{ab} - \frac{1}{2}g_{ab}R + \frac{1}{2}\partial_a\phi\,\partial_b\phi - g_{ab}\left[\frac{1}{2}\partial_c\phi\,\partial^c\phi - V(\phi)\right] = -8\pi G T_{ab}\ . \tag{1.58}$$

In the case of minimal coupling discussed here, the terms containing ϕ in this equation can be considered as an effective stress-energy contribution,

$$8\pi G\, T^{\phi}_{ab} = \frac{1}{2}\partial_a\phi\,\partial_b\phi - g_{ab}\left[\frac{1}{2}\partial_c\phi\,\partial^c\phi - V(\phi)\right]\ . \tag{1.59}$$

This is in contrast to modified gravity theories, discussed in the next section, where the coupling mixes R_{ab} and ϕ terms. The effective energy density and pressure of such a field in a homogeneous universe can be read off:

$$\rho = \frac{1}{2}\dot{\phi}^2 + V(\phi)\ , \tag{1.60}$$

$$p = \frac{1}{2}\dot{\phi}^2 - V(\phi)\ , \tag{1.61}$$

which are a kinetic and potential energy terms for ϕ. The same result for T^{ϕ}_{ab} can be obtained by applying the theorem of Noether. Thus the effective value for w is

$$w(\phi) = \frac{\frac{1}{2}\dot{\phi}^2 - V(\phi)}{\frac{1}{2}\dot{\phi}^2 + V(\phi)}\ . \tag{1.62}$$

One can see that if the potential energy of the field dominates over the kinetic energy the value of $w \to -1$ and accelerated expansion of the universe will occur if the scalar field makes up a large enough fraction of the total energy density of the universe (equation 1.61).

In scalar field models the values of ϕ_0 and $\dot{\phi}_0$ must be set by hand and the potential $V(\phi)$ is a free function. If these parameters are carefully chosen they can reproduce the observed late time acceleration of the Universe. Depending on the potential the value of w will change over time and this can produce observable effects in the expansion of the universe that can, in principle, be distinguished from pure ΛCDM. However, one should note that such models can produce a universe which looks arbitrarily similar to a vanilla ΛCDM universe. If the potential is a constant and the field is stationary then $w = -1$ for all times and the model is indistinguishable from vacuum energy or cosmological constant. However, one difference is that scalar field dark energy will in general cluster on scales of the size of the horizon, in contrast to vacuum energy. Although, whether dark energy clusters on super-horizon scales or not is a function of the model; one can introduce sound speeds by hand to allow or disallow clustering of dark energy.

1.8 Modified gravity

It was shown by Lovelock (1971) that the gravitational field equations derived from the Einstein-Hilbert action in equation (1.54) are the unique, second order (in g_{ab} derivatives), theory possible in 4 dimensions if one assumes that the connection is symmetric and that the equations

are tensorial. It follows that in order to generate modified gravity theories, at least one of the following is required; higher than second order terms must appear; the number of dimensions must be increased; additional fields must interact with gravity; the tensor nature of the equations must be changed; or the equations must be non-local. A range of possible theories is discussed in detail in Clifton et al. (2012). This section briefly discusses some theories that work at the level of the action and that are perhaps the simplest possible ways of modifying the law of gravity.

The most obvious modification is to allow functions of R, rather than just a linear R term, to appear in the action. These are so-called $f(R)$ theories (Carroll et al. 2005), which have an action of the form

$$S = \int \mathrm{d}^4x \, \sqrt{|g|} \left[\frac{R + f(R)}{16\pi G} + \mathcal{L}_\mathrm{m}(\psi_i, g_{ab}) \right] \, . \tag{1.63}$$

Minimising this with respect to g_{ab} results in a modified field equation

$$R_{ab} - \frac{1}{2} g_{ab} \left[R + f(R) \right] + (g_{ab} \Box - \nabla_a \nabla_b + R_{ab}) f'(R) = -8\pi G T_{ab} \, . \tag{1.64}$$

These equations have the potential to be 4^th order in metric derivatives because R is second order in metric derivatives and two further derivatives are taken by the terms within the circular brackets. $f(R)$ theories avoid the Ostrogradski instability (see Woodard 2007 for an explanation) by being degenerate in second order derivatives of g_{ab} (they only appear linearly in R). This is not true of theories constructed from the scalars $R_{ab}R^{ab}$ or $R_{abcd}R^{abcd}$ for example, and is one of the features that makes $f(R)$ theories appealing. If $f(R)$ takes the simple form of a constant, or linear function, then $f'(R) = 0$ and the equations remain second order. A particularly simple case is if the modification is a (cosmological) constant term, so that $f(R) = -2\Lambda$ then $f'(R) = 0$ and the field equation becomes

$$R_{ab} - \frac{1}{2} R g_{ab} + g_{ab}\Lambda = -8\pi G T_{ab} \, , \tag{1.65}$$

which, in a Friedmann Universe, gives rise to 'natural' accelerated expansion via the Λ term without needing to invoke any dark energy as long as Λ is positive, as discussed in Section 1.7. If Λ is negative then this would introduce a deceleration term to the Friedmann equations. Generally $f(R)$ can be any desired function and a goal of $f(R)$ theorists is to find functional forms that produce the necessary cosmic acceleration without simply adding a constant term into the action. This must be done in a way that is compatible with the numerous tests of gravity conducted within the Solar System. $f(R)$ models have also been proposed to produce inflation (discussed in the next section) in the early Universe (*e.g.* Starobinsky 1980), and even as a way of explaining dark matter (Böhmer et al. 2008).

A seemingly distinct approach from $f(R)$ theories is to couple gravity to some other fields in the action. The motivation for this comes from particle physics, which is fully understood via an action principle and interactions between different fields (for example, photons and electrons) manifest themselves as coupling terms in the action. For a single scalar field coupled to gravity

a possible action is

$$S = \int \mathrm{d}^4x\sqrt{|g|}\left\{\frac{1}{16\pi G}\left[F(\phi)R + Z(\phi)\,\partial_a\phi\,\partial^a\phi - 2V(\phi)\right] + \mathcal{L}_{\rm m}(\psi_i, g_{ab})\right\}\ , \tag{1.66}$$

where ϕ is the new field and F, Z, and V are all arbitrary functions of ϕ. In fact, by a suitable redefinition of ϕ either F can be set to ϕ or Z can be set to 1, so such theories really only contain two free functions of the field. Such a theory is known as a 'scalar-tensor' theory. F provides some direct coupling between ϕ and gravity, which can be thought of loosely as R; Z relates to the kinetic term for ϕ and V is a potential term. If $F = 1$ then the theory is purely a 'dark energy' theory with no direct gravitational couplings. For example, the action shown in equation (1.55) could simply be embedded into equation (1.54) (with $Z = 1$ in that specific case), however dark energy fields like this are necessarily coupled to gravity via the $\sqrt{|g|}$ term. Such a coupling is called a 'minimal coupling' provided that matter fields follow the geodesics of the metric g_{ab}. In order to directly modify gravity $F(\phi)$ must be present. Clearly the effective value of the gravitational constant in the new theory is given by $G_{\rm eff} = G/F(\phi)$ and ϕ can be thought of as providing some $5^{\rm th}$ force to the Universe, noting the possibility of the gravitational 'constant' depending on environment if the value of ϕ is different. This then leads to the possibility of 'screening' (*e.g.* Khoury & Weltman 2004; Hu & Sawicki 2007a) where 'normal' gravity may be recovered in regions such as the Solar System and/or Galaxy and the modifications only being important on cosmological scales. For completeness the field equations of both g^{ab} and ϕ follow from variation of the action in equation (1.66) (*e.g.* Esposito-Farèse & Polarski 2001). Variations with respect to ϕ lead to

$$2Z(\phi)\Box\phi = F'(\phi)R - Z'(\phi)g^{ab}\partial_a\phi\,\partial_b\phi - 2V'(\phi)\ , \tag{1.67}$$

whereas variations with respect to g^{ab} give

$$\left(R_{ab} - \frac{1}{2}g_{ab}R\right)F(\phi) + (g_{ab}\Box - \nabla_a\,\nabla_b)\,F(\phi) \\ + Z(\phi)\partial_a\phi\,\partial_b\phi - g_{ab}\left[\frac{1}{2}Z(\phi)g^{cd}\partial_c\phi\,\partial_d\phi - V(\phi)\right] = -8\pi G T_{ab}\ . \tag{1.68}$$

The trace of this equation then gives energy conservation

$$(3\Box - R)F(\phi) - Z(\phi)g^{ab}\partial_a\phi\,\partial_b\phi + 4V(\phi) = -8\pi G T\ . \tag{1.69}$$

As one can see, these equations couple the scalar to gravity in a non-trivial manner.

It can be shown that any $f(R)$ theory can be mapped onto a scalar-tensor theory and thus that $f(R)$ theories represent a sub class of scalar-tensor theories. The easiest way to see this is to write the $f(R)$ action in the following, perverse way

$$S = \int \mathrm{d}^4x\,\sqrt{|g|}\left\{\frac{[1 + f'(R)]R - f'(R)R + f(R)}{16\pi G} + \mathcal{L}_{\rm m}(\psi_i, g_{ab})\right\}\ , \tag{1.70}$$

then let $1 + f'(R) = \phi$ and $-f'(R)R + f(R) = -2V(\phi)$ which leaves the action with the form of a non-minimally coupled scalar-tensor theory

$$S = \int \mathrm{d}^4x\,\sqrt{|g|}\left[\frac{\phi R - 2V(\phi)}{16\pi G} + \mathcal{L}_{\rm m}(\psi_i, g_{ab})\right]\ , \tag{1.71}$$

thus all $f(R)$ theories can be mapped to scalar-tensor theories with the restricted functional form, $F = \phi$ and $Z = 0$, in equation (1.71). That this mapping exists is related to the fact that $f(R)$ theories avoid the Ostrogradski instability.

The equation of motion for $f'(R)$ can be derived by taking the trace of equation (1.64). With the notation $f_R = f'(R)$ the trace is

$$\Box f_R = \frac{1}{3}[R + 2f(R) - Rf_R - 8\pi GT] \ , \tag{1.72}$$

which is reminiscent of a Klein-Gordon type equation for a scalar:

$$(\Box + m^2)\phi = 0 \ . \tag{1.73}$$

ϕ has a Compton wavelength $\lambda = 1/m$, which approximately governs the scale over which effects of the field are felt with this tending to be infinite for massless fields.

Both equation (1.64) and equation (1.72) are completely general, and apply for any $f(R)$, but at this point it is worth considering theories that produce a viable cosmological history; one at least not too dissimilar from that observed. These theories should leave the expansion history of the Universe essentially unchanged, which means that equation (1.64) must be approximately the same as ΛCDM for the homogeneous Universe. A way of achieving this constrains $f(R)$ to have the limiting form of a (cosmological) constant plus a correction term. An example of such a theory is that of Hu & Sawicki (2007a) where $f(R)$ has the form of a broken power law

$$f(R) = -R_0 \frac{c_1 (R/R_0)^n}{c_2 (R/R_0)^n + 1} \ , \tag{1.74}$$

which has parameters c_1, c_2, R_0 and n. If one expands this function in the regime where $R \gg R_0$ then $f(R) \to -R_0 c_1/c_2$ which can be equated to the standard cosmological constant term of -2Λ in the action. In the opposite limit $R \ll R_0$ and $f(R) \to 0$ and the cosmological constant vanishes from the action. Thus such models can plausibly create an accelerated expansion of the Universe, although it should be noted that fine tuning is necessary to produce the accelerated expansion at the present, noting that it will vanish in the future as $R \ll R_0$. One should also note that in regions of high curvature $R \gg R_0$ and gravity will be modified via a pure cosmological constant term and this can be unobservable in regions of high density. If one explores the $R \gg R_0$ limit in more detail then the asymptotic form of $f(R)$ is

$$f(R) \approx -R_0 \frac{c_1}{c_2} + R_0 \frac{c_1}{c_2^2} \left(\frac{R_0}{R} \right)^n \ , \tag{1.75}$$

which is a cosmological constant plus a correction term that depends on the local value of the curvature. At the background level, as in ΛCDM, the curvature can be considered as a proxy for density because equation (1.72) is $R \approx 8\pi GT$ for these models, with an error $O(|f_{R0}|)$, if they are to produce a viable cosmological history. For homogeneous cosmological models $f(R)$ thus tends to a constant and the Friedmann equation is almost identical to standard ΛCDM. The derivative of $f(R)$ can be calculated in this limit,

$$f'(R) = -n \frac{c_1}{c_2^2} \left(\frac{R_0}{R} \right)^{n+1} \ , \tag{1.76}$$

with the value today ($R = R_0$) defined to be f_{R0}. $f(R)$ can then be written as

$$f(R) = -2\Lambda - R_0 \frac{f_{R0}}{n} \left(\frac{R_0}{R} \right)^n \quad . \tag{1.77}$$

This form of $f(R)$ is that used in the literature and is used throughout this thesis. Rather than specifying c_1, c_2 and n the theory is usually specified via Ω_Λ, f_{R0} and n. Note that based on the effective form of $f(R)$ in equation (1.77) Wang et al. (2012) have disputed that an $f(R)$ theory like this is a modified gravity theory, since essentially the modification to gravitational forces (governed by f_{R0} and n) is completely independent of the accelerated expansion of the cosmos (governed by Ω_Λ) and this is the limit in which the theory is most often considered.

1.9 Inflation

Up to now, the picture painted of our Universe discussed seems strange in several ways: The isothermal CMB – how can parts which have had no causal contact be the same temperature? The flatness of the Universe – of all possible configurations that the Universe could be in why does it seem to be exactly flat? The big bang problem – the equations seem to suggest that $a = 0$ at some point in the past, but this represents a singularity in the Friemann metric (key quantities become infinite, such as ρ, and certain coordinates disappear *etc.*), so what exactly happens as $a \to 0$? The expansion problem – why is the Universe expanding at all, and why is it doing this in such a uniform, smooth manner? This last problem is not often addressed but it is a mystery in itself as to why the Universe is so smooth and featureless on large scales and why it expands uniformly given the vast number of other possible inhomogeneous, anisotropic configurations one could dream up.

There is also another problem which relates more to grand unified theories of particle physics. These theories suggest that all the electromagnetic, strong and weak forces were all unified at some point in the past. A consequence of this is the magnetic monopole problem (*e.g.* Linde 1983; Rajantie 2012) – magnetic monopoles, the equivalent of electric charge carriers but for the magnetic field, should exist in abundance in the Universe. However, they obviously do not ($\nabla \cdot \mathbf{B} = 0$), so some mechanism is required to dilute the abundance of monopoles relative to charged particles.

These problems can be explained to a certain degree by a period of exponential expansion in the early Universe. This idea, named inflation, was first proposed by Guth (1981) and says that rather than the Universe going to $a = 0$ at the point that the conventional Friedmann equations would imply this would happen, the Universe actually shrinks exponentially into the past. This means that the singularity is avoided and that time could, in principle, continue all the way back to $-\infty$. The simplest way of producing such an expansion is with a scalar field which is very similar to that discussed in the context of dark energy in Section 1.7, but at a very different energy scale. The field has an equation of state which is governed by equation (1.62) and if the field is in 'slow roll' then the potential energy dominates the kinetic and $w \to -1$. If

this is the dominant contribution to stress energy the Friedmann equation becomes

$$\left(\frac{\dot{a}}{a}\right)^2 = H_\phi^2 = \frac{8\pi G}{3}\rho_\phi \approx \frac{8\pi G}{3}V(\phi) \tag{1.78}$$

where H_ϕ is approximately constant. The solution to this equation is exponential expansion for a

$$a \propto e^{H_\phi t} \tag{1.79}$$

such that a never reaches 0 and time can extend indefinitely into the past.

This expansion is often described as being 'rapid' but in fact it is extremely slow compared to the only relevant timescale at that point, which is the timescale that the Universe would collapse on, based on being dominated by radiation. This relatively slow accelerating start to the Universe allows the actual particle horizon of the Universe to be much larger than one would otherwise infer from a singularity followed by a period of radiation domination, so a small patch initially in thermal equilibrium can inflate so as to contain the current observable Universe. The theory also allows the number of magnetic monopoles to be diluted away and this can be done to any desired degree based on how long the period of inflation lasts for. Inflation also naturally drives the Universe towards flatness, this is not to say that an initially curved Universe can be uncurved but more that it can be expanded so much that any deviation from perfect flatness would be arbitrarily hard to measure. This can be seen in the case of homogeneous Universes (it is more difficult to see what effect inflation would have for non-homogeneous initial matter distributions) via the evolution of the total density parameter. If only vacuum energy is important

$$1 - \Omega(a) = \frac{(1 - \Omega_\Lambda)}{a^2\Omega_\Lambda} \ , \tag{1.80}$$

as a increases $\Omega(a) \to 1$ and the curvature scale becomes ever more distant.

What happened before inflation, or even if inflation could have lasted indefinitely into the past, are still open questions in cosmology (Linde 1986; Peacock 2007). Initially it was believed that inflation could convert an arbitrary configuration of pre-inflationary Universe into something that resembled our Universe to a high degree of accuracy (Guth 1981). The period following this when the Universe expands rapidly, but decellerating, while dominated by the energy density in radiation is then the conventional hot big bang. However, the generality of initial conditions required for inflation have been called into question (Penrose 1989) and some believe that initial conditions that would allow inflation to arise are even more contrived than the special conditions in the Universe that it is then able to generate. This is particularly because conditions for inflation to begin seem to require a very low entropy initial state.

An additional benefit of an inflationary scenario is that it provides a mechanism for producing structure in the Universe. This was not realised when the theory was initially put forward but came to light later as an additional benefit later. Essentially small, inevitable quantum mechanical fluctuations in the fields responsible for inflation are produced but are quickly stretched out by the expansion and stretched out of causal contact so that they do not disappear and are

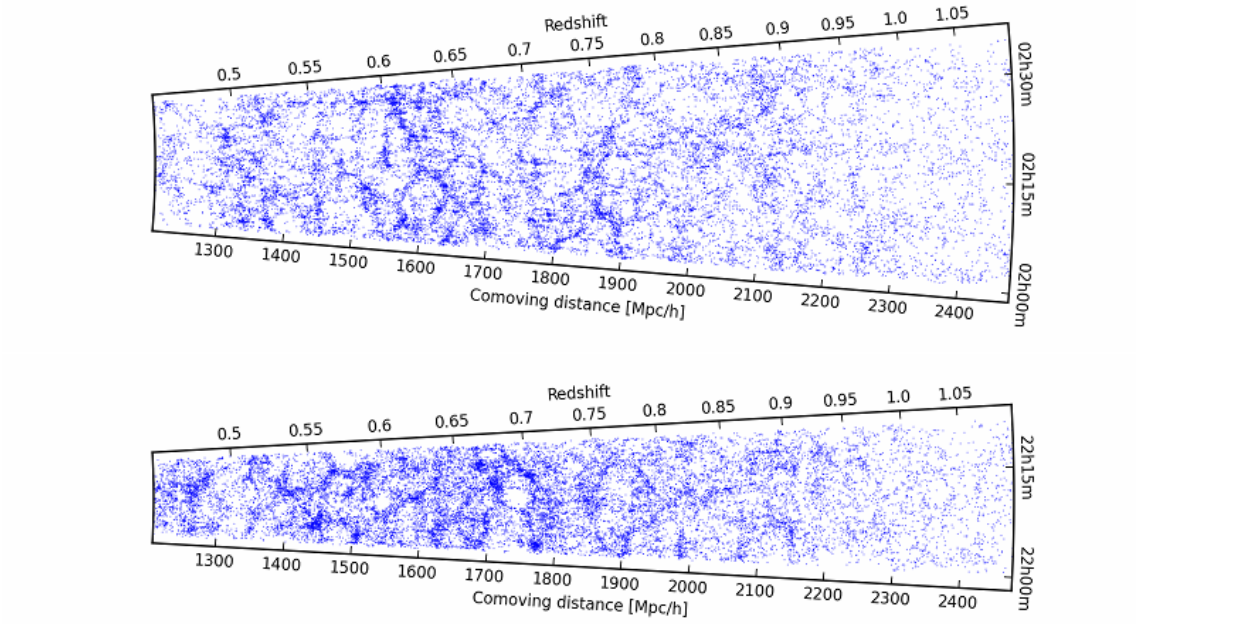

Figure 1.5: The distribution of galaxies as observed in the 'W1' and 'W4' fields VIPERS. Very clearly the distribution is not random and a clear filamentary structure can be seen in the distribution. [Image credit – VIPERS team]

instead imprinted upon the space-time as the expansion progresses. When inflation stops small fluctuations in field values eventually manifest themselves as small fluctuations in density in the Universe and these inevitably grow under the influence of their own gravity. These then go on to produce all of the complex structure now observed in the Universe. This is one of the great achievements of the inflationary theory and it is all the more impressive given that it came as a by-product of the theory, rather than the theory being designed to produce this outcome.

1.10 Inhomogeneity in the cosmos

So far the discussion of the Universe is valid in the case of perfectly smooth, homogeneous universe. However, this thesis concerns itself with theoretical descriptions for the formation and evolution of structure directly. The rest of this introduction will discuss various ways of analysing structure formation and growth in an expanding universe.

When one looks out into the cosmos one sees that galaxies, far from being randomly distributed, form a complicated looking filamentary pattern which contains very over-dense clusters of galaxies and gaping voids. One of the great goals of cosmology is a calculation of the statistical properties of this pattern to arbitrary precision for any desired set of cosmological parameters, or any desired theory of dark energy or gravity. The main goal of this thesis is to

carry out some approximate forms of this calculation.

The pattern in galaxies is set down initially probably by some inflation-like process in the very early Universe which seeds an initially smooth matter distribution with small perturbations. Initially these perturbations are in the value of the inflation field but when this decays the perturbations end up in the dark matter, baryonic matter and radiation densities. These perturbations then grow and evolve over the history of the cosmos and eventually develop into all of the structure observed. Galaxies today represent the visible points in what is thought to be an underlying skeleton of dark matter. The distribution of galaxies can be seen by any state of the art survey and Fig. 1.5 shows a recent example from the VImos Public Extragalactic Redshift Survey (VIPERS; Guzzo et al. 2013), where the distribution can be seen to be obviously not random.

Presented with the problem of calculating the evolution of the distribution of structure initially one might think that the solution would be to set some initial conditions and solve the Einstein Field Equations to see how this pattern evolves in general. However, so far no solution to the field equations capable of describing such an evolution has been found and therefore more approximate methods are used: Perturbation theory deals with solutions to equations in a regime where certain parts of the equations are 'small' relative to other parts. This is useful in cosmology because density departures from homogeneity start off very small. Perturbation theory is discussed in Section 1.10.1. Approximate full solutions to the evolution of density perturbations can be achieved using n-body simulations in which the density field is decomposed into pseudo-particles and the gravitational forces acting on these are calculated in a brute-force manner. The result of this is that the initial cosmic web structure is seen fragment into dense haloes on small scales. Simulations are discussed in Chapter 2. Most of this thesis concerns itself with a full phenomenological model, known as the halo model, of the density field which takes inspiration from both perturbation theory and simulations: the halo model is discussed in detail in Chapter 3.

1.10.1 Perturbation theory

When considering departures from homogeneity in the universe it is standard to use the matter density perturbation, δ, defined via,

$$\rho(\mathbf{x}) \equiv \bar{\rho}[1 + \delta(\mathbf{r})] \ . \tag{1.81}$$

Here $\rho(\mathbf{x})$ is the total matter density field of the universe, which is defined in physical coordinates $\mathbf{x}$ and may vary as a function of the coordinates and of time. δ is defined in terms of comoving coordinates $\mathbf{r}$. $\bar{\rho}$ is the homogeneous mass density as described by the standard cosmology via the Friedmann equation (1.3), which varies only as a function of time.

It can be shown (see for example Peacock 1999) that if the density perturbations are suitably small ($\delta \ll 1$), of sub-horizon scale, and interact only through gravity, then the linear evolution

of perturbations in the matter, δ, proceeds according to the equation

$$\ddot{\delta} + 2H\dot{\delta} = 4\pi G\bar{\rho}_{\rm m}\delta = \frac{3}{2}H^2\Omega_{\rm m}(t)\delta \ . \tag{1.82}$$

Since there is only temporal dependence in this equation it is also valid in Fourier Space for $\delta \to \delta_k$. Here $\bar{\rho}_{\rm m}$ is the homogeneous matter density. This equation can be interpreted as the Gravitational Law of Newton for the density perturbation where the acceleration is caused by the gravitational forces due to the perturbed component of the universe. The perturbation is also subject to a 'Hubble drag' ($2H$) term which is an artefact of working in non-inertial, comoving coordinates. Note that the perturbation does not evolve spatially in these comoving coordinates (there are no spatial derivatives) so although perturbations can grow in magnitude (or shrink) they cannot change position in comoving space at linear order. This means that equation (1.114) is agnostic about the initial spatial distribution of δ as long as δ remains suitably small. It is also worth noting that the above equation assumes that no substantial perturbations exist in any other components of the energy density, for example that there are no perturbations in the dark energy, and this is why the $\Omega_{\rm m}(a)$ term alone appears in the driving term on the RHS of equation (1.114). If a universe contains multiple components with perturbations δ_i, all with different constant equations of state w_i, then the evolution equations are

$$\ddot{\delta}_i + 2H\dot{\delta}_i = 4\pi G(1+w_i)\sum_j (1+3w_j)\bar{\rho}_j\delta_j = \frac{3}{2}H^2(1+w_i)\sum_j (1+3w_j)\Omega_j(a)\delta_j \ , \tag{1.83}$$

which must all be solved simultaneously. Here one can see that if dark energy is a fluid with $w = -1$ then the right hand side of this equation must be 0 so that perturbations in the dark energy will not grow. The continuity equation expresses energy conservation and is

$$\dot{\rho} + \nabla \cdot (\rho\dot{\mathbf{r}}) = 0 \ , \tag{1.84}$$

which simply says that the rate of change of energy in a region is given by the flow through the edges. This equation can also be expanded to linear order to provide a relation between comoving velocity, $\mathbf{u}$, and the matter density perturbation

$$\dot{\delta} = -\nabla \cdot \dot{\mathbf{r}} \ , \tag{1.85}$$

or for perturbations in a general fluid this relation is

$$\dot{\delta}_i = -(1+w_i)\nabla \cdot \dot{\mathbf{r}}_i \ . \tag{1.86}$$

For the simple case of matter perturbations only in a matter dominated universe ($\Omega_{\rm m}(a) = 1$) equation (1.114) can be solved analytically to find the rate of growth of small perturbations. As it is a second order equation and thus there are two solutions

$$\delta(a) = Aa + Ba^{-3/2} \ . \tag{1.87}$$

If perturbations are put down at suitably early times, almost independently of their initial motion the first term in this equation will come to dominate after a few expansion factors.

This first term is known as the growing mode and the result is that linear perturbations grow proportionally to the scale factor $\delta \propto a$.

In the case of the far future of a ΛCDM universe equation (1.114) can once again be solved. In this case $\Omega_{\rm m}(a) \to 0$ and $H \to H_\infty$ (a constant) and the growing mode solution becomes $\delta \to$ const so perturbations cease growing. This makes physical sense because as the expansion proceeds ever more rapidly it becomes harder for material to come together to grow perturbations. This is an interesting feature of ΛCDM universes – the growth of (at least linear) structure will cease at some point in the future. This is not the case for flat matter dominated universes where growth, $\propto a$, proceeds forever into the future. This means that the most massive structures that will ever exist in our Universe are more or less already formed given that $\Omega_\Lambda \gtrsim 0.5$.

If one considers the super-horizon growth of perturbations in the radiation, during the epoch of radiation domination, then one can use equation (1.83) in the regime where $\Omega_{\rm m}(a) \to 0$ to derive the equation

$$\ddot{\delta}_{\rm r} + 2H\dot{\delta}_{\rm r} = \frac{32\pi G}{3}\bar{\rho}_{\rm r}\delta_{\rm r} = 4H^2\delta_{\rm r} \ , \tag{1.88}$$

which can be solved to get the growing mode as

$$\delta_{\rm r} = Aa^2 + Ba^{-2} \ . \tag{1.89}$$

Radiation perturbations can grow on super-horizon scales because free-streaming is not possible whereas on sub-horizon scales the perturbation erases itself. On super-horizon scales the matter perturbation is essentially forced to follow the radiation perturbation during radiation domination so also grows $\propto a^2$, which is different to growth in the matter dominated era. However, if one considers the evolution of the peculiar gravitational potential:

$$\nabla^2\Phi = 4\pi G a^2 \bar{\rho}\delta \ , \tag{1.90}$$

one can see that in each epoch the evolution of perturbations is such that the peculiar gravitational potential is conserved due to the conspiring time dependence of ρ and δ in each case. For matter perturbations on sub-horizon scales during radiation domination there is effectively no source term to equation (1.83)

$$\ddot{\delta}_{\rm m} + 2H\dot{\delta}_{\rm m} = 0 \ , \tag{1.91}$$

the solution is

$$\delta(a) = A\ln a + B \ , \tag{1.92}$$

so matter perturbations can only grow logarithmically while radiation dominates. This fact is important in order to understand both the fluctuations seen in the galaxy distribution, discussed in Section 1.12.1 and also the CMB temperature fluctuations, discussed in Section 1.11.

In the case that $\Omega_{\rm m}(a)$ departs from 1 it is difficult or impossible to solve equation (1.114) analytically so one must resort to numerical techniques. In doing this one considers that perturbations were set up at an early time of matter domination so that the boundary conditions

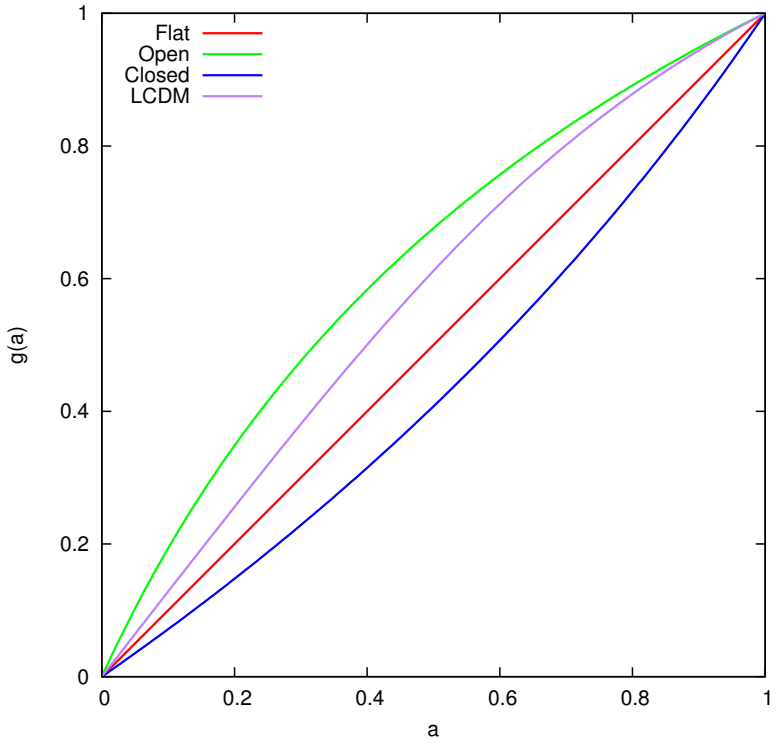

Figure 1.6: The linear growth factor for a number of cosmological models all normalised so that $g(a) = 1$ when $a = 1$. 'Flat' is $\Omega_{\rm m} = 1$ ($\delta \propto a$), 'Open' is $\Omega_{\rm m} = 0.3$, 'Closed' is $\Omega_{\rm m} = 2$ and 'LCDM' is $\Omega_{\rm m} = 0.3$ and $\Omega_\Lambda = 0.7$. One can see that in ΛCDM and open models that growth is suppressed at the present day, which is due to the matter density dropping. The rate of suppression is different in the two different models however, despite the equal matter densities today. In the closed model perturbation growth is amplified as the expansion of the universe slows down.

are $\delta \propto a$ and $\delta' = 1$ where the dash represents a derivative with respect to a. Converting equation (1.114) to derivatives in terms of a gives

$$\delta'' + \left(2 + \frac{A}{H^2}\right)\frac{\delta'}{a} = \frac{3}{2}\Omega_{\rm m}(a)\frac{\delta}{a^2} \ , \tag{1.93}$$

where A is related to $\ddot{a}$ and is defined in equation (1.11). A set of numerical solutions to this equation for various different cosmologies are shown in Fig. 1.6 in terms of the growth factor which is defined such that $g(a) = \delta(a)/\delta_0$ where δ_0 is the value of δ at $a = 1$. An expression of moderate accuracy for $g(a)$ is given by Carroll et al. (1992)

$$g(a) \propto \frac{a\Omega_{\rm m}}{\Omega_{\rm m}^{4/7}(a) - \Omega_\Lambda(a) + (1 + \Omega_{\rm m}(a)/2)(1 + \Omega_\Lambda(a)/70)} \ , \tag{1.94}$$

which is accurate to only around 5%. For a more accurate solution a full integration of equation (1.93) should be carried out. Another useful quantity is the logarithmic perturbation growth rate $f_{\rm g}$ defined by

$$f_{\rm g} = \frac{{\rm d}\ln g}{{\rm d}\ln a} \tag{1.95}$$

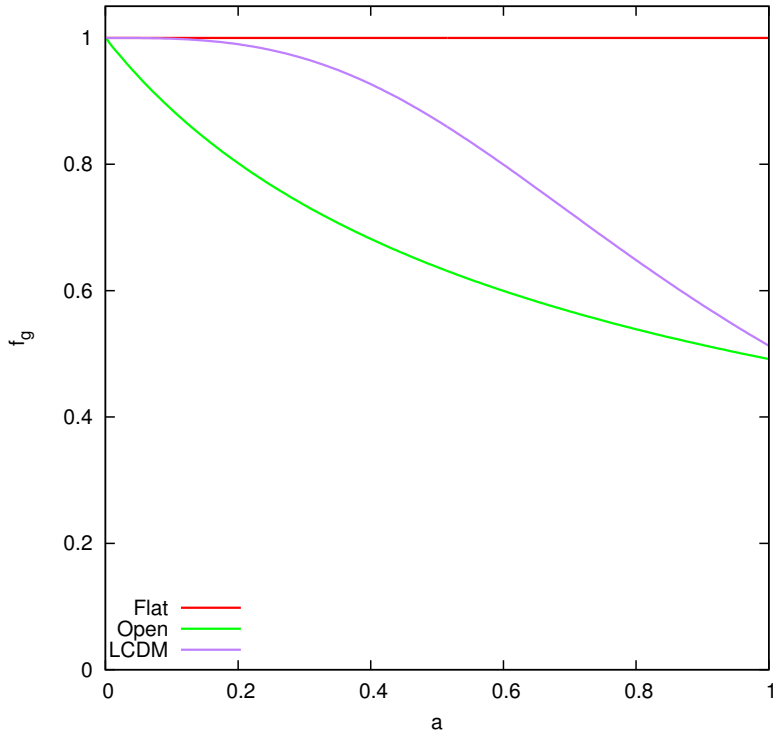

Figure 1.7: The linear growth rate for a number of cosmological models. 'Flat' is $\Omega_{\rm m} = 1$, 'Open' is $\Omega_{\rm m} = 0.3$, and LCDM is $\Omega_{\rm m} = 0.3$ and $\Omega_\Lambda = 0.7$. Once again one can see that the growth rate in ΛCDM and open models suppressed at the present but in different ways.

as long as matter dominates in the past $f_{\rm g} \to 1$ in the past. However the rate can deviate from this at later times depending on the cosmological model. An equation for $f_{\rm g}$ can be derived from equation (1.93):

$$\frac{{\rm d}\ln f_{\rm g}}{{\rm d}\ln a} + \left(1 + \frac{A}{H^2}\right) f_{\rm g} + f_{\rm g}^2 = \frac{3}{2}\Omega_{\rm m}(a) \ . \tag{1.96}$$

Some example numerical solutions to this equation for various different cosmological models are shown in Fig. 1.7. An accurate approximation to $f_{\rm g}$ for a flat ΛCDM model is given by Linder (2005) as $f_{\rm g} = \Omega_{\rm m}^{0.55}(a)$.

Equation (1.114) is only valid while δ is small. Higher order perturbation theory has been considered by many authors and a summary of recent results can be found in Bernardeau et al. (2002). However, it remains true, even if one sums all of the infinity of orders in perturbation theory, that all of these analytic results break down when the perturbation becomes too large. Even fairly diffuse structures such as galaxy clusters are many hundreds of times denser than the background universe so clearly perturbation theory will not be able to provide a description of the formation and evolution of such objects. In Chapter 3 of this thesis the halo model is discussed, which is able to explain the main features of the formation of all structure in the universe using both perturbation theory and results from non-linear theoretical arguments and simulations.

1.10.2 Analysis methods

Theoretical analysis of large-scale structure (LSS) is usually done in terms of the density perturbation in Fourier Space. The main reason for this is that the structure of the cosmos is inherently random, any theory pertaining to the LSS of the cosmos will not be able to give exact locations of each and every structure in the cosmos, but rather will be able to say how likely structures of certain sizes are, and how clustered they will be. It therefore makes sense to talk in terms of 'scales' as opposed to positions and these scales are related to $\mathbf{k}$, the wave-number Fourier Transform coordinate of comoving $\mathbf{r}$.

Throughout this work the density perturbation in Fourier Space, $\delta_{\mathbf{k}}$, is used and is defined by the convention of Peebles (1980)

$$\begin{aligned} \delta_{\mathbf{k}} &= \frac{1}{V}\int \delta(\mathbf{r}) e^{-i\mathbf{k}\cdot\mathbf{r}}\,\mathrm{d}^3 r\,, \\ \delta(\mathbf{r}) &= \sum_{\mathbf{k}} \delta_{\mathbf{k}} e^{i\mathbf{k}\cdot\mathbf{r}}\,. \end{aligned} \tag{1.97}$$

Note that because $\mathbf{r}$ is a comoving coordinate $\mathbf{k}$ is also a comoving wave number. Here V is the volume over which the Fourier Transform takes place, which can be formally taken to be infinite if required, in which case the summation in the second equation is turned into an integration.

The Fourier modes $\delta_{\mathbf{k}}$ are in general complex numbers with phase factors that relate to spatial positions in the density field and amplitudes which relate to the size of fluctuations at the scale of k. Due to the reality of δ, the $\delta_{\mathbf{k}}$ will be Hermitian. If one is not interested in spatial positions it makes sense to work with quantities in which the phase information is erased and an average is taken over all modes with a given amplitude. The simplest such quantity is the power spectrum, a real valued quantity defined by

$$P(\mathbf{k}) \equiv |\delta_{\mathbf{k}}|^2\,. \tag{1.98}$$

Note that the factor of V in equation (1.97) makes sure that $\delta_{\mathbf{k}}$, and therefore $P(\mathbf{k})$, is dimensionless (for finite V, and can be made so in the infinite case with suitable factors of V in the Fourier transform definitions). If space is homogeneous and isotropic (but finite and periodic, relevant to simulations discussed in the next chapter) then one can write

$$\langle \delta_{\mathbf{k}} \delta^*_{\mathbf{k}'} \rangle = \delta^{\mathrm{K}}_{\mathbf{k}\,\mathbf{k}'} P(|\mathbf{k}|) \tag{1.99}$$

where $\delta^{\mathrm{K}}_{\mathbf{k}\,\mathbf{k}'}$ is the Kronecker delta. No directions are preferred and $P(\mathbf{k})$ depends only on $k = |\mathbf{k}|$ which means that properties of δ are *statistically* isotropic. No positions are preferred and this is reflected in the Kronecker delta that means each mode is statistically independent. To create $P(k)$ from δ an average must be made over all modes with a given $|\mathbf{k}|$.

Another quantity of interest is the spatial variance in the density field, defined by

$$\sigma^2 \equiv \frac{1}{V}\int \delta^2(\mathbf{r})\,\mathrm{d}^3 r\,, \tag{1.100}$$

which provides a measure of how distorted the density field is in a given region of interest. Such quantities can be evaluated in either position space or Fourier Space to within numerical

factors (the theorem of Parseval) so the variance can therefore also be written as

$$\sigma^2 = \frac{V}{(2\pi)^3}\int |\delta_k|^2 \, \mathrm{d}^3k \ , \\ = \int \frac{V}{(2\pi)^3} 4\pi k^3 P(k) \, \mathrm{d}\ln k \ , \tag{1.101}$$

the integrand here is known as the 'dimensionless power'

$$\Delta^2(k) \equiv \frac{V}{(2\pi)^3} 4\pi k^3 P(k) \ . \tag{1.102}$$

$\Delta^2(k)$ gives the contribution to the variance per logarithmic interval in k. So for a given sample of $\log k$ axis the value of $\Delta^2(k)$ is a measure of how distorted the density field is at that scale.

For the spectra of fluctuations usually discussed in cosmology (not band limited) the variance in equation (1.101) diverges. However, in reality this will not be the case because even CDM particles will have a cut off in their spectrum corresponding to their free streaming in the hot early Universe, even if this free streaming only occurred for a short time. A useful quantity to consider is the variance in the smoothed density field when smoothed by a filter of some comoving size R. This removes the high frequency modes that make the variance formally infinite. The smoothed variance in the density field at a given scale is defined as

$$\sigma^2(R) = \int \Delta^2(k) W^2(kR) \, \mathrm{d}\ln k \ , \tag{1.103}$$

where W is the filter function. The form usually used for this in cosmology is the real space spherical top hat of radius R, the Fourier Transform of which is

$$W(kR) = \frac{3}{(kR)^3}\left(\sin kR - kR\cos kR\right) \ . \tag{1.104}$$

equation (1.103) give the variance expected in the density field up to a scale R. Note that this will evolve with time as $\Delta^2(k)$ evolves (the density field gets more distorted with time). Note that one can also define the variance exclusively in the linear field, and it turns out (see Chapter 3) that many features of the full non-linear field can be understood in terms of the variance in the linear field, even if in reality this no longer exists at a given epoch.

One can define a non-linear 'collapse' scale at a given epoch as the scale at which the variance in the density field is 1; so that $\sigma(R_{\rm NL}) = 1$. An associated non-linear wavenumber is defined via $k_{\rm NL} = 1/R_{\rm NL}$. The effective spectral index of the power spectrum at this collapse scale is

$$3 + n_{\rm eff} = \left.\frac{\mathrm{d}\ln\Delta^2(k)}{\mathrm{d}\ln k}\right|_{k_{\rm NL}} \ . \tag{1.105}$$

1.10.3 Initial conditions

In attempting to find solutions of the perturbation equation (1.114) one must first identify some initial conditions. In doing so one is inevitably led to consider what perturbation spectrum the Universe was set up with. Any theory that purports to explain the initial inhomogeneities that

does not define a special scale must have an initial matter power spectrum which is a power law

$$P(k) = Ak^n \ , \quad \Delta^2(k) = \frac{4\pi AVk^{3+n}}{(2\pi)^3} \tag{1.106}$$

where n is known as the spectral index and A is a normalisation. The values of A and n depend on the model for the initial conditions in question, inflation theories tend to predict values of n that are approximately, but not exactly equal to 1 (Mukhanov & Chibisov 1981; Hawking 1982). This means that the density field is more distorted on smaller scales. One should also note that large scale homogeneity requires values of n greater than -3 given that equation (1.103) diverges with lower values of n. The value of A depends on the form of the inflationary potential and the value of the inflation field and A can be inferred by cosmological observations at the present day (*i.e.* what perturbations must have existed initially in order to produce the observed perturbations today). Historically this is done in an awkward way; a quantity σ_8 is defined as being the variance in the *linear* power spectrum, grown to the present day by the solution to equation (1.114) when smoothed by a spherical window of radius $8\,h^{-1}\,\mathrm{Mpc}$,

$$\sigma_8^2 = \int \Delta^2_{\rm lin}(k) W^2(k\,R = 8\,h^{-1}\,\mathrm{Mpc}) \mathrm{d}\ln k \ . \tag{1.107}$$

Specifying a value for σ_8 thus implicitly sets a value for A (although the general relation is complicated) and σ_8 can be measured. σ_8 was chosen historically because it is a number that can be determined observationally in the local Universe and has the virtue of being close to 1. Any measurement of the amplitude of $\Delta^2(k,z)$ at any epoch together with a growth factor constitute a measurement of σ_8.

1.10.4 Gaussian fields

In order to understand the structure of the cosmos one also needs to consider the statistical properties of the field, not just an average as given by equation (1.106). It seems probable that any process that develops initial fluctuations would produce Gaussian distributed perturbations due to the central limit theorem. This is true of inflation as well as most other processes one can dream up to explain the initial conditions. If fluctuations are Gaussian this means that both the real and imaginary parts of $\delta_{\mathbf{k}}$ are independently Gaussian distributed random numbers with zero mean and variance given by $P(k)$. In order to generate such a field for each $\mathbf{k}$ mode of the field the value of $P(|\mathbf{k}|)$ would be used to assign each mode a variance with probability

$$P(\delta) = \frac{1}{\sqrt{2\pi P(k)}} \mathrm{e}^{-\delta_{\mathbf{k}}^2/2P(|\mathbf{k}|)} \ . \tag{1.108}$$

Frequently it makes sense to assign modes an amplitude and phase, rather than real and imaginary parts. In this case one must transform the distribution into polar coordinates. The result is that the amplitude is assigned with probability

$$P(r) = \frac{r}{P(|\mathbf{k}|)} \mathrm{e}^{-r^2/2P(|\mathbf{k}|)} \ , \tag{1.109}$$

while the phase is a random number distributed uniformly between 0 and 2π. Note that this means that the average amplitude of a mode at scale k is $\sqrt{\pi P(k)/2}$, rather than $P(k)$.

1.11 The cosmic microwave background

The initial spectrum of perturbations laid down in the very early Universe evolve in the early radiation dominated universe which exists subsequently. In some ways the evolution of perturbations at this epoch is simple because the evolution is entirely linear, but interactions between matter and radiation, and the interaction of different particle species at different times make the mathematics more complicated. A full discussion of this topic can be found in Lyth & Liddle (2009) and is beyond the scope of this thesis. However, a brief heuristic summary of the topic is provided here.

Post-inflation perturbations exist in all components of the Universe including dark matter, radiation and baryonic matter. The simplest models of inflation suggest that the perturbations would be *adiabatic* – they sit on top of each other, a high photon density region is also a high matter density region. This can be thought of as being due to regions where the inflation field has a higher than average value decay into areas with a density of all species with a higher than average value. Initially all species will have high enough energy to be relativistic, but in the case of massive particles the particles slow quickly due to momentum redshifting as the Universe expands, although the epoch at which this happens depends on the particle mass. Throughout most of the rest of this thesis matter particles are taken to be 'cold', unless otherwise stated, meaning that they are massive enough to have become non-relativistic very early in the history of the Universe. This is certainly the case for conventional matter (protons and neutrons ~ 1 GeV) but given the unclear nature of the dark matter it is less obvious that dark matter is cold. Cosmological observations discussed in the next section can put limits on the 'hotness' of the dark-matter particle.

There are two distinct regimes for perturbations – those that exist outside the size of the particle horizon and those that exist within the horizon – and the particle horizon also grows with time. During radiation domination the particle horizon is given by

$$R_{\rm p}(a) = \frac{a}{H_0\sqrt{\Omega_{\rm r}}} \,. \tag{1.110}$$

Within the horizon photons move relativistically and smear out perturbations in themselves. This means that perturbations that exist in the matter are unable to grow since at this epoch growth in matter perturbations can only be sourced by the radiation perturbations due to the overwhelming contribution of their energy at these times. Perturbations outside the horizon (defined in the synchronous gauge) are able to grow independently of this because radiation is unable to smear itself out on acausal large scales. This means that there will be a characteristic scale in the Universe given by the horizon size at matter-radiation equality. Perturbations greater than this size will have grown unimpeded whilst those below this scale will be damped

in proportion to the amount of time they spent within the horizon. Whilst the Universe can be considered to contain only matter and radiation (which is certainly true at the time of matter radiation equality) the particle horizon is given by

$$R_{\rm p}(a) = \frac{2\sqrt{\Omega_{\rm r}}}{H_0\Omega_{\rm m}}\left(\sqrt{1+\frac{\Omega_{\rm m}}{\Omega_{\rm r}}a}-1\right) , \tag{1.111}$$

so the size at matter-radiation equality is

$$R_{\rm eq} = \frac{16.1}{\Omega_{\rm m}h}\,h^{-1}\,{\rm Mpc} , \tag{1.112}$$

which can roughly be converted to a k scale via $k = 2\pi/R$ of

$$k_{\rm eq} = 0.39\,\Omega_{\rm m}h^2\,{\rm Mpc}^{-1} , \tag{1.113}$$

where the standard value of $\Omega_{\rm r}h^2 = 4.2\times10^{-5}$ determined from the CMB temperature, together with expected three neutrino species contribution, has been assumed. Given current constraints on the values of $\Omega_{\rm m}$ and h one expects a break feature in the matter power spectrum on scales of $\sim 100\,h^{-1}\,{\rm Mpc}$. This is known as the Mészáros effect (Meszaros 1974). The resultant modifications to the matter power spectrum can be seen in Fig. 1.8, where an initial power spectrum of $\Delta^2 \propto k^{n+3}$ has been bent and modified to $\Delta^2(k) \propto k^{n-1}$ at the smallest scales.

Another important feature present in the matter power spectrum due to physics in the early Universe are baryonic acoustic oscillations (BAOs). At early times the hot plasma of baryons is connected to radiation by Thomson scattering, as well as by gravitational interactions. This creates a pressure force so that the pressure in any perturbation that tries to collapse increases and pushes back, the result is an oscillation of sound waves in this plasma in the early Universe. This is imprinted upon the power spectrum of all matter because the dark matter eventually responds to the perturbed baryons, the resultant feature in the full matter spectrum is a damped version of that which initially featured only in the baryons. At $z = 0$ these oscillations can be seen as small wiggles at slightly smaller scales than the main break feature in Fig. 1.8. Baryon waves are caused by a pressure term in the perturbation equations that appears as an additional forcing (pp. 463-464 Peacock 1999)

$$\ddot{\delta} + 2H\dot{\delta} = \left(4\pi G\bar{\rho} - \frac{c_s^2k^2}{a^2}\right)\delta , \tag{1.114}$$

on large scales the gravitational collapse term is more important, but on small scales BAO waves are supported.

A full treatment of the evolution of perturbations at this epoch is a difficult problem and one needs to take into account the evolution of perturbations in radiation, dark matter and baryonic matter both inside and outside the event horizon. One also needs to account for the fact that the fluid approach to perturbations described above is not perfectly valid and the full phase space distribution needs to be taken into account via the Boltzmann equations. An important development in this discipline was the introduction of fast Boltzmann codes which were able

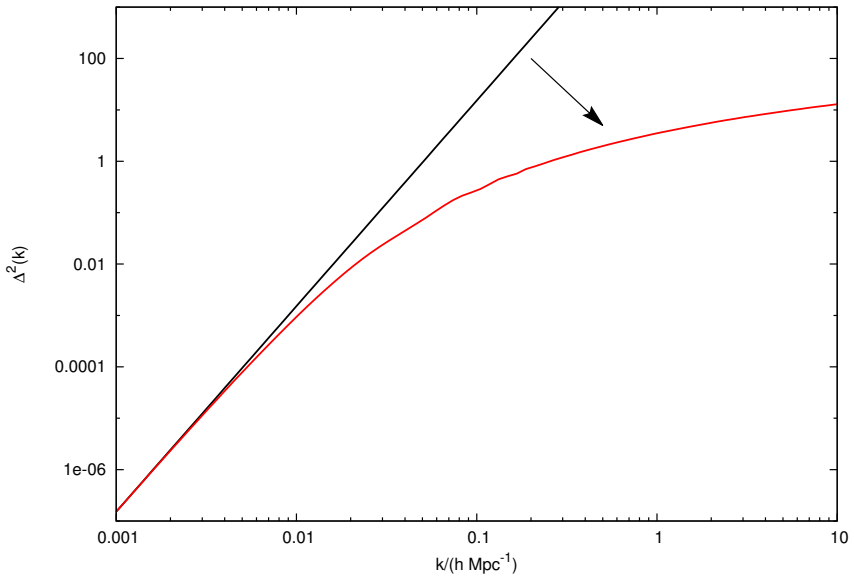

Figure 1.8: The linear matter power spectrum extrapolated to $z = 0$. The black curve shows the initial power law spectra ($n = 1$ in this example) as predicted by inflation whereas the red curve shows the modifications due to the response of matter to conditions in the early radiation dominated Universe. The initial departure from power law shape is due to the Mészáros effect where perturbations within the horizon at this time have had their evolution suppressed and the wiggles at slightly smaller scales are due to baryonic acoustic oscillations.

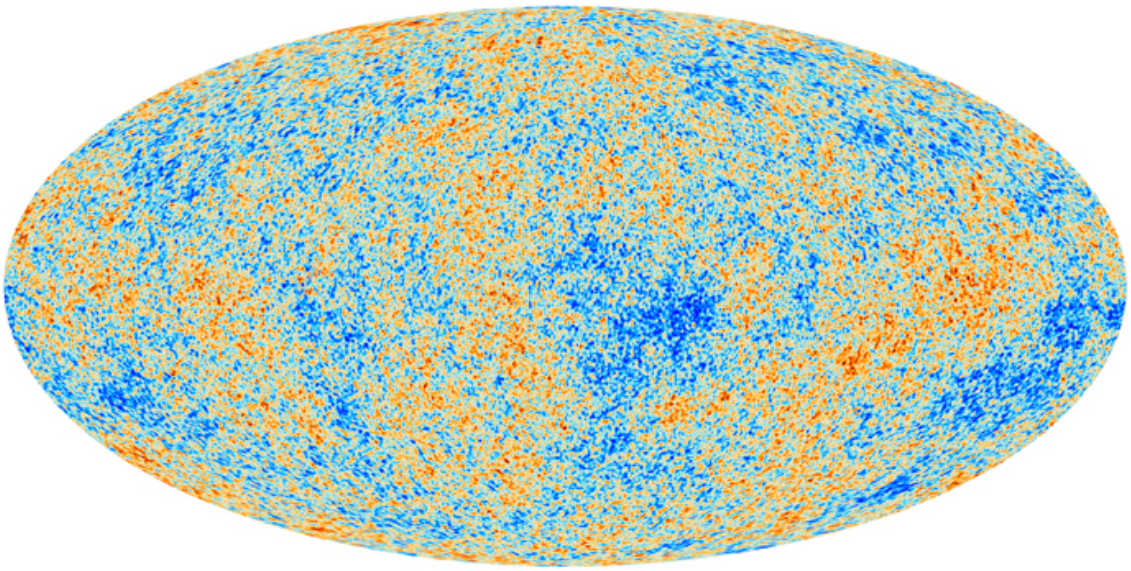

Figure 1.9: Temperature fluctuations in the CMB as mapped by the *Planck* collaboration. The mean temperature of the CMB is 2.73 K, the hot (redder) and cold (bluer) spots shown here represent departures from the mean of the order of 10^{-4}.

to calculate the evolution of any initial power spectrum through the radiation dominated era comparatively quickly. These were introduced in 1996 as 'CMBFast' (Seljak & Zaldarriaga 1996) and now in the updated form of the 'CAMB' code (Lewis et al. 2000); both approaches are compared in Seljak et al. (2003). In Eisenstein & Hu (1998) a heroic effort was made to write down an accurate analytic approximation to the matter power spectrum based on theoretical arguments together with the output of such codes. In this way, based on any given cosmology, the evolution of the density field during the radiation era can be calculated numerically to good accuracy for any set of cosmological parameters and this provides the boundary conditions for studying the further evolution of the Universe, when matter dominates the universe and the perturbations become non-linear.

Importantly the perturbations to density left over at the epoch of the CMB can be studied via the temperature field of the CMB can be studied directly. A variety of physical processes translate density and velocity perturbations into temperature fluctuations seen on the 2D CMB sky. Briefly these include: the Sachs-Wolfe effect – photons in gravitational wells need to climb out to reach us, thus losing energy, the adiabatic effect – photons in higher density regions are hotter, and the Doppler effect – the last scattering a photon experiences before decoupling is determined by the peculiar velocity of the environment. These effects are all important on different scales and the full superposition is seen in the temperature perturbation map of the CMB as shown in Fig. 1.9, which comes from the *Planck* collaboration.

The spectrum of fluctuations of CMB temperature depends very much on the underlying cosmology and thus by comparing theoretical spectra to the measured one tight constraints

can be put on the cosmological model. The CMB is particularly good at constraining certain parameter combinations: the curvature of the Universe is well determined because hot and cold spots in the CMB are lensed very differently in open and closed universes – CMB data strongly favour a flat universe with $\Omega = 1$, in agreement with what one would expect from inflation (Planck Collaboration et al. 2013a). When measuring the spectrum of the CMB one measures the angular size of fluctuations, since these are related to the 'real' size of the features by the angular diameter distance ($D_{\rm A}$) this means that $D_{\rm A}$ is strongly constrained by the CMB – a corollary being that models which predict the same $D_{\rm A}$ can be difficult to distinguish using CMB data alone. Additionally the baryon density is well measured because the amplitude of the BAO is determined by the baryon fraction. CMB experiments favour $\Omega_{\rm b} \simeq 0.05$ in agreement with measurements from big bang nucleosynthesis. The matter density can also be well measured as this affects the epoch of matter-radiation equality which determines the scales below which the processes described above can operate, the CMB suggests $\Omega_{\rm m} \simeq 0.3$. This backs up the hypothesis of dark matter by saying that baryons represent a small fraction of the total and also that of dark energy by saying that matter cannot make up the total energy density required for flatness. However the CMB says less about the nature of dark energy, and really leaves $\Omega \simeq 0.7$ to be made of something, although what this is is constrained by the angular-diameter distance to the last scattering surface. The spectral index of perturbations n can also be measured, this has been shown to be $n \simeq 1$ but it is now certain to 5σ that it cannot be exactly 1 – with best fit values around 0.97. This lends weight to the inflationary paradigm, the simplest models of which predicted exactly this tilt well in advance of measurements. However, the latest results from Planck Collaboration et al. (2013b) show that the amount of gravitational waves predicted by the simplest inflation models is high, with the current measurement of waves being consistent with zero. However, just as this thesis was about to reach the printers the *BICEP2* (Background Imaging of Cosmic Extragalactic Polarizatio collaboration) collaboration announced a detection of gravitational waves in the CMB that was 5.9σ away from zero (BICEP2 Collaboration et al. 2014). If this result survives scrutiny then it would seem the the early Universe did really undergo a period of very rapid expansion in line with the inflationary paradigm. The amount of gravitational waves seen by BICEP2, combined with n measurements from CMB temperature maps, is in very good agreement with the simplest of inflationary potentials: $V(\phi) \propto m^2\phi^2$.

1.12 Cosmology from clustering

1.12.1 Galaxy clustering

Although supernovae cosmologists are usually credited with the discovery of the accelerated expansion of the cosmos it should also be noted that there were hints of the acceleration present in data from early galaxy surveys (*e.g.* the APM survey Maddox et al. 1990). This section contains a brief discussion of how cosmological parameters can be extracted from large-

scale galaxy surveys.

In Section 1.11 it was shown how the shape of the linear matter power spectrum depends on various cosmological parameters. It follows that by somehow measuring the matter power spectrum cosmological parameters can be inferred. Crudely the matter power spectrum can be thought of as an initial power law rise $\Delta^2(k) \propto k^{3+n}$ followed by a break $k_{\rm eq} \sim 0.4\Omega_{\rm m}h^2\,{\rm Mpc}^{-1}$ then a BAO wiggle $k_{\rm BAO} \sim \sqrt{3}k_{\rm eq}$ where the $\sqrt{3}$ comes from the speed of sound waves in a baryon-photon plasma. Measurements of the matter power spectrum are thus sensitive to the combination $\Omega_{\rm m}h$ from measuring the break feature.

For small perturbations it was shown in Section 1.10.1 that the growth can be calculated. This means that the evolution of the matter power spectrum can also be calculated because

$$\Delta^2(k,z) = g^2(z)\Delta^2(k,0)\ , \tag{1.115}$$

where g is the linear growth factor. Since g depends on cosmological parameters (a dependence which be seen approximately in equation (1.94) for standard cosmology) it follows that by making measurements of the amplitude change of $\Delta^2(k)$ at different redshifts one can constrain $\Omega_{\rm m}$ and Ω_Λ as well as models of dark energy and modified gravity which would generally have different perturbation growth rates. In doing this it must be borne in mind that the calculations of $g(z)$, shown in Section 1.10.1, are correct only for linear perturbations such that $|\delta| \ll 1$. Since $\Delta^2(k)$ is a monotonically increasing function it follows that smaller scales will become non-linear first. Thus without a proper model for the full non-linear growth of structure the matter power spectrum that is measured in a survey must be 'cut' at a suitable wave-number to avoid contamination from non-linear effects that are not understood. Chapter 4 of this thesis concerns itself with models of non-linear growth to address precisely these issues.

The matter power spectrum refers to perturbations in all matter, dark and baryonic. But since dark matter is impossible to observe directly (at least, not via photons emitted by the dark matter directly, see Section 1.12.5) only the luminous matter is visible. This luminous matter comes in the form of stars in galaxies but also as gas which emits radiation across a large portion of the electromagnetic spectrum depending on what state it is in. Although baryons in any state can in principle be used to measure the underlying matter distribution it is most usual to use optical light and thus to use galaxies as probes of the underlying matter power spectrum. Clearly there is a problem here as galaxies represent large over-densities $\delta \sim 200$ and are clearly very non-linear structures. However if averaged over suitably large scales the galaxy population can be taken to be linear and can then be related to the underlying matter. However, galaxies also form in a biased way relative to the total matter distribution as they represent the very highest peaks of the density field, so that $\delta_{\rm g} = b\delta$. In most theories of bias it is a constant on linear scales. Thus the power of galaxies can be related to the power of matter via

$$\Delta^2_g(k,z) = b^2\Delta^2(k,z)\ . \tag{1.116}$$

In principle b can depend on the scale, halo mass and environment. That bias affects the amplitude of the clustering signal makes it difficult to disentangle the effect of changing bias

and the effect of the different linear growth factor when comparing samples of galaxies at different redshifts.

By inferring the density field via its tracer galaxies, information regarding the constitution of the universe can be deduced by measuring the form and the rate of evolution of perturbations in the LSS. In this way, galaxy surveys have made major contributions towards establishing the current era of precision cosmology – *e.g* 2dFGRS (Cole et al. 2005), SDSS (Reid et al. 2010), COSMOS (Schrabback et al. 2010), 6dFGRS (Beutler et al. 2011), CFHTLenS (Heymans et al. 2012), BOSS (Anderson et al. 2014). By measuring the fluctuations in the galaxy distribution LSS surveys have the ability to constrain the amplitude of fluctuations at the present epoch and most agree on $\sigma_8 \simeq 0.8$.

An additional complicating factor is the fact that in measuring galaxies in a survey one has the angle that the galaxy is observed at on the sky together with the redshift, or an approximation of the redshift. Measuring $\Delta^2(k)$ requires computing $\mathbf{k}$ and this can only be done by converting the redshift into a position which assumes a cosmological model:

$$R_0 r(z_0) = \int_0^{z_0} \frac{\mathrm{d}z}{H(z)} \ . \tag{1.117}$$

This provides an additional complication. Alternatively, redshift information can be thrown out and just the angular clustering used to compute a projected version of $\Delta^2(k)$ although this limits the cosmological information that can be inferred. More usefully the positions of galaxies in 'redshift-space' can be used directly and theory can be used to calculate what the redshift-space positions of galaxies would be expected to be in a given cosmological model or gravity theory, this is discussed in Section 1.12.3.

1.12.2 Dark matter temperature

It is worth noting that LSS measurements allow one to constrain the properties of dark-matter particles. If the particles are light enough they will be then have large thermal velocities for substantial portions of the history of the Universe. This means that they will erase the primordial perturbations in themselves on scales corresponding to the distance that they will be able to travel whilst having substantial thermal velocities (so-called free streaming; this velocity dies away as the cosmos expands). An extreme case of this is that of photons which are able to free stream up to the size of the horizon, because they are massless, and thus there is no radiation perturbation on sub-horizon scales. In this way constraints can be placed on the mass of the dark-matter particle based on perturbations existing on small scales.

Dark-matter candidates that have large free streaming lengths are referred to as hot dark matter (HDM) and those that have negligible free streaming are cold dark matter (CDM), the intermediate case is warm dark matter (WDM). The standard 1 GeV WIMP would be very much a CDM candidate. Neutrinos with masses in the eV range (as implied by a variety of earth based neutrino experiments) are HDM. The fact that the Universe contains an array of

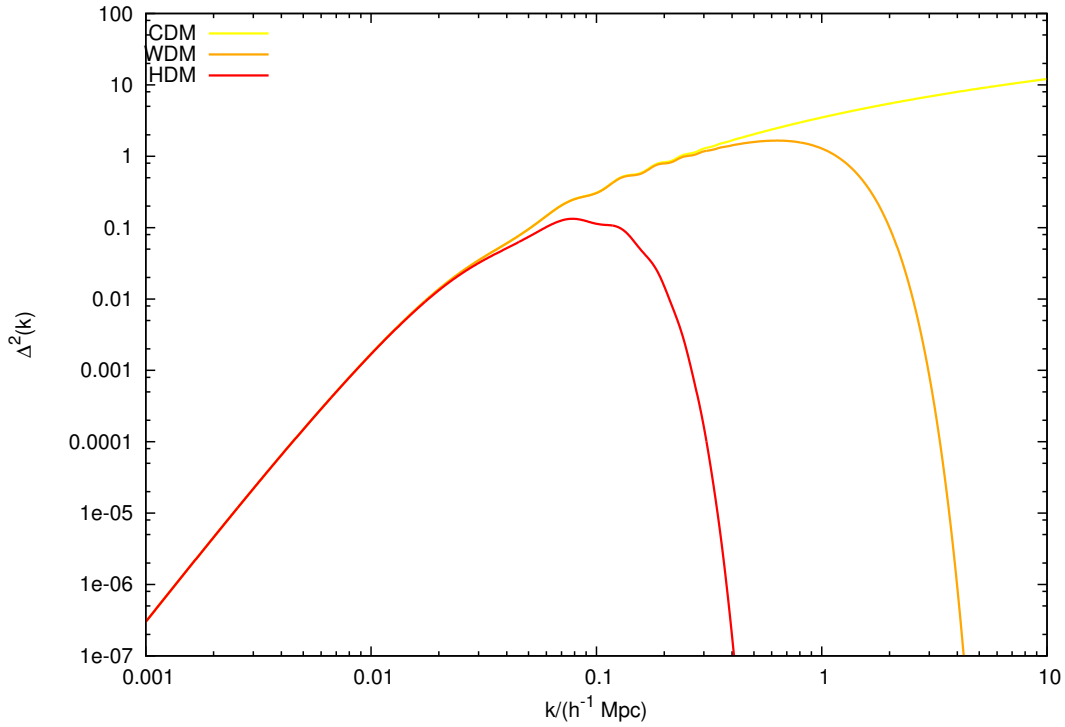

Figure 1.10: Example power spectra for different 'temperatures' of dark matter. Particles of lower mass are hotter and erase perturbations in themselves to larger scales.

small scale structures means that the dark matter cannot be entirely composed of neutrinos or other HDM.

The standard cosmological paradigm assumes that the Universe contains only CDM, based on theoretical prejudice that the particle is probably a WIMP and that no concrete evidence for dark-matter warmth has been seen. However there is some indication (*e.g.* Lovell et al. 2012, Lovell et al. 2013) that a certain amount of warmth to the dark matter would help to make the amount of substructure seen in cosmological N-body simulations of Milky Way like haloes agree with the observed Galactic substructure.

1.12.3 Redshift-space distortions

If one looks at the galaxy distribution seen in Fig. 1.5 is obviously anisotropic, which is strange given the isotropy of the cosmos. Anisotropy arises because galaxies are measured by their angular position and redshift, and mapping between redshift and a physical position is only approximate due to galaxy peculiar velocities. The most obvious effect seen in Fig. 1.5 is that of the fingers-of-God (FOG); virialised motions of objects within dense clusters are as likely to scatter a galaxy towards, or away from, the observer in redshift space. This means that clusters and other virialised structures are splayed out along the line of sight, that these features point towards the observer leads to the name FOG.

Redshift-space anisotropy means that the power spectrum will no longer be isotropic; different fluctuations will be measured perpendicular and parallel to the line of sight. This is usually measured by breaking the power spectrum down into a function of k and $\mu = \cos\theta$ where θ is the angle to the line of sight. Modes with $|\mu| = 1$ are parallel to the line of sight and modes with $\mu = 0$ are perpendicular. For unbiased tracers the relation between the linear theory power spectrum of fluctuations in redshift space, $\Delta_{\rm s}$, and matter was first calculated in Kaiser (1987):

$$\Delta^2_{\rm s}(k,\mu) = (1 + f_{\rm g}\mu^2)^2\Delta^2(k) \ , \tag{1.118}$$

where $f_{\rm g}$ is the linear theory growth rate given in equation (1.96). This expression is a boost in power for modes with larger values of μ while undistorted transverse modes with $\mu = 0$ are unaffected and the fluctuation amplitude is identical to that in real space. Line-of-sight modes have their power boosted because they are in the process of collapse, so are disconnecting from the Hubble flow, this brings them closer in redshift space, thus enhancing their clustering and boosting the power. If the tracers of matter are biased with linear bias b then

$$\Delta^2_{\rm s,g}(k,\mu) = b^2(1 + \beta\mu^2)^2\Delta^2(k) \ , \tag{1.119}$$

where $\beta = f_{\rm g}/b$. $\Delta^2_{\rm s,g}(k,\mu)$ can be directly probed by galaxy surveys and thus with a suitable model for $\Delta^2(k)$ constraints can be placed on β. The single power of b in equation (1.119) is because tracers are positionally biased but their velocities should be unbiased due to the equivalence principle. If the bias of the galaxy sample can be estimated by other means then

constraints can be placed directly on the growth rate which makes redshift-space distortions an ideal probe of modified gravity and dark energy.

If one computes an angle averaged power spectrum of a density field then the effect of the Kaiser boost can be seen by averaging over μ in equation (1.118)

$$\Delta_0^2(k) = \int_0^1 \Delta_\mathrm{s}(k,\mu)\,\mathrm{d}\mu = \left(1 + \frac{2}{3}f_\mathrm{g} + \frac{1}{5}f_\mathrm{g}^2\right)\Delta^2(k)\ , \tag{1.120}$$

which is valid for $b = 1$ dark matter. In a $\Omega_\mathrm{m} = 1$ model $f_\mathrm{g} = 1$ and the Kaiser boost to the matter power spectrum is 28/15. Alternatively the redshift space power in terms of k and μ can be decomposed into orthogonal Legendre Polynomials (Cole et al. 1994)

$$\Delta_\mathrm{s}^2(k,\mu) = \sum_{\ell=0}^{\infty} P_\ell(\mu)\Delta_l^2(k)\ , \tag{1.121}$$

where the P_l satisfy the orthogonality relation

$$\int_{-1}^{1} P_n(x)P_m(x)\,\mathrm{d}x = \frac{2}{2n+1}\delta_{nm}\ . \tag{1.122}$$

The first few Legendre polynomials are

$$P_0(x) = 1\ , \tag{1.123}$$

$$P_1(x) = x\ , \tag{1.124}$$

$$P_2(x) = \frac{1}{2}(3x^2 - 1)\ , \tag{1.125}$$

$$P_3(x) = \frac{1}{2}(5x^3 - 3x)\ , \tag{1.126}$$

$$P_4(x) = \frac{1}{8}(35x^4 - 30x^2 + 3)\ . \tag{1.127}$$

Due to orthogonality the polar spectra of $\Delta_\mathrm{s}^2(k,\mu)$ can be computed as weighted averages

$$\Delta_\ell^2(k) = \frac{2\ell+1}{2}\int_{-1}^{1} P_\ell(\mu)\Delta_\mathrm{s}^2(k,\mu)\,\mathrm{d}\mu\ , \tag{1.128}$$

and are known as the monopole, dipole, quadrupole, octopole and hexadecapole for $\ell = 0$ to $\ell = 4$. For odd ℓ these integrals will vanish due to the symmetry of $\Delta_\mathrm{s}^2(k,\mu) = \Delta_\mathrm{s}^2(k,-\mu)$ and anti-symmetry of $P_\ell(\mu) = -P_\ell(-\mu)$. For linear scales, where the Kaiser formula applies, the first three non-vanishing moments can be computed as

$$\Delta_0^2(k) = \left(1 + \frac{2}{3}\beta + \frac{1}{5}\beta^2\right)\Delta^2(k)\ , \tag{1.129}$$

$$\Delta_2^2(k) = \left(\frac{4}{3}\beta + \frac{4}{7}\beta^2\right)\Delta^2(k), \tag{1.130}$$

$$\Delta_4^2(k) = \left(\frac{8}{35}\beta^2\right)\Delta^2(k)\ . \tag{1.131}$$

where the monopole is the simple average over all μ discussed above. The ratios of these can be used to eliminate $\Delta^2(k)$ and obtain expressions for β directly, this is most often done with the quadrupole to monopole ratio:

$$\frac{\Delta_2^2(k)}{\Delta_0^2(k)} = \frac{1 + \frac{2}{3}\beta + \frac{1}{5}\beta^2}{\frac{4}{3}\beta + \frac{4}{7}\beta^2}\ , \tag{1.132}$$

which can be used to constrain the growth rate of structure f_g if one can estimate the bias of the tracer by some other means (Cole et al. 1994; de la Torre et al. 2013). One should note that only a biased version of the redshift-space power is ever observable, because the spectrum must be observed via a tracer population of galaxies.

Unfortunately non-linearities affect redshift-space to a greater extent than real space. Various schemes are able to extend the Kaiser calculation to smaller scales (*e.g.* Peacock & Dodds 1994, Scoccimarro 2004, Taruya et al. 2010 – compared in de la Torre & Guzzo 2012). Some of these methods rely on higher-order perturbation theory and combine this with a non-linear model for the FOG. A simple model is that of Peacock & Dodds (1994) where the Kaiser formula is combined with a Lorentzian term to account for FOG damping:

$$\Delta_s^2(k,\mu) = \frac{(1+\beta\mu^2)^2\Delta^2(k)}{1+k^2\mu^2\sigma^2/2} \ , \tag{1.133}$$

where σ is the 1D particle-particle dispersion. At linear scales the Kaiser formula can be used to compute theoretical values of the multipole spectra, but this fails as halo velocity dispersion becomes important. The exact multipole spectra of equation (1.133) can be calculated and are plotted in Fig. 1.11 where the assumption of linear theory holds at large scales where the curves are constant. The linear approximation breaks down sooner for the higher multipoles. At small scales the monopole is highly damped with respect to linear theory, the quadrupole becomes negative (after the excursion to 0) and the hexadecapole remains positive (after the excursion to 0) and is boosted relative to the linear prediction.

1.12.4 Baryon acoustic oscillations

Constraining cosmology by measuring the full matter power spectrum or associated correlation function can be difficult. Particularly because the amplitude can be uncertain due to galaxy populations with different bias factors and the possibility of scale dependent bias. However, cosmology can be constrained by focussing on one particular feature of the spectrum – the BAO feature is particularly prominent in the correlation function and the comoving size of this feature is very well constrained from the CMB. It follows that by measuring the angular size of the BAO scale that the angular diameter distance can be accurately determined and cosmological parameters can then be inferred. This is very similar in spirit to using thermonuclear supernovae as standard candles, but instead using the BAO as a standard ruler. Simply measuring the wavenumber of the BAO feature is easier than trying to constrain cosmology via the full correlation function because of the prominence of the BAO. A low redshift approximation for the angular diameter distance is

$$D_{\rm A} = \frac{z}{H_0}\left\{1-\frac{z}{4}[\Omega_{\rm m}+(1+3w)\Omega_w+6]\right\} \ ; \tag{1.134}$$

based on this one would expect measurements of the BAO scale to be degenerate in the same directions as SN measurements. However, this is not the case (see Figs. 1.2 and 1.4) because

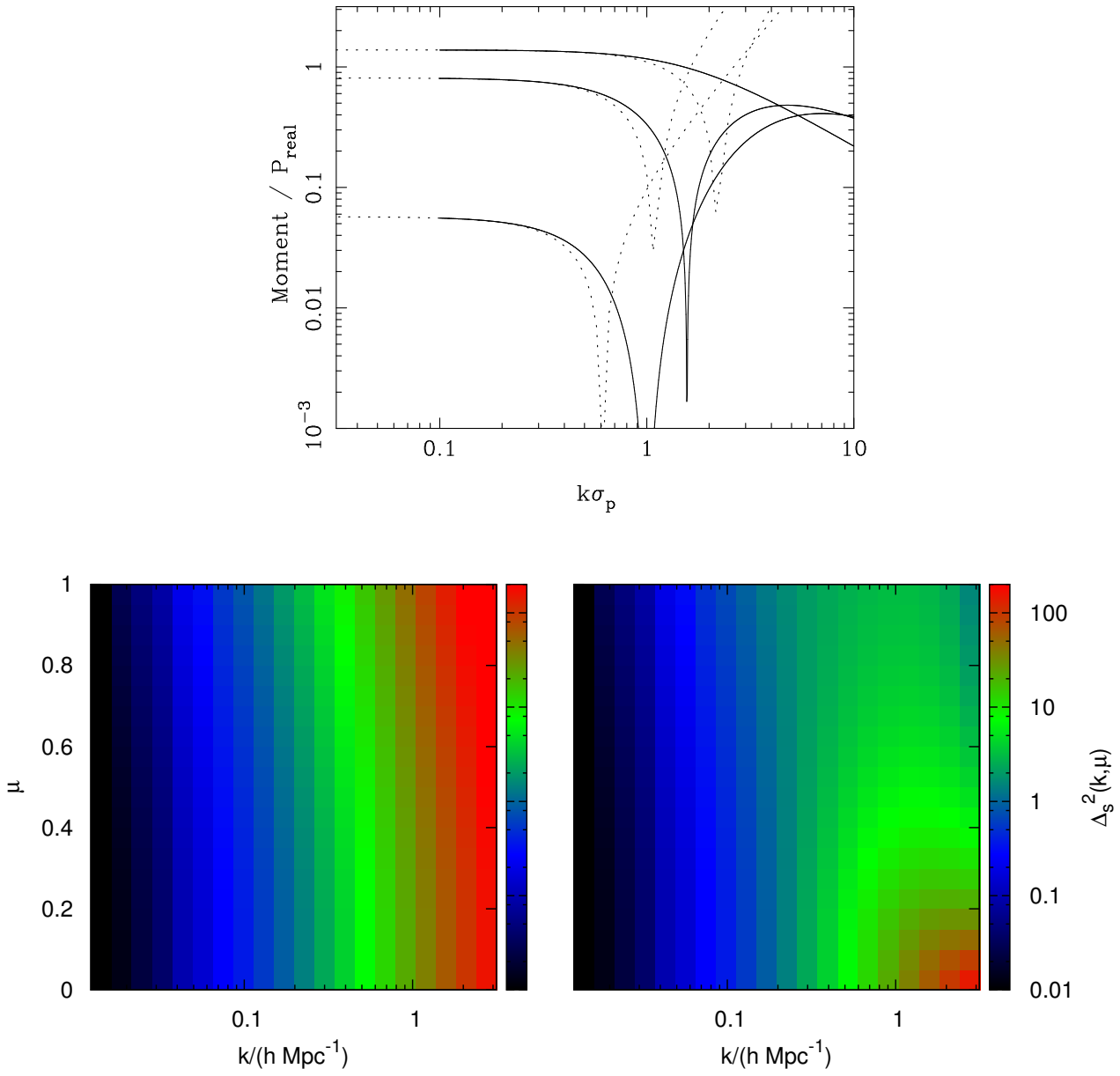

Figure 1.11: The top panel shows the theoretical multipole spectra of the Kaiser model with $\beta = 0.5$ and a Lorentzian damping term to account for the fingers-of-God effect, all relative to the matter power spectrum. At large scales the ratio can be seen to be constant, as predicted by the Kaiser effect in linear theory, but this breaks down on smaller scales with the breakdown happening at larger scales for the higher multipoles. The quadrupole becomes negative at small scales whereas the monopole and hexadecapole remain positive throughout. The lower panel shows the 2D redshift-space power for the Kaiser model (left) and that with additional Lorentzian damping (right). The Kaiser effect can be seen as the distinctive curve in the left panel as μ increases, and the fingers-of-God as the lack of power at higher μ for small scales in the right panel. In the bottom two panels the power is identical for undistorted $\mu = 0$ modes.

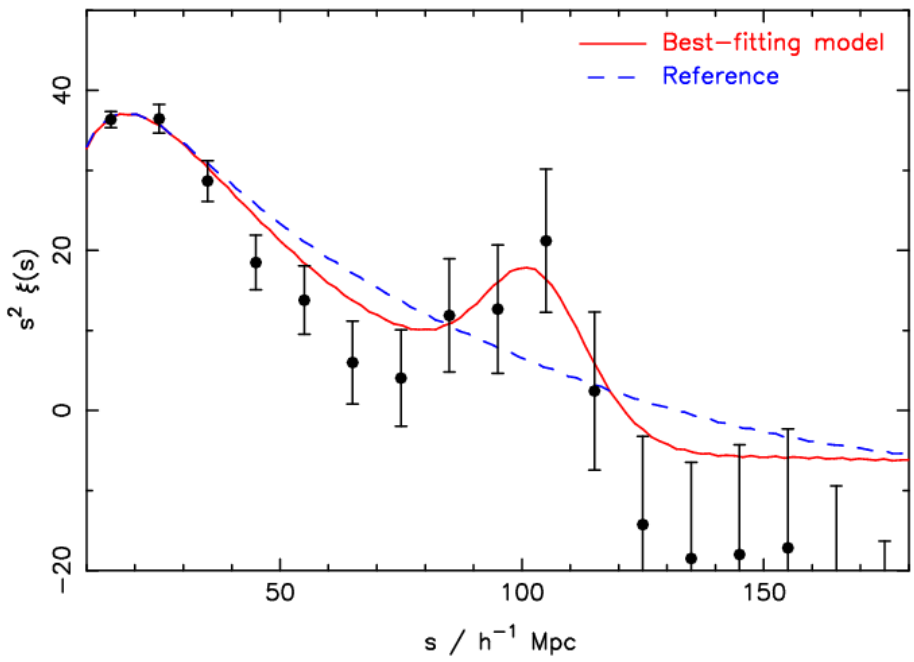

Figure 1.12: The correlation function of galaxies as seen in the *WiggleZ* Dark Energy Survey (Blake et al. 2011). The pronounced bump is the BAO seen at scales of around $100\,h^{-1}$ Mpc. Cosmological parameters can be constrained by attempting to accurately constrain the position of the peak alone, rather than the full correlation function.

BAO measurements tend to be made at higher redshifts and thus the perturbative expression is less valid.

The BAO peak seen in the correlation function from the WiggleZ Dark Energy survey (Blake et al. 2011) is shown in Fig. 1.12 where an obvious bulge can be seen in the data together with the best fitting cosmological model. The additional constraining power from BAO measurements can be seen via the BAO contours in Figs. 1.2 and 1.4.

1.12.5 Gravitational lensing

It is a remarkable fact that matter distributions in the Universe can bend light. Light from distant galaxies falls towards observers on earth along geodesics and these are perturbed for both non-relativistic matter and light, due to intervening material. The prediction of GR is for light to be bent twice as much as the classical physics calculation for non-relativistic material, essentially because light feels perturbations to both the space and time parts of the metric whereas non-relativistic matter is only sensitive to time perturbations. Light can be bent quite

severely around very massive structures, such as Abell clusters. Around black holes light can even be forced into orbits around the hole, or fall into the hole directly, vanishing forever from observability unless one were to follow it in. A comprehensive review of gravitational lensing is given by Bartelmann & Schneider (2001).

Most light that arrives on earth from the deep recesses of cosmic space is only slightly lensed by the intervening material. This 'weak' gravitational lensing can be used to give information about the matter distribution directly. One huge advantage of this is that, although it is the distortions of galaxies that are measured, the distortions are produced by the entire matter distribution along the path between the source and observer, therefore an unbiased version of the perturbation distribution is measured. This disadvantages are that for an average galaxy the shape distortions are tiny and difficult to measure, and so a large sample of galaxies are needed in order to see the effect. Lensing tends to shear background galaxies in the same region of the sky in the same direction, but care needs to be taken for the fact that galaxies are sheared on average (not circular to begin with) and that correlated shape change can be produced by unlensed physically close galaxies by tidal fields (*e.g.* Joachimi et al. 2013a; Joachimi et al. 2013b).

Deflection by a single lens is produced by the lensing potential ψ

$$\boldsymbol{\theta}_i - \boldsymbol{\theta}_s = \nabla_\theta \psi \ , \tag{1.135}$$

where θ_i is the intrinsic angular position vector of the source and θ_s is that observed. The lensing potential is given by $\nabla^2_\theta \psi = 2\kappa$ where κ is the dimensionless surface mass density

$$\kappa = 4\pi G \int \frac{D_\mathrm{L} D_\mathrm{LS}}{D_\mathrm{S}} \rho(\ell)\, \mathrm{d}\ell \ , \tag{1.136}$$

where the D are angular distances and it has been assumed that the dimensions of the lens are small compared to the separation between observer and source and ℓ is comoving distance along the line of sight. If $\kappa \ll 1$ then linearity holds and the effect of many lenses is simply a sum over lenses. In cosmology deflection is only caused by the fluctuating part of the density field and this is projected on the sky by a weight function W. To get the weight, ρ in equation (1.136) needs to be replaced by the comoving, fluctuating density so that the cosmic overdensity in κ is

$$\kappa = \frac{3H_0^2 \Omega_\mathrm{m}}{2} \int \frac{D_\mathrm{L}(y) D_\mathrm{LS}(y)}{D_\mathrm{S}} \frac{\delta(y)}{a^3} a\, \mathrm{d}y \ , \tag{1.137}$$

where y is a comoving distance. This formula assumes that the geometry of the Universe is flat. Projecting κ into 2D gives and computing the power gives

$$\Delta^2_\kappa(K) = \frac{9\pi}{4K} H_0^4 \Omega_\mathrm{m}^2 \int_0^{r_\mathrm{H}} \Delta^2(K/y, y) G^2(y)\, \mathrm{d}y \ , \tag{1.138}$$

where G is a weighting function that relates to the distribution of sources along the line of sight from the observer at $r = 0$ to the horizon $r = r_\mathrm{H}$, with factors of angular diameter distance. Here Δ^2 has been decomposed into a component along the line of sight and a component

parallel to the line of sight. Equation (1.138) assumes a fixed value of the source plane, more realistically one has a distribution of sources and this must be averaged over.

It can be shown (*e.g.* Bartelmann & Schneider 2001) that the power spectrum of galaxy shear is equal to that of the projected mass over-density in the weak lensing limit. Thus weak lensing constrains a projected version of the matter power spectrum. Equation (1.138) shows one important disadvantage of the weak lensing method in that the shear power is an integral over all k of the matter power spectrum, which means that the theoretical matter spectrum needs to be known into the non-linear regime in order to understand the form of the Δ_κ even at relatively large scales. Chapter 4 of this thesis concerns itself with models of the full matter power spectrum, concentrating on the non-linear portion, for precisely this reason. In 2D lensing one does not have the luxury of being able to cut the measured spectrum at non-linear k modes which one knows to be problematic.

Lensing is theoretically able to measure the matter power spectrum directly – it is the only cosmological survey tool able to measured the unbiased matter field. However the power measured is a projected quantity and equation (1.138) shows that the amplitude of the power spectrum which is related to σ_8 is degenerate with Ω_m. This is simply a statement of the fact that the same amount of lensing can be produced either by a high matter density with small fluctuations or by higher matter fluctuations in a lower matter density.

1.13 Our ΛCDM Universe and units

So far, various models of the Universe have been discussed, but it seems likely that we live in a flat universe with current substantial energy densities only in matter and vacuum energy, specifically with $\Omega_\mathrm{m} \simeq 0.3$ and $\Omega_\Lambda \simeq 0.7$ so that $\Omega_\mathrm{m} + \Omega_\Lambda = 1$. Although the Universe contains radiation the current value of this parameter is $\Omega_\mathrm{r} h^2 = 4.2 \times 10^{-5}$ means that it was only important in the past. The late time Friedmann equation for such a ΛCDM universe is

$$H^2 = H_0^2 \left(\frac{\Omega_\mathrm{m}}{a^3} + 1 - \Omega_\mathrm{m} \right) \ , \tag{1.139}$$

which can be solved to find a relationship between the scale factor and time

$$a(t) = \left[\left(\frac{\Omega_\mathrm{m}}{1-\Omega_\mathrm{m}} \right) \sinh^2 \left(\frac{3}{2} \sqrt{1-\Omega_\mathrm{m}} H_0 t \right) \right]^{1/3} \ , \tag{1.140}$$

such a universe has a big bang ($a \to 0$ at $t = 0$ in the above equation) and the age of the universe can be found by inverting the above relation

$$t_0 \approx 6.52 \frac{1}{\sqrt{1-\Omega_\mathrm{m}}} \mathrm{arcsinh} \left(\sqrt{\frac{1-\Omega_\mathrm{m}}{\Omega_\mathrm{m}}} \right) h^{-1} \, \mathrm{Gyr} \ . \tag{1.141}$$

In the far future when vacuum energy is the only important contribution to the energy density and expansion becomes exponential,

$$a \propto \mathrm{e}^{\sqrt{1-\Omega_\mathrm{m}} H_0 t} \ . \tag{1.142}$$

Matter density	$\Omega_{\rm m}$	0.3
Vacuum density	Ω_Λ	0.7
Hubble constant	H_0	70 km s^{-1} Mpc^{-1}
Dimensionless Hubble	h	0.7
CMB temperature	T_0	2.73 K
Radiation density	$\Omega_{\rm r}$	8.57×10^{-5}
Age	t_0	13.4 Gyr
Matter-radiation equality time	$t_{\rm eq}$	164,000 yr
Matter-radiation equality redshift	$z_{\rm eq}$	3,500
Horizon size at equality	$r_{\rm eq}$	110 Mpc
Decoupling redshift	$z_{\rm dec}$	1,100
Decoupling time	$t_{\rm dec}$	362,000 yr
Matter-Λ equality scale factor	a_Λ	0.754
Matter-Λ equality redshift	z_Λ	0.326
Matter-Λ equality time	t_Λ	9.81 Gyr
Acceleration scale factor	$a_{\rm a}$	0.598
Acceleration redshift	$z_{\rm a}$	0.671
Acceleration time	$t_{\rm a}$	7.31 Gyr
Particle horizon	$R_{\rm p}$	13.9 Gpc
Event horizon	$R_{\rm E}$	4.89 Gpc
Total horizon (particle+event)	$R_{\rm H}$	18.8 Gpc
Eventual Hubble value	H_∞	58.6 km s^{-1} Mpc^{-1}
Furthest galaxy to which signals can be sent	z_∞	1.81
Redshift beyond which $D_{\rm A}$ decreases	$z_{\rm A}$	1.63
Saturation growth factor	g_∞	1.39

Table 1.1: Numerical data for an example universe, with $\Omega_{\rm m} = 0.3$, $\Omega_\Lambda = 0.7$, $w = -1$ and $h = 0.7$, similar to that currently favoured by the data.

The value of H will saturate at $H_\infty = H_0\sqrt{1-\Omega_{\rm m}}$. This implies that the universe will expand forever with matter becoming exponentially more and more dilute as time passes – a bleak future indeed.

While $\Omega_{\rm m}(a) = 1$ linear perturbations grow according to $\delta \propto a$ but as $\Omega_{\rm m}(a) \to 0$ perturbations will cease to grow. The transition between these two regimes of perturbation growth is non-analytic in a ΛCDM model. The linear growth saturation level, g_∞, can be calculated via the solution to equation (1.114) as $t \to \infty$. In some models (*e.g.* $\Omega_{\rm m} = 1$) growth continues indefinitely.

Redshifts and scale factors can be calculated for the epoch (a_Λ) when the cosmological constant begins to dominate the energy by considering the epoch at which the two terms in

G	$4.302 \times 10^{-9}\, h^{-1}\,\mathrm{Mpc}\,(h^{-1}\,\mathrm{M}_\odot)^{-1}\,\mathrm{km\,s^{-1}}$
H_0	$3.241 \times 10^{-18}\, h\,\mathrm{s}^{-1}$
$1/H_0$	$9.778\, h^{-1}\,\mathrm{Gyr}$
c/H_0	$2998\, h^{-1}\,\mathrm{Mpc}$
c^2/G	$2.090 \times 10^{19}\ h^{-1}\,\mathrm{M}_\odot\,(h^{-1}\,\mathrm{Mpc})^{-1}$
H_0^2/G	$2.325 \times 10^{12}\ h^{-1}\,\mathrm{M}_\odot\,(h^{-1}\,\mathrm{Mpc})^{-3}$
G/H_0^2	$4.302 \times 10^{-13}\,(h^{-1}\,\mathrm{M}_\odot)^{-1}\,(h^{-1}\,\mathrm{Mpc})^3$
$\bar{\rho}_\mathrm{m}$	$2.775 \times 10^{11}\,\Omega_\mathrm{m}(1+z)^3\,h^{-1}\,\mathrm{M}_\odot\,(h^{-1}\,\mathrm{Mpc})^3$

Table 1.2: Numerical values of constants in units suitable for large-scale structure cosmology.

equation (1.139) are equal

$$a_\Lambda = \left(\frac{\Omega_\mathrm{m}}{1-\Omega_\mathrm{m}}\right)^{1/3} , \tag{1.143}$$

and also for the epoch (a_a) at which acceleration begins by considering the derivative of equation (1.139)

$$a_\mathrm{a} = \left[\frac{\Omega_\mathrm{m}}{2(1-\Omega_\mathrm{m})}\right]^{1/3} . \tag{1.144}$$

Unfortunately in a ΛCDM universe expressions for the event horizon and particle horizon are not analytic, but a useful approximation (Peacock 1999) is

$$R_\mathrm{p}(a) \simeq \frac{2\Omega_\mathrm{m}^{-0.4}(a)}{H_0} . \tag{1.145}$$

However, it is interesting to know that the event horizon is a finite quantity in ΛCDM – light can only travel so far in terms of comoving coordinates before the acceleration of the expansion prevents it from travelling further. Numerical values of the horizon sizes in an example ΛCDM universe are given in Table 1.1. This has an interesting corollary; if light can only travel a fixed amount of comoving distance into the infinite future it means there are observed galaxies that it is not possible to send signals to. They are simply too far away for light sent today to ever reach them. The limiting redshift, z_∞, can be calculated by equating the current comoving distance of the event horizon, to the comoving distance of a galaxy at the limiting redshift as observed today:

$$\int_0^{z_\infty} \frac{\mathrm{d}z}{H(z)} = \int_{-1}^{0} \frac{\mathrm{d}z}{H(z)} . \tag{1.146}$$

One should note that the existence of this limit is a direct effect of the vacuum energy term – if the universe contains only matter then $z_\infty \to \infty$ and signals can be sent to any far flung corner of the universe given enough time. Unfortunately this equation has no analytic solution in a ΛCDM universe but a numerical solution in an example universe is given in Table 1.1.

Another interesting quantity is the redshift beyond which the angular diameter distance increases. This can be calculated by finding the value of z at which the derivative of equation (1.22) is zero. For a flat universe this value z_A is given by

$$\int_0^{z_\mathrm{A}} \frac{\mathrm{d}z}{H(z)} = \frac{1+z_\mathrm{A}}{H(z_\mathrm{A})} , \tag{1.147}$$

unfortunately this equation has no analytic solution in a ΛCDM model but a numerical solution in an example ΛCDM universe is given in Table 1.1.

To summarise Table 1.1 is included that contains numerical quantities relevant for a vanilla ΛCDM universe with $\Omega_{\rm m} = 0.3$, $\Omega_\Lambda = 0.7$ and $h = 0.7$. And Table 1.2 is included which contains constants and quantities in units suitable to LSS cosmology.

Chapter 2

N-body simulations

The full solution for the evolution of initially small, Gaussian distributed, density perturbations in the Universe is unsolved. This is not to say that the problem is not understood, but simply that no full solution has ever been found. The perturbation theory discussed in the previous chapter deals with evolution when perturbations are small, $|\delta| \ll 1$, but breaks down as overdensities grow. Galaxy clusters in the present day Universe represent overdensities of at least several hundred and so understanding their formation and evolution clearly requires understanding more than just perturbation theory.

The standard approach to calculate the full nonlinear cosmological dynamics is to use N-body computer simulations (for a simple review of this see Trenti & Hut 2008). These are a brute force approach: a computational box is set up and populated with particles in a distribution that represents the distribution of matter perturbations present in the universe at some early epoch when they are small and well understood. The particles are then allowed to evolve under their mutual gravitational attraction with as fine a resolution as possible. Results can be extracted at various points in the simulation by 'dumping' the position and velocity of every particle at a given time. Obviously the higher the computing power invested the more particles can be used to sample the phase space and the evolution of the cosmos can be computed in more detail. As an example of the numbers and computing power involved; the Millennium Simulation of Springel et al. (2005) evolved $\approx 10^9$ (2160^3) matter particles under their mutual gravitational attraction for the vast majority of the history of the universe (from $z = 127$ to $z = 0$). The volume considered was a $500\,h^{-1}\,\mathrm{Mpc}$ cube and each particle had a mass of $\approx 10^9\,h^{-1}\,\mathrm{M}_\odot$. The computational resources for such tasks are enormous; the Millennium Simulation took two months to run on a supercomputer in 2005, distributed across 2048 cores; the output required 25Tb of storage space.

Simulations discussed in this chapter are 'dark matter only' which means that they aim to evolve particles considering gravitational forces only. While the simulation is running there is no distinction between baryons and dark matter. However, cosmologically relevant initial conditions are usually generated taking the effects of baryonic physics in the early Universe into account. For example, initial conditions can be set up to have a BAO feature. Throughout this chapter, and in the field of cosmological simulations, the phrase 'dark-matter particle' really means 'matter particle' with gravitational interactions only. The hydrodynamic effects of baryons are ignored due to an incomplete understanding baryonic physics; the accuracy of treating baryonic matter in this way is discussed in Section 2.2.2. Additionally the particles in simulations are really pseudo particles that represent blobs of matter. Even for a standard high resolution simulation each particle usually represents $\sim 10^9\,h^{-1}\,\mathrm{M}_\odot$ of matter (more for larger volumes) and are thus not really individual dark-matter particles but more tracers which hope to sample the phase space of true dark matter accurately.

2.1 Uses, requirements and limitations

Simulations are expensive, in terms of computer power, and time consuming to run. In principle a separate simulation is needed for each different set of cosmological parameters under investigation and this becomes prohibitive for the large cosmological parameter space that is now under investigation which includes: dark energy (Durrer & Maartens 2008), massive neutrinos (Lesgourgues & Pastor 2006); warm dark matter (Colombi et al. 1996); modified gravity theories (Clifton et al. 2012); non-Gaussianity in the initial conditions (Bartolo et al. 2005). In order to compare to the real Universe many different simulations have to be run at high resolution and computationally this is an unrealistic prospect at the moment. Also these alternatives introduce some additional complications in the simulating process; for example, the neutrinos or modified gravity fields need to be simulated together with the dark-matter particles. However, progress has been made in running simulations of these scenarios including: dark energy (Jennings et al. 2010); massive neutrinos (Agarwal & Feldman 2011); warm dark matter (Lovell et al. 2012); modified gravity (Li et al. 2012); non-Gaussianity (Wagner et al. 2010).

Simulations are used in many ways throughout cosmology: They are the only way so far of accurately calculating the deeply non-linear regime of structure formation (although see Chapter 3 for analytical arguments but bear in mind that many of these have been justified via simulations) and can be used to attempt to understand the evolution of perturbations in the non-linear regime when perturbation theory breaks. This is useful for its own sake but is particularly relevant for weak lensing (see Section 1.12.5) where the lensing power spectrum mixes both linear and non-linear modes of the matter power spectrum, so information about the matter power spectrum beyond linear evolution is needed. Simulations are also useful and necessary for testing higher order perturbation theory calculations (*e.g.* Bernardeau et al. 2002). Additionally, simulations are required to calibrate real survey analysis methods so as

to take into account features such as the survey mask and selection function. In order to put error bars on a survey analysis it is necessary to generate a covariance matrix, which gives the probability that one will measure a certain quantity given that a measurement of a specific value for another quantity has been made. If the over-density field is Gaussian random then each mode is statistically independent and the covariance matrix is diagonal. However, as non-linear gravitational evolution takes place this ceases to be true and a realistic covariance matrix requires many (up to many 1000 see Taylor et al. 2013) of simulations to investigate mode coupling effects (*e.g.* the effects on the non-linear power of having particular realisations of the linear regime). One of the major challenges facing precision cosmology is that the number of simulations required is very large. Despite the qualitative success finding the cosmic web structure seen in Fig. 1.5 (compare to *e.g.* Fig. 2.1) it seems that such structure is fairly generic and the non-linear dependence on the statistical properties of the density field on cosmology may be quite subtle.

In order to be cosmologically useful a simulation must contain modes in the linear regime – the box must span enough of the Universe so as to be linear at the box size because missing linear modes can affect non-linear growth (Cole 1997; Power & Knebe 2006). For the currently accepted cosmological paradigm this means that simulation boxes must be at the very least $100\,h^{-1}\,\mathrm{Mpc}$ a side. To overcome this, one must either simulate large volumes, or many different realisations of small volumes, in order to cover mode coupling effects. For survey analysis the simulation must be at least big enough to encompass the entire survey within it, for current surveys this is quite large (*e.g.* several Gpc^3 for surveys like WiggleZ described in Blake et al. 2011) and the simulation mass resolution must also be sufficient to resolve all galaxies within the volume. Surveys such as VIPERS (Guzzo et al. 2013) resolve satellite galaxies of large haloes that can be as low as $10^9\,h^{-1}\,\mathrm{M}_\odot$ and these requirements mean that the volume, resolution and number of simulations that need to be run is very large. Additionally, if simulations are used to compute the covariance matrix a simulation suite should technically be run for every cosmology under consideration. This is *not* done in practice because it is too demanding on computer time. Chapter 5 deals with a way of rescaling simulations that have already been run so that they accurately recreate what would have been seen had simulations of a different cosmological model been run and in this way future survey analyses will be able to use cosmology dependent simulations to test analysis methods and will be able to generate covariance matrices as a function of cosmological model.

If one is *only* interested in using simulations to compute the matter power spectrum as a function of cosmology then some progress has been made in this direction, by running a sample of simulations over a grid of parameters and then interpolating between the outputs to cover the full parameter grid (*e.g.* the 'Coyote Universe' – Heitmann et al. 2010; Heitmann et al. 2009; Lawrence et al. 2010; Heitmann et al. 2014: neural network techniques Agarwal et al. 2012; Agarwal et al. 2013). These approaches can be very accurate but suffer from the fact that they are not physically motivated and so it is difficult to extend them with additional parameters or

different cosmological models (such as modified gravity) without running many more simulations to add in to the interpolator. A separate approach is to use physically motivated fitting formulae such as `HALOFIT` (Smith et al. 2003; Takahashi et al. 2012) that are fit to simulations but include some physical insight based on the halo model discussed in Chapter 3. Chapter 4 discusses using a full calibrated version of the halo model, fit to simulations, to compute the matter power spectrum accurately.

2.2 Running a simulation

2.2.1 Equations of motion

Once particles have been set down in a simulation box their positions need to be evolved based on the gravitational force that each particle feels. In cosmology one is faced with the issue that the Universe is very probably infinitely big (indeed, if it described exactly by the Friedmann metric and is flat then it is infinite) but one can only simulate a finite region given finite computational resources. To deal with this one simulates a finite cubic comoving volume but takes this volume to be periodic so that there is no 'edge' thus making it infinite. The volume is taken to be comoving so that the gross expansion of space is automatically included and the simulation can focus on evolving the perturbations to particle positions, rather than their bulk motions.

The equation of motion for a particle at inertial position coordinate $\mathbf{x}$ moving in a gravitational potential Φ is

$$\ddot{\mathbf{x}} = -\nabla\Phi \ . \tag{2.1}$$

If coordinates are now changed to comoving coordinates $\mathbf{r}$ such that $\mathbf{x} = a\mathbf{r}$ then

$$a\ddot{\mathbf{r}} + 2\dot{a}\dot{\mathbf{r}} + \ddot{a}\mathbf{r} = -\frac{\nabla'\bar{\Phi}}{a} - \frac{\nabla'\delta\Phi}{a} \ , \tag{2.2}$$

where the derivatives of $\nabla \rightarrow \nabla'$ have also been changed to comoving derivatives and the potential has been split into the average $\bar{\Phi}$ and the perturbed part $\delta\Phi$. The bulk motion of the Universe is caused by the average potential, which causes the $\ddot{a}\mathbf{r}$ term (note $\dot{\mathbf{r}} = 0$ and $\ddot{\mathbf{r}} = 0$ for the unperturbed Universe) and so these cancel which leaves the equation

$$\ddot{\mathbf{r}} + 2H\dot{\mathbf{r}} = -\frac{\nabla'\delta\Phi}{a^2} \ , \tag{2.3}$$

which simply says that perturbations to particle positions from the Hubble flow are caused by the perturbed part of the gravitational potential. The $2H$ term is known as the 'Hubble drag' and is simply an artefact caused by working in non-inertial, comoving coordinates. The perturbed gravitational potential (here Φ rather than $\delta\Phi$ – standard notation) is given by

$$\nabla^2\Phi = 4\pi G\bar{\rho}\delta = \frac{3}{2}H^2\Omega_{\rm m}(a)\delta \ , \tag{2.4}$$

where the last equation follows from the Friedmann Equation (1.3). The fact that only $\Omega_{\rm m}(a)$ appears in the equation, and not other energy densities, is because it is the matter component

which is perturbed and vacuum energy or dark energy is (usually) taken to be homogeneous. Equation (2.4) is exact and it can be used to derive the linear perturbation equation (1.114) by combining it with the linearised continuity equation:

$$\nabla \cdot \dot{\mathbf{r}} = -\dot{\delta} \ . \tag{2.5}$$

Solving the N-body system then proceeds as follows: the potential is calculated from the over-density of all particles via equation (2.4), which is then used to update particle positions using equation (2.3) as each particle responds to the global gravitational forces. Usually this is done in a two stage process: equation (2.4) is solved on a mesh using a Fast Fourier Transform (FFT) technique which naturally takes the periodicity of the computational universe into account. The resolution of the gravitational field available from this method is limited by how fine the mesh can be made to be for the FFT, which in turn is limited by available computational memory. Solving the gravitational equations on a Fourier mesh in this way is known as a Particle-Mesh (PM) technique. Additionally, almost all codes then solve for the motions of particles sub-FFT-grid by additionally calculating the forces between particles that reside in the same, or adjacent, cells. The gravitational force is then a sum of the large scale FFT component and the short range part. Since each dark-matter particle in the simulation in reality is a blob that represents the phase space distribution of dark matter, two-body scattering events must be avoided. As discussed on p190 of Binney & Tremaine 2008 the 'relaxation time' on which two body scatterings become important for a system is $t_{\rm relax} \approx N t_{\rm cross}/\ln(N)$ where N is the number of particles in the system and $t_{\rm cross}$ is the typical time for a particle to cross the system. For any reasonable dark-matter candidate, two-body scatterings can be entirely neglected and the evolution of the system is collisionless. The simulation particles should follow the mean gravitational potential generated by all other particles and not be affected by scattering events. To account for this the gravitational force is usually softened so that it a constant below some scale ϵ, rather than tending to be infinite as particles get arbitrarily close to one another. This can be done either at the level of the force:

$$\mathbf{F}_{\rm g} = -\frac{Gm^2}{(r+\epsilon)^2}\hat{\mathbf{r}} \ , \tag{2.6}$$

or at the level of the potential, so-called Plummer softening:

$$\Phi_{\rm g} = -\frac{Gm}{\sqrt{r^2+\epsilon^2}} \ . \tag{2.7}$$

The softening can be chosen to be either in physical or comoving units and can be set to come into effect at different times in the simulation; depending on what is being simulated different softening criteria may be employed. Given the unphysical nature of softening it is unclear just what the resolution of a simulation is. Clearly by setting $\epsilon = 0$ one is not able to resolve arbitrarily small scales because of the discretisation of the density field into massive dark-matter pseudo particles. The only way to be sure about resolution issues is to do convergence testing for a particular quantity of interest to make sure it is insensitive to all unphysical simulation

parameters. In the simple case of PM the spatial resolution of the simulation is roughly the physical size of the mesh cells used to compute the gravitational force. The 'mass resolution' of a simulation refers to the simulation particle mass, which governs the mass of strucutures that are resolveable, and 'force resolution' refers to the gravitational softening; clearly features below this scale will not be well resolved.

N-body codes are publicly available and work in a variety of different ways. Simple (PM) codes, such as `PMCODE` (Klypin & Holtzman 1997), just calculate the gravitational force on a mesh, and are thus unable to resolve forces below the mesh size, but are simple to use and modify. P^3M codes such as MacFarland et al. (1998) order particles in a clever way so computing the submesh forces between nearby particles is quick. `RAMSES` by Teyssier (2002) uses an adaptive PM such that when cells contain multiple particles a new mesh is generated and forces calculated on this new mesh. This procedure can be repeated as many times as memory and computing time allow. `GADGET-2` of Springel (2005) uses a 'tree' code to group particles into sub clumps and then calculates forces between these clumps, using a multipole expansion of the gravitational field of the clump, to make the computation more efficient. There are some tree codes that do not even use a PM step in their calculations as essentially all the gravitational forces are due to nearby particles and a tree of sufficient depth can be used to calculate these.

In summary: if one sets down some particles with sensible, cosmologically relevant, initial conditions (see section 2.2.3) then one can evolve these under gravity using equation (2.3) to high precision given enough computing power. Bottlenecks for N-body techniques include both computational power (calculating the gravitational forces) and memory (for the Fourier mesh and the sheer number of particle positions and velocities). A visualisation of the end result of a typical simulations is shown in Fig. 2.1 where the dark matter can be seen to have condensed into a complicated network of filaments and knots which in detail are comprised of approximately spherical haloes, thought to be where galaxies reside. Haloes continually collide and merge, which suggests that galaxy formation process is a violent process; first described by White & Rees (1978). Comparisons between Figures 2.1 and 1.5 show that this distribution of dark matter seen in a simulation is reflected qualitatively in the distribution of galaxies in the real Universe.

2.2.2 Baryons

Most large N-body simulations completely ignore the effects of baryonic physics, except in the initial conditions. In reality baryonic matter is affected by a variety of complicated electromagnetic and nuclear processes that allow the gas to cool and thus become much denser in the cores of dark-matter haloes. The eventual result of this process is that stars will form in cold gas and a 'galaxy' can be said to have been born, a scenario first put forward by White & Rees (1978). A variety of feedback processes are known to occur on very small scales in the Universe which can result in the large scale redistribution of gas, and thus matter, both within

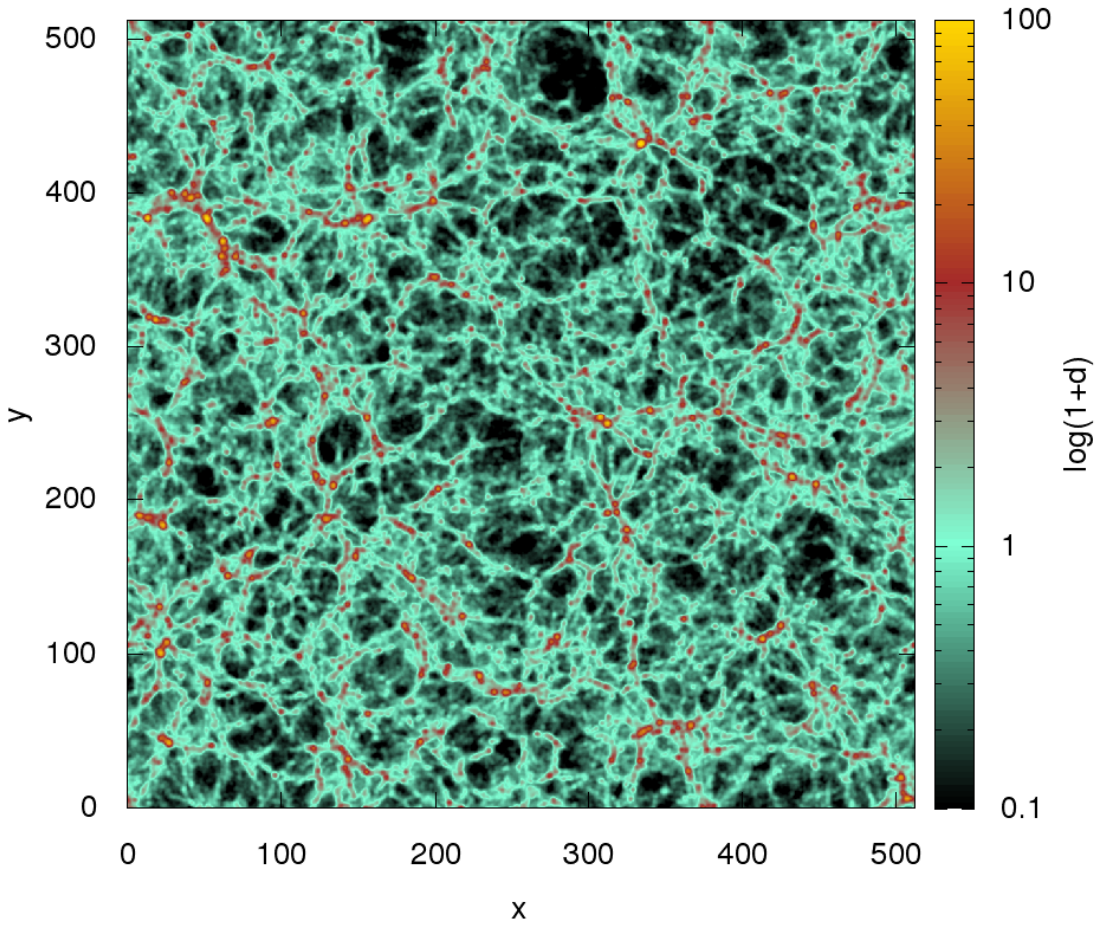

Figure 2.1: A visualisation of a 2% thickness slice of density field from a standard ΛCDM simulation in a $512\,h^{-1}$ Mpc box at $z = 0$. The density field is smoothed on scales of $1\,h^{-1}$ Mpc. Haloes can clearly be seen, as well as the filamentary nature of the density field.

and out of galaxies. Massive stars generate winds which blow off the outer layers of the star and the most massive stars explode as supernovae which are hugely energetic and can heat the surrounding gas. In the centres of most, if not all, galaxies massive black holes are known to reside; as material accretes onto the central black hole the black hole grows in mass but some of the matter that is attempting to accrete is blown out from near the black hole at large speeds and can end up gravitationally unbound from the galaxy. The energy produced by an accreting black hole is thought to be the main source of observed active galactic nuclei (AGN). These non-gravitational processes result in gas being moved around a dark-matter halo and inevitably this will affect the distribution of the dark matter because it is gravitationally coupled to the baryons. Since the total mass of the universe is comprised of $\sim 20\%$ baryons this can hardly be considered to be a 'small' effect.

The problem with modelling baryonic physics in a simulation is that the physics associated with galaxy formation is relatively poorly understood and far more complicated than simple gravitational interactions. Effects that certainly matter, but that are not fully understood include gas physics, star formation, stellar winds, AGN formation, evolution and jet production, the production and effect of metallicity and supernovae feedback. These can be included in N-body simulations via hydrodynamics for the gas particles (so that effects like gas cooling can be taken into account) and as 'sub-grid' recipes; where quantities such as metallicity and stellar populations are included in grid cells. The numbers of, as an example, supernovae that one would then expect can be calculated and the momentum from this can then be fed into the surrounding gas particles. However it is fair to say that baryonic simulations such as these are in their infancy. Work comparing a variety of baryonic feedback recipes in van Daalen et al. (2012) and van Daalen et al. (2013) has shown that particularly AGN feedback could have a substantial effect on the full matter power spectrum. However, the details depend very heavily on poorly understood physical processes and it is certainly possible that recipes used were too extreme. However, the effects of baryons are scale dependent and certainly cannot affect structure formation on the very largest of scales. It is still an open question in cosmology as to exactly how small a scale the approximation of pure gravitational evolution is valid.

Another approach, rather than running direct simulations, is to use 'semi-analytic' recipes for galaxy formation (*e.g.* Baugh 2006; Benson 2012) where initially a dark matter only simulation is run and this is used to generate trees that contain the halo merger histories. Recipes are then run through these merger trees to attempt to compute the properties of the galaxies that would end up residing in each halo (for example, mass and colour). This has the advantage of being relatively quick to run (certainly much quicker than running a full simulation) but the disadvantage of being unable to compute any of the back reaction effects that baryonic processes may have on the background dark-matter structures.

2.2.3 Initial conditions

In order to run a simulation, an initial particle distribution needs to be generated that contains the correct perturbation spectrum for the cosmology in question. This perturbation spectrum needs to include all of the effects that distort perturbations during the early universe and so that the gravity only simulation can be started at a redshift where only gravity is important for the evolution of the cosmos. Clearly an initially uniform random distribution will develop some structure when evolved under gravity, but this will have little relevance to cosmology. What is required is some way of imprinting a realisation of the initial density and velocity perturbation spectra on a distribution of particles that is initially uniform in some sense.

The approximation of Zel'dovich (1970) (hereafter ZA) is a method for approximating the gravitational evolution of a system of particles that uses linear perturbation theory. Initially particles are considered to be placed down in a uniform way at coordinates $\mathbf{q}$ and they are then transported to positions $\mathbf{x}$, where they have the correct perturbation field, by the displacement field $\mathbf{f}$.

$$\mathbf{x} = \mathbf{q} + \mathbf{f} \ . \tag{2.8}$$

The ZA approximates the properties of $\mathbf{f}$ required to carry out this movement. Comoving coordinates $\mathbf{q}$ are known as Lagrangian coordinates and do not change even as the particles move. Eulerian coordinates $\mathbf{x}$ follow the motions of each particle. By mass conservation the relation

$$\rho \, \mathrm{d}^3\mathbf{x} = \bar{\rho} \, \mathrm{d}^3\mathbf{q} \ , \tag{2.9}$$

must hold, where $\bar{\rho}$ is the unchanging (Lagrangian) density because the particles are not moving in these coordinates. It therefore follows that

$$1 + \delta = \left| \frac{\mathrm{d}^3\mathbf{x}}{\mathrm{d}^3\mathbf{q}} \right|^{-1} \ , \tag{2.10}$$

where the quantity on the right is the inverse of the determinant of the deformation tensor, which is symmetric (as long as density perturbations are irrotational – true in cosmology when perturbations originate from a growing mode) and can therefore be diagonalised. In a diagonal coordinate system (primed) the eigenvalues of the tensor are $(\partial x_i'/\partial q_i')^{-1}$ so that

$$1 + \delta = \left| \frac{\partial x_1'}{\partial q_1'} \frac{\partial x_2'}{\partial q_2'} \frac{\partial x_3'}{\partial q_3'} \right|^{-1} \ . \tag{2.11}$$

In the same diagonal coordinate system, the eigenvalues of the deformation tensor must also be the components of the divergence of the displacement field via equation (2.8) (*e.g.* $1 + \partial f_i'/\partial q_i' = \partial x_i'/\partial q_i'$ etc.). For small displacements, $\mathbf{f}$ therefore relates to the over-density field via

$$\nabla \cdot \mathbf{f} = -\delta \ , \tag{2.12}$$

and in Fourier space

$$i\mathbf{k} \cdot \mathbf{f}_\mathbf{k} = \delta_\mathbf{k} \ . \tag{2.13}$$

Note that this means that the linear displacement field grows over time via the growing mode, exactly like the overdensity.

Thus by having a realisation of the overdensity field $\delta_{\mathbf{k}}$ this can be related to $\mathbf{f}_{\mathbf{k}}$ in the linear regime where $\mathbf{f}$ is parallel to $\mathbf{k}$ and can be written as $\mathbf{f} = f(\mathbf{x})\hat{\mathbf{k}}$. In order to generate a realisation of $\delta_{\mathbf{k}}$ one must assume the statistical properties of the field: As discussed in Section 1.10.4 the field is usually taken to be Gaussian and thus everything is specified by the power spectrum. To generate a Gaussian random field, each Fourier mode of the real and imaginary part of δ is Gaussian distributed with mean 0 and a variance given by $P(k, z)$. The field is automatically isotropic if $P(k, z)$ depends on $|\mathbf{k}|$ only and will be periodic over the length of the simulation box. Clearly by doing this the simulation will have a fundamental mode $k_{\rm box} = 2\pi/L$ the maximum scale resolvable, specified by the length of the box L. Theoretically the fields can be specified to arbitrarily fine scales but in practice this is limited by the resolution of the FFT used to transform the field from Fourier space to real space so that they may be used to shift particles around. FFTs are limited by the number of mesh cells, m^3, used for the transform and so the finest scale that is resolved by the transform is the Nyquist frequency $k_{\rm NY} = m\pi/L$.

Velocities can also be given to particles via the ZA from the linear continuity equation, $\nabla \cdot \dot{\mathbf{r}} = -\dot{\delta}$, where $\dot{\mathbf{r}}$ is the comoving velocity. Comparison with equation (2.12) shows that $\dot{\mathbf{r}} = \dot{\mathbf{f}}$ up to constants which can be set to 0 because at early times there should be no peculiar velocity ($\mathbf{v} \equiv a\dot{\mathbf{r}}$) and no displacement. Thus velocities can be assigned to particles by taking the time derivative of the displacement field. This time derivative can be converted into an expression involving the logarithmic growth rate for the linear fields (because $\mathbf{f}$ grows over time with the linear growth factor):

$$\dot{\mathbf{r}} = f_{\rm g} H \mathbf{f} \ . \tag{2.14}$$

That simulations take place in finite periodic volumes means that there is a large scale limitation on what can be seen. Clearly the simulation has no information on what perturbations could be present on scales above the simulation box size. It therefore becomes necessary to either simulate large volumes so that one can be sure that the small perturbations that should exist outside of the simulation volume should have little effect or to simulate many different realisations of smaller boxes to see how the coupling between the (limited number of) large-scale modes affect the small scale evolution.

The starting redshift should be chosen to be high enough that particles are only displaced slightly, so that the approximation of linear motions and constant velocities is accurate, but not so high that the simulation wastes lots of computer power calculating well understood linear theory. A good guide is that particles should not have moved very far in terms of the mean inter-particle separation; a standard choice is 0.2 times the mean inter-particle separation. This means that, for a fixed particle number, a larger simulation volume can be started at a later time. An increase in particle number for a given simulation volume then means the simulation should be started at an earlier time.

When generating initial conditions an initial 'particle load' must be set which gives the

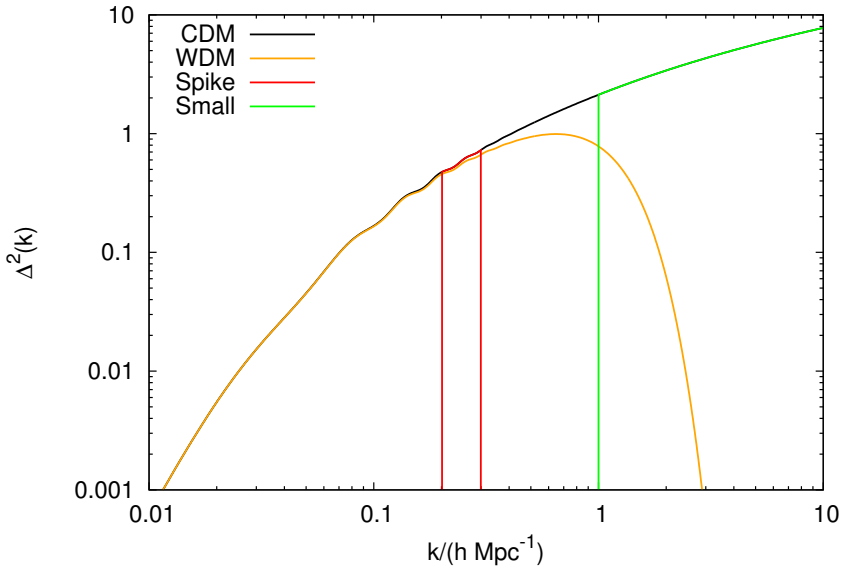

Figure 2.2: Power spectra for the different ZA particle distributions realised in Fig. 2.3.

q from which particles are displaced. This initial distribution should have as little power as possible so that there are no residual effects once the initial conditions are imposed. One could decide to initially put particles down uniformly at random over the box but it is shown later, in Section 3.2.2, that a random distribution has a power $\Delta^2(k) \propto k^3/\bar{n}$, where $\bar{n}$ is the average number density of particles. Note that $\Delta^2(k) \to 0$ if $\bar{n} \to \infty$ in this case which makes sense because this is tending towards uniformity. What is required is a distribution which has less power than this and is sub-random. Two possibilities present themselves: One would be to start with a uniform grid of particles, which only has power on scales of order the grid separation scale. Another is to generate a 'glass' by evolving a random distribution of particles with an N-body code with gravity reversed (Baugh et al. 1995). This essentially pushes particles as far apart from each other as possible and thus reduces the clustering power. How the initial particle load can influence what is later observed in simulations is discussed in Baugh et al. (1995), Smith et al. (2003) and Crocce & Scoccimarro (2006).

The ZA can be used to generate an approximate particle distribution at any redshift, even though the fine structure produced may not be accurate at later times. This is quite useful because the ZA is very quick to run (only requiring 3 FFTs once the Fourier realisation of the overdensity field has been generated) and the large scales will be approximately correct for cosmologically relevant power spectra, even at $z = 0$ with large enough L. For interest Fig. 2.2 shows four example matter power spectra: a standard ΛCDM power spectrum; a model with smoothed out small-scale structure for scales smaller than $1\,h^{-1}\,\mathrm{Mpc}$; a 'spike' of power around $k = 0.25\,h\,\mathrm{Mpc}^{-1}$ and a model with *only* small-scale structure and no power for wavenumbers below $k = 1\,h\,\mathrm{Mpc}^{-1}$. These power spectra are converted into particle distributions via the ZA

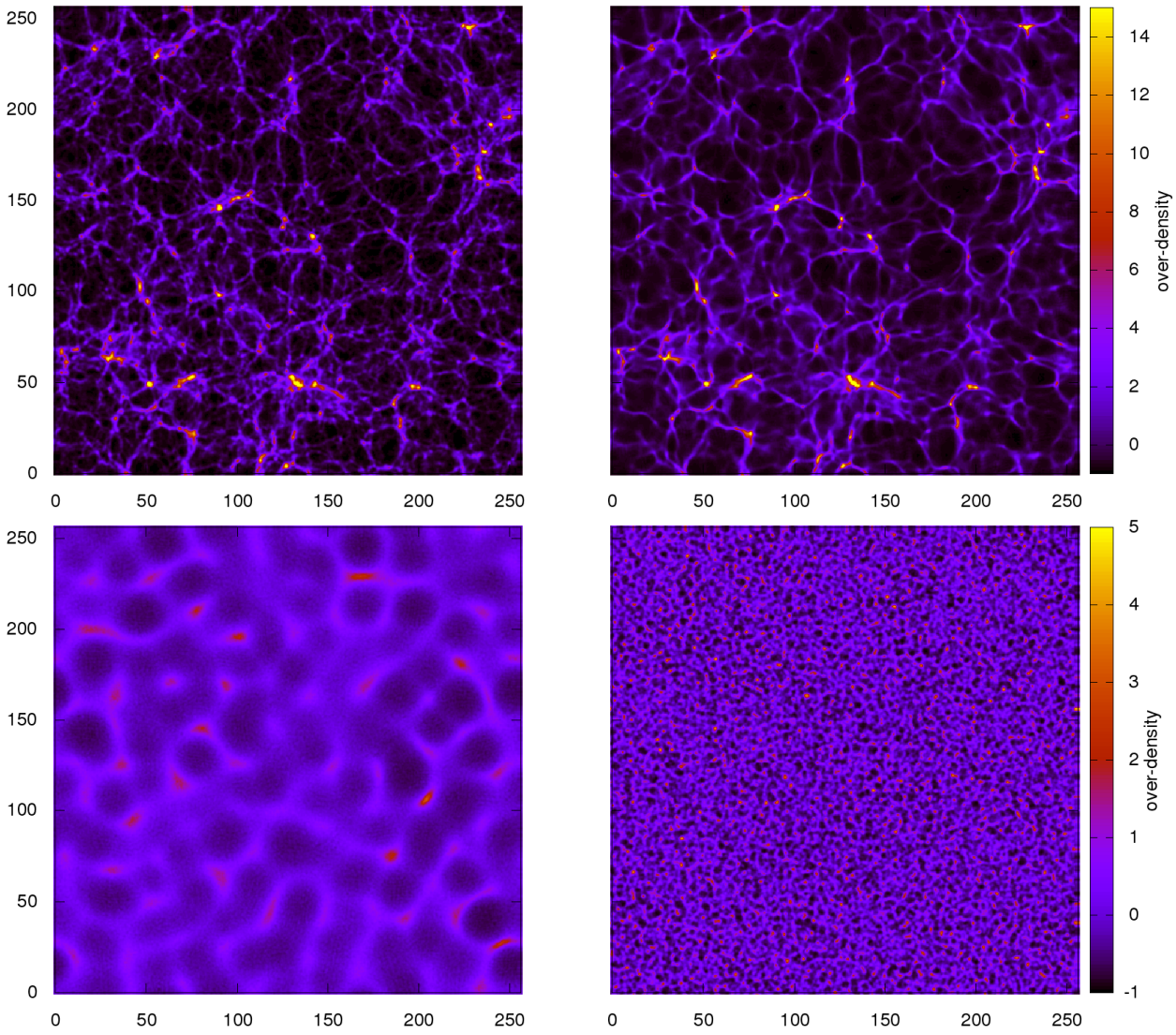

Figure 2.3: The density field given by the ZA evolved to $z = 0$ for the 4 example power spectra shown in Fig. 2.2. The top left shows a standard ΛCDM power spectrum, top right is a model in which small scale structure has been smoothed with a Gaussian for scales smaller than $1\,h^{-1}\,\mathrm{Mpc}$, the bottom left panel is for a spike of power around $k = 0.25\,h\,\mathrm{Mpc}^{-1}$ of width $0.1\,h\,\mathrm{Mpc}^{-1}$ and the bottom right is for a spectrum with no power for scales larger than $k = 1\,h\,\mathrm{Mpc}^{-1}$.

in Fig. 2.3, which shows the overdensity field in each case. The effect of removing small scale power by smoothing can be seen by comparing the top two panels; the spike density field clearly only has structure on scales that are approximately 2π times the inverse of the wavenumber of the spike ($\simeq 25\,h^{-1}\,\mathrm{Mpc}$) and the small-scale model clearly has no large-scale structure visible in the density field at all.

`N-GenIC` is a code that is commonly used to generate initial condition files and it creates binary particle files that in the `Gadget-2` file format. Other codes are available in the literature such as Crocce & Scoccimarro (2006) that uses 2^{nd} Order Lagrangian Perturbation Theory (2LPT) to generate initial conditions more accurately than the ZA, but this comes at the expense of using more computer memory and time because there are additional FFT meshes associated with the 2^{nd} order parts of the perturbation theory. In most initial condition generation procedures no distinction is made between dark matter and baryonic particles, even though in reality at high redshift both dark matter and baryons have very different distributions because they interact differently with radiation in the early Universe. The power spectra of baryons and of dark matter look very different at the epoch of recombination and this continues until late times when agnostic gravitational attraction brings them together. Usually initial conditions are set such that evolution with linear theory for a one component universe that will produce the $z = 0$ total matter distribution. This is because at $z = 0$ linear perturbation theory predicts there will be almost no difference in power spectrum between the dark matter and baryons. The accuracy of this approximation was investigated in Angulo et al. (2013b) in which it was shown that it was a fair assumption for most practical purposes.

2.3 Measuring power spectra

2.3.1 Real space

Once a simulation has been run it can be useful to calculate the matter power spectrum. In order to do this one must construct an overdensity field from the particle positions. This can be done by laying down a mesh with m^3 cells over the simulation volume and then assigning particles to the mesh cells in some way. In this thesis particles are assigned to the mesh using a Nearest Grid Point (NGP) technique in which the value of the particle count on the mesh is simply the count of the number of particles in each mesh cell.

By assigning particles to a cubic mesh one is effectively convolving the underlying density field with an unphysical cubic bin. The effect of doing this can be undone to some extent by deconvolution (Jing 2005) – dividing the Fourier Transform of the density field by the normalised Transform of a cubic bin of width L/m

$$W_{\square}(\mathbf{k}) = \mathrm{sinc}\left(\frac{k_x L}{2m}\right)\mathrm{sinc}\left(\frac{k_y L}{2m}\right)\mathrm{sinc}\left(\frac{k_z L}{2m}\right) . \tag{2.15}$$

Once the overdensity field has been transferred to Fourier Space, $\Delta^2(k)$ can then be calculated via its definition as the contribution to the field variance per log bin in k. Essentially one bins

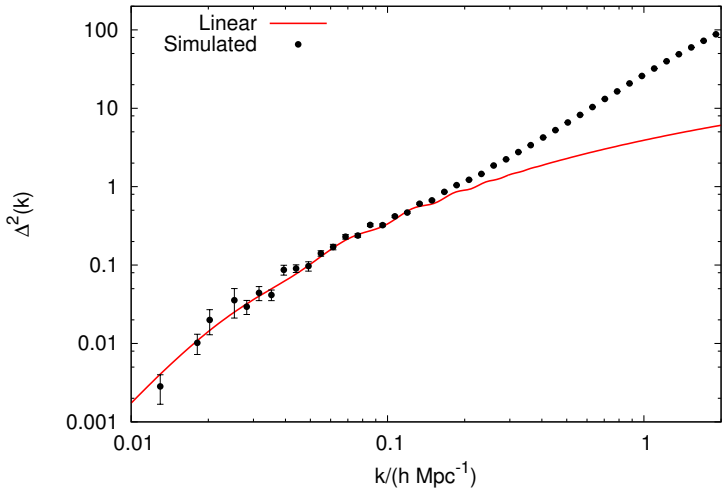

Figure 2.4: An example matter power spectrum from a simulation, together with the input linear spectrum at $z = 0$ for a typical ΛCDM cosmological model. The error bars on the measured power show the Poisson error due to finite numbers of modes. The error bars are large only around the size of the box where the finite geometry ensures a sparse sampling of modes. At large scales the simulated power agrees well with the input linear spectrum, however the simulation is noisy due to having a finite number of low k modes. At small scales non-linear growth means that the power departs from the linear form.

up k and assigns the value of $|\delta_{\mathbf{k}}|^2$ to the correct bin by taking $|\mathbf{k}|$ for each mode. Each bin is then divided through by the logarithm of its width to compute $\Delta^2(k)$ (Smith et al. 2003).

The final effect that needs to be taken into account when computing power spectra from a discrete set of particles is that of shot noise. On small scales in the simulation the density field no longer looks like a smooth distribution and is obviously discretised due to the fact it is comprised of a finite number of particles, and this can be corrected for. In Smith et al. (2003) it was shown that on small scales the effect of this could be remedied simply by subtracting the power spectrum due to particles placed at random: shot noise.

The power spectrum due to N^3 particles being placed at random is calculated in Section 3.2.2 and is given by

$$\Delta^2_{\rm SN}(k) = \frac{4\pi k^3 L^3}{(2\pi)^3 N^3} \ , \tag{2.16}$$

which tends to 0 in the limit of the density field becoming perfectly sampled $N \to \infty$. The final power spectrum is thus related to the raw one by

$$\Delta^2(k) = \frac{\Delta^2_{\rm raw}(k)}{W^2_{\Box}(k)} - \Delta^2_{\rm SN}(k) \ . \tag{2.17}$$

An example matter power spectrum measured from a simulation in shown in Fig. 2.4. Here one can see that at low k the simulation is noisy, a consequence of being in a finite box and having a small number of low k modes. At higher k non-linear growth is important and the matter spectrum is far above the predictions of simple linear theory.

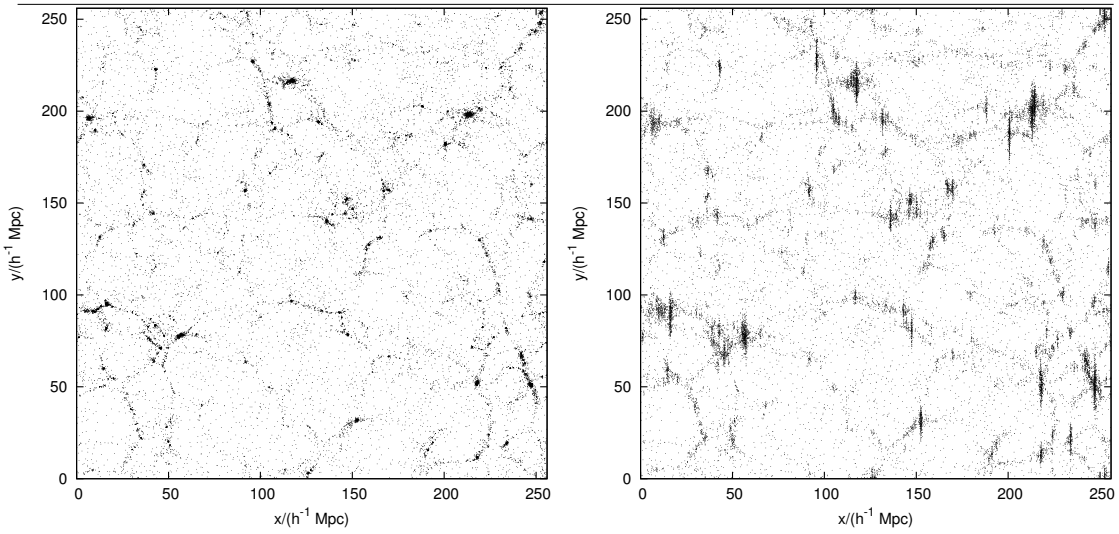

Figure 2.5: An example density field before and after the transformation into redshift space. The transformation has been done along the $\hat{\mathbf{y}}$ direction in this example according to equation (2.19). The most obvious difference that can be seen is that clusters are splayed along the redshift direction due to particles within them being essentially randomly shifted in position due to their virial motions. Less obvious is the Kaiser (1987) effect in which linear structure is compressed slightly, but this cannot easily be seen by eye.

2.3.2 Redshift space

In real cosmological surveys galaxies are measured by their angular position on the sky together with a redshift. The redshift can be converted into a distance, but this requires assuming a cosmological model, which is a disadvantage if one is trying to constrain the cosmological model using the data. Additionally there is no one-to-one mapping between redshift and real positions due to effects such as virialised motions within clusters – two galaxies can have exactly the same redshift and position on the sky but be in different physical positions. It thus makes sense to compute theoretical quantities in redshift space so as to make better contact with real observations.

The full redshift-space power can be computed by binning the Fourier Transform of a density field in terms of both $|\mathbf{k}|$ and $\mu = |\cos\theta|$ where θ is the angle between the mode in question and the line-of-sight direction. Obviously this is noisier than in real space because there are fewer modes per bin but it does allow an exploration of the power as a function of the angle of the mode of density fluctuation to the line of sight. The dimensionless redshift-space power as a function of both k and μ is defined as

$$\sigma_{\rm s}^2 = \int_0^1 \mathrm{d}\mu \int_0^\infty \Delta_s^2(k,\mu)\,\mathrm{d}\ln k \ , \tag{2.18}$$

where the subscript s denotes redshift space quantities. $\Delta_s^2(k,\mu)$ is defined such that it gives the contribution to the redshift-space variance per logarithmic k bin and per linear μ bin. An example theoretical power spectrum binned in this way is shown in Fig. 1.11 for a simple model

of the redshift space power.

Simulations take place in real space, however a simulated particle distribution can be shifted into redshift space by moving the particles to their comoving redshift-space positions, $\mathbf{s}$, along an arbitrary coordinate axis according to

$$\mathbf{r} \rightarrow \mathbf{s} = \mathbf{r} + \frac{\dot{\mathbf{r}} \cdot \hat{\mathbf{x}}_i}{H(a)} \hat{\mathbf{x}}_i \ , \tag{2.19}$$

where the transformation is along $\hat{\mathbf{x}}_i$. The form of the transformation follows from combining $\delta z = \delta \dot{r}$, $\delta z = -\delta a/a^2$, $\delta a = H(a) a \delta t$ and $\delta t = a \delta r$. Example power spectra binned in this way are shown in the lower panels of Fig. 2.6 where the power binned in μ and $\ln k$ is shown before and after the transformation into redshift space. Before the transformation the power is isotropic, showing no μ dependence, whereas after the transformation this is no longer true. The most obvious features are the sharp drop in power as μ increases at high k. This is the FOG effect and comes about because haloes along the line of sight are splayed out, lowering their overdensity and thus the power. A careful comparison at large scales can see the Kaiser boost in power as μ increases. The patchy nature of the signal at low k is due to the finite size of the Fourier mesh only accommodating a sparse sample of μ values.

The monopole power can be computed in the same way as described for real space but applied to the particle distribution in redshift space. This essentially averages over all angles with an equal weighting to create the monopole. In theory, the various polar spectra of $\Delta^2_{\rm s}(k, \mu)$ discussed in Section 1.12.3 can be computed by weighting each mode by a Legendre polynomial for the particular multipole of interest. However, in practice this is a bad way of proceeding because the polar spectra are integrals over μ, and μ is poorly sampled at low k due to the Cartesian geometry of the Fourier mesh, so the integration is poorly approximated by a sum. The simplest way of proceeding is to fit a monopole + quadrupole + hexadecapole model to $\Delta^2_{\rm s}(k, \mu)$, effectively truncating the multipole expansion at:

$$\Delta^2_s(k, \mu) \approx \Delta_0(k) + \frac{1}{2}(3\mu^2 - 1)\Delta_2(k) + \frac{1}{8}(35\mu^4 - 30\mu^2 + 3)\Delta_4(k) \ . \tag{2.20}$$

The monopole, quadrupole and hexadecapole obtained in this manner are shown in the top panel of Fig. 2.4 where it can be seen that the quadrupole and hexadecapole are very noisy at low k, where they flit between positive and negative values, contrary to the Kaiser expectation. At intermediate expressions the Kaiser expectation for the quadrupole is roughly realised, but not for the hexadecapole. However at high k the power agrees well with that shown in the Lorentzian damping theoretical model shown in Fig. 1.11. The ratio of quadrupole to monopole can be used to determine the growth rate, as discussed in Section 1.12.3, by realising that the Kaiser expectation for this quantity is solely dependent on β

$$\frac{\Delta^2_2(k)}{\Delta^2_0(k)} = \frac{1 + \frac{2}{3}\beta + \frac{1}{5}\beta^2}{\frac{4}{3}\beta + \frac{4}{7}\beta^2} \ , \tag{2.21}$$

although one has to be very careful to not be biased by non-linearities.

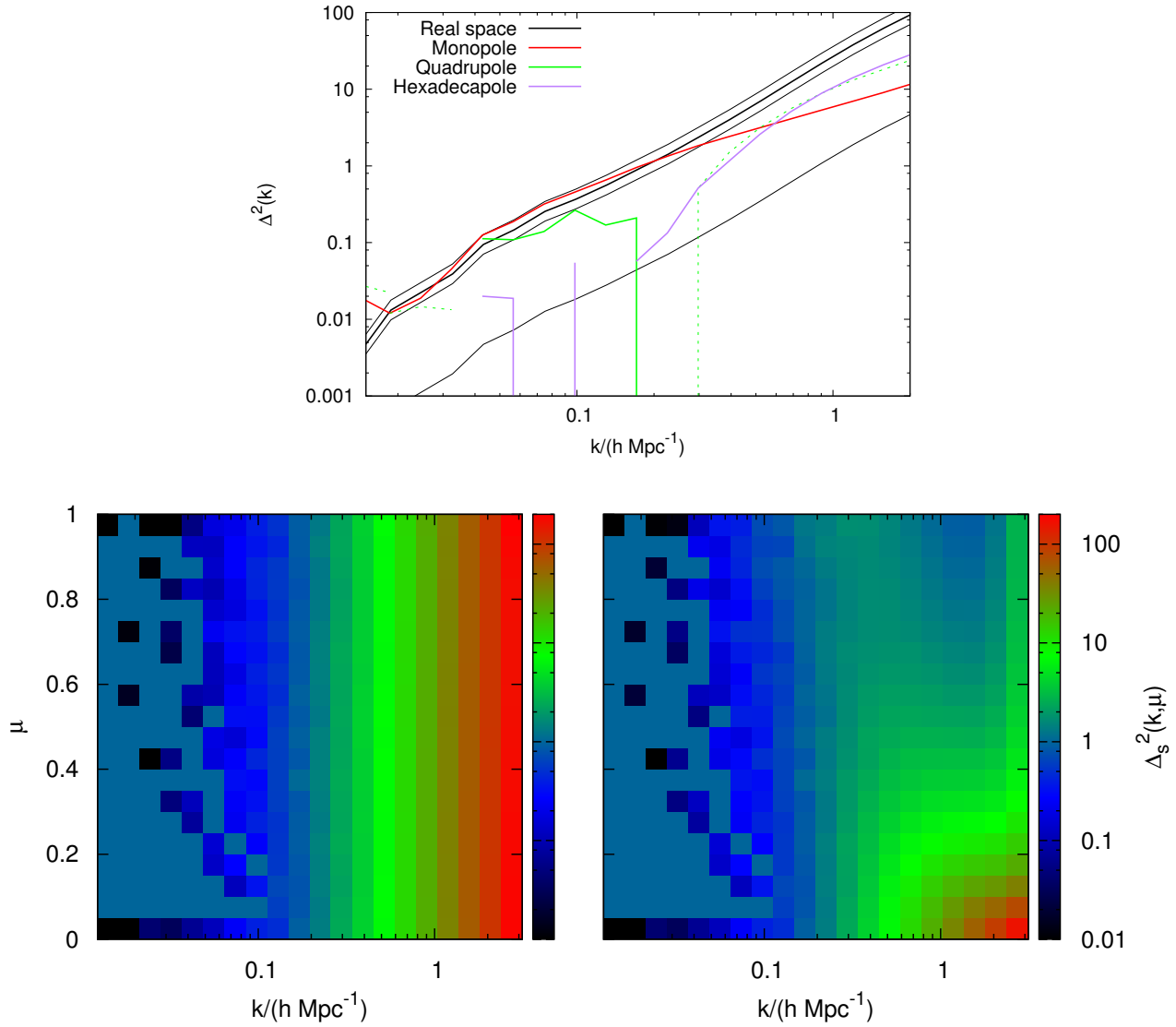

Figure 2.6: Example redshift space power spectra from a $512\,h^{-1}$ Mpc cube ΛCDM simulation. The top panel shows a comparison of the real power and redshift space power from the first three non-zero multipoles. In the monopole The Kaiser boost can be seen at linear scales whereas the FOG suppression can be seen at non-linear scales. The lower panel shows power as a function of k and μ before and after the transformation into redshift space. One can see that power is essentially constant as a function of μ in the left panel apart from some noise. For the right panel the lowest line of power along $\mu = 0$ is equivalent to the real space power spectrum because the transverse direction is undistorted. As one increases in μ the Kaiser boost can be seen at linear scales and FOG can be seen at non-linear scales. The power in the top panel can be constructed from that in the bottom panel by averaging over all μ with the appropriate Legendre polynomial.

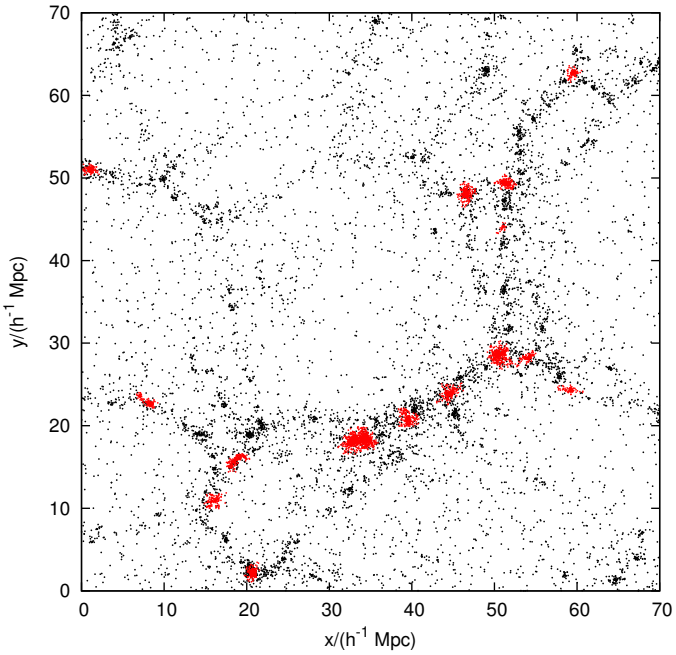

Figure 2.7: An example of a particle distribution from a thin slice through a typical simulation. Particles that are linked together into haloes of greater than 100 particles are shown in red while particles that are not are shown in black.

2.4 Haloes

One very noticeable feature of simulations once they have been run is that on large scales the structure remains in place (the filaments, knots, voids etc. seen in the ZA in Fig. 2.3) but that on small scales the dark matter has collected itself into quite distinct, approximately spherical clumps, known as haloes. The properties of these haloes are discussed in detail in Chapter 3 but in order to study their properties in a simulation one needs a way of defining what a halo is and which particles are considered to belong to it.

The simplest algorithm for halo finding is Friends-of-Friends (FOF) (Davis et al. 1985) whereby dark-matter particles are linked into a structure if they are close to each other. An FOF algorithm is thus specified by a single parameter that is the maximum separation within which particles are linked together, known as the linking length, ℓ. The cleverness of an FOF algorithm is in organising the particles such that only nearby particles are questioned as to whether they come within the linking length, rather than needlessly questioning all particles.

The linking length of an FOF algorithm can be related to the minimum overdensity that an algorithm will find as follows (*e.g.* Manera et al. 2013). On average 2 particles will be 'just' linked together if they are contained within a volume given by a sphere of radius the linking

length ℓ. The density contrast of this sphere ($\Delta \equiv \rho/\bar{\rho}$) is then calculated via

$$\Delta = \frac{2/\frac{4}{3}\pi\ell^3}{N^3/L^3} = \frac{3}{2\pi b^3} \ , \tag{2.22}$$

where N^3 is the total number of particles in the simulation and b is the dimensionless linking length in terms of the mean inter-particle separation: $b = \ell N/L$. In this way a given linking length can be related to a given density contrast. Usually haloes are defined as objects that contain a certain average overdensity. If an isothermal profile is assumed that is truncated at the virial radius then the overdensity at the boundary of the profile is related to the average overdensity by $\rho_{\rm bound} = \frac{1}{3}\rho_{\rm v}$ so the virial overdensity can be approximately related to the linking length as

$$\Delta_{\rm v} \approx \frac{9}{2\pi b^3} \ . \tag{2.23}$$

If $b = 0.2$ the implied virial density is $\Delta_{\rm v} \approx 180$, this is the 'standard' value used in the literature and is also the value used throughout this thesis. With an FOF algorithm one also specifies the minimum number of particles that one considers to constitute a halo. Depending on the simulation resolution objects containing small numbers of particles may or may not be representative of a structure that would emerge if the simulation was run at higher resolution. A possible problem with FOF is that structures one would visually classify as distinct haloes can be linked together into one single halo via a bridge; this is particularly apparent when mergers are occurring and FOF will group merging haloes into a single entity. It is also difficult to find sub-structure within a halo using an FOF algorithm.

The other commonly used algorithm for defining a halo is Spherical Overdensity (SO) (Press & Schechter 1974) in which the density field is measured directly in the simulation and a spherical window is put down and the density measured within the window. In this way the window can be extended until the region falls below some user-defined value of $\Delta_{\rm v}$.

Chapter 3

The Halo Model

In an ideal world one would be able to come up with a theory of how gravitating matter clusters on all scales in an expanding Universe, starting from arbitrary Gaussian initial conditions. This would follow the evolution of small perturbations in the early Universe through to the formation of dark-matter haloes and galaxies today. Unfortunately the theoretical apparatus for such a calculation does not exist and the type of simulations discussed in Chapter 2 must be employed to glean an understanding of the non-linear structure of the cosmos. The alternative to simulations is to use non-linear theoretical arguments – these are the subject of this chapter.

This chapter discusses the halo model which is a way of describing the distribution and evolution of the density field in terms of a clustered distribution of haloes. This approach uses a combination of theory and results taken from N-body simulations. The idea was first put forward by Seljak (2000) and Peacock & Smith (2000) and a comprehensive review of this method is given in Cooray & Sheth (2002).

3.1 The Spherical Model

Some insight into the full non-linear evolution of the density field can be gained by considering the idealised symmetric case of a spherical perturbation. In this case a full solution is possible without resorting to perturbation theory or to N-body simulations. The solubility of this problem is a result of the Theorem of Birkoff, the relativistic version of the Law of Gauss and states that in situations of spherical symmetry the gravitational field within a spherical region is due entirely to the matter distribution within the sphere, and the distribution outside this sphere can be ignored (*e.g.* p. 52 of Peacock 1999). By considering a spherical region at

the origin with an enhanced matter density relative to the flat, matter-dominated ($\Omega_{\rm m} = 1$) background it is easy to see that this region will evolve like a closed universe. The radius, r, of such a perturbation can be shown (*e.g.* p. 488 of Peacock 1999) to evolve in time t according to

$$r(\theta) = A(1 - \cos\theta) \ , \tag{3.1}$$

$$t(\theta) = B(\theta - \sin\theta) \ , \tag{3.2}$$

these equations are in terms of the parameter θ which provides the most transparent way of relating r to t. An equation for $t(r)$ can be written down but is unenlightening to work with. A and B are constants which can be related to the total mass within the spherical region and its radius as $A^3 = GMB^2$, by considering the Law of Newton. From these equations one can see that $t = 0$ when $\theta = 0$, the spherical region then expands and reaches a maximum size when $\theta = \pi$. When $\theta = 2\pi$, $r = 0$, and the spherical region can be said to have collapsed; taking a total time $t_{\rm c} = 2\pi B$.

It is useful to calculate the value that linear perturbation theory would predict that density field would have reached when the full spherical region has collapsed, even though it is clearly not valid here. The calculation can be made by considering the early time evolution of the sphere and equating this with the result from linear perturbation theory in the flat matter dominated case, in which case perturbations evolve according to $\delta \propto t^{2/3}$. The linear density field evolves as a function of the parameter θ as

$$\delta_{\rm lin} = \frac{3}{20}[6(\theta - \sin\theta)^2]^{2/3} \ . \tag{3.3}$$

Collapse occurs when $\theta = 2\pi$ and so the linear density has the value $\delta_{\rm c}$

$$\delta_{\rm c} = \frac{3}{20}(12\pi)^{2/3} \approx 1.686 \ . \tag{3.4}$$

Note that this is certainly not the value of the density of the sphere when it has collapsed but the value of the linear density field would have were it still to exist and evolve linearly.

Another useful quantity to calculate is the real overdensity of the region when the collapse has occurred. Taking the equations so far literally suggests that when collapse occurs $r = 0$ and the density of the region will be infinite so one might suspect that perhaps a back hole will form. However, in reality perturbations are not symmetric, a sensible suggestion then would be that after some amount of time the sphere will have reached virial equilibrium after dynamically relaxing as discussed by Lynden-Bell (1967). The radius of the relaxed sphere can be calculated using the virial condition that the negative of the potential energy is equal to twice the internal kinetic energy which leads to the conclusion that the relaxed potential energy is half of the maximum potential energy, achieved when the sphere is at maximum radius $\theta = \pi$. This means that the virial radius occurs at a time when $\theta = 3\pi/2$, when $r = A$. The full overdensity of the sphere can be calculated to be

$$1 + \delta = \frac{\bar{\rho}_{\rm halo}}{\bar{\rho}_{\rm universe}} = \frac{9GMt^2}{2r^3} \ . \tag{3.5}$$

By considering collapse to have occurred when $\theta = 2\pi$ but that the object formed has a radius given by the virial radius ($\theta = 3\pi/2$) the virialised overdensity at the point of collapse is given by

$$1 + \delta_{\rm v} \equiv \Delta_{\rm v} = 18\pi^2 \approx 178 \ , \tag{3.6}$$

so that one would expect virialised structure to have an over-density at collapse of the order of several hundred. This general trend is found in N-body simulations (*e.g.* Navarro et al. 1997) where objects that are sensibly identified as distinct haloes tend to be of the order of 200 times denser than the background at all times (as they continually expand and accrete matter after initial formation). This is also seen in data when galaxy clusters are measured to be of the order of several hundred times denser than the average Universe. In reality it is unclear where exactly to define the boundary of a halo or cluster (or even if a boundary for such things is a sensible concept) and so a value of $\Delta_{\rm v}$ is usually chosen and haloes are then *defined* as regions which contain this over-density of matter. Halo finding in simulations is discussed in Section 2.4 and an over-density value of 200 is the standard used.

So far the discussion has focussed on spherical perturbations to a background $\Omega_{\rm m} = 1$ universe. In a more general case the background cosmology will differ from this and in this case the calculation of $\delta_{\rm c}$ and $\Delta_{\rm v}$ becomes more difficult. The general trend is that $\Delta_{\rm v}$ increases (relative to the background matter density) as $\Omega_{\rm m}$ decreases and that $\delta_{\rm c}$ is very weakly dependent on cosmology. Fitting functions for full numerical results for $\delta_{\rm c}$ and $\Delta_{\rm v}$ are available in the literature in this case for a variety of cosmological models including ΛCDM, open and closed models (Bryan & Norman 1998, Coles & Lucchin 1995), the case of various dark energy models is discussed in Percival (2005). The cosmology dependence of $\delta_{\rm c}$ and $\Delta_{\rm v}$ is discussed in more detail in Chapter 4.

3.2 Computing the halo-model power spectrum

3.2.1 1-halo term

It is possible to calculate the power spectrum associated with a distribution of haloes and their internal structure: Lay down a series of points drawn from a uniform random distribution in a finite but large universe in comoving coordinates. Assign each point a mass drawn from a mass distribution function and then assign each a mass-dependent density profile. In order to calculate the power spectrum, one then takes the Fourier Transform of this density field and averages over k modes. In this approach every bit of mass in the universe is assigned to a halo, which have a variety of sizes and density profiles which vary with epoch and cosmology.

Initially consider a finite, but large, universe containing N haloes each at position $\mathbf{r}_i$. The total density of the universe, $\rho(\mathbf{r})$ is then

$$\rho(\mathbf{r}) = \sum_{i=1}^{N} \rho_i(\mathbf{r} - \mathbf{r}_i) \ , \tag{3.7}$$

where ρ_i is the density profile of each halo. This can then be related to the overdensity parameter δ

$$\delta(\mathbf{r}) = \frac{1}{\bar{\rho}} \sum_{i=1}^{N} \rho_i(\mathbf{r} - \mathbf{r}_i) - 1 \ , \tag{3.8}$$

where $\bar{\rho}$ is the average density of the universe. This can then be Fourier Transformed using the convention discussed in 1.10.2 and shown in equation 1.97 to express the overdensity in Fourier Space:

$$\delta_{\mathbf{k}} = \frac{1}{V\bar{\rho}} \int \sum_{i=1}^{N} \rho_i(\mathbf{r} - \mathbf{r}_i) e^{-i\mathbf{k}\cdot\mathbf{r}} \, \mathrm{d}^3 r - \frac{1}{\mathrm{V}} \int \mathrm{e}^{-\mathrm{i}\mathbf{k}\cdot\mathbf{r}} \, \mathrm{d}^3 r \ . \tag{3.9}$$

The second integral gives a delta function at $\mathbf{k} = 0$ but this is cancelled by the corresponding $\mathbf{k} = 0$ term from the first integral (which simply expresses that $\langle\delta\rangle = 0$). If the $\mathbf{k} = 0$ mode is ignored and coordinates changed via $\mathbf{y} = \mathbf{r} - \mathbf{r}_i$ then

$$\delta_{\mathbf{k}} = \frac{1}{V\bar{\rho}} \sum_{i=1}^{N} e^{-i\mathbf{k}\cdot\mathbf{r}_i} \int \rho_i(\mathbf{y}) e^{-i\mathbf{k}\cdot\mathbf{y}} \, \mathrm{d}^3 y = \frac{1}{\mathrm{V}\bar{\rho}} \sum_{\mathrm{i}=1}^{\mathrm{N}} \mathrm{e}^{-\mathrm{i}\mathbf{k}\cdot\mathbf{r}_\mathrm{i}} \rho_{\mathbf{k},\mathrm{i}} \ , \tag{3.10}$$

which removes all spatial dependence of the halo position from the Fourier Transform $\rho_{\mathbf{k},i}$ which is simply that of the density profile. If the density profile is spherically symmetric (which is the case taken throughout this thesis) then $\rho_{\mathbf{k}}$ is a real quantity and can be written as

$$\rho_{\mathbf{k}} = \int_0^\infty \frac{\sin(kr)}{kr} 4\pi r^2 \rho(r) \, \mathrm{d}r \tag{3.11}$$

This Fourier Transform can be written in terms of the halo 'window function' $W(k)$ which has the mass factored from it such that $W(0) = 1$ and $\rho_{\mathbf{k}}(0) = M$, so $\rho_{\mathbf{k}}(k) = MW(k)$. The expression for the Fourier overdensity is then

$$\delta_k = \frac{1}{V\bar{\rho}} \sum_{i=1}^{N} e^{-i\mathbf{k}\cdot\mathbf{r}_i} M_i W_i(k) \ , \tag{3.12}$$

and the power spectrum is therefore

$$P(k) = \frac{1}{V^2\bar{\rho}^2} \sum_{i=1}^{N} \sum_{j=1}^{N} e^{-i\mathbf{k}\cdot(\mathbf{r}_i - \mathbf{r}_j)} M_i M_j W_i(k) W_j(k) \ . \tag{3.13}$$

If the haloes were laid down at random their positions are completely independent. If one then takes an average of the equation for a given i with $i \neq j$ the sum over j will take place over complex numbers with phases distributed randomly between 0 and 2π. The result of this will be that this sum will average to zero unless $i = j$. In this case halo positions are obviously correlated with themselves so that

$$\langle P(k) \rangle = \frac{1}{V^2\bar{\rho}^2} \sum_{i=1}^{N} M_i^2 W_i^2(k) \ , \tag{3.14}$$

and the dimensionless power is given by

$$\Delta^2(k) = 4\pi \left(\frac{k}{2\pi}\right)^3 \frac{1}{V\bar{\rho}^2} \sum_{i=1}^{N} M_i^2 W_i^2(k) \ . \tag{3.15}$$

At this point it is possible to take the limit of the universe becoming infinitely large such that $V \to \infty$ and $N \to \infty$. The inverse of V from outside the sum can be brought inside the summation to create the measure for the newly formed integral which takes the form of a measure over halo number density $\frac{1}{V}\sum \to \int \mathrm{d}N$. This is usually written as an integral over mass, $\mathrm{d}N = n(M)\ \mathrm{d}M$, where the distribution $n(M)$ gives the number density of haloes in the region $M \to M + \mathrm{d}M$ such that $\int Mn(M)\ \mathrm{d}M = \bar{\rho}$. The full expression for the dimensionless halo model power spectrum is then

$$\Delta^2_{\mathrm{halo}}(k) = 4\pi \left(\frac{k}{2\pi}\right)^3 \frac{1}{\bar{\rho}^2} \int_0^\infty M^2 W^2(k, M) n(M) \mathrm{d}M \ . \tag{3.16}$$

The same result can be derived by an argument due to Peebles (1980) in which one considers microcells which are made to be so small that they contain either 0 or 1 halo only.

3.2.2 Shot noise

At this point it is useful to consider the power spectrum due to randomly placed point particles, rather than haloes, a calculation similar to, but simpler than, that in the previous section. Start by writing the density field as a sum of N delta functions each of which has mass m in a large box of volume V

$$\rho(\mathbf{x}) = \frac{m}{V} \sum_{i=1}^{N} \delta_{\mathrm{D}}(\mathbf{x} - \mathbf{x}_i) \ . \tag{3.17}$$

The average density in the box is $\bar{\rho} = Nm/V$ and so the over-density (ignoring the zero mode) is

$$\delta = \frac{1}{N} \sum_{i=1}^{N} \delta_{\mathrm{D}}(\mathbf{x} - \mathbf{x}_i) \ . \tag{3.18}$$

In Fourier Space the over-density can then be calculated to be

$$\delta_{\mathbf{k}} = \frac{1}{N} \sum_{i=1}^{N} e^{-i\mathbf{k}\cdot\mathbf{x}_i} \ , \tag{3.19}$$

and the power spectrum is

$$P(\mathbf{k}) = \frac{1}{N^2} \sum_{i=1}^{N} \sum_{j=1}^{N} e^{-i\mathbf{k}\cdot(\mathbf{x}_i - \mathbf{x}_j)} \ , \tag{3.20}$$

taking an average then gives contributions only when $i = j$ if the delta functions are uniform random distributed within the box

$$\langle P(k) \rangle = \frac{1}{N} \ , \tag{3.21}$$

and so the dimensionless shot noise power spectrum is then

$$\Delta^2_{\mathrm{SN}}(k) = 4\pi \left(\frac{k}{2\pi}\right)^3 \frac{1}{\bar{n}} \ , \tag{3.22}$$

where $\bar{n} \equiv N/V$ is the average number density of particles. Note that $\Delta^2_{\mathrm{SN}} \to 0$ as $N \to \infty$ as one would expect – this represents the limit of complete uniformity when there is no power. equation (3.22) is useful because it allows one to approximately compute the power associated with the discritised nature of the density field in a simulation or galaxy catalogue.

3.2.3 2-halo term

As it stands this approach has one serious drawback; it fails to take into account of any large scale correlations in halo positions because, in deriving the expression, it was assumed that the haloes were placed at random. This can be improved by making the approximation that, on large scales, the linear power dominates and that the evolution here has been entirely linear, but that on small scales the power is dominated by contributions from haloes of varying size. The full halo model prediction for the power is therefore

$$\Delta^2(k) = \Delta^2_{\rm lin} + \Delta^2_{\rm halo} \ , \tag{3.23}$$

and within the parlance of the halo model $\Delta^2_{\rm lin}$ is known as the '2-halo term' while $\Delta^2_{\rm halo}$ is known as the '1-halo term'.

It should be noted that, in reality, the shot noise from the halo contribution does not extend to arbitrarily large scales but that the power in equation (3.16) ($\propto k^3$) will eventually, unphysically take over from the linear spectrum ($\propto k^4$) at very large scales. It may therefore be necessary to enforce a truncation of this 1-halo term on very large scales by hand.

Seljak (2000) deals with the 2-halo term in a slightly different way and considers it to be due to correlations only between separate haloes, and not between all of the mass. In this approach the 2-halo term is the linear power spectrum filtered by the bias and mass weighted halo profiles. In practice this makes very little difference to the shape of the halo model power spectrum as can be seen in Fig. 11 of Cooray & Sheth (2002). Tinker et al. (2005) and Smith & Markovic (2011) consider a 'halo exclusion' term to take account for the fact that haloes cannot be situated within a virial radius of each other, a factor that is ignored by the analysis presented here.

3.2.4 Summary

In summary, in order to calculate the contribution to the full halo model power spectrum one adds the linear power spectrum to that given by randomly placed haloes. For haloes one must specify a density profile as a function of mass, calculate its Fourier Transform and then integrate this over the full range of halo masses as specified by a mass function. These ingredients are discusses in the remainder of this chapter.

3.3 Halo profiles

Some insight into the eventual structure of dark-matter haloes can be gleaned from theoretical arguments that were first put forward by Lynden-Bell (1967). Due to the collisionless nature of dark matter one would not expect that a dark-matter halo should virialise and come into thermal equilibrium once it had collapsed. However Lynden-Bell (1967) showed that thermalisation *was* possible because perturbations in the gravitational potential structure of the halo allowed

energy to be exchanged by gravitational forces, rather than collisionally. The result is that given enough time one *would* expect haloes to come into thermal virial equilibrium – a process known as 'violent relaxation'. A spherically symmetric self gravitating isothermal distribution has an isothermal profile,

$$\rho(r) \propto \frac{1}{r^2} \ , \tag{3.24}$$

and this is the density profile one would expect for an isolated, isothermal gas, such as a nebula. However this would not necessarily be expected for a dark-matter halo because as the halo smooths itself out towards the $1/r^2$ form the very perturbations that are necessary to continue the violent relaxation are being smoothed away. Thus one expects isolated dark-matter haloes to evolve towards, but not to reach, the $1/r^2$ form. In addition real cosmological dark-matter haloes are very different to the isolated case discussed, with events such as accretion of matter, mergers and surrounding tidal fields are all important to their evolution. The end result is that haloes seen in simulations have all sorts of density profiles and tri-axiality depending on their environment. Some are nearer to virial relaxation than others and many are accreting matter or merging with other haloes.

Density profiles that are used in this work are taken from N-body simulations where haloes are identified and fitted with an appropriate spherically symmetric profile. This is not saying that all haloes identified in a simulation are spherical or identical, only that, on average, a spherically symmetric density profile with a single free parameter (that depends on halo mass) fits the haloes fairly well. Navarro et al. (1997) (NFW) show that all of the haloes identified within their simulations over a broad mass range could be fitted with a universal profile, the 'NFW profile'

$$\rho_{\rm N}(r) = \frac{\Delta_{\rm N}}{(r/r_{\rm s})(1+r/r_{\rm s})^2} \ , \tag{3.25}$$

This profile is then specified by three parameters, the virial radius $r_{\rm v}$, the characteristic density $\Delta_{\rm N}$ and the scale radius, $r_{\rm s}$. However, guided by the spherical model and justified via the simulations one knows that haloes are continuously accreting matter and always have a characteristic overdensity compared to the background of $\Delta_{\rm v} \approx 200$ and this criterion is used to define the halo in the simulation. This eliminates one of the parameters in the model as follows: The halo mass, M, can be written in terms of the average overdensity within the halo as

$$M = \frac{4\pi}{3} r_{\rm v}^3 \bar{\rho}_{\rm m} \Delta_{\rm v} \ . \tag{3.26}$$

but can also be obtained by directly integrating the density profile,

$$M = 4\pi\Delta_{\rm N} \left(\frac{r_{\rm v}}{c}\right)^3 \left[\ln(1+c) - c/(1+c)\right] \ , \tag{3.27}$$

where c is the concentration of a halo, $c = r_{\rm v}/r_{\rm s}$. Equating the above two expressions shows that $\Delta_{\rm N}$ can be related to c via

$$\Delta_{\rm N} = \frac{\bar{\rho}_{\rm m}\Delta_{\rm v} c^3}{3\left[\ln(1+c) - c/(1+c)\right]} \ . \tag{3.28}$$

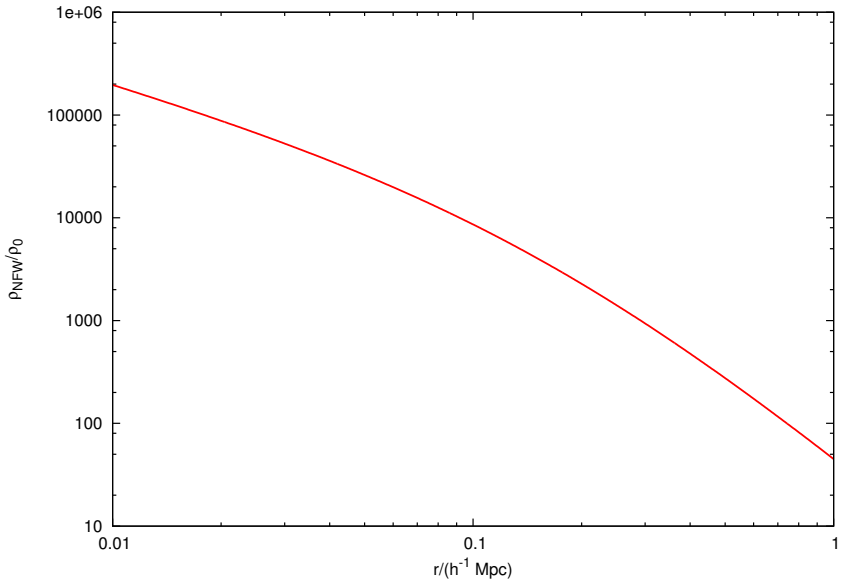

Figure 3.1: A typical NFW profile with $r_{\rm v} = 1\,h^{-1}\,{\rm Mpc}$ and $c = 6$ which is quite standard for a $\mathrm{O}(5 \times 10^{13}\,h^{-1}\,{\rm M}_{\odot})$ halo in a standard ΛCDM cosmology. The scale radius for such a halo is $\simeq 0.17\,h^{-1}\,{\rm Mpc}$ (using the relationship of Bullock et al. 2001) and the density profile can be seen to change slope around this radius.

An example NFW profile is shown in Fig. 3.1.

Specifying a halo mass implicitly sets the halo virial radius by equation (3.26) and then setting a concentration implicitly sets the value of $\Delta_{\rm N}$ via equation (3.28). The only remaining freedom for the haloes is then a relationship between the concentration and mass. Many such relationships have been proposed over the years including the original one of NFW. However the redshift evolution of the NFW $c(M)$ relationship was disputed by Bullock et al. (2001) who calibrated a different relation based on a diverse suite of cosmological N-body simulations. Many other $c(M)$ relations exist in the literature such as those of Eke et al. (2001). More recently Neto et al. (2007) has proposed a revised relation calibrated to high resolution ΛCDM simulations which have been shown to have superior accuracy when compared to older models. This thesis considers many different cosmological models, some of which depart fairly drastically from the currently fashionable ΛCDM, and therefore the $c(M)$ relations of Bullock et al. (2001) are used due to their large coverage of cosmological parameter space and the fact that an FOF algorithm was used to define their haloes similar to what is used in the work in this thesis. The relations of Bullock et al. (2001) are also theoretically motivated, rather than a simple fitting formula, which makes them easier to extend to very non-standard cosmologies for which simulations may not exist to measure $c(M)$.

The concentration relations of Bullock et al. (2001) relate the concentration of a halo iden-

tified at redshift z to its formation redshift $z_{\rm f}$, via

$$c(z) = 4\left(\frac{1+z_{\rm f}}{1+z}\right) \ , \tag{3.29}$$

where the factor of 4 is a result of fitting to simulations. In the approach of Bullock et al. (2001) the formation redshift is calculated by finding the time at which a fraction (0.01 in the case of their model) of the eventual halo mass has collapsed into objects

$$\frac{g(z_{\rm f})}{g(z)}\sigma(0.01M, z) = \delta_{\rm c} \ , \tag{3.30}$$

where $g(z)$ is the linear theory growth function, σ^2 is the variance of the linear density field and $\delta_{\rm c}$ is the linear-theory collapse threshold. In the fits of Bullock et al. (2001) this was kept at a fixed $\delta_{\rm c} = 1.686$, the $\Omega_{\rm m} = 1$ result, the rationale being that $\delta_{\rm c}$ changes very slowly as a function of cosmological parameters in standard cosmologies (see Eke et al. 1996 for flat models with Λ and Lacey & Cole 1993 for matter-dominated open models). As an example in $\Omega_{\rm m} = 0.3$ ΛCDM $\delta_{\rm c} = 1.676$ which differs from the $\Omega_{\rm m} = 1$ result by less than 1%.

One issue with the Bullock et al. (2001) relations is that for very high mass haloes $\sigma(0.01M, z)$ can be very small and this in term means that a value of $g(z_{\rm f}) \gtrsim 1$ is necessary to satisfy equation (3.30). This in turn leads to the bizarre prediction that these haloes should have 'collapsed' in the future. However, the relations work rather well in practice and given the various other dubious assumptions in the model (such as the collapse redshift being defined as the time when the halo has accreted a tiny 1% of its final mass) this should perhaps not be considered to be too much of a bother. For each halo mass a value of $z_{\rm f}$ can be calculated via equation (3.30) and this is then converted into a concentration via equation (3.29) thus specifying everything about the haloes.

In addition to their full model, Bullock et al. (2001) provide a simple power-law fit in their work, which can be used at the expense of some accuracy:

$$c(M, z) = \frac{9}{1+z}\left(\frac{M}{M_*(z)}\right)^{-0.13} \ . \tag{3.31}$$

Cosmological dependence is included via the definition of M_* as the characteristic mass scale of the Universe at a given epoch

$$\sigma(M_*, z) = \delta_{\rm c} \ , \tag{3.32}$$

defining the 'peak threshold' ν via

$$\nu = \frac{\delta_{\rm c}}{\sigma} \ , \tag{3.33}$$

means that the definition of M_* is equivalent to $\nu = 1$. In this simpler case the value of M_* at a given epoch can be calculated and the concentration as a function of mass can simply be read off from equation (3.31). A plot of this concentration relation is shown in Fig. 3.2.

In Moore et al. (1999) it was shown that the NFW profile is in error at small radii. The 'M99' profile was proposed in order to remedy this, this profile has the same asymptotic behaviour at large radii but a slightly steeper core slope (1.5 vs. 1),

$$\rho_{\rm M} = \frac{\Delta_{\rm M}}{(r/r_{\rm c})^{3/2}[1+(r/r_{\rm c})^{3/2}]}. \tag{3.34}$$

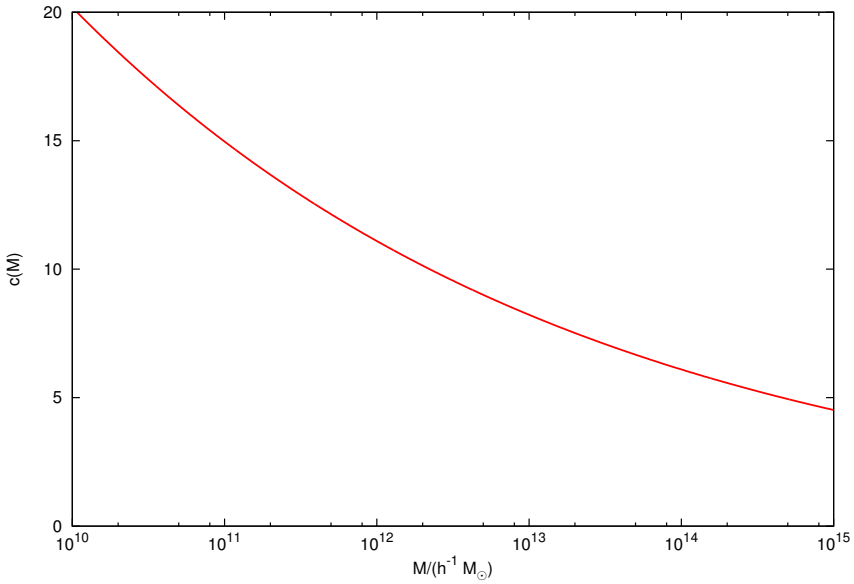

Figure 3.2: The concentration relation of Bullock et al. (2001) shown in equation (3.31) for a population of haloes with $M_* = 5 \times 10^{12}\, h^{-1}\, \mathrm{M}_\odot$; typical for $z = 0$ ΛCDM models with $\Omega_\mathrm{m} \sim 0.3$. Higher mass haloes are less concentrated with a minimum value approaching $c = 4$, which reflects their recent formation.

the parameters of the fit are r_c and Δ_M. In Peacock & Smith (2000) it was shown how to apply the arguments of NFW to the M99 profile and thus how to relate concentrations derived for an NFW halo to an M99 halo. It should be noted that M99 provides a better fit to the core regions but is less good at matching the gross structure of an average halo. Both NFW and M99 are incorrect in detail in the core regions, but these regions are likely to be baryon dominated and thus all the profiles obtained from fits to DM only simulations will be wrong in detail here in any case.

Recently work by Dhar & Williams (2010) has shown that an exponential profile, the Einasto profile,

$$\rho(r) \propto \mathrm{e}^{-Ar^\alpha}\ , \tag{3.35}$$

may provide an even better description of halo density profiles found in simulations, particularly in the core regions. Neither this profile, nor the M99 profile, has been used in this work since it has been shown that (a) NFW profiles fit data remarkably well, (b) most of the work on dark-matter haloes has focussed on the NFW model and its parameterisation via the mass and concentration described above, (c) in the work of this thesis the core regions are less important than the gross structure of the halo.

Busha et al. (2007) shows that the NFW profile may not be the convergent end point for relaxed haloes. In this work simulations were run into the future (to $a = 100$, $64\, h^{-1}$ Gyr after the big bang) with a ΛCDM cosmology and it was shown that haloes in the far future are better

fit with a Hernquist (1990) profile of the form

$$\rho(r) \propto \frac{1}{(r/r_{\rm s})(1+r/r_{\rm s})^3} \ . \tag{3.36}$$

3.4 Mass functions

In order to calculate the power due to randomly placed haloes using equation (3.16) one needs to provide a mass function $n(M)\mathrm{d}M$, the number density of haloes in the range $M \rightarrow M+\mathrm{d}M$. The mass function is also useful for a whole host of other reasons, including as a cosmological probe. If one knows how the number density of haloes of a given mass should vary as a function of cosmology then one can hope to constrain cosmological parameters via by attempting to measure the mass function of haloes in the real Universe.

A theoretical guess at the mass function can be made by the approach of Press & Schechter (1974) (hereafter PS), which draws on results from the spherical model discussed in Section 3.1. The PS argument is that one can extrapolate the linear density field beyond the linear regime and use the spherical model to judge when a region of the density field will have collapsed into a structure. As shown in equation (3.4) the value of the linear density field when the real perturbation has collapsed is $\delta_{\rm c} \approx 1.686$. If one filters the linear density field on a mass scale M then one can compute an estimate of the fraction of the density field that is collapsed into objects of mass greater than M at a given epoch. If the distribution of δ is taken to be Gaussian then the fraction of the filtered density field that exceeds this critical threshold for collapse is given by

$$P(\delta_c|M) = \sqrt{\frac{2}{\pi}}\frac{1}{\sigma(M)}\int_{\delta_c}^{\infty} \mathrm{e}^{-\delta^2/2\sigma^2(M)}\,\mathrm{d}\delta \ , \tag{3.37}$$

where $\sigma(M)$ is defined in equation (1.103) (note that it is the *linear* field that is filtered) with M being the mass contained in a homogeneous universe within a window of radius R

$$M = \frac{4}{3}\pi R^3 \bar{\rho}_{\rm m} \ , \tag{3.38}$$

where $\bar{\rho}_{\rm m}$ is the average mass density of the Universe at the epoch of interest. It is therefore structures at approximately the non-linear scale that are judged to be collapsing. The fact that the variance increases as R decreases means that structure formation should be hierarchical with smaller objects forming first.

The PS argument then postulates that the fraction of the mass, F, of the universe collapsed into objects of mass greater than M is given by equation (3.37). $\mathrm{d}F$ can then be related to the mass fraction in haloes of in the range $M \rightarrow M+\mathrm{d}M$ via

$$\mathrm{d}F = \sqrt{\frac{2}{\pi}}\frac{1}{\sigma(M)}\mathrm{e}^{-\delta_{\rm c}^2/2\sigma^2(M)}\,\mathrm{d}\delta_{\rm c} \ , \tag{3.39}$$

which can be conveniently cast in terms of the single variable $\nu = \delta_{\rm c}/\sigma$.

$$\mathrm{d}F = \sqrt{\frac{2}{\pi}}\mathrm{e}^{-\nu^2/2}\,\mathrm{d}\nu \equiv f(\nu)\,\mathrm{d}\nu \ , \tag{3.40}$$

the quantity $f(\nu)$ is known as the 'mass function' and is normalised such that

$$\int_0^\infty f(\nu)\mathrm{d}\nu = 1 \ . \tag{3.41}$$

$f(\nu)\mathrm{d}\nu$ gives the fraction of mass in the universe in haloes with masses between ν and $\nu + \mathrm{d}\nu$. It is often referred to as being universal because it depends on cosmology only through the dependence of $\nu = \delta_\mathrm{c}/\sigma(M)$ on the variance $\sigma^2(M)$. For the PS argument with a Gaussian density field the mass function is also a Gaussian

$$f(\nu) = \sqrt{\frac{2}{\pi}} e^{-\nu^2/2} \ , \tag{3.42}$$

which tends to a constant for low masses and cuts off quickly at high masses.

The typical mass of objects, M_*, at a given epoch is given by $\nu = 1$ or

$$\sigma(M_*) = \delta_\mathrm{c} \ . \tag{3.43}$$

The effective spectral index was defined in equation (1.105) and determines the properties of the collapse at an epoch. For cosmologically relevant power spectra n_eff varies from -3 at high redshift to 1 in the future, so the properties of the collapse vary over cosmological times. Initially when $n_\mathrm{eff} = -3$ many scales reach the collapse threshold simultaneously but as time passes structure formation becomes more hierarchical with smaller objects forming first and then coalescing into larger objects. This pattern then continues into the future.

In the PS approach a fudge factor of 2 has been applied to $f(\nu)$ to normalise the mass function because half the density field has $\delta < 0$ and thus never undergoes collapse, contrary to the expectation that mass in low density environments ends up accreted onto higher mass haloes.

The factor of 2 deficit of the PS model was remedied by Peacock & Heavens (1990), Bond et al. (1991) and Lacey & Cole (1993) by considering the evolution of $\delta(\mathbf{r}, R)$ (over-density at $\mathbf{r}$ when the field is smoothed on scale R) as a random walk. If the smoothing filter is a sharp k-space top hat and then each time the over-density is smoothed on a new scale the result is uncorrelated with the previous step, if the over-density field is Gaussian. The mass function is then obtained by considering the first time that this trajectory crosses a collapse threshold as the smoothing scale is decreased. This approach is known as the excursion set formalism and a typical trajectory is shown in Fig. 3.3 corrects the missing factor of 2 in the PS formula. The formalism can also be extended to more general problems with moving collapse barriers (*e.g.* Mo & White 1996) and includes a way of solving the cloud-in-cloud problem which is the question of what to do if an excursion set trajectory crosses the collapse barrier on multiple different scales (which they all will do if the smoothing scale is made arbitrarily small).

The halo number density $n(M)$ in the range can be calculated via

$$\mathrm{d}F = f(\nu)\mathrm{d}\nu = \frac{Mn(M)\mathrm{d}M}{\bar{\rho}_\mathrm{m}} \ . \tag{3.44}$$

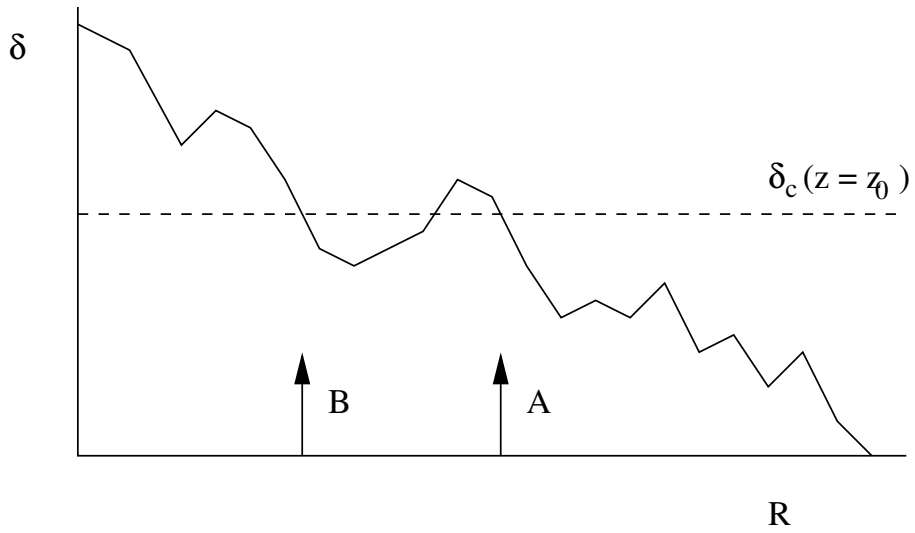

Figure 3.3: A typical excursion set. Shown is the density field at a single point in space when the density field is convolved with filters of different sizes R. At large scales homogeneity is approached and $\delta \to 0$ but at smaller scales the trajectory essentially performs a random walk. The point is associated with a halo mass related to point A, the largest scale at which it crosses the collapse threshold. Although the trajectory crosses again at point B this is not taken as the size of the halo, thus solving the cloud-in-cloud problem. [Image credit - Peacock (1999)].

It is often convenient to talk in terms of the 'multiplicity function', which gives the contribution to the total mass of the Universe from haloes in a given range of $\ln M$

$$\frac{M^2 n(M)}{\bar{\rho}}\,\mathrm{d}M = \frac{\mathrm{d}F}{\mathrm{d}\ln M}\,\mathrm{d}M = Mf(\nu)\,\mathrm{d}\nu\ . \tag{3.45}$$

This theoretical mass function can then be compared to N-body simulations as was done in Sheth & Tormen (1999) (hereafter ST) where it was shown that although the mass function reproduced the general trend seen in simulations it under predicted the abundance of high-mass objects, over predicted the abundance of low-mass objects and is in error by a factor of 2 at the peak of the mass function (around M_*). ST calibrated a new mass function using N-body simulations,

$$f(\nu) = A\left[1 + (q\nu^2)^{-p}\right] e^{-q\nu^2/2}, \tag{3.46}$$

which is used throughout this thesis. The fitted parameters of the model are $A = 0.216$, $q = 0.707$ and $p = 0.3$. Again this mass function has the normalisation property that the integral of $f(\nu)$ over all ν is equal to one. One should note that at small masses the mass function diverges as $\nu^{-0.6}$ (although this does *not* mean that the integral diverges) and so a large amount of the mass in the cosmos is stored in low mass haloes. Equation (3.46) has been shown to be accurate at the 10% level across a wide range of redshifts, cosmologies and halo masses and its form for is shown for a standard ΛCDM cosmology in Fig. 3.4. 10% level discrepancies are probably due to the fact that the mass function is not universal in detail (does

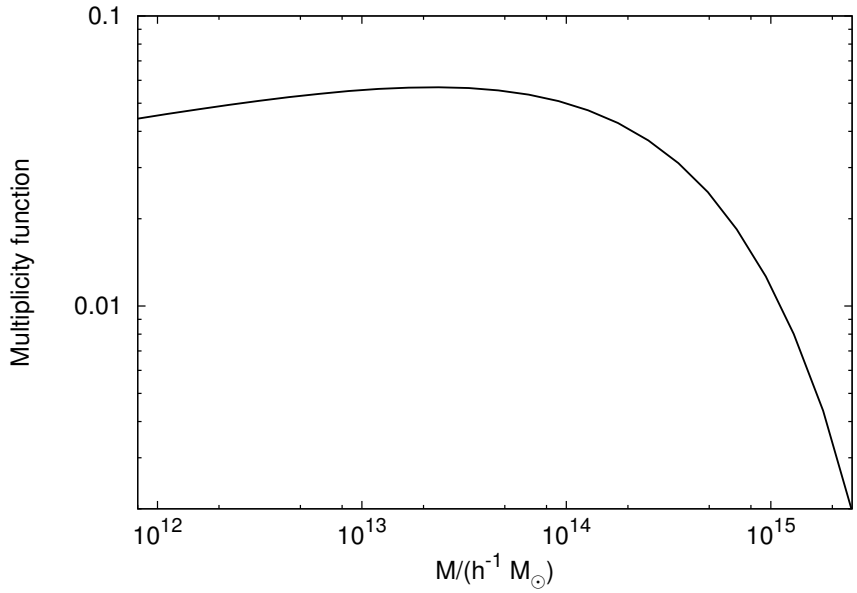

Figure 3.4: The mass function as a function of halo mass for a $\Omega_{\rm m} = 0.3$ ΛCDM cosmology as predicted by the ST formula (equation 3.46). Theoretically these functions depend on ν and so $\sigma(M)$ must be numerically inverted to produce functions of mass. The mass function is shown as the multiplicity function (equation 3.45) which gives the contribution to the total mass of the Universe from haloes in intervals of $\ln M$. One can see that the ST formula predicts that high mass haloes will be very rare.

not depend on ν alone). For example Reed et al. (2007) showed that better fits were possible for a parameterisation in terms of σ and $n_{\rm eff}$.

The form of the ST mass function in equation (3.46) was later justified in Sheth et al. (2001) where it was derived from a model of ellipsoidal collapse of structure, rather than of spherical collapse, together with the full excursion set formalism. The ST mass function is that used throughout this thesis due to its sound theoretical basis and the fact that it was fit to simulations over a wide range of cosmological parameters. Many other mass functions exist in the literature including Jenkins et al. (2001), Peacock (2007), Reed et al. (2007) and Tinker et al. (2008). The mass function of Tinker et al. (2008) is particularly popular but is ignored in this work because it was calibrated only on simulations of a specific cosmology, rather than many different cosmologies, and also because it does not satisfy the normalisation condition. It has also been shown (*e.g.* Tinker et al. 2008, Knebe et al. 2011) that the exact way that haloes are identified in simulations can have a significant impact on the recovered mass function. For example, Tinker et al. (2008) does contain mass functions for haloes identified using various different methods of halo identification and so differences depending on the algorithm used can be seen. It was shown that mass functions are much more universal when identified with the FOF technique than with SO.

3.5 Example halo model power spectra

At this point it is useful to show an example matter power spectrum as predicted by the halo model. On large scales this will be the linear power spectrum but at small scales almost all the power comes from haloes. The full power spectrum, together with the decomposition into 1- and 2-halo terms is shown in the upper panel of Fig. 3.5 for a standard ΛCDM cosmological model at $z = 0$ using NFW haloes, Bullock et al. (2001) concentrations and the ST mass function. In the lower panel of Fig. 3.5 a decomposition of the 1-halo term into power coming from haloes of different masses is shown. One can see that the total 1-halo power initially rises on large scales as $\Delta^2 \propto k^3$ with the majority of the power from the few higher mass haloes. At small scales the high mass haloes cease to contribute significantly to the power and it is increasingly dominated by lower mass haloes, and mainly reflects their internal structure, this is manifested as a departure from the k^3 form. The end result is a smooth function that rises as k^3 before being tapered at a scale that corresponds to the size of a typical halo.

3.6 Halo bias

In the first galaxy surveys it was noticed that there was a tension between the observed clustering of galaxies (Kirshner et al. 1981, Maddox et al. 1990) and the expectation of matter clustering from perturbation theory. Somehow galaxies, and thus haloes, needed to form preferentially in high density regions and hardly at all in low density regions. This is the phenomenon of bias and it was observed in early simulations (Davis et al. 1985; Efstathiou et al. 1985) where haloes were seen to trace the mass in a biased manner depending on their mass.

It is a remarkable fact that for a given mass function an analytical prescription can be applied to find the bias of the dark-matter haloes as a function of mass. The 'peak-background split' formalism (Cole & Kaiser 1989; Mo & White 1996) views the density field as comprised distinctly of a low amplitude, large wavelength component modulated by a high frequency, larger amplitude, component. This is exactly the case with the standard ΛCDM power spectrum as shown in Fig. 1.8 where one can see that the contribution to the variance increases for smaller scales. It is only in regions where there is a maximum in both the large and small wavelengths that peaks are able to cross the δ_c density threshold and form haloes; this can be seen schematically in Fig. 3.6

This necessarily leads to a biased formation process where higher mass objects are more strongly clustered than lower mass objects. Bias can be measured in N-body simulations and can be seen visually in Fig. 3.7 where halo positions in a thin slice of a large volume simulation are plotted with masses both size and colour coded – visually haloes of higher mass can be seen to be more strongly clustered compared to haloes of lower mass.

The peak-background split provides a way of calculating halo bias as a function of mass

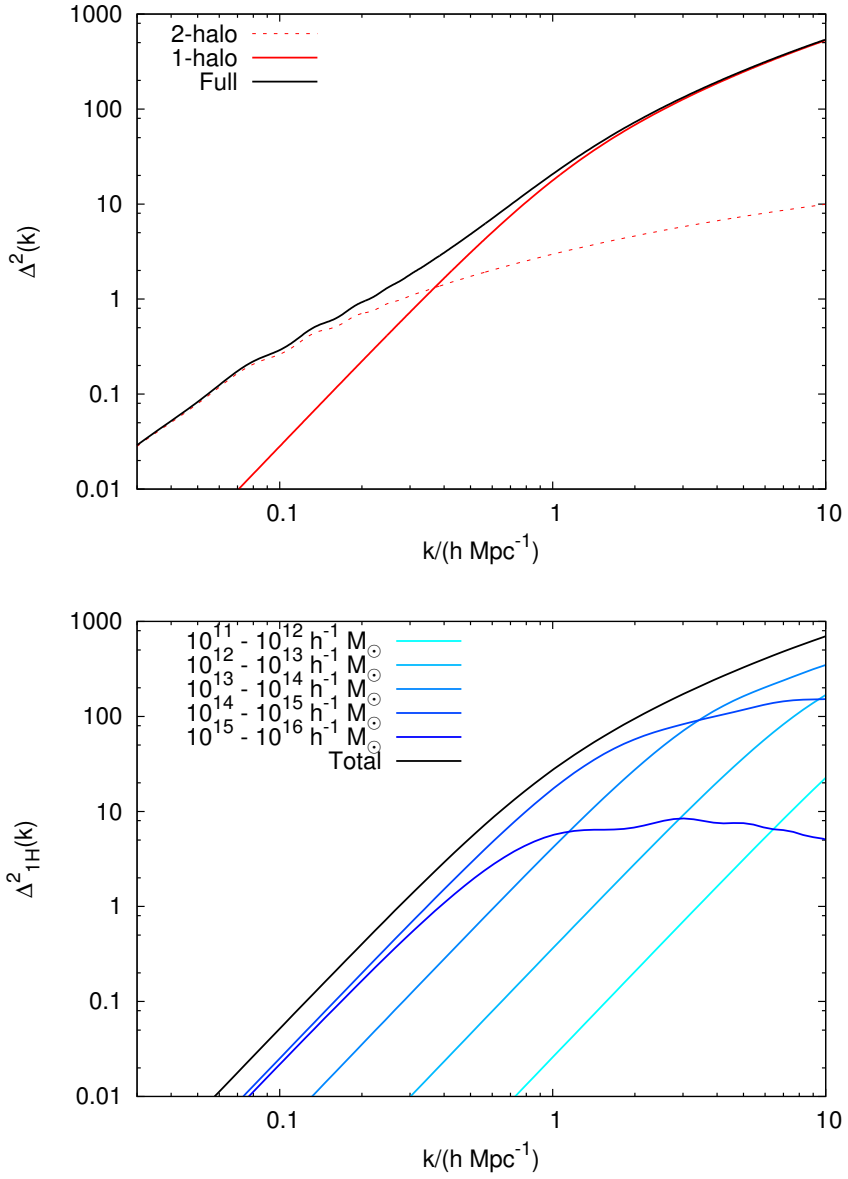

Figure 3.5: The top panel shows the 1- and 2-halo terms together with their sum, which is the full power spectrum as predicted by the halo model. The cosmology is a standard ΛCDM model at $z = 0$. The 2-halo term dominates on large scales whereas the 1-halo term dominates on small scales. This initially rises as k^3 before tapering off at a scale which corresponds to the typical size of a halo. The lower panel shows a decomposition of the 1-halo term into power arising from haloes of various different masses. The halo mass range that contributes most to the 1-halo term will depend on epoch.

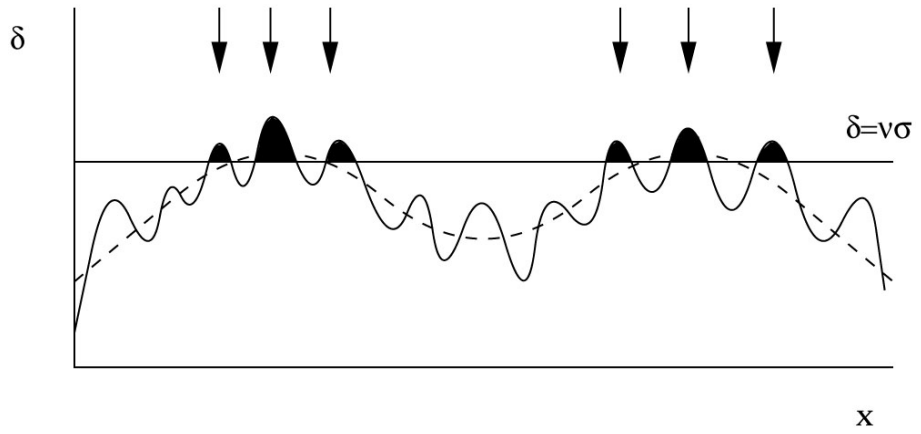

Figure 3.6: A pictorial representation of the peak-background split. Over-density is plotted against position and the curve shows an over-density distribution composed of a high and low frequency contribution. Haloes can only form in regions where the collapse threshold, represented by the solid horizontal line, is crossed which leads to haloes forming such that their clustering is biased with respect to the underlying matter. [Image credit - Peacock (1999)].

which leads to a formula for halo bias of

$$b(\nu) = 1 - \frac{1}{\delta_{\rm c}}\left[1 + \nu\frac{\mathrm{d}}{\mathrm{d}\nu}\ln f(\nu)\right] \ . \tag{3.47}$$

It should also be noted that with this formula, for any normalised and sensible $f(\nu)$ the average bias of matter in the universe is 1, as would be expected, and can be seen from

$$\langle b\rangle = \int_0^\infty b(\nu)f(\nu)\mathrm{d}\nu = 1 - \frac{1}{\delta_{\rm c}}\left[1 - \int_0^\infty \nu\frac{\mathrm{d}f(\nu)}{\mathrm{d}\nu}\mathrm{d}\nu\right] = 1 \ , \tag{3.48}$$

where the final integral can be shown to be 1 by integrating by parts. The average bias of all haloes is not a useful quantity and is just the value of $b(0)$ because the number density of haloes diverges at small masses for almost all models of $f(\nu)$.

For the PS mass function (equation 3.42) the bias can be calculated to be

$$b_{\rm PS}(\nu) = 1 + \left(\frac{\nu^2 - 1}{\delta_{\rm c}}\right) \ , \tag{3.49}$$

at low masses the bias tends to a constant $1 - 1/\delta_{\rm c} \approx 0.407$, M_* haloes ($\nu = 1$) are unbiased, and at high masses the bias is quadratic $\approx \nu^2/\delta_{\rm c}$. The same calculation can also be done for the ST mass function

$$b_{\rm ST}(\nu) = 1 + \frac{1}{\delta_{\rm c}}\left[q\nu^2 - 1 + \frac{2p}{1 + (q\nu^2)^p}\right] \ , \tag{3.50}$$

at low masses the bias tends to a constant $1 + \frac{1}{\delta_{\rm c}}(2p - 1) \simeq 0.763$ and at high masses the bias is again quadratic $\propto q\nu^2/\delta_{\rm c}$, M_* haloes are, again, nearly unbiased, $b(\nu = 1) \simeq 1.01$.

The general trend here is that low mass haloes are anti-biased compared to the total mass distribution, they are predominantly found in under-dense regions, whereas high mass haloes

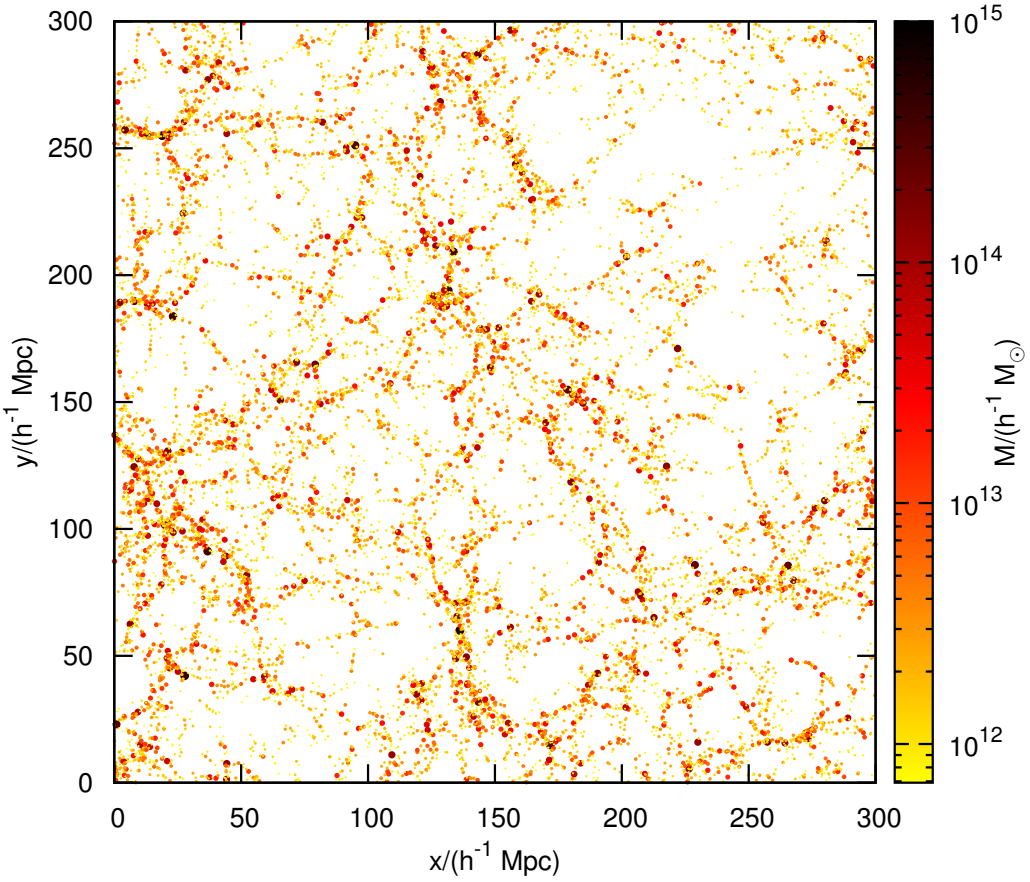

Figure 3.7: A slice of thickness $25\,h^{-1}$ Mpc through a simulation, together with the positions and masses of haloes. Haloes are size and colour coded according to their masses. One can see that higher mass haloes group together and are therefore more strongly clustered and that clustering is less strong for haloes of lower mass. Higher mass haloes tend to live in the centres of knots while the lower mass haloes populate the filaments sheets and, to a lesser extent, voids.

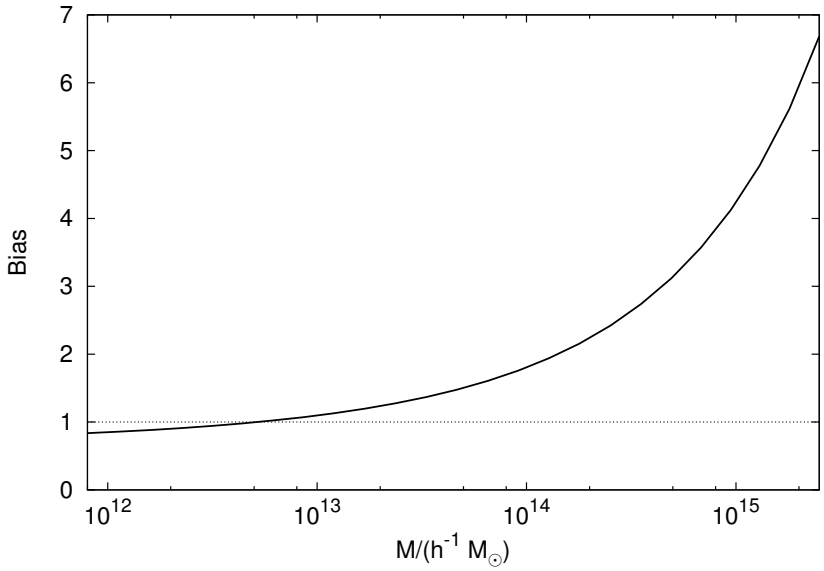

Figure 3.8: The bias as a function of halo mass for a $\Omega_{\rm m} = 0.25$ ΛCDM cosmology as predicted by the ST formula (equation 3.50). Theoretically this function depend on ν and so $\sigma(M)$ must be inverted numerically to produce functions of mass. One can see that theoretically rare, higher mass haloes are highly biased, haloes around $5 \times 10^{12}\, h^{-1}\, \mathrm{M}_\odot$ are unbiased and lower mass haloes are anti-biased. This can be seen visually in Fig. 3.7.

are very biased tracers of the matter, they only exist in regions where the primordial background density perturbation was very large (several σ from the mean) and are thus very clustered.

The bias predicted from the peak-background split has been compared to simulations in Sheth & Tormen (1999) and shown to be relatively accurate (at the 10% level) across a range of cosmologies and halo masses. More accurate fitting formula are available in the literature such as Tinker et al. (2010) which exchange some of the theoretical motivation behind equation (3.47) for increased accuracy for a specific cosmology. Unfortunately these formulae break the 'universal' form of the bias (it depends on quantities other than just ν) and the average bias property shown in equation (3.48) is no longer respected. For these reasons the bias given in equation (3.50) is used in this thesis, it is shown as a function of mass for a standard ΛCDM cosmology in Fig. 3.8.

Chapter 4

Calibrating the halo model

4.1 Preamble

In this chapter an optimised variant of the halo model is presented, which is designed to produce accurate matter power spectra well into the non-linear regime for a wide range of cosmological parameters. Physically-motivated free parameters are introduced into the model and these are fit to data from high-resolution dark matter simulations. For a standard ΛCDM model the predicted power at low redshifts is accurate to $\simeq 1\%$ for $k < 10\,h\,\mathrm{Mpc}^{-1}$. This method also makes accurate predictions for power spectra in models with a wide variety of different cosmological parameters: to $\simeq 1\%$ for concordance cosmologies at $z = 0$ and to $\simeq 5\%$ for other cosmologies for the small-scale $k > 1\,h\,\mathrm{Mpc}^{-1}$ regime. In all cases, the accuracy degrades at higher redshift, especially in the quasi-linear regime. It is shown how this problem can be efficiently cured by using the halo model to extrapolate results from moderate-resolution simulations such as the library of the Coyote Universe project (Lawrence et al. 2010). The method detailed here removes the deficiencies of the commonly-used `HALOFIT` code, which tends to underpredict the true power, largely as a result of unrecognised resolution corrections in the numerical data used to calibrate that method. Results are also compared with recent revisions of `HALOFIT`, where the small-scale power can still be underestimated.

When this work was initially carried out, the aim was to create a means of extrapolating the power spectrum emulator of the Coyote Universe project (Lawrence et al. 2010) to smaller scales. At the time, the emulator was only calibrated up to $k = 1\,h\,\mathrm{Mpc}^{-1}$. As this work was coming to completion Heitmann et al. (2014) released their own extension to the emulator from within the collaboration: It extends the cosmic emulator to $k = 10\,h\,\mathrm{Mpc}^{-1}$ using a library

of high resolution simulations. This chapter has therefore been refocussed on a comparison between the improved halo model and recent numerical results.

4.2 Introduction

Bound structures in the universe today represent large departures from the mean density and can only be accurately modelled by running the type of large cosmological N-body simulations, discussed in Chapter 2. Even so, accurate simulations are computationally expensive and do not allow the space of possible cosmological parameters to be explored quickly. Furthermore, it can also be difficult to understand which physical processes are at work in yielding a given simulation output. Thus an analytic model for the evolution of structure can be invaluable, both in terms of speed and of insight. In this chapter the halo model is used (see Chapter 3): this has become established as an important tool for explanation, and it is shown that it can also deliver accurate predictions.

As discussed, a key measure of scale-dependent inhomogeneity, which can be calculated via perturbation theory and also measured in simulations, is the power spectrum of the density field. Based on analytical insights that are calibrated with N-body simulations, various approximate formulae for the non-linear power spectrum have been generated. The most widely used of these to date has been the `HALOFIT` method of Smith et al. (2003), which uses ideas from the halo model. A different approach is that of the emulator code based on the 'Coyote Universe' suite of simulations (Heitmann et al. 2009; Heitmann et al. 2010; Lawrence et al. 2010; Heitmann et al. 2014): the so called *cosmic emu*. This interpolates between simulated power spectra, calculated on a Latin hypercube grid, as a function of cosmology. The authors claim that the above emulator produces the power spectrum to an accuracy of 1% for $k \leq 10\mathrm{Mpc}^{-1}$ and it currently covers a small, but interesting, range of cosmological parameter space (Ω_m, Ω_b, n_s, σ_8, h and w) for flat universes. However, information to smaller scales is essential (e.g. Huterer & Takada 2005) in the analysis of current and future weak lensing surveys (for example *Euclid*) and it would be useful to be able to explore a greater range of parameter space than *cosmic emu* currently allows.

In this chapter an optimised variant of the halo model is presented, which is able to predict the matter power spectrum accurately to the wave numbers of interest for current and future surveys ($k \simeq 10\,h\,\mathrm{Mpc}^{-1}$). One should note that on these scales, baryon physics will almost certainly have important effects, and the goal in this chapter is to provide fits to the power spectrum, measured in dark matter simulations, up to this wavenumber, so that comparison of theory with observation is limited by uncertain physics and not by inaccuracy of fitting to numerical results. This method can be used either in isolation, or as an extension to *cosmic emu*, in which case the data is matched to the emulator in the region where it claims to be accurate. The approach taken here has been to identify parameters in the halo model that can be made to vary in a physically-motivated way and then to fit these to high resolution

simulation power spectra. This approach is distinct from that of HALOFIT: an empirical fitting formula motivated by the principles of the halo model but which does not use the halo model directly.

The preliminary discussion of the halo model has already taken place in Chapter 3. Section 4.3 gives details of a set of simulations together with a convergence study and it is discussed how to produce accurate power spectra from simulations taking into account their finite resolution. In Section 4.4 the halo model ingredients used here are reiterated and modifications discussed. Section 4.5 discusses an analytical toy model of the halo model power spectrum that facilitates understanding of the modifications to the full halo model calculation. The modified model is then fit to the accurate simulated spectra in Section 4.6. In Section 4.7 the reasons for the under prediction of power seen in HALOFIT are discussed. The modified halo model is then compared to to power spectra from of a wide range of non-standard cosmologies in Section 4.8. The work is summarised in Section 4.9 and also in Chapter 7.

4.3 N-body simulations and convergence

The aim of this chapter is to calibrate the halo model power spectrum using data obtained from simulations. This necessitates testing the convergence of simulations with respect to their finite resolutions. For this work the cosmological N-body code GADGET-2 was used (Springel 2005) which is discussed in detail in Chapter 2. A series of simulations were run with various different mass resolutions, particle numbers and box sizes. The force softening was set so that it is a fixed fraction of the mean interparticle spacing $\ell_{\rm s} = 0.02LN^{-1/3}$ where L is the box side and N is the total particle number. The factor 0.02 was chosen to coincide with the softening used in the Millennium Simulation.

4.3.1 Measuring power spectra

Power spectra of the simulations are computed using the method described in Section 2.3: an NGP mass assignment scheme on a 2048^3 grid. For the simulations discussed in the next section the Nyquist wavenumber, $k_{\rm Ny} = 2048\pi/L$, is $25.1\,h\,{\rm Mpc}^{-1}$ for the $256\,h^{-1}\,{\rm Mpc}$ simulations and $18.4\,h\,{\rm Mpc}^{-1}$ for the $350\,h^{-1}\,{\rm Mpc}$ simulations, both wavenumbers comfortably above the limit of interest which is $k = 10\,h\,{\rm Mpc}^{-1}$. The power spectrum is sharpened and shot noise subtracted as discussed in Section 2.3. At $k = 10\,h\,{\rm Mpc}^{-1}$ the total shot noise is $\simeq 51(L/\,h^{-1}\,{\rm Mpc})^3/N$ which can be a sizeable fraction of the total measured power in the lowest resolution simulations, but is negligible in the higher-resolution runs. At lower k the contribution to the power spectrum from shot noise is negligible can be ignored (Smith et al. 2003). This is good considering the k^3 shot noise correction is not correct at large scales due to our use of glass initial conditions.

$\Omega_{\rm m}$	Ω_Λ	$\Omega_{\rm b}$	h	σ_8	$n_{\rm s}$
0.25	0.75	0.045	0.73	0.90	1.00

Table 4.1: Cosmological parameters of the Millennium simulation, which were adopted for the simulations used in the convergence study.

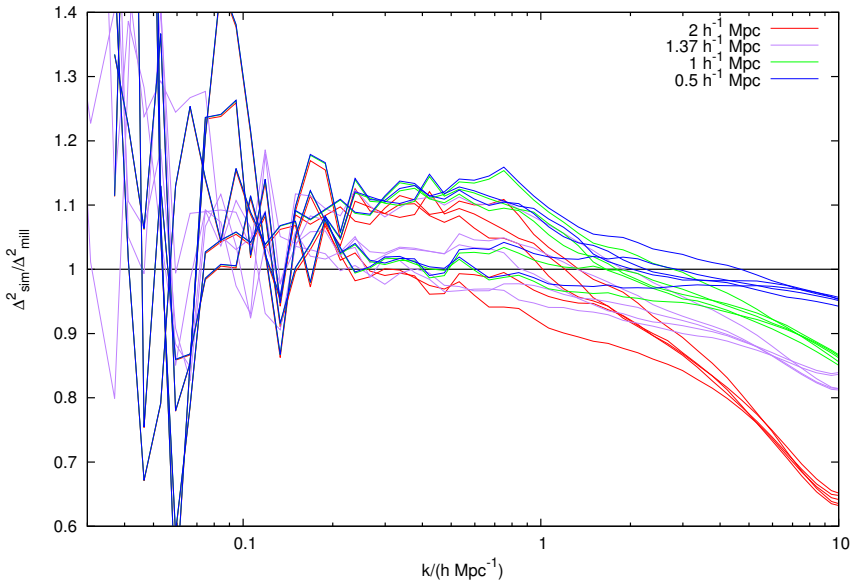

Figure 4.1: The power spectra of simulations with different resolutions and a number of different realisations of each resolution compared to that of the Millennium Simulation at $z = 0$. Resolution is expressed in terms of the mean inter-particle separation. One can see large variations in power depending on realisation around $k = 1\,h\,\mathrm{Mpc}^{-1}$, due to sample variance, and a systematic underprediction in power in lower-resolution simulations at smaller scales.

4.3.2 Convergence study

A series of simulations was run using the cosmological parameters (see Table 4.1) and transfer function of the Millennium Simulation (Springel et al. 2005), which was generated using the CMBFAST code of Seljak & Zaldarriaga (1996), at a variety of resolutions given in Table 4.2. All simulations were started at an initial redshift of $z_{\rm i} = 199$. For comparison the Millennium Simulation was started at $z_{\rm i} = 127$.

Ratios of the power spectra measured in these simulations to that of the Millennium Simulation at $z = 0$ are shown in Fig. 4.1. One can see that there are large run-to-run fluctuations around $k = 1\,h\,\mathrm{Mpc}^{-1}$ due to sample variance, but that less variance occurs at smaller scales, where the data reveal systematically low values depending on the resolution – with the underprediction being more severe at lower resolutions.

With this in mind it is reasonable to ask how sure one can be that the power spectrum from even the high resolution Millennium Simulation has converged. The power measured in

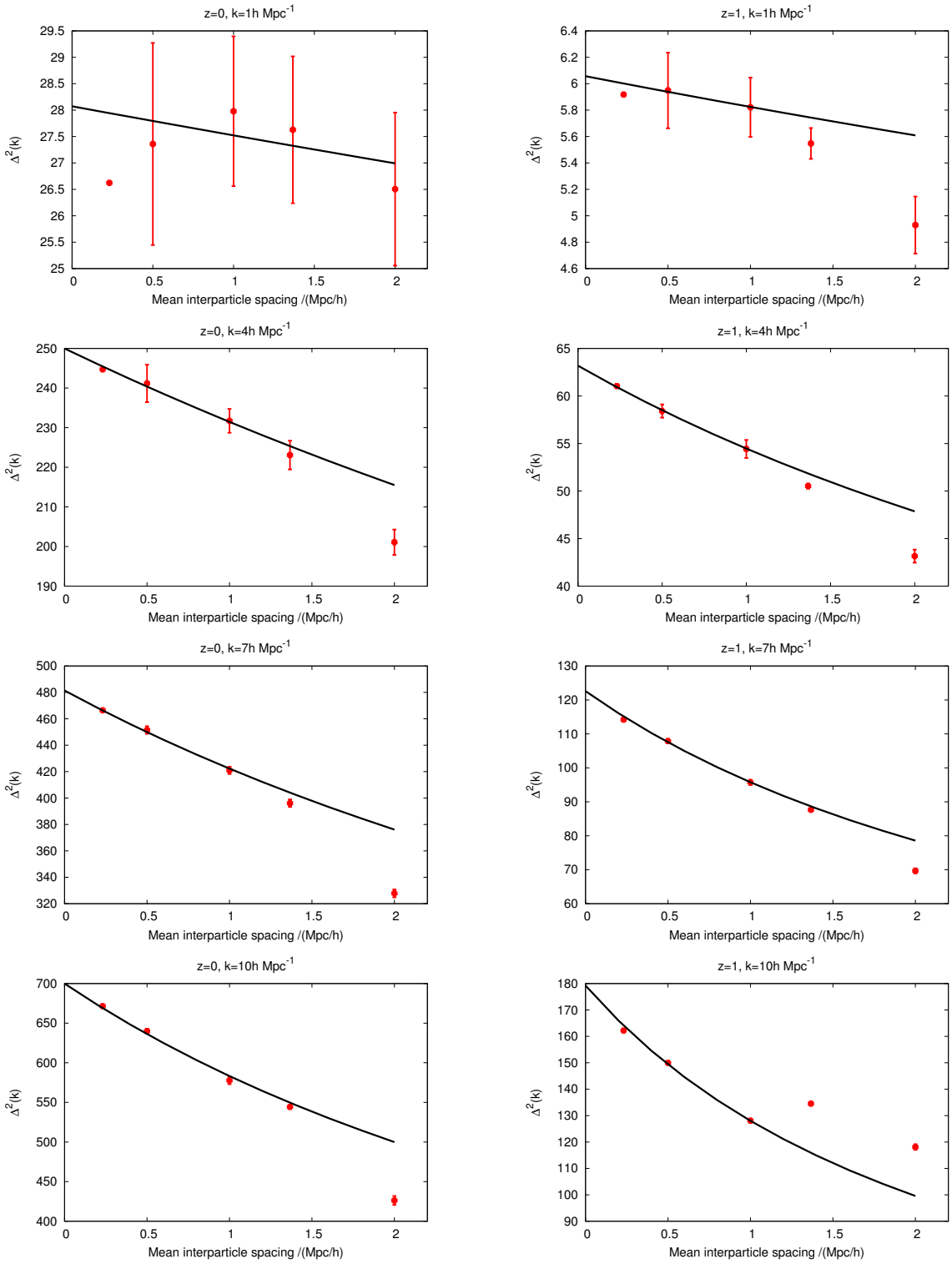

Figure 4.2: The average (over realisations) power produced by simulations at $z = 0$ (left column) and $z = 1$ (right column) as a function of resolution for scales $k = 1$ (top), 4, 7, 10 (bottom) $h\,\mathrm{Mpc}^{-1}$ with error bars given by the standard error over realisations (unavailable for the Millennium Simulation, the furthest left point). The curves show the convergence model in equation (4.1). This works impressively well given that all panels are well described with a single free parameter. That the point at $2\,h^{-1}\,\mathrm{Mpc}$ falls off this curve indicates a departure from the simple form of the correction.

Realizations	N	$L/(h^{-1}\mathrm{Mpc})$	$\ell_s/(h^{-1}\mathrm{kpc})$	$s/(h^{-1}\mathrm{Mpc})$
5	128^3	256	40	2
3	256^3	350	27	1.37
5	256^3	256	20	1
3	512^3	256	10	0.5
1	2160^3	500	5	0.23

Table 4.2: Convergence simulation details. These show the number of realizations for a simulation of N particles in a box of length L with gravitational softening ℓ_s and a mean inter-particle spacing s. The final entry in the table is the Millennium Simulation of which there is one a single realization.

simulations as a function of resolution is shown for various k in Fig. 4.2, which shows an obvious trend for lower resolutions to underpredict the true power, especially at high k. However, there is a clear convergence trend, allowing a smooth curve to be used to extrapolate to infinite resolution. On this basis, it can be seen that the Millennium Simulation power spectrum has not converged at the higher ($k > 2\,h\,\mathrm{Mpc}^{-1}$) wavenumbers with the correction being as large as 10% at $k = 10\,h\,\mathrm{Mpc}^{-1}$, $z = 1$.

A simple model, fitted to the data in Fig. 4.2, for correcting the average power of a simulation with resolution r to that of an infinite resolution is

$$\Delta^2_\infty(k) = \Delta^2_\mathrm{r}(k)[1 + 0.02kr(1+z)], \qquad (r < 1h^{-1}\,\mathrm{Mpc}) \tag{4.1}$$

where $r = L/N^{1/3}$ is the mean inter-particle spacing for simulations with the same ratio of softening to r as the Millennium Simulation. This model is the solid curve seen in Fig. 4.2. r should not be more than $1\,h^{-1}\,\mathrm{Mpc}$ as this leads to deviations from the simple model as can be seen in Fig. 4.2.

Based on this a best estimate of the true power spectrum was created for the cosmology given in Table 4.1 by averaging over the high resolution ($N^3 = 512^3$) independent realisations (of which there are 6, including the Millennium Simulation itself) in order to beat down sample variance and then averaging after applying the correction given in Equation (4.1). Based on 4.2 it is felt that the simulated power can be trusted to $k = 10\,h\,\mathrm{Mpc}^{-1}$ out to $z = 1$ which is sufficient for current and future weak lensing surveys. Although this correction formula has been calibrated in detail for the cosmology of the Millennium Simulation, it is used below in other models, in the spirit that (a) the cosmologies investigated as part of this work are similar to the Millennium simulation, and (b) the correction to the power measured in simulations with the smallest mean inter-particle separation is small. The halo model discussed in the rest of this chapter is only compared to simulations with the power corrected for finite resolutions as discussed here.

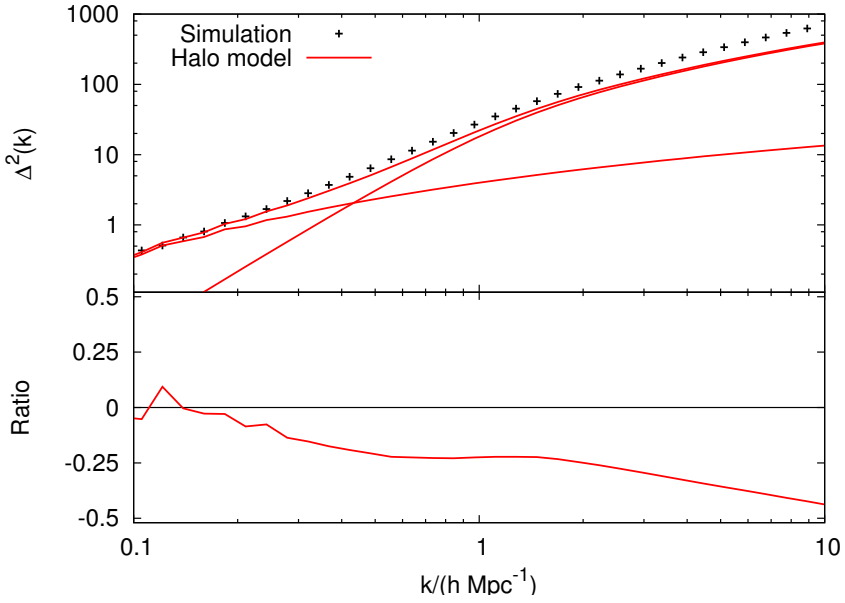

Figure 4.3: The $z = 0$ power spectrum produced from simulations (which have the cosmological parameters of the Millennium Simulation; see Table 4.1) compared to the original version of the halo model. The lower panel shows ratios of the model to the simulation. There is a 20% underprediction in power around $k = 1\,h\,\mathrm{Mpc}^{-1}$ which worsens at smaller scales with the underprediction being close to 50% around $k = 10\,h\,\mathrm{Mpc}^{-1}$. This is far from the accuracy required by current lensing surveys.

4.4 Perturbing the halo model

In this chapter the halo model prediction for the matter power spectrum is used extensively and this is given in equation (3.16). For numerical calculations it makes more sense to compute the integral for $\Delta^2_{\rm 1H}$ in terms of $\nu = \delta_{\rm c}/\sigma(M)$. The mass fraction in haloes of a given mass $\mathrm{d}F$ can be related to the mass function in terms of M, and that in terms of ν via

$$\mathrm{d}F = \frac{M}{\bar{\rho}} n(M)\,\mathrm{d}M = f(\nu)\,\mathrm{d}\nu\ , \tag{4.2}$$

so that the one-halo power is

$$\Delta^2_{\rm 1H}(k) = 4\pi \left(\frac{k}{2\pi}\right)^3 \frac{1}{\bar{\rho}} \int_0^\infty M(\nu) W^2(k, M) f(\nu)\,\mathrm{d}\nu\ , \tag{4.3}$$

where W is the normalised Fourier transform of a halo profile of mass M, $f(\nu)$ is the normalised mass function. For clarity, throughout this section NFW halo profiles are used (equation 3.25) and these are truncated at a virial radius $r_{\rm v}$ defined as the radius that contains an average density $\Delta_{\rm v}$ times greater than the background. Haloes have a concentration $c = r_{\rm v}/r_{\rm s}$ given by the full relations of Bullock et al. (2001) and shown in equations (3.29) and (3.30). For the mass function the form of Sheth et al. (2001), given in equation (3.46), is used. In the original version of the halo model described here the standard values $\Delta_{\rm v} = 200$ and $\delta_{\rm c} = 1.686$ are adopted.

The one-halo term calculates the power associated with randomly-placed haloes and their internal structure; but large-scale displacements of haloes with respect to one another mean that one should add a two-halo term to the power. As discussed in Section 3.2.3 the latter is approximately the linear theory power spectrum, but in detail this requires modification. For example, linear theory overpredicts the current magnitude of the BAO peaks in the matter power spectrum, which are damped by the quasilinear effect of small-scale displacements. This is commonly corrected by assuming a model for the damping predicted from perturbation theory by Crocce & Scoccimarro (2006):

$$\Delta^2_{\rm lin}(k) \to {\rm e}^{-k^2\sigma_{\rm f}^2}\Delta^2_{\rm lin}(k) \ , \tag{4.4}$$

where $\sigma_{\rm f}$ is the 1D rms linear-theory displacement given by

$$\sigma_{\rm f}^2 = \frac{1}{3}\int_0^\infty \frac{\Delta^2_{\rm lin}(k)}{k^3}\,{\rm d}k \ . \tag{4.5}$$

However the derivation of this expression assumes that the scales of interest are large compared to $\sigma_{\rm f}$, so the damping factor cannot be trusted when $k\sigma_{\rm f}$ is large. It was found that the best fit to numerical data required an expression equal to equation (4.4) to quadratic order, but without extreme high-k truncation. This can be achieved via a tanh function:

$$\Delta^2_{\rm 2H}(k) = \left[1 - 0.9\tanh^2\left(k\sigma_{\rm f}/\sqrt{0.9}\right)\right]\Delta^2_{\rm lin}(k) \ . \tag{4.6}$$

Here the factor of 0.9 was fit to power spectra from cosmic emu to best match the BAO feature. The full expression for the halo model power spectrum is then

$$\Delta^2(k) = \Delta^2_{\rm 2H} + \Delta^2_{\rm 1H} \ , \tag{4.7}$$

where $\Delta^2_{\rm 1H}$ is given by equation (4.3) and $\Delta^2_{\rm 2H}$ is given by equation (4.6). One should note that empirically the damping has been found to apply just to the 'wiggle' of the BAO rather than to the whole power spectrum at the BAO scale (Seo & Eisenstein 2003). This is ignored in this work because equation (4.4) is the result from theoretical calculations and this is in the 1- to 2-halo transition region anyway so any drop in power can feasibly be recovered by fitting the 1-halo term. Although it is shown later that the quasilinear regime that corresponds to this cross over is problematic, and where the calibrated halo model performs the least well.

For the calculation of the growth factor the approximate expression for the logarithmic growth rate in ΛCDM given in Linder (2005) and derived in Linder & Cahn (2007) is integrated explicitly,

$$\frac{{\rm d}\ln g}{{\rm d}\ln a} = \Omega_{\rm m}^{\gamma}(z) \ . \tag{4.8}$$

where g is the growth factor normalised to be 1 today, $\gamma = 0.55$. This fitting formula and subsequent integration to find the growth factor is valid at the sub percent level.

In Fig. 4.3 a comparison of the halo model in its original form ($\Delta_{\rm v} = 200$, $\delta_{\rm c} = 1.686$) to the power spectrum created from resolution corrected simulations at $z = 0$ is shown. It is immediately obvious that the halo model prediction is qualitatively reasonable in form, but

deviates in detail from the data. There are a number of possible reasons for the relatively poor performance of the halo model here. Halo-finding algorithms tend only to assign half of the particles in a simulation into haloes at $z = 0$ (*e.g.* Jenkins et al. 2001; More et al. 2011) so the non-linear distribution of half of the mass in the simulation is treated by the halo model via an extrapolation of the formula for the mass function. It is also clearly an approximation to treat the small scale clustering of matter as a random distribution of perfect spheres, there are un-virialised objects in the quasi-linear regime that are not taken into account in the halo model formalism. But it is also possible that much of the inaccuracy of the power spectrum calculation results simply from incorrect parameter choices. The model contains quantities such as $\Delta_{\rm v}$ and $\delta_{\rm c}$, whose values are adopted from simplified analytic arguments. Improved results may then be possible by fitting the halo model to power spectra from a simulation using these quantities as physically-motivated, but free, parameters. The proposed changes represent a prescription for producing effective haloes whose power spectrum mimics the true one, even if these haloes differ slightly from those measured directly in simulations. Nevertheless, it is desirable to retain the large amount of tested theoretical input that goes into the halo model as described in Chapter 3. For example: the input cosmology changes the linear power spectrum, which then in turn affects the mass function through the variance and the halo density profiles through the concentration and size relations. In addition the linear growth rate will change, which also affects the concentration relations directly as well as the amplitude of the linear power spectrum. All of these ingredients have been tested against simulations and are theoretically motivated. The aim is therefore to retain these elements while exploring the impact of variations in less well-specified ingredients.

The parameters that should certainly be allowed to vary in this approach are the virialized overdensity of a halo, $\Delta_{\rm v}$, defined in equation (3.26) and the linear collapse threshold, $\delta_{\rm c}$, defined in equation (3.33). Both of these parameters are derived from the spherical model (see e.g. p488 of Peacock 1999) and rely on a somewhat arbitrary definition of the exact time of halo collapse.

In an $\Omega_{\rm m} = 1$ universe the spherical model gives the value of $\Delta_{\rm v} = 18\pi^2 \simeq 178$, but this number changes as a function of cosmology (*e.g.* Bryan & Norman 1998). The original halo model used here takes the value $\Delta_{\rm v} = 200$, and one should note that changing this is not really consistent with numerical halo-finding algorithms, which use a criterion based on the mean interparticle separation. The necessary relations for the cosmological variation of $\Delta_{\rm v}$ are given by the fitting formulae of Bryan & Norman (1998):

$$\Omega_{\rm m}(z)\Delta_{\rm v} \approx 18\pi^2 + 82[\Omega_{\rm m}(z) - 1] - 39[\Omega_{\rm m}(z) - 1]^2 \ , \tag{4.9}$$

in a flat Universe with Λ and

$$\Omega_{\rm m}(z)\Delta_{\rm v} \approx 18\pi^2 + 60[\Omega_{\rm m}(z) - 1] - 32[\Omega_{\rm m}(z) - 1]^2 \ , \tag{4.10}$$

in an open Universe. The general trend in the variation of $\Delta_{\rm v}$ is that collapsed haloes are denser relative to the mean as the Universe departs from $\Omega_{\rm m} = 1$ form although the dependence is

different in a flat ΛCDM universe compared to an open Universe. These equations are slightly different from those in Bryan & Norman (1998) because they are defined here relative to the mean background matter density rather than to the critical density.

Although the variations of $\Delta_{\rm v}$ in a fitted halo model may not follow the simple theoretical variation exactly, this trend will serve as a useful initial guide when parameter space is explored. In addition, for flat models with a single component of dark energy it is expected that $\Delta_{\rm v}$ would be a function of $\Omega_{\rm m}(z)$ only and this will be a useful principle in parameterising fitting formulae.

The value of $\delta_{\rm c}$ can be calculated from the spherical collapse model: In an $\Omega_{\rm m} = 1$ universe $\delta_{\rm c} \simeq 1.686$ and it has a very weak dependence on cosmology (see Eke et al. (1996) for flat models with Λ and Lacey & Cole (1993) for matter-dominated open models). As an example, for a $\Omega_{\rm m} = 0.3$ ΛCDM model $\delta_{\rm c} = 1.676$ which differs from the flat case by less than 1%. Based on this it is expected for $\delta_{\rm c}$ to be effectively independent of cosmology around the standard ΛCDM type.

4.5 An analytical approximation

Before presenting the results of fitting the full halo model to accurate, simulated power spectra it will be useful to investigate an analytical toy model. From the form of the '1-halo' power in equation 4.3 it is difficult to see how variations in parameters such as $\delta_{\rm c}$ and $\Delta_{\rm v}$ will alter the form of the halo model prediction for the matter power spectrum. However it is possible to derive an exact equation for $\Delta^2_{\rm 1H}$ by making some crude approximations for the halo model ingredients. These approximations are certainly unsuitable for accurate calculations, or comparisons with data, but give insight into the effects of halo model parameters on the prediction for the non-linear power spectrum.

The aim is to evaluate the exactly the integral for the 1-halo power given in 4.3 which can be written entirely in terms of halo virial radii and ν as

$$\Delta^2_{\rm 1H}(k) = 4\pi \left(\frac{k}{2\pi}\right)^3 \frac{1}{\bar{\rho}} \int_0^\infty r_{\rm v}^3(\nu) W^2(k, r_{\rm v}) f(\nu)\, {\rm d}\nu \ . \tag{4.11}$$

In order to compute this integral analytically one can approximate the Window Function $W(k, r_{\rm v})$ as a Gaussian which turns over at the virial radius of the halo in question and that tends to 1 as $k \to 0$

$$W(k, r_{\rm v}) = e^{-k^2 r_{\rm v}^2/2} \ . \tag{4.12}$$

For simplicity the Gaussian mass function from Press & Schechter (1974) can be used

$$g(\nu) = \sqrt{\frac{2}{\pi}} e^{-\nu^2/2} \ . \tag{4.13}$$

All that remains is to specify a relation between virial radius and halo size via $r_{\rm v}(\nu)$. Since $\sigma(M) = \delta_{\rm c}/\nu \propto M^{-(3+n_{\rm eff})/6}$ it is reasonable to postulate a power law relation between M and $\delta_{\rm c}/\nu$, $M = M_*(\nu/\delta_{\rm c})^\alpha$ where $\alpha > 0$ to ensure that higher mass haloes have higher ν values.

Due to the relation between halo mass and virial radius the relation between ν and $r_{\rm v}$ is then

$$r_{\rm v}^3 = \frac{3M_*}{4\pi\bar{\rho}\Delta_{\rm v}}\left(\frac{\nu}{\delta_{\rm c}}\right)^{\alpha} = \frac{r_*^3}{\bar{\rho}\Delta_{\rm v}}\left(\frac{\nu}{\delta_{\rm c}}\right)^{\alpha} \ , \tag{4.14}$$

where r_* approximately represents the radius of a sphere in the homogeneous universe that contains the mass of a typical M_* halo. In order to make the integral in equation (4.11) have a simple exact solution it is necessary to set $\alpha = 3$, implying $n_{\rm eff} = -1$. Conveniently this is approximately the correct index in the quasi-linear regime at $z = 0$. The idealised 1-halo term is then

$$\Delta^2_{\rm 1H}(k) = \sqrt{\frac{32}{9\pi^3}}\frac{(kr_*)^3}{\delta_{\rm c}^3}\left[1 + 2\left(\frac{kr_*}{\delta_{\rm c}\Delta_{\rm v}^{1/3}}\right)^2\right]^{-2} \ . \tag{4.15}$$

This equation shows the main effects on the power spectrum of changing the spherical model parameters $\delta_{\rm c}$ and $\Delta_{\rm v}$. $\delta_{\rm c}$ governs how many haloes the density field gets split in to – the large scale part of the halo model power is governed by shot noise relating to the number density of haloes. $\delta_{\rm c}$ controls the overall amplitude of the 1-halo power, increasing $\delta_{\rm c}$ has the effect of decreasing the power and visa versa. If $\delta_{\rm c}$ is lower the collapse threshold is easier to reach and the density field splits into fewer haloes of higher mass and if $\delta_{\rm c}$ is higher more difficult to reach the opposite happens and the density field is comprised of many more, lower mass haloes. $\Delta_{\rm v}$ governs the virial radius of haloes, the effect of changing this can be seen in the denominator in equation (4.15), which is one until scales which approximately correspond to the virial radius of a typical ($\nu = 1$) halo. One can see that the '1-halo' power in the halo model initially rises as k^3 with amplitude controlled by $\delta_{\rm c}$ before being moderated to k^{-1} at a scale that corresponds to the size of a typical halo.

4.6 Fitting

In order to produce improved fits via the halo model $\Delta_{\rm v}$ and $\delta_{\rm c}$ were varied and the effect of different choices for these two parameters is shown in Fig. 4.4. However, an extra ingredient was found to be needed in order to control the curvature of the power spectrum beyond $k \sim 1\,h\,{\rm Mpc}^{-1}$, where the filtering effect from the typical haloes has a major effect on the shape of the 1-halo term. At higher k values, the properties of lower-mass haloes become increasingly important, and it is difficult for the fits to track the 1-halo term to the smallest scales without introducing an empirical perturbation of the concentration-mass relation. An additional parameter, η was also varied, defined by:

$$W(k) \to W(\nu^{\eta}k) \ , \tag{4.16}$$

which effectively changes the halo concentrations in a mass dependent way. The effect of varying η is shown in Fig. 4.5. A similar approach would have been to vary $c(M)$ in a mass dependent way, but this has not been persued here because η variations were sufficient to get good matches across all scales.

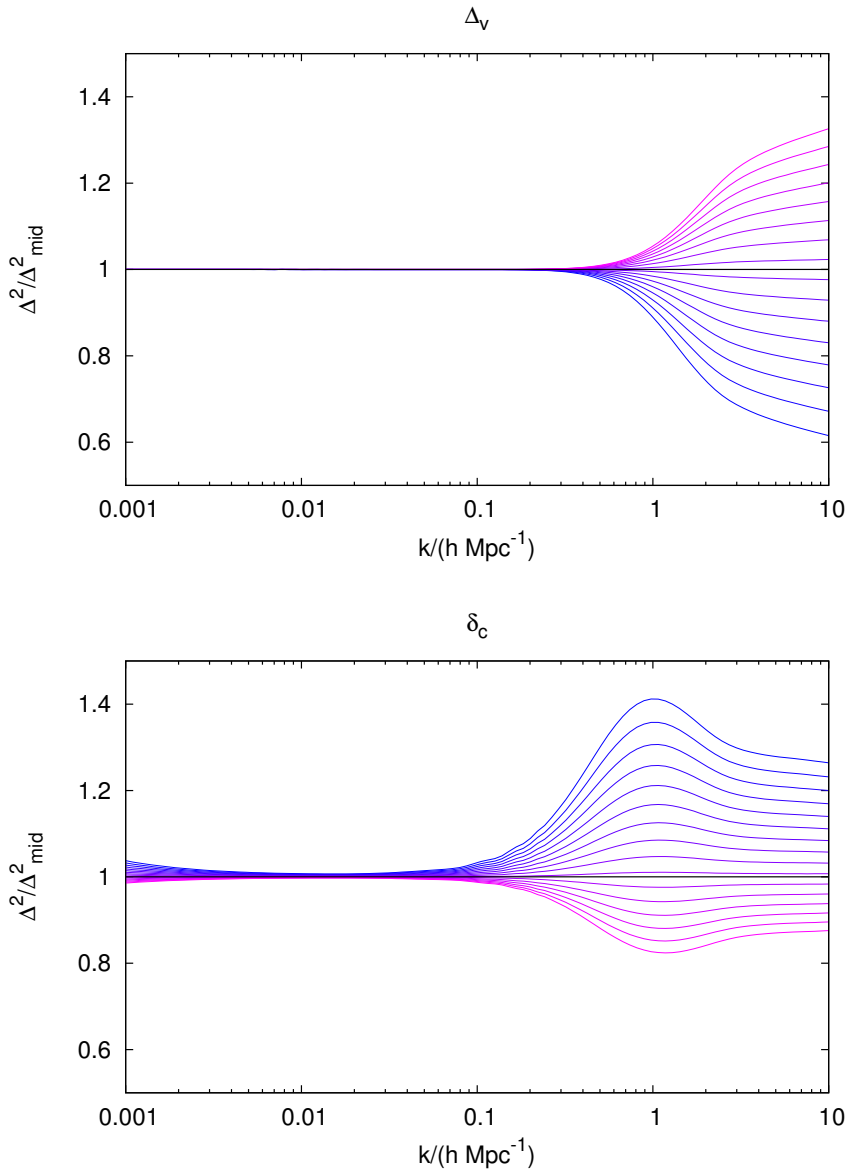

Figure 4.4: The effect of varying the parameters Δ_v and δ_c on the halo model power spectrum for a standard ΛCDM cosmology with all other parameters held fixed. The upper panel shows variations in Δ_v between 100 and 300 compared to the standard value of 200. The lower panel shows variations in δ_c between 1.5 and 1.8 compared to the standard value of 1.686. In each case the lowest value for the parameter is the bluest curve and the highest value is the pinkest. One can see that δ_c variations are able to affect the curvature of the power spectrum at larger scales than Δ_v, in line with the analytical approximation described in the text. The surprising effect of varying δ_c on very large scales is due to an unphysical feature of the halomodel in which the 1-halo power will eventually overtake the 2-halo term on very large scales. In reality this feature should be surpressed however it does not matter for the fitting carried out as part of this work because fitting is restricted so scales of $k \gtrsim 0.1\,h\,\mathrm{Mpc}^{-1}$.

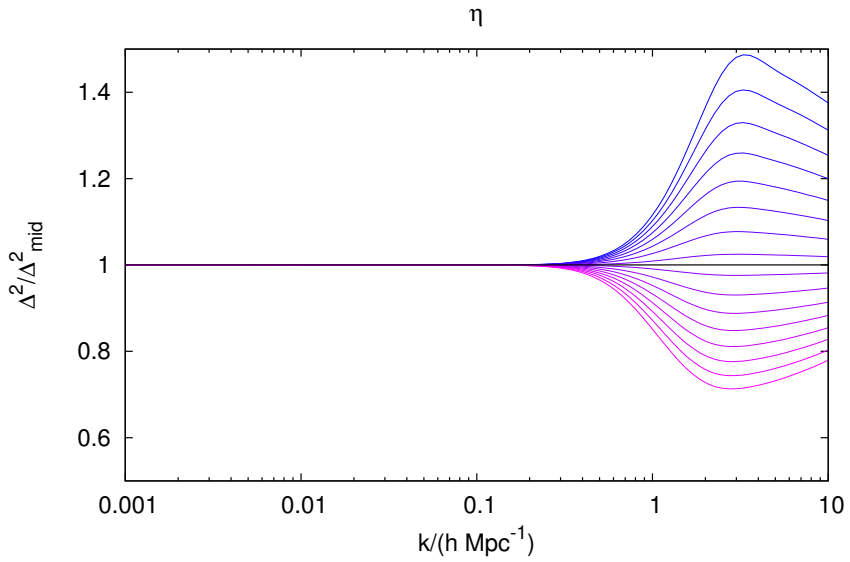

Figure 4.5: The effect of varying the parameter η on the halo model power spectrum for a standard ΛCDM cosmology with all other parameters held fixed. Shown are variations in η between -0.3 and 0.3 compared to the standard value of 0, the lowest value for the parameter is the bluest curve and the highest value is the pinkest. Variations in η are only able to effect the power spectrum on small scales but do so in a different way to $\Delta_{\rm v}$ variations shown in Fig. 4.4 and this allows a better fitting of the highly non-linear portion of the spectrum. Modifying η is very similar to slightly changing the mass-concentration relation.

With this approach, the parameters that best match the (slightly-corrected) power spectrum data from the simulations at redshifts between 0 and 2 are

$$\Delta_{\rm v} = 312.4 + 33.05\ \Omega_{\rm m}^{-1.15}(z)\ , \tag{4.17}$$

$$\delta_{\rm c} = 1.525\ , \tag{4.18}$$

$$\eta = 0.33\ . \tag{4.19}$$

The fit of this model is shown as a comparison of power spectra and as ratios to the corrected simulation at a range of redshifts in Fig. 4.6. One can see that the fitted halo model predictions are mainly accurate to within 5% across all redshifts for $k > 1\,h\,{\rm Mpc}^{-1}$ although the precision is poorer at higher redshifts and at lower k. The prediction at redshift 0 is within 1% across the k range where the simulation is not noisy due to cosmic variance. It is impressive that the halo model is able to perform so well across this range of scales and redshifts with just three free parameters being introduced, only one of which varies with redshift.

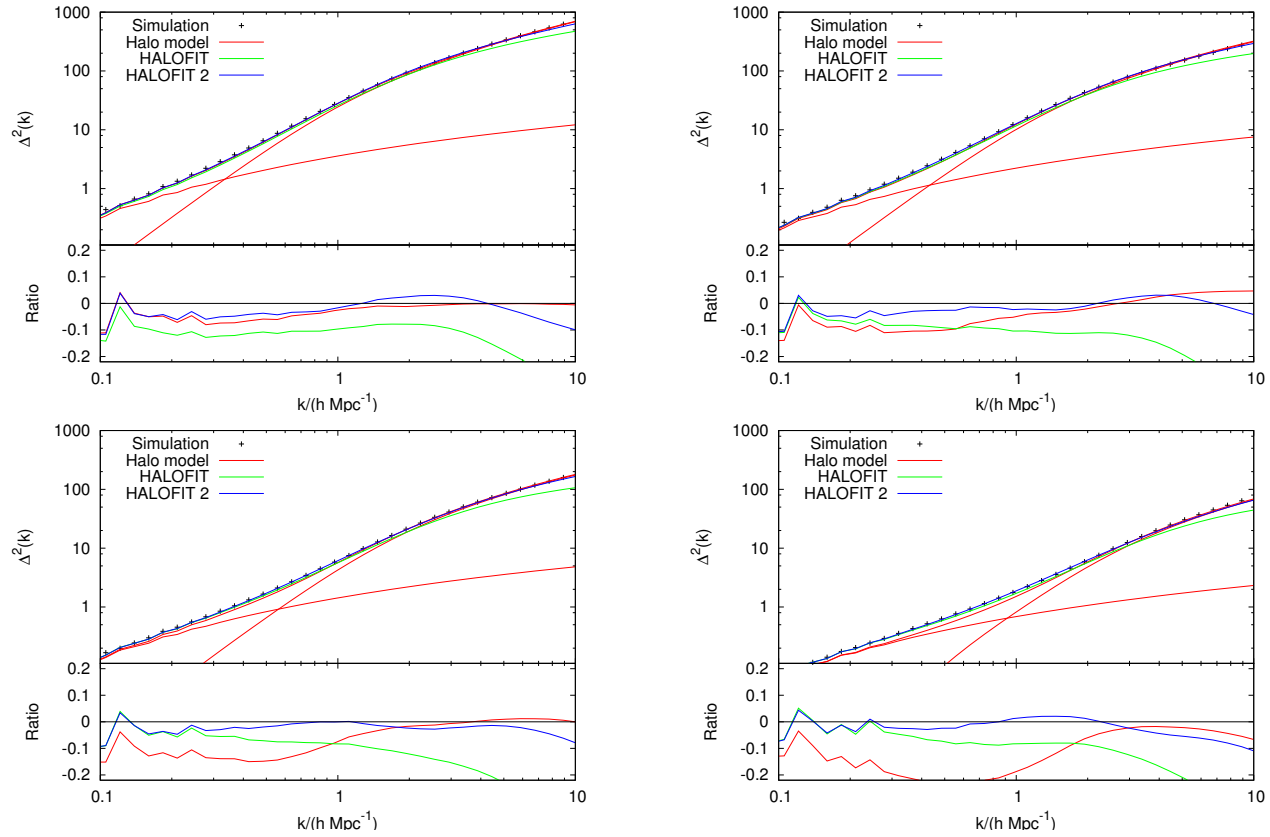

Figure 4.6: The power spectrum of simulations (black crosses) and that of the modified halo model (red) which has been fit to these simulations. Also shown is `HALOFIT` (blue) and the `HALOFIT` of Takahashi et al. (2012) (pink) at redshifts 0 (top left), 0.5 (top right), 1 (bottom left) and 2 (bottom right). One can see that the halo model prediction for the power at redshift 0 is perfect to within the simulation noise, it remains good at small scales at all redshifts but begins to underestimate the power in the quasi-linear regime at higher redshifts. The poor prediction in the linear regime ($k \simeq 0.1\,h\,\mathrm{Mpc}^{-1}$) at higher redshifts indicates that the suppression of linear power according to equation (4.6) is not appropriate at high z. The original `HALOFIT` consistently underestimates power at almost all scales whereas `HALOFIT` of Takahashi et al. (2012) performs much better but still underestimates power at the smallest scales by around 10%.

4.7 Comparison with HALOFIT

Fig. 4.6 also shows the prediction of HALOFIT: this is systematically low across most of the range in k at around the 10% level, but the error is worse at high k, and the underprediction is around 50% on the smallest scales shown. This deficiency of HALOFIT has been noted by a number of authors (*e.g.* White & Vale 2004; Springel et al. 2005; Hilbert et al. 2009; Heitmann et al. 2010) and it is interesting to seek the origin of the discrepancy. Fig. 4.7 plots the raw power spectrum at $z = 0$ measured in a simulation of similar resolution to those on which HALOFIT was trained (Jenkins et al. 1998) together with the correction to this raw power spectrum to take account of the finite resolution. One can see that HALOFIT predicts the raw power spectrum well here but not that which has been corrected. This implies that the reason for the under-prediction of power in HALOFIT is an artifact of the fact that it was trained on simulations with low resolution because the simulations themselves systematically underestimate the power spectrum at small scales.

The additional underprediction of power around $k = 10\,h\,\mathrm{Mpc}^{-1}$ seen in Fig. 4.7 when compared to the raw simulation is probably due to the fact that the raw simulation has a gravitational softening of $l_\mathrm{s} = 20\,h^{-1}\,\mathrm{kpc}$ whereas those in Jenkins et al. (1998) had softenings of $30\,h^{-1}\,\mathrm{kpc}$. This additional softening produces an additional systematic underprediction in power at small scales. This under prediction is still present in the revisited HALOFIT fitting function of Takahashi et al. (2012) but to a far lesser extent (this can be seen in the ratio panels of Fig. 4.6). This work implies that this underprediction in the new HALOFIT is a less severe manifestation of the very same problem that was present in the original, the fit was trained on simulations of finite resolution and this was not considered by Takahashi et al. (2012).

4.8 Other cosmologies

So far this approach has only been tested and trained on a single simulation, with a single set of cosmological parameters. This alone is a weak test, even though it should be noted that the different redshifts in the Millennium Simulation cover a range of effective Ω_m and σ_8 values. This section discusses fits to simulations with different cosmologies *without* performing any additional calibration of the model.

The cosmological parameters for these simulations are given in Table 4.3 and the results of the comparisons are shown in Figs 4.8, 4.9 and 4.10. The cosmological parameters for these simulations were chosen to be in the vicinity of the WMAP7 (Komatsu et al. 2011) parameters in Ω_m, h, σ_8 and n_s while being constrained to be flat.

The numerical properties of these simulations were the same as for the best recreation of the Millennium Simulation in Table 4.2: $N = 512^3$ in a box of side $L = 256\,h^{-1}\,\mathrm{Mpc}$. To correct for finite resolution effects, a simple universal correction factor was adopted from the ratio of the power spectrum obtained from a single realization of the Millennium cosmology at this resolution to that of the full corrected power spectrum which is itself typically no larger

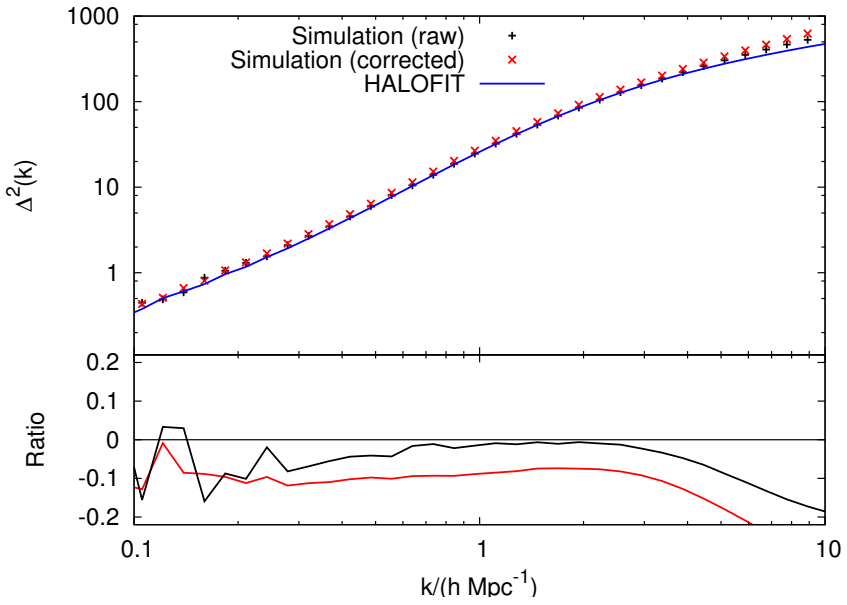

Figure 4.7: The $z = 0$ power spectrum produced from a simulation in its raw form (black crosses) and when corrected for finite resolution (red crosses) together with the prediction from the original `HALOFIT` (blue line). The ratio panel shows residuals for the ratio of halofit to the original simulation (black) and corrected simulation (red). One can see that the `HALOFIT` prediction for the low resolution simulation is very accurate at large scales while it is very inaccurate for the corrected simulation. This suggests that the underprediction in power for `HALOFIT` is due to it being trained on simulations of low resolution.

than $\sim 10\%$.

The results of comparisons to these simulations are shown in Figs. 4.8, 4.9 and 4.10. It can be seen that the revised halo model performs well, particularly at lower z, and is very competitive with the model of Takahashi et al. (2012) for scales $k > 1\,h\,\mathrm{Mpc}^{-1}$ across a wide range of cosmological models. This is impressive when one considers that the halo model approach uses only 5 free parameters compared to the ~ 30 used in Takahashi et al. (2012).

However, it is also apparent from these plots that the halo-model approach can have a problem at larger scales: it can systematically underpredict the power spectrum in the region of the transition between the 1- and 2-halo terms and also at linear scales ($k \simeq 0.1\,h\,\mathrm{Mpc}^{-1}$). The underprediction of power at linear scales is due to the dampening of linear power in equation (4.6) not being appropriate for a wide range of models and redshifts. It would seem that the set of parameters required for matching linear and quasi-linear scales for the original simulations does not translate well into a wider range of cosmological models. In practice, a difficulty in robust power prediction at $k < 1\,h\,\mathrm{Mpc}^{-1}$ is not an insuperable obstacle, since direct simulations in this regime are relatively inexpensive. It is therefore suggested that the best approach is to marry such direct determinations with the halo-model results providing an accurate extension to the $k \sim 10\,h\,\mathrm{Mpc}^{-1}$ regime that is otherwise expensive to compute.

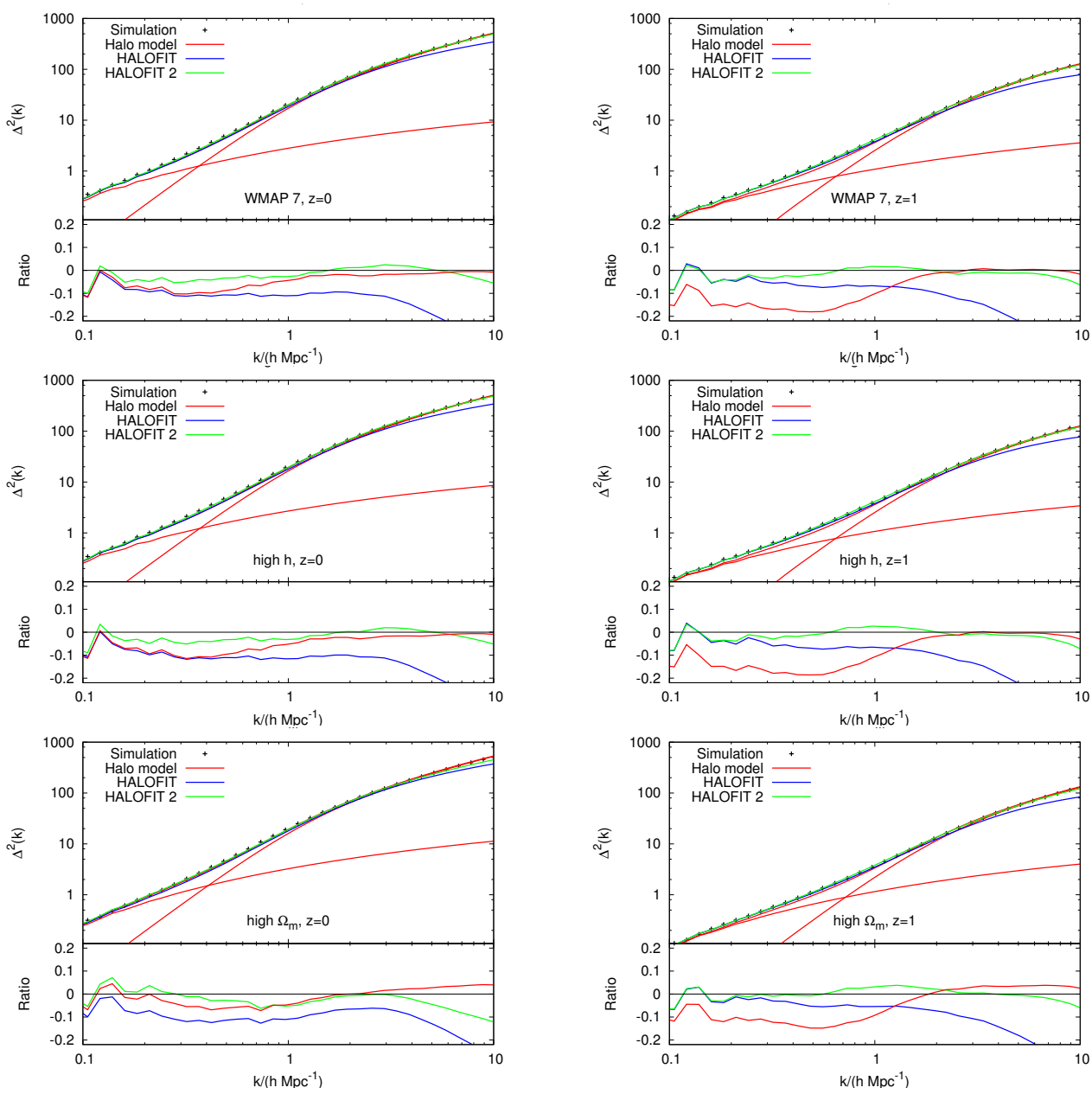

Figure 4.8: The power spectrum of simulations (black points) compared to that of the modified halo model (red), HALOFIT (blue) and HALOFIT2 (pink) at redshifts 0 (left column) and 1 (right column) for simulations WMAP (top), high_h (middle) and high_m (bottom).

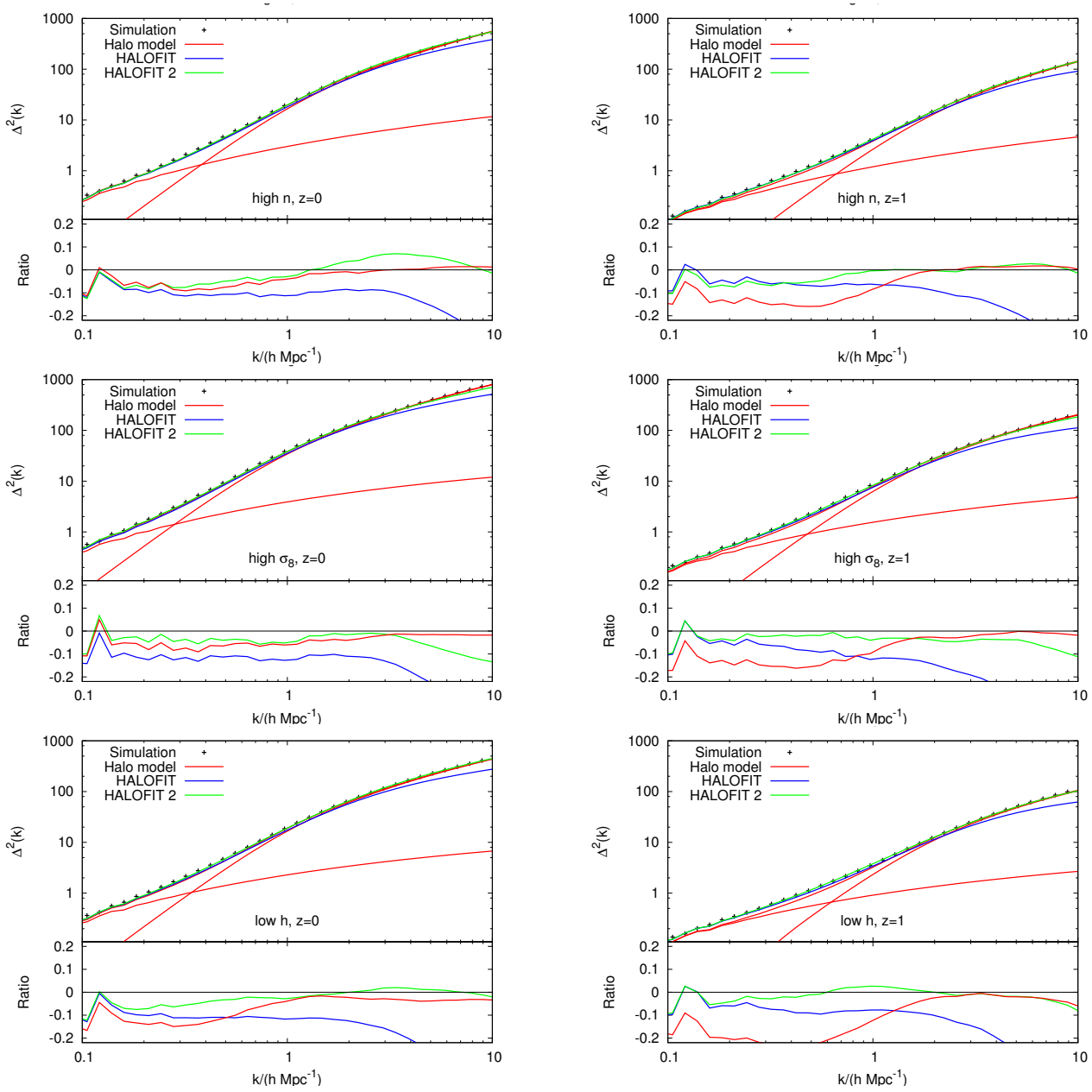

Figure 4.9: The power spectrum of simulations (black points) compared to that of the modified halo model (red), HALOFIT (blue) and HALOFIT2 (pink) at redshifts 0 (left column) and 1 (right column) for simulations high_n (top), high_s (middle) and low_h (bottom).

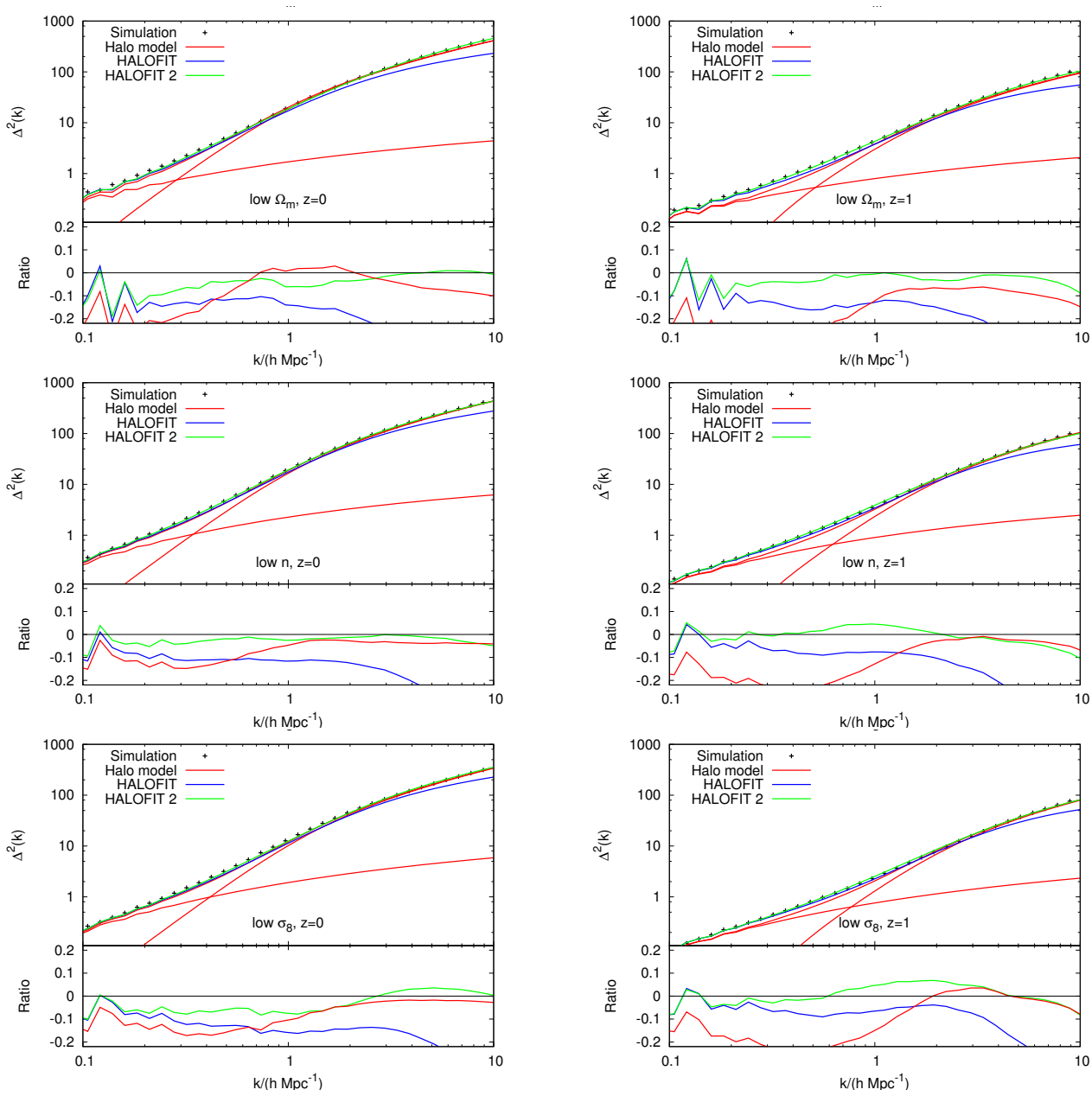

Figure 4.10: The power spectra of the broader simulations (black points) compared to that of the modified halo model (red), HALOFIT (blue) and HALOFIT2 (pink) at redshifts 0 (left column) and 1 (right column) for simulations low_m (top), low_n (middle) and low_s (bottom).

Simulation	$\Omega_{\rm m}$	Ω_Λ	h	σ_8	$n_{\rm s}$
WMAP7	0.25	0.75	0.7	0.8	0.95
high_m	**0.35**	**0.65**	0.7	0.8	0.95
high_n	0.25	0.75	0.7	0.8	**1.05**
high_s	0.25	0.75	0.7	**1.0**	0.95
high_h	0.25	0.75	**0.8**	0.8	0.95
low_m	**0.15**	**0.85**	0.7	0.8	0.95
low_n	0.25	0.75	0.7	0.8	**0.9**
low_s	0.25	0.75	0.7	**0.7**	0.95
low_h	0.25	0.75	**0.6**	0.8	0.95

Table 4.3: Cosmological parameters for an extended set of simulations. The first model is approximately a WMAP7 cosmology and the others are perturbations around this basic model with the perturbed quantity being in bold in each model, in each case $\Omega_{\rm b} = 0.05$.

Finally, it is shown in Figs. 4.11 and 4.12 how the power spectrum of linear theory and that from the calibrated halo model (equation 4.19) varies as cosmological parameters are varied. Shown are parameter variations within the bounds of *cosmic emu*. These can be compared with similar plots in Heitmann et al. (2014). The centre of the parameter space, about which the parameters shown in the plots are varied, is $\omega_{\rm m} = 0.1375$, $\omega_{\rm b} = 0.0225$, $n_{\rm s} = 0.95$, $w = -1$, $\sigma_8 = 0.775$ and $h = 0.7$. Differences with Heitmann et al. (2014) are due to their use of k rather than k/h as the variable.

4.9 Discussion

It has been shown that the halo model can accurately reproduce power spectra that are measured from N-body simulations, even at the smallest scales of interest ($k \sim 10\,h\,{\rm Mpc}^{-1}$), provided one is willing to introduce a small number of empirical modifications of its ingredients – in particular the parameters describing halo virialization and concentration. Initially the halo model was calibrated using the power spectra of the Millennium Simulation at redshifts between 0 and 2. It was then shown that this calibrated halo model is able to accurately reproduce the small-scale power spectra in a range of different cosmologies without further adjustment. This success reflects the fact that the halo model is built on well motivated theoretical ingredients, which naturally adapt to changes in cosmology in a robust fashion.

This statement comes with the caveat that it has only been tested on a limited range of plausibly interesting cosmologies. In particular, it was only tested in cases where the linear power spectra of the simulations had similar spectral shape to that of standard ΛCDM; this should not be a restriction for practical applications. In addition it should be noted that the density profiles of Navarro et al. (1997) and the concentration relations of Bullock et al. (2001) were not calibrated for models where w differs from -1. However, these are calculated

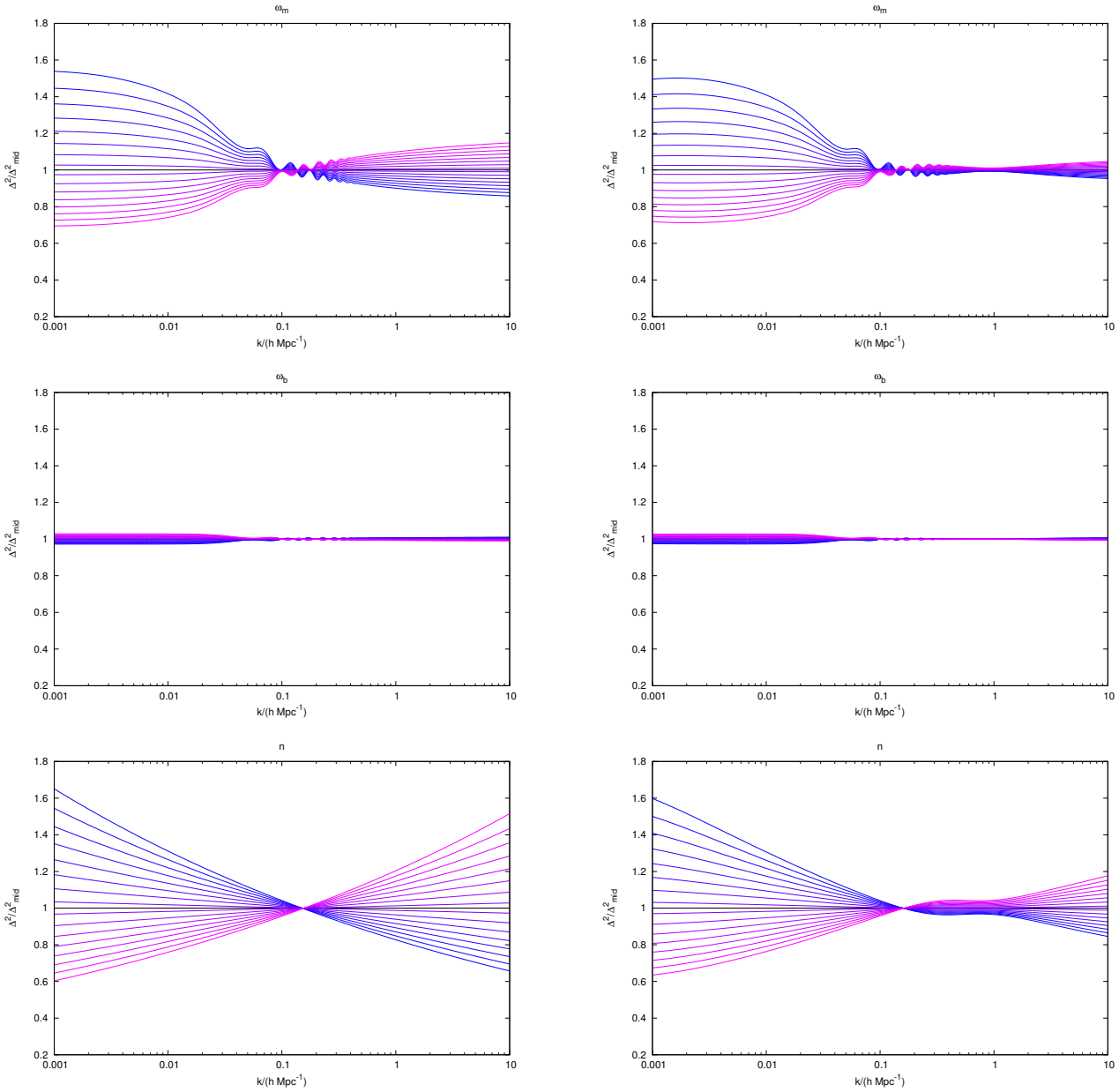

Figure 4.11: The ratio of power spectra when varying cosmological parameters at $z = 0$. Shown is linear theory (left column) and that of the calibrated halo model (right column) with variations about a central value for $0.120 \leq \omega_{\rm m} \leq 0.155$, $0.0215 \leq \omega_{\rm b} \leq 0.0235$ and $0.85 \leq n_{\rm s} \leq 1.05$. Bluer curves show lower values of the parameter whilst pinker curves show higher values. Note that in the case of $\omega_{\rm m}$ and $\omega_{\rm b}$ the universe is constrained to be flat so that $\Omega_{\rm v}$ also varies with $h = 0.7$ fixed. The changes in power caused by altering $\omega_{\rm b}$ are difficult to see but are a maximum of 3% in linear power. One can see that differences in power at small scales in linear theory are smoothed by non-linear evolution in the case of these three parameters which indicates that non-linear evolution is relatively insensitive to these paramters.

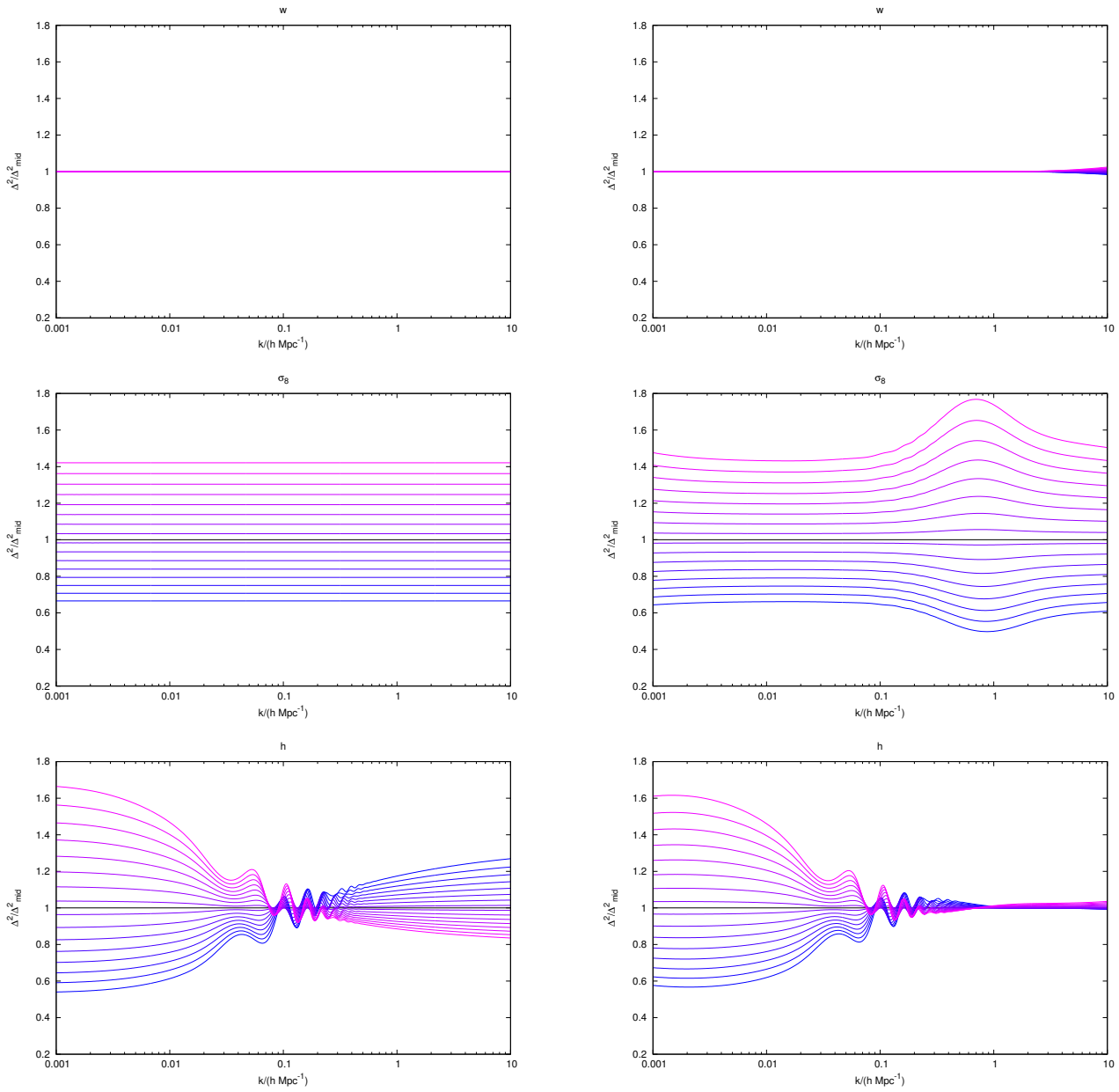

Figure 4.12: The ratio of power spectra when varying cosmological parameters at $z = 0$. Shown is linear theory (left column) and that of the calibrated halo model (right column) with variations about a central value for $-1.3 \leq w \leq -0.7$, $0.616 \leq \sigma_8 \leq 0.9$ and $0.55 \leq h \leq 0.85$. Bluer curves show lower values of the parameter whilst pinker curves show higer values. The nonlinear difference that w causes at small scales (maximum 3% at $k = 10\,h\,\mathrm{Mpc}^{-1}$) is due to the models having differing halo concentrations via alterations to the halo formation redshift. There is no linear difference at $z = 0$ due to the models all having identical σ_8. The effect of increased/decreased σ_8 is amplified in the non-linear regime but the non-linear change seen at very large scales due to σ_8 variations is unphysical and due to the nature of the 1-halo term at very large scales where it begins to dominate over the 2-halo term once more. Initial linear differences in h are smoothed out by nonlinear evolution.

using general concepts such as linear perturbation growth and formation redshift, and so it is fully expected that the approach detailed here will yield sensible results in models with more complicated forms of dark energy. Mass-concentration relations exist in the literature for $w \neq -1$ models (Bhattacharya et al. 2011; Kwan et al. 2013) and these could be used in principle if relations such as Bullock et al. (2001) proved to be not accurate enough.

The halo model approach performs less well in the transition region between the 1-halo and 2-halo terms (which is around $k = 1\,h\,\mathrm{Mpc}^{-1}$ at $z = 0$) and also performs less well at higher redshifts. Unfortunately a simple parametrisation of this behaviour was not found.

The discrepancy at higher redshift could feasibly be due to the very different effective spectral index of the power spectrum at low and high redshifts. At very high z, $n_{\mathrm{eff}} \to -3$, and so peaks reach collapse threshold at a variety of scales simultaneously – structure formation is no longer hierarchical. This potentially invalidates some of the assumptions in the halo model, notably that the Universe is comprised of virialised structures. It is also true that the fitting of relations such as mass-concentration and halo mass functions tends to be done around $z = 0$ with less emphasis being at higher z. It is possible that these two issues are related, certainly structure is more difficult to define at high z due to the simultaneous collapse of a wide range of scales.

One issue that has not been addressed is the effect of baryons on the matter power spectrum. It is inevitable that baryons and dark matter will separate to some extent on small scales owing to gas pressure, with further possible complications arising from feedback in galaxy formation as discussed in Section 2.2.2. At a minimum it is probably fair to say that the deviations between theory and dark-matter simulations seen here at $k \simeq 10\,h\,\mathrm{Mpc}^{-1}$ are becoming within the range of uncertainty introduced by baryonic effects (Semboloni et al. 2011; van Daalen et al. 2013). Nevertheless, in principle the method used in this chapter may help remedy the problem, by using extra physically motivated ingredients such as modified concentration-mass relations and halo profiles that capture the effects of galaxy formation and evolution.

This last point emphasises the potential of the approach described in this chapter. The halo model can readily be extended to take account of new physical processes and changes in the cosmological paradigm. One interesting example would be an application to modified gravity models where revised growth rates, collapse thresholds and internal halo structures can be predicted in part on analytic grounds, and where there is a growing effort on detailed simulations. In such cases, being able to produce *accurate* power spectra will be important in order to distinguish standard and nonstandard cosmological models. Moreover, exploration of a large parameter space of models will inevitably be necessary, and there will therefore be a strong motivation to explore rapid means of generating nonlinear power spectra. Extensions of the halo model such as the one explored here have the potential to be an invaluable tool in such studies.

Chapter 5

Rescaling halo catalogues

5.1 Preamble

In this chapter a method is presented for modifying the catalogue of dark matter haloes produced from a given cosmological simulation. This is done so that the rescaled catalogue resembles the result of a simulation with an entirely different set of parameters. This extends the method of Angulo & White (2010), which rescales the full particle distribution from a simulation. Working directly with the halo catalogue offers an advantage in speed, and also allows modifications of the internal structure of the haloes to account for nonlinear differences between cosmologies. This method can be used directly on a halo catalogue in a self contained manner without any additional information about the overall density field; although the large-scale displacement field is required by the method, this can be inferred from the halo catalogue alone. Proof of concept of the method is shown by rescaling a matter-only simulation with no BAO features to a more standard ΛCDM model containing a cosmological constant and a BAO signal. In conjunction with the halo occupation approach, this method provides a basis for the rapid generation of mock galaxy samples spanning a wide range of cosmological parameters.

The majority of work in this chapter has been published in Monthly Notices of the Royal Astronomial Society as Mead & Peacock (2014); and can be found at – `http://arxiv.org/abs/1308.5183`.

5.2 Introduction

As discussed in Chapter 2 the extraction of fundamental cosmological information from surveys increasingly requires a major input from cosmological N-body simulations, for two reasons: The statistical quantities to be measured from the data tend to have complicated correlations, and the only practical way of computing the required covariance matrix is by averaging over an ensemble of mock datasets. More seriously, an analytical understanding of the development of cosmological structure is restricted to large-scale linear fluctuations, whereas the measurements are inevitably affected by small-scale nonlinearities to some extent. The mildly nonlinear regime can be explored with perturbation theory (*e.g.* Bernardeau et al. 2002) but this fails on smaller scales. If nonlinear information is to be exploited, it is necessary to run simulations for different sets of cosmological parameters, to measure the matter distribution and derive halo catalogues. Mock galaxy samples can then either be generated using semi-analytic methods (*e.g.* Baugh 2006) or from Halo Occupation Distribution (HOD) models (Seljak 2000; Peacock & Smith 2000; Zheng et al. 2005).

However, it is computationally prohibitive to run simulations of large enough volumes at a high enough resolution in order to cover the current cosmological parameter space, which has now grown to encompass neutrinos (masses and numbers of species); warm dark matter; plus complex dark energy models and modified gravity theories amongst others. A way is therefore needed to span this range of cosmologies without having to run a simulation for each particular set of parameters. This idea was investigated by Angulo & White (2010; hereafter AW10), who showed that it was possible to rescale an N-body particle distribution in order to approximate the results of a simulation with a different set of cosmological parameters. Their algorithm consisted of two steps: (i) reinterpreting the length and time units in the original simulation so that the halo mass function was as close as possible to that which would be measured in the new cosmology (ii) modifying individual particle positions so as to reproduce the expected linear clustering in the new cosmology.

AW10 showed that their method successfully reproduced the statistics of the target cosmology at the level of the matter power spectrum and halo mass function. AW10 has been applied by Guo et al. (2013) to look at theoretical differences in galaxy formation between WMAP1 and WMAP7 cosmologies and by Simha & Cole (2013), who looked at measuring cosmological parameters by comparing the galaxy two-point correlation function of SDSS with that computed from galaxy catalogues that were rescaled using the AW10 method.

Despite the success of the AW10 algorithm, it has some disadvantages. Firstly, the algorithm is applied to large particle datasets that can be difficult to communicate; often it is only halo catalogues that are made publicly available by large collaborative simulation groups (*e.g.* the DEUSS simulations of Rasera et al. 2010). Secondly, the algorithm uses the displacement field that was employed to generate the initial conditions; again this may not be publicly available. Finally, the algorithm reproduces the linear clustering in the target simulation, but does not reproduce the deeply nonlinear clustering, which can be considered to be associated

with correlations within individual haloes. In this chapter an extension to the AW10 algorithm is developed and tested, designed to deal with these issues.

The new method rapidly converts a halo catalogue from a given simulation into one that is characteristic of a different cosmology. Other methods for the fast generation of halo catalogues have been developed in the literature: Monaco et al. (2002) developed an algorithm called `PINOCCHIO`, which uses a combination of perturbation theory and an ellipsoidal halo collapse model to generate catalogues. Manera et al. (2013) produced mock catalogues for the Baryon Oscillation Spectroscopic Survey (BOSS) using second order Lagrangian perturbation theory (2LPT) on a particle distribution and then collecting mass from the evolved field into haloes; this approach is called `PTHaloes`. Tassev et al. (2013) use an approach called `COLA` (COmoving Lagrangian Acceleration), which involves a coordinate transform based on 2LPT, followed by a particle mesh (PM) gravity solver with coarse time-stepping, which is able to yield halo statistics rapidly. Nevertheless, all these methods are approximate in their treatment of nonlinearities, and an attractive feature of AW10 is that it is based on a fully nonlinear simulation. A reduced version of the AW10 method has been applied to halo catalogues by Ruiz et al. (2011), in which the authors scaled a halo catalogue in time and length units but did not apply the final stage of the algorithm, in which the linear clustering is reproduced by modifying individual halo positions. In this case Ruiz et al. (2011) showed that AW10 works very well on halo catalogues, but only for simulations of small box sizes ($< 50\,h^{-1}\,\mathrm{Mpc}$) in which large-scale shifts in the displacement field are unimportant and would only manifest themselves as translations of the entire box. Nevertheless the authors showed that halo positions and velocities were recovered with almost no detectable biases and information useful for galaxy formation modelling, such as merger histories, could also be accurately recovered.

The extended algorithm presented here consists of the following steps: The length and time units in the original halo catalogue are rescaled exactly as in the original AW10 algorithm. The particles or halo distribution itself is used to compute the linear displacement field, from which the particle or halo positions are modified so that they reproduce the correct large-scale clustering in the target cosmology. Eisenstein et al. (2007) showed how to recreate the displacement fields via the over-density field in a simulation by using a reverse of the approximation due to Zel'dovich (1970). In Padmanabhan et al. (2012) a variant of this approach was used to improve the sharpness of the BAO feature in BOSS data. Finally, the halo internal structure is directly modified – either by 'restructuring' the density profiles around haloes so that they have the correct sizes and internal structure for the target cosmology (if the particle information is still available), or by removing halo particles from the scaled particle distribution and then 'regurgitating' theoretical 'reconstituted' haloes with the correct internal structure back into the distribution of non-halo particles. In this way consistent particle and halo distributions are created for any desired cosmological model. It is important to emphasise that this is able to be done in an entirely self-contained manner from only a pre-existing halo catalogue and without any tuneable parameters.

This chapter is set out as follows: In Section 5.3 the AW10 algorithm is reviewed and the extension to the method is explained. In Section 5.4, the cosmology dependence of the internal structure of haloes is discussed. In Section 5.5 simulations are described that were designed to test the method. The generation of halo catalogues is also discussed. In Section 5.6 it is first shown that the method for computing the displacement field from the halo positions is reasonable and then results for the mass functions, clustering of matter, clustering of haloes and clustering of material in the interiors of haloes are shown. Results are then presented in redshift space in Section 5.7. A summary is given in 5.9.

5.3 Rescaling

The first part of the AW10 algorithm relabels redshifts and rescales the box size in the original simulation, so that the halo mass function becomes as similar as possible to the desired target cosmology over the range of masses probed by haloes in the simulations. As discussed in Chapter 3 cosmological mass functions have been shown to be nearly universal in form (*e.g.* Sheth & Tormen 1999; Tinker et al. 2008) and depend on cosmology almost entirely through the linear variance, defined in equation (1.100), and which in turn depends only on the linear power spectrum. Because the CDM power spectrum is continuously curved, a suitable scaling in redshift and length units can always make the linear variances as a function of smoothing scale in two different cosmologies coincide almost perfectly around the nonlinear scale. In this way, the re-interpreted simulation output should have the desired halo mass function. This is closely related to the small-scale nonlinear power spectrum via the one-halo term in the halo model (Seljak 2000; Peacock & Smith 2000), where structure is considered to be made of a distribution of clustered virialized haloes with a certain internal structure and mass distribution. If the re-interpreted simulation has the correct mass function then the one-halo term should be approximately correct. The two-halo term in the power is essentially the linear clustering of matter, and this will not be perfectly reproduced by the rescaling. The second part of the AW10 algorithm therefore aims to correct this latter problem, using the approximation of Zel'dovich (1970) to displace individual particles so that the linear clustering is exactly matched.

As pointed out in AW10, one of the remaining sources of difference between the two cosmologies after this scaling will be the different internal halo structure caused in part by the haloes being concentrated differently due to collapsing at different redshifts depending upon the background cosmology, thus altering the one-halo term. In this work this is addressed by modifying the internal structure of the haloes directly so that the structure can be updated to that of the new cosmology. This can be done do either by equipping catalogued haloes with the correct internal structure for the new cosmology (a method called reconstitution) or by finding halo particles in the scaled particle distribution and replacing these with a set of particles designed to have the correct internal structure (a method called regurgitation).

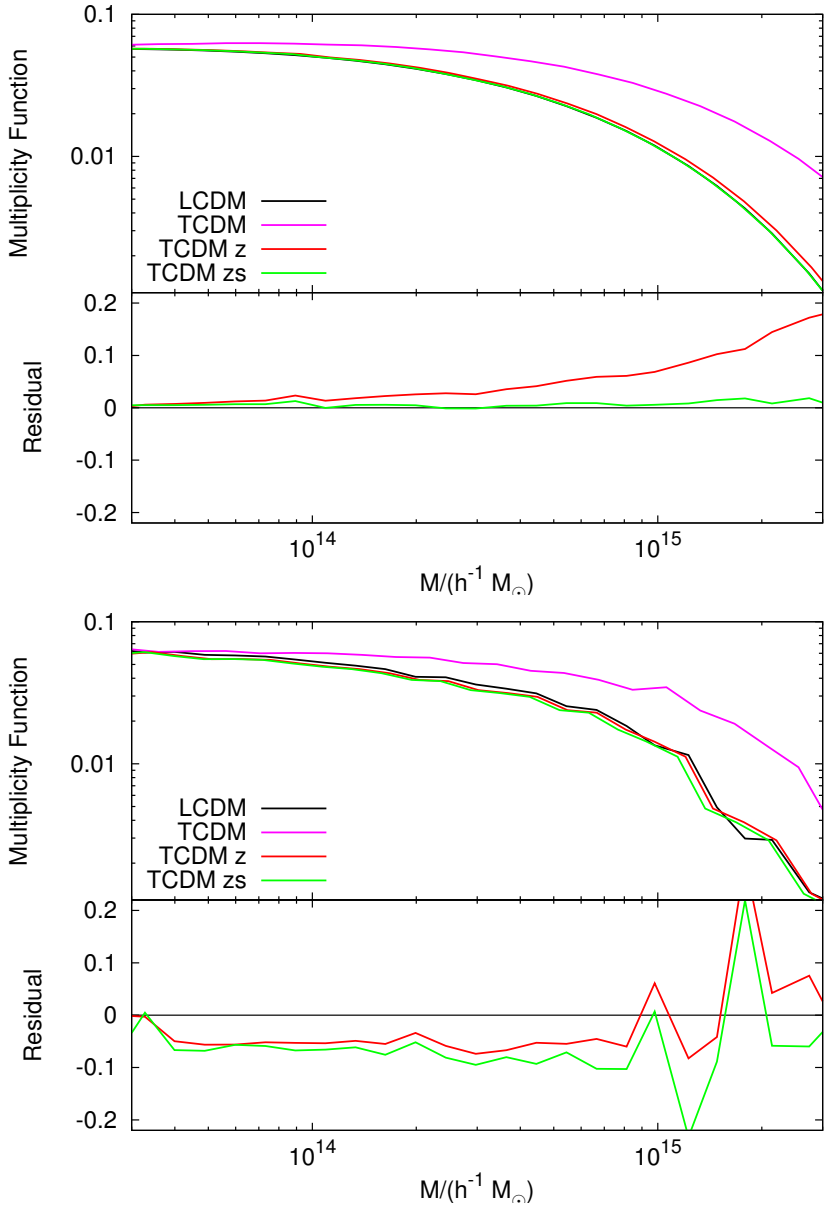

Figure 5.1: Halo mass functions before and after the scaling procedure. The top panel shows the theoretical mass function of Sheth & Tormen (1999), whereas the bottom panel shows measurements from simulations (discussed in Section 5.5). In each panel the mass functions are shown for the target ΛCDM cosmology (black); the original τCDM cosmology (pink); the effect of relabelling the redshift of τCDM (red); and the effect of then also scaling the simulation box size (green), which simultaneously changes individual halo masses. The values of the scaling parameters z and s used to achieve this are given in Table 5.2 and the details of the simulations are discussed in section 5.5. the fractional residual between the mass function in the scaled simulations and in the target cosmology is also shown; this does not vanish perfectly for the simulation data, indicating that the mass function is not perfectly universal at the few per cent level.

5.3.1 Matching the mass function

Throughout this chapter quantities in the target cosmology are denoted with primes and quantities in the original simulation are unprimed.

The AW10 algorithm first chooses a rescaling in length units of the simulation such that

$$L' = sL \tag{5.1}$$

and a rescaling in redshift so that outputs in the original simulation at redshift z are matched to a different redshift in the target simulation z'. Note that the box side, L, is measured in comoving units, so that s rescales all comoving lengths. Units of $h^{-1}\,\mathrm{Mpc}$ for L are also chosen; this is not mandatory, but it simplifies some related scalings, such as that of mass (equation 5.3). The appropriate powers of h must then be carried in the units of all quantities, such as $h^{-1}\,\mathrm{M}_\odot$.

For a given z', s and z are chosen so as to minimize the difference in the halo mass function between the two cosmologies. To achieve this the rms difference in the linear variance in density between the two cosmologies is minimized over both s and z:

$$\delta^2_{\mathrm{rms}}(s, z \mid z') = \frac{1}{\ln(R'_2/R'_1)} \int_{R'_1}^{R'_2} \frac{\mathrm{d}R}{R} \left[1 - \frac{\sigma(R/s, z)}{\sigma'(R, z')}\right]^2 \ , \tag{5.2}$$

where R'_1 and R'_2 are the radial scales, measured in the target cosmology, corresponding to the least massive and most massive haloes in the original catalogue. The radial scale R is given by the radius that would enclose a mass M in a homogeneous Universe equation (3.38). Scales in the two simulations are related by $R' = sR$; this size rescaling here thus implies a rescaling of the mass via

$$M' = s_{\mathrm{m}} M; \quad s_{\mathrm{m}} \equiv s^3 \frac{\Omega'_{\mathrm{m}}}{\Omega_{\mathrm{m}}} \ , \tag{5.3}$$

such that the total mass enclosed in the simulation volume matches the cosmological mass after the rescaling has been applied. Again note that the definition of M includes the units $h^{-1}\,\mathrm{M}_\odot$. The linear variance in over-density can be expressed in Fourier space as shown in equation (1.100).

By numerically minimising equation (5.2) over z and s one finds a rescaling such that the linear variance of the simulations are as similar as possible to each other across the range of scales that correspond to the mass range of the haloes in the original simulation. This is equivalent to minimising the difference in halo mass function because, in the simplest models, the mass function depends only on σ (Press & Schechter 1974; Sheth & Tormen 1999) as shown in the mass function in equation (3.46). However, in more complicated models, such as those with collapse thresholds that depend on environment (*e.g.* Mo & White 1996), this is no longer the case – note also that strong environmentally dependent mass functions are the case for most modified gravity theories (*e.g.* Lombriser et al. 2013a) and this should is discussed in Chapter 6.

The result of this exercise has the issue that the desired value of z will almost certainly not be one of the values stored as a simulation output; alternatively, each stored value of z

can be assigned a corresponding z', none of which will be exactly the desired target value. In practice, this is not too important: simulation outputs are used to build mock data on a light cone, which always involves some degree of interpolation between outputs. The main thing is that the grid of effective z' values is known. The problem can be eased if the outputs from the original simulation are finely spaced in redshift. It can also be an advantage to run this simulation with a high value of σ_8 or alternatively into the future (negative redshifts) in order to produce a large range in fluctuation amplitudes, as this allows the algorithm to find scalings between different cosmological parameters more easily. (*e.g.* AW10, Ruiz et al. 2011, Harker et al. 2007).

It may also be the case that, before or after remapping, the lowest mass halo in the simulation is too massive to allow generation of a realistic galaxy population. This is a problem with most simulations, where the parent haloes of dwarf galaxies lie below the resolution limit. In all cases a reconstruction algorithm is thus required in which the distribution of missing low-mass haloes is inferred from the distribution of the known haloes, such a model is presented in de la Torre & Peacock (2012) and Angulo et al. (2013a).

In Fig. 5.1 both the theoretical and measured mass functions are illustrated at various stages of the scaling process for two rather different example cosmologies. This plot makes use of simulations that are discussed in Section 5.5 and summarised in Table 5.1; briefly the two cosmologies are a vanilla ΛCDM model and τCDM, a matter only model. Theoretical agreement can be achieved almost perfectly (within 1%) by rescaling, but in the measured mass function there remains some disagreement at around the 5% level. A similar level of disagreement in the measured mass function was found by AW10 (their Fig. 7); this plausibly reflects the fact that the mass function is not perfectly universal (Tinker et al. 2008; Lukić et al. 2007; Manera et al. 2010). In principle one could minimise the difference in mass function directly, with some alternative, non-universal mass function prescription such as Tinker et al. (2008). However this is not persued here because haloes analysed as part of this work are found with a FOF algorithm and Tinker et al. (2008) was calibrated on haloes found with a SO algorithm (for examples see Knebe et al. 2011). In addition Tinker et al. (2008) focusses on a specific ΛCDM cosmology and this work considers cosmologies that depart quite dramatically from this type.

5.3.2 Matching the displacement field

The second part of the AW10 algorithm involves a shift in the individual particle positions in the rescaled simulation so as to reproduce the large-scale clustering of the target cosmology. This is achieved by taking the linear displacement field in the scaled original cosmology and then using the Zel'dovich Approximation (Zel'dovich 1970; hereafter ZA) to perturb the particle or halo positions: the phase of each mode is preserved, but the amplitude is altered to match the target power spectrum.

Rescaling to match the halo mass function in effect forces the initial simulation to take up the desired linear power spectrum in the region with $\Delta^2_{\rm lin} \simeq 1$. But in general the target

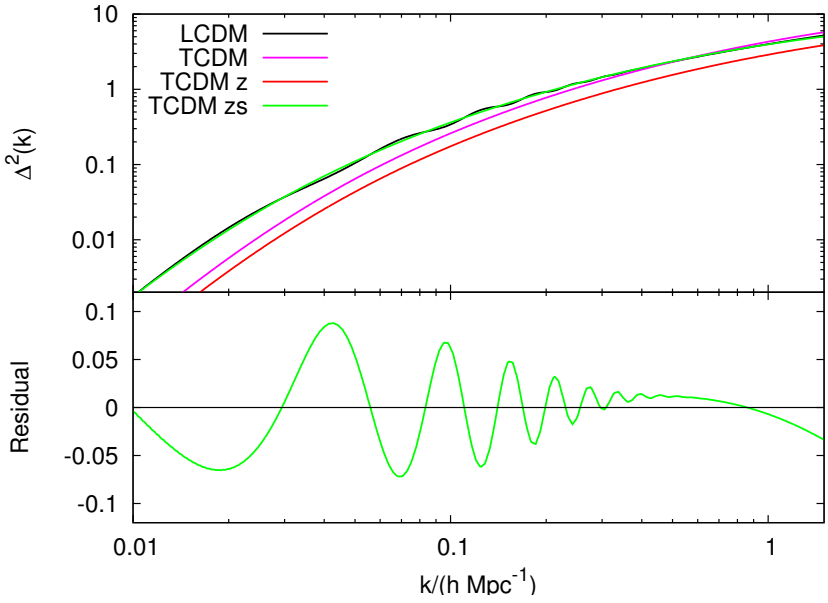

Figure 5.2: The linear power spectrum of the original and target cosmologies described in Section 5.5 at each stage of the rescaling process. The black curve shows the target ΛCDM simulation whereas the other lines show the various stages of the rescaling method: original τCDM simulation (pink); scaling in redshift (red); and scaling in redshift and size (green). The residual difference in linear power after redshift and size scaling has taken place is shown in the lower panel, this is mainly obvious as the residual wiggle which arises because there is no BAO in the τCDM model. This difference in linear power is corrected for by modifying particle positions, described in Section 5.3.2.

spectrum will not be matched on very different scales. This problem is illustrated clearly in Fig. 5.2, where the target cosmology has BAO features, whereas the original simulation adopted a zero-baryon transfer function. It is precisely these residual differences in linear power that the next part of the algorithm aims to correct by displacing particles using the ZA.

At each redshift in the target cosmology a nonlinear scale $R'_{\rm nl}$ is defined such that

$$\sigma'(R'_{\rm nl}, z') = 1 \ ; \tag{5.4}$$

all fluctuations on scales larger than this are considered to be in the linear regime. AW10 then use this to define a nonlinear wavenumber $k'_{\rm nl} = R'^{-1}_{\rm nl}$ that determines which Fourier components of the density field and displacement field are taken to be in the linear regime.

As discussed in detail in Chapter 2 the displacement field $\mathbf{f}$ is defined so as to move particles from their initial Lagrangian positions $\mathbf{q}$ to their Eulerian positions $\mathbf{x}$:

$$\mathbf{x} = \mathbf{q} + \mathbf{f} \ . \tag{5.5}$$

At linear order the displacement field is related to the matter over-density δ via

$$\delta = -\nabla \cdot \mathbf{f} \ , \tag{5.6}$$

which in Fourier space is

$$\mathbf{f_k} = -i\frac{\delta_\mathbf{k}}{k^2}\mathbf{k} \ . \tag{5.7}$$

If the displacement field in the original simulation is known, then an additional displacement can be specified in Fourier space to reflect the differences in the linear matter power spectra between the two cosmologies:

$$\delta\mathbf{f}_{\mathbf{k}'} = \left[\sqrt{\frac{\Delta'^2_{\rm lin}(k',z')}{\Delta^2_{\rm lin}(sk',z)}} - 1\right]\mathbf{f}_{\mathbf{k}'} \ , \tag{5.8}$$

where $\mathbf{f}$ is measured in the original simulation after it has been scaled. Equation (5.7) is only valid for the linear components of both fields, so in practice the displacement field must be smoothed with a window of width the nonlinear scale R_{nl}.

In AW10 the authors saved the initial displacement field of the simulation and so equation (5.8) could be used directly to make the required modification of the particle positions. But in the next Section it is shown how the displacement field can be reconstructed directly from the distribution of haloes in the original simulation.

5.4 Recasting haloes

The AW10 algorithm produces a new particle distribution, but many practical applications would need to seed this density field with galaxies, for which the first step is locating the dark matter haloes. This takes time, and will also yield incorrect results since the density field is not correct on the smallest scales (*i.e.* the internal halo properties should change as a result of the altered cosmology). For both these reasons it makes sense to work directly with the halo catalogue. Therefore, in this section, it is shown how both the halo catalogue itself can be used to recover the large-scale displacement field (if it is not provided), and how the halo internal strucuture should be changed after the simulation has been remapped.

5.4.1 Reconstruction of displacement fields

Following Eisenstein et al. (2007), the displacement field can be obtained from the over-density field using equation (5.7). This result can be used if the matter over-density field from the haloes is constructed, noting that haloes are biased tracers of the mass distribution. In this work density fields are constructed on a mesh with m^3 cells by a NGP mass assignment scheme. Cubic binning is corrected for by deconvolution. The over-density of haloes $\delta_{\rm H}$ is related to the matter over-density via the bias b:

$$\delta_{\rm H} = b\delta \ , \tag{5.9}$$

where the bias can, in principle, be a function of mass and other halo properties.

Throughout this work the mass function of Sheth & Tormen (1999) is used (equation 3.46). Although more up to date mass functions exist in the literature (Warren et al. 2006; Peacock

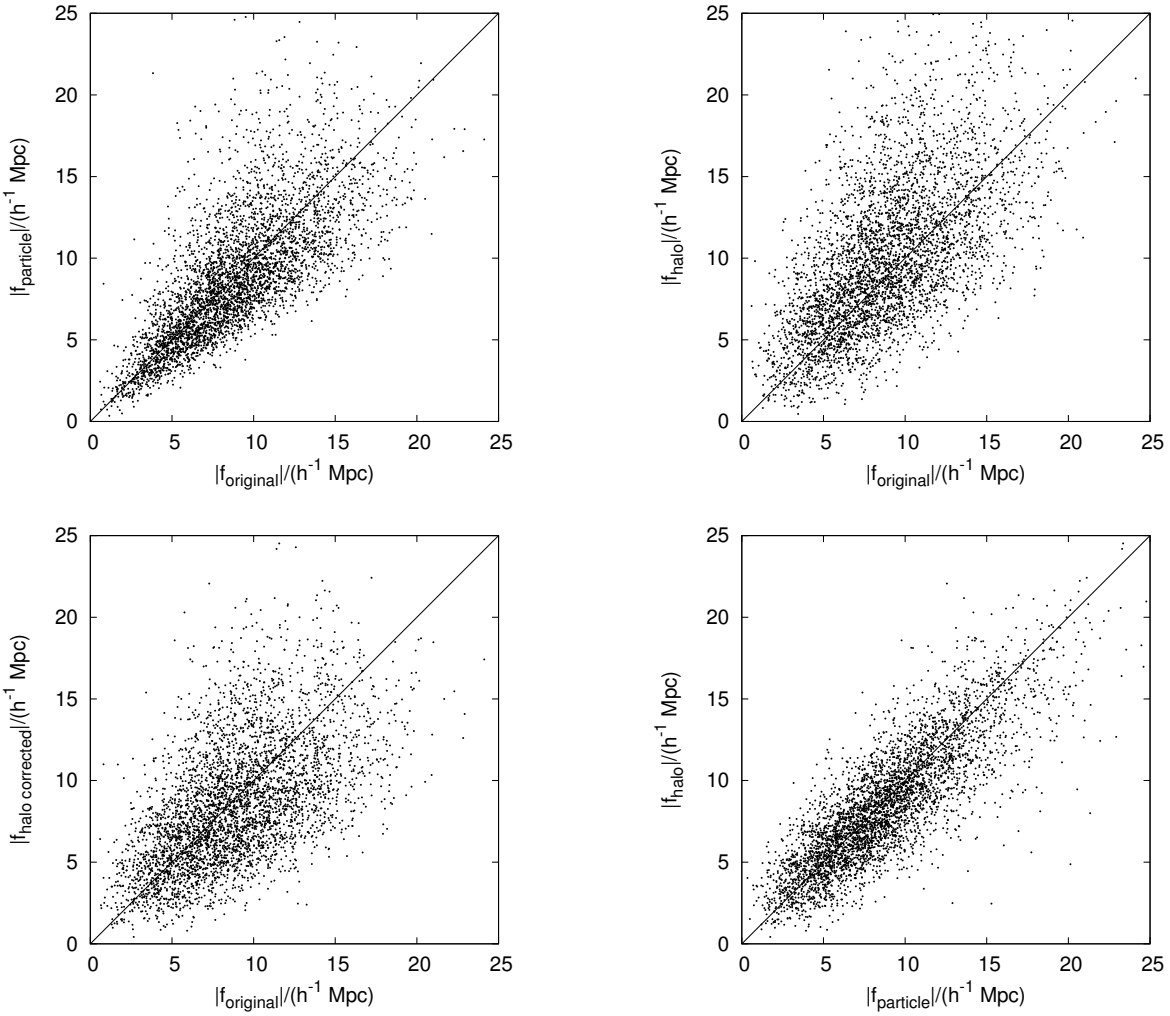

Figure 5.3: A comparison of the values of the linear displacement fields reconstructed from a scaled (in s and z' by the first part of the method) τCDM simulation (see Section 5.5). The displacement field is calculated from the density field using equation (5.7) and debiased in the case of haloes using equation (5.9). The points show values of the fields in cells for a randomly selected subset (1%) of cells measured on a 75^3 mesh and convolved with a Gaussian to filter out the nonlinear components. The top left panel shows the displacement reconstructed from the particles compared to the original displacement field used to run the simulation. The top right panel shows the same thing but for the displacement field recovered from the debiased halo field. The lower left panel shows the halo displacement field corrected according to equation (5.13) so as to have the correct theoretical variance. The bottom right panel shows a comparison between this corrected displacement field from haloes and the field from the particles.

2007; Reed et al. 2007; Tinker et al. 2008) that of Sheth & Tormen (1999) was chosen because it was calibrated to simulations that cover a greater range of cosmological parameter space than more modern ones. Given a mass function, an analytic expression for the linear halo bias can be derived via the peak-background split formalism as discussed in Section 3.6. The bias formula associated with the mass function of Sheth & Tormen (1999) is given in equation (3.50).

In order to calculate the over-density field from halo catalogues a halo-number weighted 'effective' bias is taken for the haloes in the catalogue based on the theoretical models given above in equations (3.46) and (3.50):

$$b_{\rm eff} = \frac{\int_{\nu_{\rm min}}^{\nu_{\rm max}} {\rm d}\nu\, b(\nu) f(\nu)/m}{\int_{\nu_{\rm min}}^{\nu_{\rm max}} {\rm d}\nu\, f(\nu)/m} \ , \tag{5.10}$$

where $\nu_{\rm min}$ and $\nu_{\rm max}$ are the value of ν for the least massive and most massive halo in the original simulation.

Nonlinearities in the recovered matter over-density field are limited by convolving the field with a Gaussian whose width is set equal to the nonlinear scale $R_{\rm nl}$, which can then be converted to a displacement field using equation (5.7). The method then proceeds exactly as in AW10: haloes in the original simulation are moved from their old positions $\mathbf{x}$ to new positions $\mathbf{x}'$ using the small displacements implied by equation (5.8)

$$\mathbf{x}' = \mathbf{x} + \delta\mathbf{f} \ , \tag{5.11}$$

which follows from equation (5.5) given that initial positions $\mathbf{q}$ are preserved before and after this final stage of the algorithm. In Fig. 5.3 the displacement fields as predicted from the particle data and from halo catalogues in the simulation are shown (see Section 5.5). The top left panel shows a comparison between the displacement field reconstructed from the particle distribution with that generated for the simulation initial conditions and one can see that the reconstructed field shows no obvious bias compared to the original fields, although there is some scatter. The top right panel then shows the displacement field measured from debiasing the halo density field which shows a small residual bias when compared to the original field. This residual effect possibly reflects a failure of the peak-background bias calculation in the quasilinear regime. In any case, though, the true expected variance in the smoothed displacement can be calculated (*e.g.* Crocce & Scoccimarro 2006):

$$\sigma_f^2(R_{\rm nl}) = \frac{1}{3}\int_{k_{\rm box}}^{\infty} \frac{e^{-k^2 R_{nl}^2}\Delta^2_{\rm lin}(k)}{k^2}\, {\rm d}\ln k \ , \tag{5.12}$$

where $k_{\rm box} = 2\pi/L$ is the fundamental mode of the simulation. The displacement fields can therefore be scaled such that they have the desired variance:

$$\mathbf{f} \to \mathbf{f}\, \frac{\sigma_f(R_{\rm nl})}{\sqrt{{\rm Var}(|\mathbf{f}|)}} \ , \tag{5.13}$$

where ${\rm Var}(|\mathbf{f}|)$ is the measured variance in $|\mathbf{f}|$. The result of this scaling can be seen in the bottom left panel of Fig. 5.3 where there is now better agreement with the original displacement

field. The bottom right panel shows a comparison between the reconstructed displacement field from particles and from haloes where there is no obvious disagreement. This shows that the new method is able to make a reasonable reconstruction of the full simulation displacement field using only the halo catalogue.

One should note that, for a population of lower mass haloes, the value of $b_{\rm eff}$ could be less than one and an implementation of equation (5.9) could then result in cells with negative densities ($\delta < -1$). However, the reconstruction method was checked for a small volume simulation with a population of low mass haloes with $b_{\rm eff} \approx 0.83$ and found that it still works as well in reconstructing the displacement field, even though it goes through the unphysical negative density step.

5.4.2 Mass-dependent halo displacements

When dealing with the displacement field of haloes, some care is needed in ensuring that these objects display the correct degree of bias as a function of mass. Writing the matter density fluctuation in terms of the displacement field, the linear halo bias relation is

$$\delta_{\rm H} = -b(M)\nabla \cdot \mathbf{f} \ , \tag{5.14}$$

which says that in effect haloes of different masses are displaced by different amounts. This seems to violate the equivalence principle, and of course all particles in a simulation should share the same displacement field. But this displacement field then affects halo formation in a nonlinear way, which is not allowed for if subsequently the displacement field is changed 'by hand'. In order to obtain the correct statistics of large-scale clustering, the above mass dependence of the effective additional displacement must therefore be respected. To see how the argument works in an extreme case, imagine applying the AW10 method to a simulation with zero-large-scale power. Adding in the large-scale displacement field will then by construction yield a set of haloes that have $b = 1$, independent of mass. In order to avoid this unrealistic situation, a mass-dependent displacement must be applied, as in equation (5.14).

This argument reveals a subtle limitation of the original AW10 prescription. One can assume that applying a halo finder to a particle distribution that has been subject to the AW10 method will find very much the same haloes as if these were identified prior to the additional displacement, because these displacements are coherent over large scales. These haloes will thus fail to have the correct dependence of clustering on mass. In this respect, this approach is not simply faster than AW10, but working directly with haloes allows a treatment of mass-dependent biasing that is more consistent than can be achieved by scaling the particle distribution alone.

In practice one could bin haloes of differing masses and compute the displacement field for each mass bin individually, thus avoiding the issue of debiasing the over-density and then rebiasing the displacement field. However it was chosen to use the full halo catalogue to produce

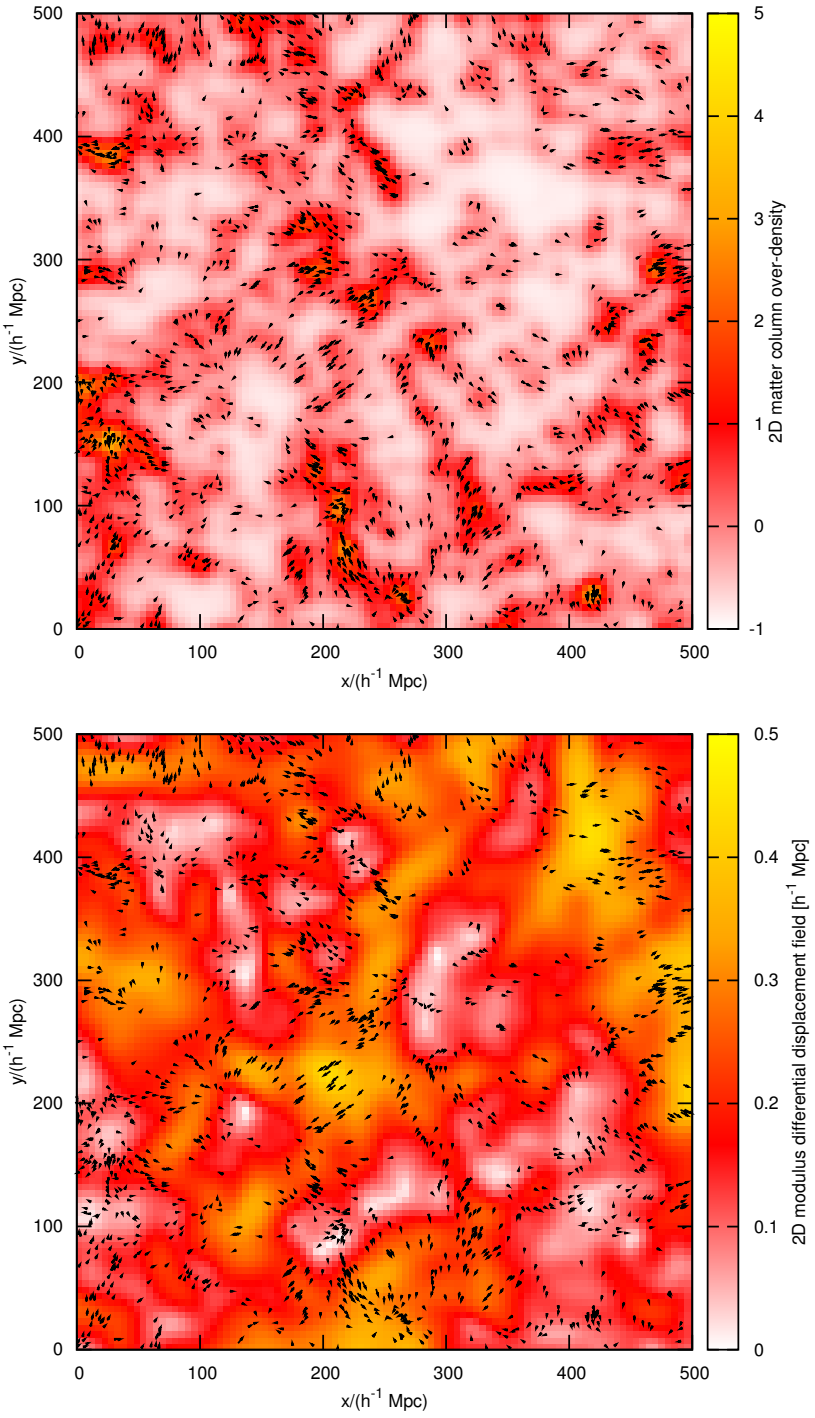

Figure 5.4: A visual summary of the rescaling method. The top panel shows the projected linearized over-density field in a slice of thickness $50\,h^{-1}\,\mathrm{Mpc}$ inferred from the distribution of haloes in the size and redshift scaled τCDM simulation (described in Section 5.5) and the bottom panel shows the magnitude of the linearized differential displacement field inferred from the over-density. In each plot the arrows then show the flow of haloes due to the differential displacement field in order to match the clustering in the target ΛCDM cosmology. The displacements are typically small in the method and the arrows in these plots have been enlarged by a factor of 10 to illustrate the halo flow more clearly.

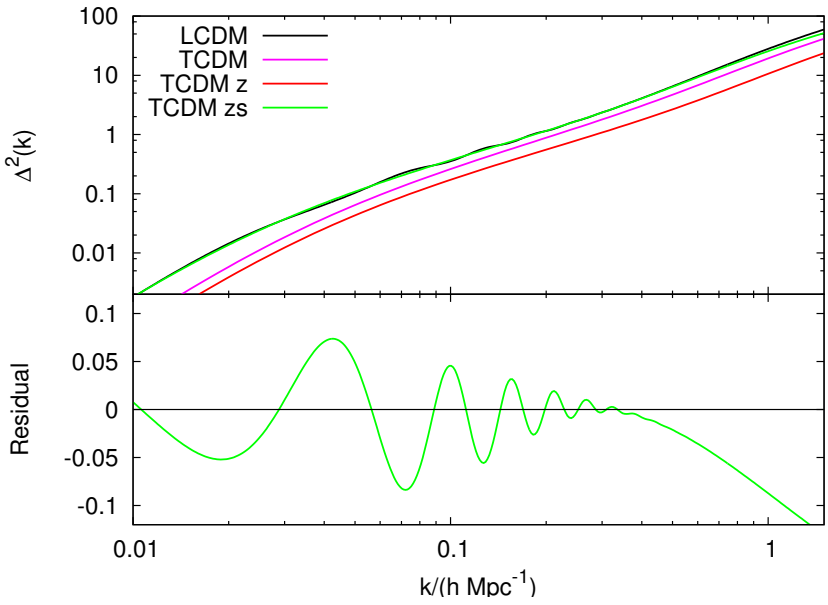

Figure 5.5: Predicted differences for the full matter power spectrum given by the calibrated halo model, discussed in the previous chapter, after the size and redshift scaling of the AW10 method has been implimented. The original model TCDM (pink) is first scaled in redshift (red) and then has dimensions reinterpreted (green) to best match the target LCDM (black). The AW10 displacement field step will recifty the mis-match at linear scales, which is mainly the difference in BAO feature. The discrepancy seen at small scales in the halo model implies that remaning differences are due to halo internal structure and thus provides justification for modifying the halo internal properties. The models shown here are the ones simulated in the next section.

the least noisy displacement field possible and then to move haloes of different masses by different amounts according to equation (5.14).

A visual summary of this method as applied to halo catalogues is given in Fig. 5.4, in which the density and displacement fields as calculated from the halo distribution are shown together with the flow of haloes that these fields imply for the two different cosmologies.

5.4.3 Reconstitution of haloes

The AW10 method reproduces the mass function and linear clustering of the target cosmology, albeit with the small error in mass-dependent halo biasing described above. But in addition, the AW10 approach does not address the deeply nonlinear clustering that arises due to correlations within individual haloes. In Halo Occupation Distribution (HOD) models, galaxies are taken to be stochastic tracers of the mass field around haloes; in order to use rescaling for generation of mock galaxy catalogues, it is therefore necessary to produce the mass field around haloes in a way that reflects the new cosmology. This is also of interest in its own right for applications such as ray-tracing simulations (*e.g.* Kiessling et al. 2011) for gravitational lensing.

Fig. 5.5 shows the predicted power spectrum of the calibrated halo model, discussed in the previous chapter, for the rescaling of a cosmology. One can see that the match at linear scales is good after a rescaling in redshift and size, and one can hope that the displacement field step of the AW10 method could rectify the residual BAO difference seen. The differences at non-linear scales ($k > 0.15\,h\,\mathrm{Mpc}^{-1}$) are mainly due to differences in halo internal structure and thus one can hope that the match may be improved by modifying the haloes directly.

This issue is addressed by methods of 'reconstitution' and 'restructuring' where the mass distribution around the final set of haloes is calculated by considering how their internal structure should depend on cosmology. Haloes are defined as spherical objects that have an average over-density with respect to the matter in the background Universe of $\Delta_{\rm v} \simeq 200$. The use of a fixed density contrast at virialization is motivated by consistency with halo finding methods such as FOF. The exact value of $\Delta_{\rm v}$ (motivated by the spherical collapse model) is not critical. The virial radius $r_{\rm v}$ for a halo of mass M is defined to be

$$r_{\rm v} = \left(\frac{3M}{4\pi\Delta_{\rm v}\bar{\rho}}\right)^{1/3} . \tag{5.15}$$

Although haloes have been defined to have a fixed virial radius for a given mass, the concentration of haloes (ratio of virial radius to internal characteristic radius) does vary as a function of cosmology and this can be accounted for, as discussed in Chapter 3. This can be traced to the haloes having different collapse redshifts, via the differing growth rate of perturbations (Navarro et al. 1997; Bullock et al. 2001; Eke et al. 2001).

The full cosmology dependent concentration relations of Bullock et al. (2001) are used here (equations 3.29 and 3.30). However these were calibrated using haloes whose virial radius was defined to vary as a specific function of cosmology according to the spherical model approximation of Bryan & Norman (1998):

$$\Delta_{\rm v}^{\rm B}(z) = \frac{178 - 82[1-\Omega_{\rm m}(z)] - 39[1-\Omega_{\rm m}(z)]^2}{\Omega_{\rm m}(z)} . \tag{5.16}$$

In the case here one should modify the Bullock et al. (2001) value for the concentration at given mass: The linking length $b = 0.2$ used by the FOF algorithm in this work corresponds approximately to $\Delta_{\rm v} = 178$ (for a perfect, spherical isothermal halo). Linking lengths can be approximately converted into halo over-densities via equation (2.23). In this work haloes are defined to have a constant virial overdensity so the concentrations will necessarily be different to those in Bullock et al. (2001) and the above equation must be used to convert the concentration relations of Bullock et al. (2001) to those for haloes with a virial radius independent of cosmology. This can be done assuming that the halo scale radius should remain unchanged as definitions of the halo boundary are changed,

$$\left[\ln(1+c) - \frac{c}{1+c}\right] = \frac{\Delta_{\rm v}}{\Delta_{\rm v}^{\rm B}}\frac{c^3}{c_{\rm B}^3}\left[\ln(1+c_{\rm B}) - \frac{c_{\rm B}}{1+c_{\rm B}}\right] . \tag{5.17}$$

Two options are available: If the full particle data are available one could restructure the particles in haloes, alternatively one could reconstitute the haloes from scratch, this is necessary

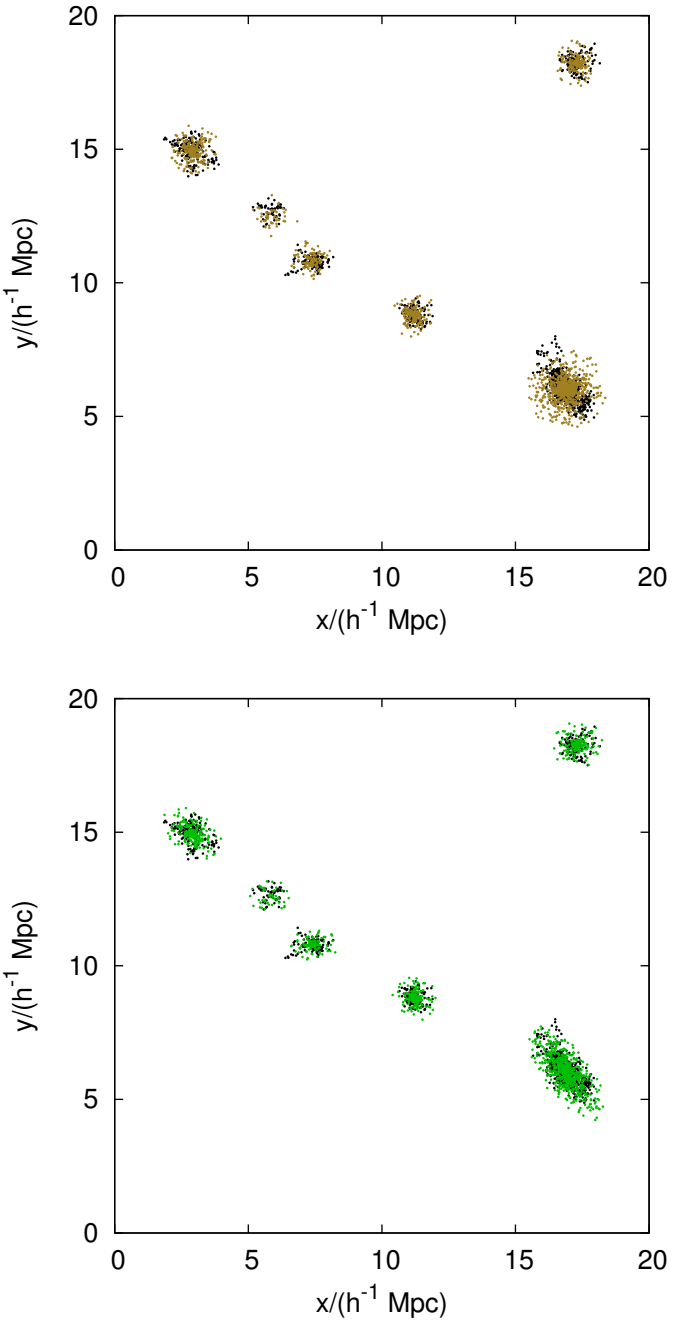

Figure 5.6: The particles in a small cube of the τCDM simulation of side length $20\,h^{-1}$ Mpc that were grouped into haloes by a FOF algorithm are shown in black. In the top panel overplotted in brown are reconstituted spherical NFW haloes; in the bottom panel reconstituted aspherical NFW haloes are shown in green, and these clearly match the haloes in the simulation much better.

if only the centre of mass (CM) and halo mass information is available. To 'restructure' haloes one would do this so as to account for the change in halo concentrations for haloes of a fixed virial radius. For an NFW halo the fraction of mass f enclosed at a radius r is given by

$$f(r) = \frac{\ln(1+rc/r_{\rm v}) - rc/r_{\rm v}/(1+rc/r_{\rm v})}{\ln(1+c) - c/(1+c)} \ , \tag{5.18}$$

so that $f(r_{\rm v}) = 1$. In order to modify halo concentrations appropriately for the new cosmology one must compute the radius of the particle from the halo centre r and reassign it to r' via

$$r' = f^{'-1}[f(r)] \tag{5.19}$$

where f^{-1} signifies the inverse function of f. Halo particle positions, relative to the CM, can then reassigned via

$$\mathbf{x} \rightarrow \mathbf{x}' = \frac{r'}{r}\mathbf{x} \ . \tag{5.20}$$

The second approach is to use the full halo information to reconstitute the particles contained in each halo by calculating the virial radius and concentration parameter for each halo in the catalogue and then filling up the density profile around the halo by a random sampling of tracer particles which correspond to those in the original simulation. A pictorial representation of this is shown in Fig. 5.6 where haloes measured in a simulation with a FOF algorithm (see Section 5.5) are shown together with those reconstituted using the halo catalogue generated from this distribution.

The top panel of Fig. 5.6 shows that 'real' haloes are often far from spherical, so it is better to reconstitute them as triaxial objects. This can be done using the moment of inertia tensor

$$I_{ij} = \sum_{k=1}^{N} (x_{k,i} - \bar{x}_i)(x_{k,j} - \bar{x}_j) \ , \tag{5.21}$$

where $k \in \{1, ..., N\}$ and there are N particles in each halo and $i, j \in \{1, 2, 3\}$ and label coordinates. In this work haloes contain 100 particles or more which was considered to be adequate for estimating this tensor. Diagonalising this tensor provides the axis ratios of the halo (via the eigenvalues) and the orientation of the halo (via the eigenvectors). The eigenvalues and eigenvectors are stored when the halo catalogue is generated from the particle distribution. Asphericity is then restored to the haloes by distorting them once they have been generated by the spherical halo reconstitution process described above. If the square roots of the eigenvalues are a, b and c then each coordinate of the reconstituted halo in the CM frame is modified according to

$$\begin{aligned} x_i &\rightarrow 3ax_i/(a+b+c) \ , \\ y_i &\rightarrow 3by_i/(a+b+c) \ , \\ z_i &\rightarrow 3cz_i/(a+b+c) \ . \end{aligned} \tag{5.22}$$

The prescription $x \rightarrow ax/(abc)^{1/3}$ *etc.* was also considered but this was found not to work as well in recovering the shapes of aspherical haloes. The CM position vector of each halo particle can then be rotated by the inverse matrix of eigenvectors in order to orient the halo correctly.

In the top panel of Fig. 5.7 the power spectrum of the particles in haloes is shown after they have been reconstituted from a halo catalogue, and this is compared to the power spectrum of the particles in haloes in the original simulation that was used to create the catalogue. Clearly the clustering will agree on large scales, but it is satisfying to see that the power spectrum of the particles in haloes can be reproduced by generating NFW haloes even out to relatively small scales ($k \simeq 1\,h\,\mathrm{Mpc}^{-1}$). One can see that there is also a significant improvement in the matching of the clustering gained by reconstructing aspherical haloes rather than purely spherical ones.

The final idea considered is a method of 'regurgitation', in order to recreate the full mass distribution in the best possible way. Once the original AW10 algorithm has been applied to a full particle distribution, haloes are then selected and removed from the particle distribution and then reconstituted in the same way as described above. These reconstituted haloes, with the correct internal structure for the new cosmology, are then reinserted into the rescaled mass distribution in order to produce a corrected full particle distribution for the new cosmology. In doing this the problem of discontinuities between the reconstituted halo and the surrounding material is avoided by using a constant Δ_v for haloes so that they have identical virial radii independent of cosmology. One should note that a limitation of this approach is that all particles in the simulation are moved according to the same displacement field and so haloes are not subject to the biased displacements discussed in Section 5.4.2. This is a general limitation of the AW10 method when one deals with the particle distribution rather than the halo distribution.

The lower panel of Fig. 5.7 shows the full matter power spectrum measured in a perfect test case where no rescaling has taken place. Haloes have been identified with a FOF algorithm and removed from the particle distribution. This halo catalogue is then used to reconstitute haloes and these are then regurgitated back into the surrounding particle distribution of the simulation. The power spectrum is able to be recreated perfectly up to $k = 1\,h\,\mathrm{Mpc}^{-1}$ where deviations arise, possibly due to lack of substructure or imperfect concentration relations in the reconstituted haloes. If the data are available, it is possible to improve this situation by using the exact 3D particle distribution of the haloes, and scaling radii according to the different concentrations in the two cosmologies.

5.4.4 Scaling velocities

All the discussion so far has been in configuration space. But galaxy surveys inhabit redshift space, in which the clustering signature is modified by peculiar velocities ($\mathbf{v} \equiv a\dot{\mathbf{r}}$ where $\mathbf{r}$ is the comoving position). This distortion is well-known to be an invaluable source of additional cosmological information, giving direct access to the growth rate of density perturbations (Kaiser 1987; Reid et al. 2012). A discussion on how to scale particle and halo velocities is therefore given.

The main element of scaling of velocities in cosmological simulations is explained in Section 15.7 of Peacock (1999). Since a computational volume has no knowledge of the physical size

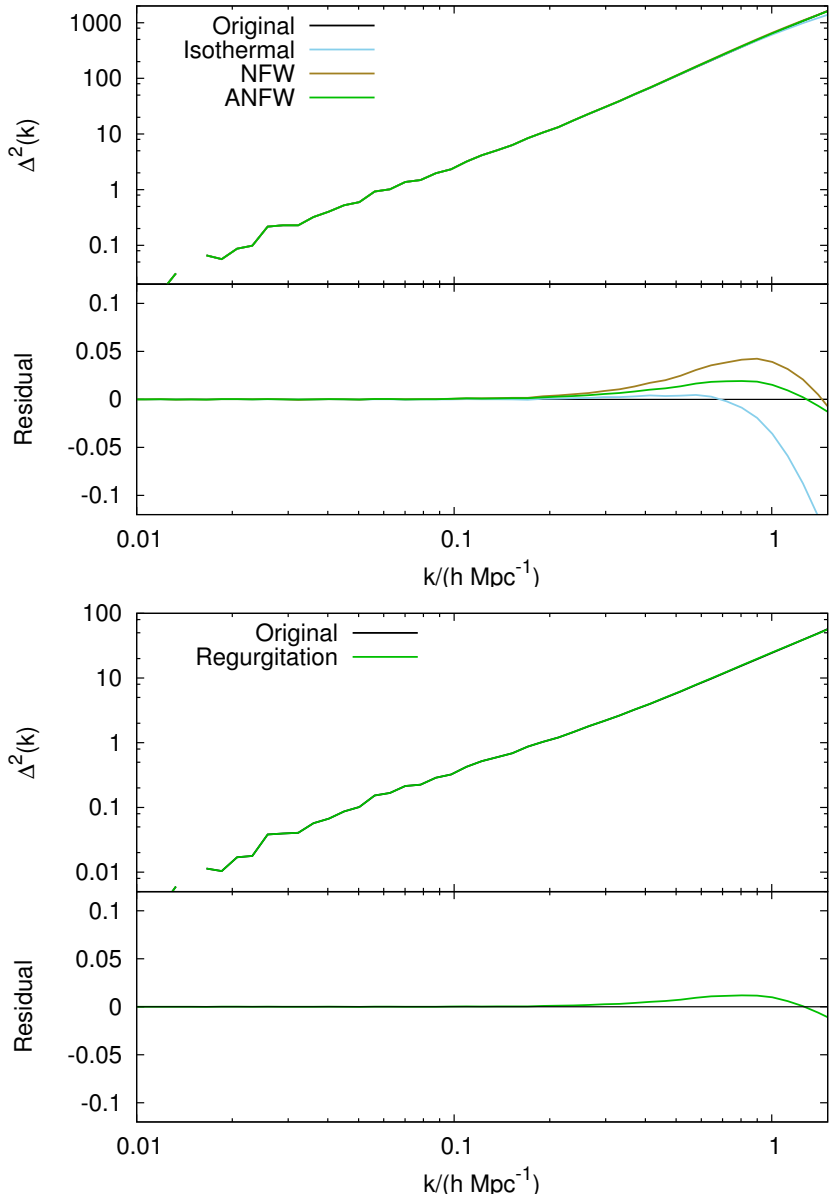

Figure 5.7: The top panel shows the power spectra of particles in haloes. The spectra of the particles in the original haloes in the ΛCDM simulation (black) are shown together with the power of spherical (brown) and aspherical (green) NFW haloes generated from the halo catalogue via the halo reconstitution process described in the text. There is a clear improvement in the match of the power spectra gained from using aspherical rather than spherical haloes. Also shown for comparison is the power spectrum for a more unrealistic halo: the singular isothermal sphere (blue); this fails to match the target even at fairly large scales. In the lower panel the full matter power spectrum is shown after reconstituted aspherical haloes have been regurgitated back into the parent particle distribution. One can see the match is essentially perfect to around $k = 1\,h\,\mathrm{Mpc}^{-1}$. The 5% drop in power at smaller scales in both panels may reflect either imperfect concentration relations or lack of halo substructure in the reconstitution.

that it is intended to represent, the natural measure of velocity is $\mathbf{U} \equiv \mathbf{v}/HaL$, *i.e.* peculiar velocity in units of expansion across the box (whose proper size is aL). According to the Zel'dovich approximation, $\mathbf{U}$ is equal to the displacement field in units of the box size, times the logarithmic growth rate $f_{\rm g} \equiv {\rm d}\ln\delta/{\rm d}\ln a \simeq \Omega_{\rm m}^{0.55}(a)$ (where the latter approximation applies for a flat Λ-dominated model). In other words, for two simulations that have identical fluctuation spectra in box units (which is exactly true by definition in reinterpreting an original simulation output), one would expect the value of $\mathbf{U}$ to be unaffected by a change in cosmology, apart from the alteration in $f_{\rm g}$. The recipe for rescaling large-scale peculiar velocities is thus

$$\mathbf{v}' = s\frac{H'f_{\rm g}'a'}{Hf_{\rm g}a}\mathbf{v} \ . \tag{5.23}$$

This argument does not apply on small scales, where velocities are due predominantly to bound motions in haloes. But the error is not large: according to the 'cosmic virial theorem' of Section 75 of Peebles (1980), the pairwise peculiar velocity dispersion for a given level of mass clustering scales as $\Omega_{\rm m}^{0.5}$. Therefore, simply rescaling the velocities according to linear theory would give a result in error on small scales by only about 7%, even when rescaling from $\Omega_{\rm m} = 1$ to $\Omega_{\rm m} = 0.25$.

However, the above scaling does not account for the large-scale modifications to displacement fields as discussed in Section 5.3.2. in the Zel'dovich approximation, peculiar velocities are assigned to particles by

$$\mathbf{v} = aHf_{\rm g}\mathbf{f} \ , \tag{5.24}$$

additional differential changes on the peculiar velocities of particles can therefore be imposed via

$$\delta\mathbf{v}_{\mathbf{k}'} = a'H'f_{\rm g}'\left[\sqrt{\frac{\Delta_{\rm lin}'^2(k',z')}{\Delta_{\rm lin}^2(sk',z)}} - 1\right]\mathbf{f}_{\mathbf{k}'} \ . \tag{5.25}$$

In this and the earlier discussion, it should be kept in mind that the velocities are in proper units, but $\mathbf{f}$ is a comoving displacement field; this accounts for the extra factor of a. Note that this additional velocity is applied independent of halo mass, unlike the mass-dependent displacement discussed earlier. The latter step was needed to preserve the mass-dependent biasing, but velocities of haloes have no such mass dependence. Therefore, in effect, it is necessary to break the Zel'dovich approximation in order to ensure correct large-scale statistics.

More normally, one might lack any internal halo velocity data, in which case the velocities would need to be generated by hand. The simplest approximation would be to assume isothermal and isotropic orbits; this is not consistent, and more detailed modelling could be carried out based on the Jeans Equation, together with assumptions about orbital anisotropy. But for the present, this work shall go no further than noting that virial equilibrium and isotropy yields an rms line-of-sight velocity dispersion for an NFW halo of

$$\begin{aligned}\sigma_v^2 &= \frac{GM}{3r_{\rm v}}\,\frac{c[1-1/(1+c)^2-2\ln(1+c)/(1+c)]}{2[\ln(1+c)-c/(1+c)]^2} \\ &\simeq \left[\frac{2}{3}+\frac{1}{3}\left(\frac{c}{4.62}\right)^{0.75}\right]\frac{GM}{3r_{\rm v}} \ .\end{aligned} \tag{5.26}$$

This can be compared with $\sigma_v^2 = GM/3r_{\rm v}$ for the truncated singular isothermal sphere. Equation (5.26) with $\Delta_{\rm v} = 200$ was found to under-predict halo velocity dispersions in ΛCDM simulations by a factor of around 1.07, implying that $\Delta_{\rm v} \simeq 300$ would be a better practical choice for this application. If haloes are identified after rescaling in the particle distribution, and then subsequently restructured, their internal velocities can be altered by the ratios of $\sigma_{\rm v}$ in the above equation.

If a halo catalogue is being rescaled then either equation (5.26) can be used to generate velocity dispersions for reconstituted halo particles, or if a halo velocity dispersion is included in a catalogue, then a scaled dispersion can be used directly to reconstitute halo particles. Because the dispersion is approximately

$$\sigma_v^2 \approx \frac{GM}{r_{\rm v}} \ , \tag{5.27}$$

and $M' = s^3 M(\Omega'_{\rm m}/\Omega_{\rm m})$ and $r'_{\rm v} = sr_{\rm v}$ the approximate correct scaling for σ_v must be $\sigma'_v = s\sigma_v\sqrt{\Omega'_{\rm m}/\Omega_{\rm m}}$. This is the prescription used in this work, although note that equation (5.26) suggests that there should be some mild concentration dependence to this rescaling relation and so a more accurate proceedure may be to include this in the rescaling.

This is shown in a perfect test case scenario when reconstituted haloes with Gaussian velocity dispersions are compared to their original counter parts in redshift-space via the power spectra in Fig. 5.8. One can see that the match is good when using the theoretical dispersions but that it is essentially perfect when using catalogued dispersions at the level of the monopole. By comparing the top and bottom panels of Fig. 5.8 one can see that the monopole agreement can be partially the result of a cancellation of positive and negative effects for k modes with differing orientations but one can see that the full redshift-space match is generally good for reconstituted haloes, particularly in the case that the true dispersion is used if that is catalogued.

5.4.5 Method summary

Here a brief summary of a practical implementation of the method for use on a halo catalogue is provided:

1. Calculate z and s by minimising equation (5.2) over the mass range of haloes in the original halo catalogue.
2. Calculate the effective bias for the haloes using equation (5.10).
3. Calculate the matter over-density field implied by the halo catalogue, taking care to debias the halo field appropriately.
4. Linearize the matter over-density field using a Gaussian with width of the nonlinear scale, defined in equation (5.4).
5. Compute the displacement field from the over-density field using equation (5.7) and then correct this so that it has the correct theoretical variance using equation (5.13).

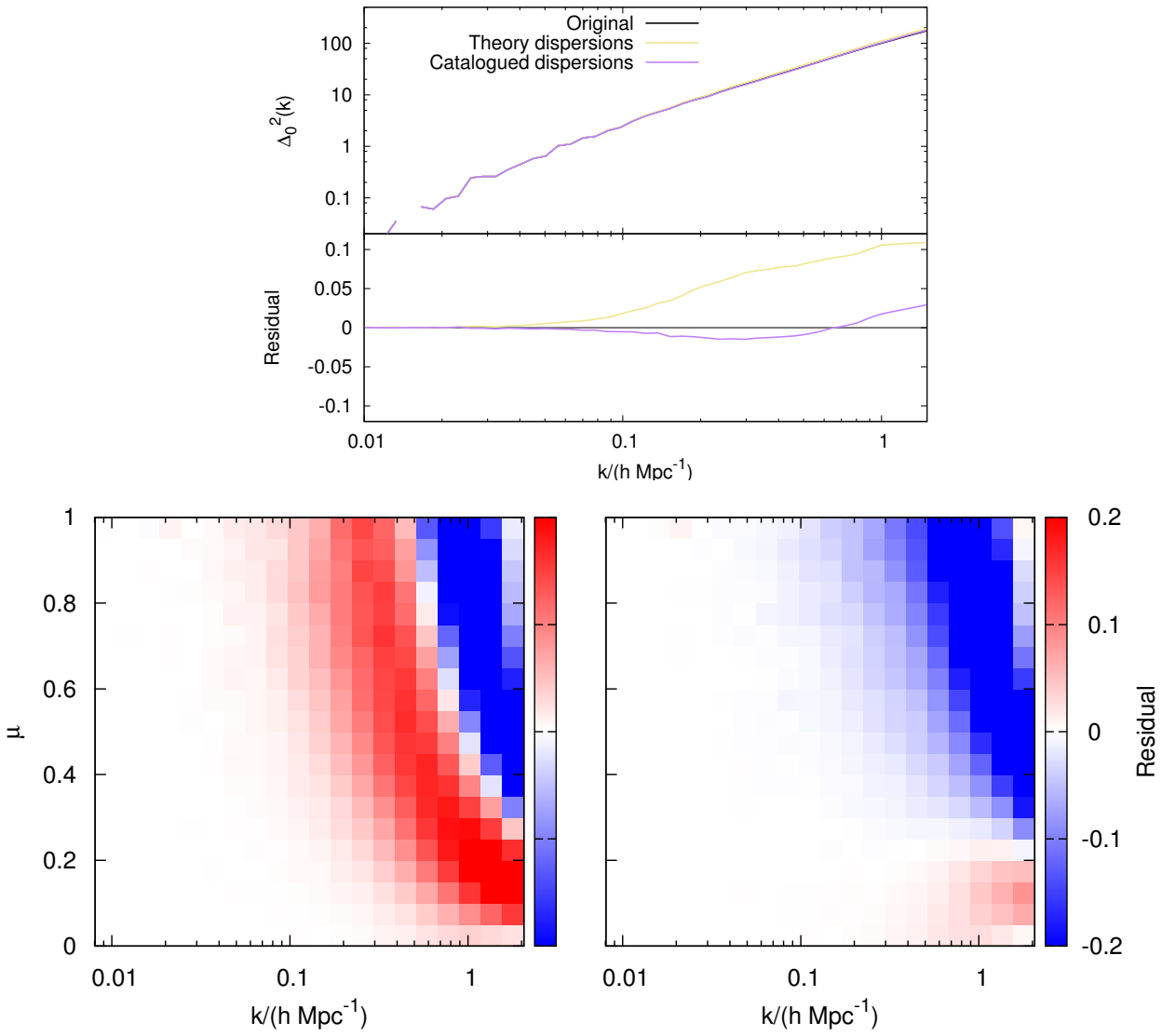

Figure 5.8: The redshift-space monopole power spectrum of particles in reconstitued haloes. The spectrum of the particles in the original haloes in the ΛCDM simulation (black) is shown together with the power of aspherical reconstituted haloes with theoretical Gaussian dispersions for NFW haloes (yellow) and Gaussian dispersions measured in the halo catalogue (purple). There is a clear improvement in the match of the power spectra gained from using catalogued dispersions rather than theoretical ones with the match to the original halo particles being essentially perfect across the range of k shown when catalogued dispersions are used. The match is worse, but not significantly, if spherical, rather than aspherical, NFW haloes are used. The lower two panels show the residuals in the full redshift space plane from using theoretical dispersions (left) and catalogued dispersions (right). Here one can see that the good agreement at the level of the monopole mainly stems from the errors redshift space in the catalogued case coming from high μ modes at high k that contribute less to the high k monopole power.

Simulation	L	Ω_m	Ω_Λ	Ω_b	h	σ_8	n_s	Γ
ΛCDM	$780\,h^{-1}\,\mathrm{Mpc}$	0.25	0.75	0.045	0.73	0.9	1	-
τCDM	$500\,h^{-1}\,\mathrm{Mpc}$	1	0	-	0.5	0.8	1	0.21

Table 5.1: Cosmological parameters for the simulations used in this work. As a 'target' a ΛCDM model with a WMAP1 type cosmology is used and as an 'original' model a matter only model with a DEFW (Davis et al. 1985) spectrum is simulated with a similar spectral shape ($\Gamma = 0.21$) to that of the ΛCDM model but that lacks a BAO feature. Each simulation ran with 512^3 particles, gravitational forces were softened at $20\,h^{-1}\,\mathrm{kpc}$ and initial conditions generated using `N-GenIC` on an initial glass load at a starting redshift $z_\mathrm{i} = 199$.

6. Taking the original catalogue at redshift z, relabel positions of haloes according to equation (5.8). This new catalogue can then be interpreted as a catalogue of haloes in the target cosmology at redshift z', complete with new halo properties.

7. If desired, reconstitute the particles in haloes using the method detailed in Section 5.4.3 and 5.4.4.

5.5 Simulations

The method is illustrated using a matched set of simulations and the halo catalogues generated from them. The simulation parameters are given in Table 5.1. The 'target' simulation ΛCDM is a WMAP1 style cosmology (Spergel et al. 2003) run with the same transfer function as that of the Millennium Simulation (Springel et al. 2005) which was generated using `CMBFAST` (Seljak & Zaldarriaga 1996). The 'original' simulation τCDM is a flat matter-only simulation run with a DEFW transfer function (Davis et al. 1985) tuned to have a similar spectral shape to that of the Millennium Simulation. τCDM models were popular in the past as a way of enabling flat matter only models to fit clustering data from contemporary galaxy surveys (*e.g.* the APM survey: Maddox et al. 1990) whose spectral shape appeared to require a sub-critical mass density. The τCDM model of White et al. (1995) dealt with this by introducing extra relativistic species, thus changing the epoch of matter radiation equality without lowering the mass density.

Initial conditions were generated for each simulation by perturbing particle positions from an initial glass configuration of 512^3 particles using the `N-GenIC` code at an initial redshift of $z_\mathrm{i} = 199$. The simulations themselves were run using the cosmological N-body code `Gadget-2` of Springel (2005). Performing direct test simulations allows the same phases for the Fourier modes in the target and original simulations to be used, so that the approximate and exact target halo fields can be compared visually, and not just at the level of power spectra. This also allows the results of the rescaling to be analysed without the added complication of cosmic variance.

z	z'	s	$M_1/(\,h^{-1}\,\mathrm{M}_\odot)$	$M_2/(\,h^{-1}\,\mathrm{M}_\odot)$	s_m	$k_\mathrm{nl}/(\,h\,\mathrm{Mpc}^{-1})$	b_eff
0.22	0	1.56	2.58×10^{13}	3.41×10^{15}	0.95	0.15	1.57

Table 5.2: Best fit scaling parameters for scaling between the original τCDM model and target ΛCDM model.

The procedure used in this work for generating the simulations was as follows: run the original simulation to $z = 0$ in a box of size L, compile a halo catalogue and then use the mass range in this halo catalogue to compute the best scaling parameters (s, z) by minimising equation (5.2). The original simulation was then re-run to redshift z because this used comparatively little computational resources. However, in practice one would interpolate particle positions between simulation outputs around redshift z if one was interested in particles or constrain the scaling redshift to be one of set z (close to the best fit) for which one already had an output. This would be necessary in the case of halo catalogues because it is not obvious how to interpolate haloes between catalogues due to mergers. For the purpose of comparisons a simulation of the target cosmology was also run to $z' = 0$ in a box of size $L' = sL$ and a halo catalogue compiled. In doing this step the same random numbers for the dimensionless mode phases and amplitudes were chosen for the realization of the displacement fields to ensure that structures appear in the same point in both simulations, despite the different box sizes. This allows direct comparisons between the simulation particle distributions and halo catalogues that are affected only by the different background cosmologies rather than by cosmic variance.

Halo catalogues were compiled using the public FOF code available at `www-hpcc.astro.washington.edu/tools/fof.html` with a linking length of 0.2 times the mean inter-particle separation in the simulation. Haloes were catalogued that contain ≥ 100 particles and halo centres were defined to be the centre of mass of all contributing halo particles. Haloes were not checked for unbound particles.

For the simulations used here the best-fit scaling parameters are given in Table 5.2. Fig. 5.1 shows the effect of each stage of the scaling on the halo mass functions; the theory of Sheth & Tormen (1999) is shown in the top panel, whereas the effect on the measured mass functions is shown in the bottom panel. The scaling makes the theoretical predictions for the mass functions agree to within 1%, but this agreement is less perfect for the measured mass functions, which display discrepancies of up to 10%. This discrepancy can be traced back to the fact that the fitting formula for the mass functions of Sheth & Tormen (1999) are only accurate to 20% and that the mass function is only 'nearly' universal (Tinker et al. 2008; Lukić et al. 2007). A similar level of disagreement in the measured mass function was found in AW10 (their Fig. 7) in converting between WMAP1 and WMAP3 cosmologies.

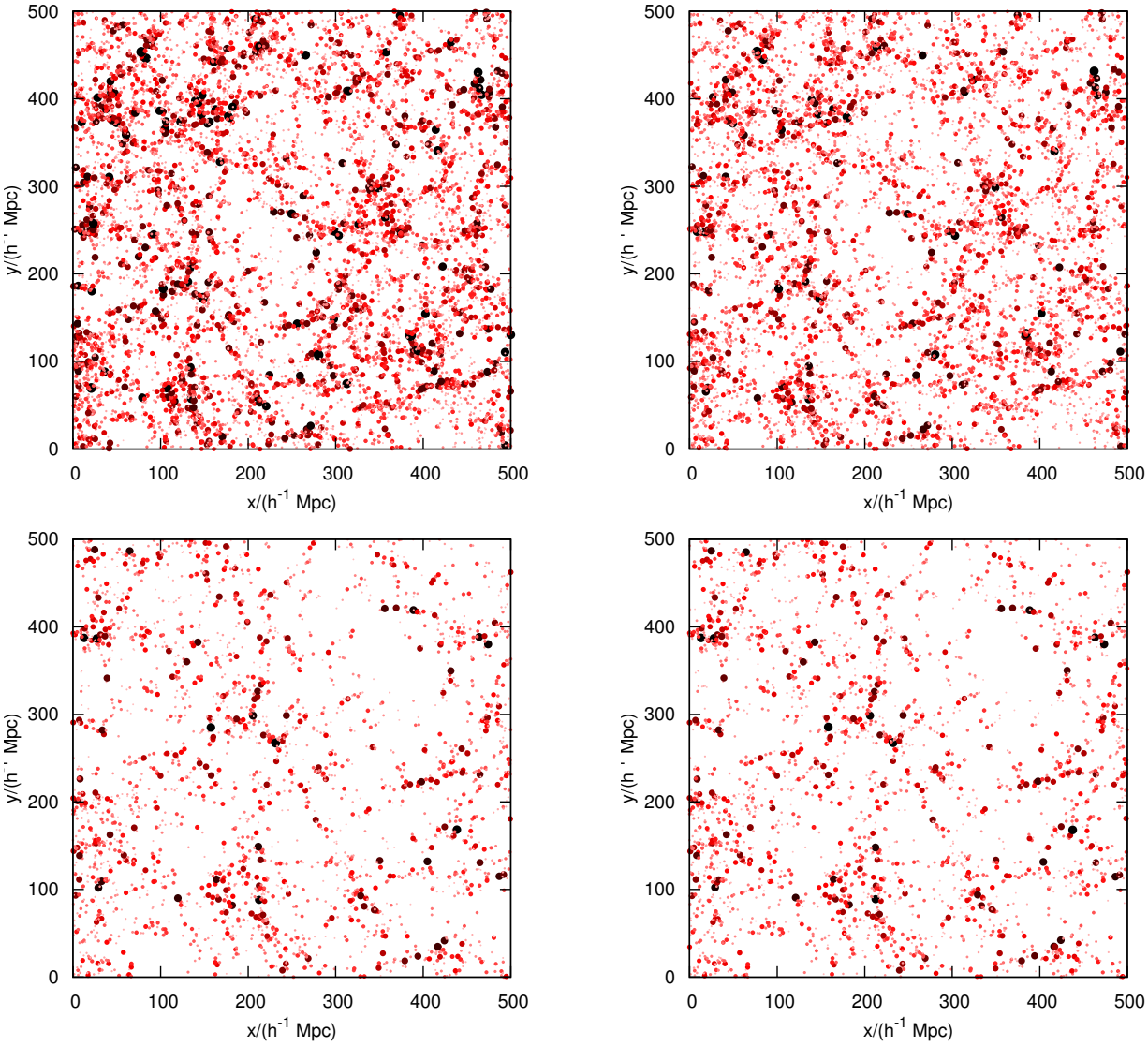

Figure 5.9: A pictorial summary of results for the rescaling of a halo catalogue. The figures all show the halo distribution in $500 \times 500\,(\,h^{-1}\,\mathrm{Mpc})^2$ slices of thickness one tenth of the box size ($50\,h^{-1}\,\mathrm{Mpc}$ for the upper two panels and $78\,h^{-1}\,\mathrm{Mpc}$ for the lower two) through different sections of the simulations. All panels show the haloes above $2.6 \times 10^{13}\,h^{-1}\,\mathrm{M}_\odot$ with a point size and colour that depends on halo mass with pink being the lowest mass and black the highest. The top left panel shows the halo distribution at redshift 0 in the τCDM simulation. The top right panel shows the distribution at redshift $z = 0.22$ which is visibly less evolved. The bottom left panel shows the result of the full scaling algorithm; this mainly has the effect of a zoom owing to the scaling of box size and halo mass ($L \to 1.56L$ and $M \to 0.95M$), plus a shifting of haloes to reproduce the correct clustering according to the ZA. In fact, the ZA displacement is hard to detect by eye, but Fig. 5.11 shows that it has a major impact on the halo power spectrum. The bottom right panel shows the excellent agreement with the final halo distribution at redshift 0 in a directly constructed target ΛCDM simulation, using the same phases as the rescaled τCDM box.

5.6 Results from simulations

A visual summary of the rescaling method is given in Fig. 5.9, where the distribution of haloes is shown at each stage of the rescaling method. This illustrates the good agreement between the distribution of haloes in the fully scaled original halo catalogue and those in the target catalogue. This comparison is facilitated by the fact that the same phases are used in the initial conditions for the two simulations, so that any differences in appearance should reflect only the treatment of nonlinear structure formation.

As a first test of the method the AW10 results for the power spectrum of the matter overdensity field are reproduced and these are shown in Fig. 5.10. This is exactly the AW10 algorithm except that the displacement fields are regenerated from the particle distribution directly. In these plots the full algorithm has been applied to the particle distribution. The top panel shows the measured power spectra at each stage of the scaling: One can see that the BAO signal in the residual is completely removed by modifying the particle positions and that the measured power spectra agree at the 1% level out to $k = 0.15\,h\,\mathrm{Mpc}^{-1}$. Beyond this the power spectra disagree at around the 20% level, reflecting the fact that the interior structure of the haloes has not been altered to account for the change in background cosmology. This is corrected for using the reconstitution and restructuring techniques below. With this exception, it is impressive that quite a broad shift in cosmological parameters (see Table 5.1) can be dealt with by the AW10 algorithm. This includes the generation of a BAO feature in the particle distribution as well as the inclusion of vacuum energy – even though the results are based on the matter-only τCDM simulation. This test is in very good agreement with AW10 and provides a useful independent confirmation of the accuracy of their algorithm albeit for a more extreme cosmology variation. The power spectrum obtained when using the original displacement field from the simulation (*i.e.* the original AW10 method), rather than reconstructed one, has been compared and negligible difference was found. This is good given the scatter in the comparison of the displacement field see in Fig. 5.3. The bottom panel in Fig. 5.5 shows an analytical halo model prediction for the full matter power spectrum, where one can see that the form of the rescaled residual is very similar to that in the top panel. This motivates the assertion that the remaining small-scale differences are due to the treatment of halo internal structure.

A more demanding test of rescaling is to ask if the method can reproduce the desired clustering of haloes. The results of the method of directly scaling a halo catalogue are shown in Fig. 5.11 as the number weighted power spectra of haloes above $2.6 \times 10^{13}\,h^{-1}\,\mathrm{M}_{\odot}$ in the upper panel and the number weighted spectra of those above $5 \times 10^{13}\,h^{-1}\,\mathrm{M}_{\odot}$ in the lower panel at each stage of the scaling process. The displacement field required to move haloes around according to the ZA has been generated entirely from the halo distribution using the method described in the text. Without this displacement, the power spectra are clearly in error, with a residual that reflects the BAO signal. This error is reduced when the differential displacement field is applied to the haloes, but it is not eliminated. However, if the displacement applied to each halo is scaled according to the mass-dependent bias, $b(M)$, this problem is cured. This confirms the

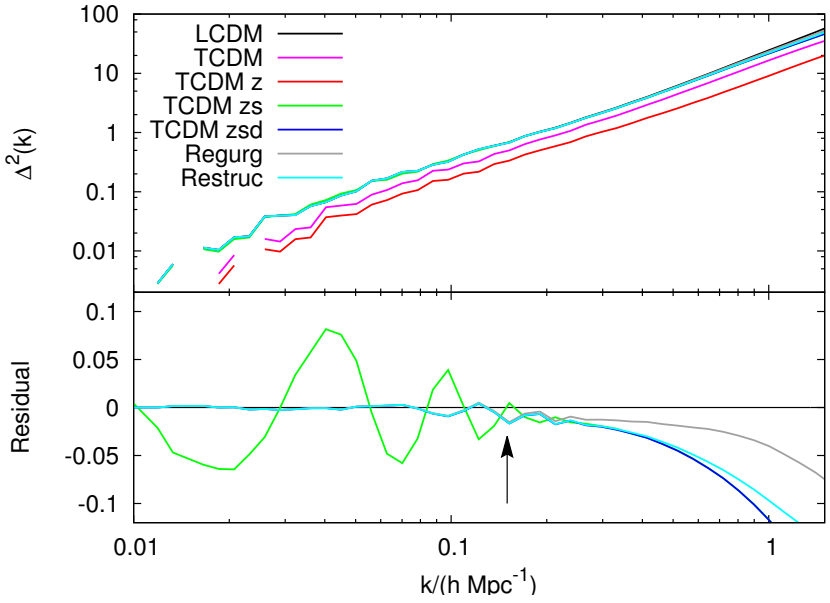

Figure 5.10: The matter power spectra measured in the simulations at various stages of the method scaling between the τCDM and ΛCDM simulations. The black line is the target ΛCDM power spectrum whereas the other lines show the various stages of the method, original τCDM simulation (pink), scaling in redshift (red), scaling in redshift and size (green), full AW10 scaling including position modifications using the displacement fields (blue), a power spectrum in which haloes have been removed from the scaled simulation and replaced with aspherical haloes of the correct concentrations for this cosmology (regurgitation, gray) and finally power when particles in haloes have been reshaped to account for the new cosmology (restructing; cyan). One can see that adjusting particle positions using the ZA almost completely removes the residual BAO feature in the power spectrum, leaving the agreement between simulations at the level of 1% up to the nonlinear scale (black arrow, equation 5.4). The remaining disagreement of the blue curve can be compared to the halo-model disagreement in Fig. 5.5 where it can be seen to be very similar, thus justifying modifying the halo internal properties. Employing regurgitation improves the match at small scales leaving the agreement at the level of 5% up to $k = 1\,h\,\mathrm{Mpc}^{-1}$, but restructuring the haloes shows litte improvement at non-linear scales.

need to apply a mass-dependent differential displacement to haloes, an aspect which is absent in the original AW10 algorithm. However at the largest scales shown the rescaling method seems to degrade the match slightly and no reason for this was found. However the same effect was seen the method was tested on smaller volume simulations at the largest scales probed by *those* simulations, scales that the method shown in Fig. 5.11 corrects well, so this is plausibly to do with resolution on scales of order the box size.

The final part of the investigations discussed here involves reconstituting the particles in haloes using only the halo catalogues. In order to do this the power spectrum of only the particles in haloes reconstituted from the *scaled* τCDM halo catalogue is compared to the power spectrum of particles in the haloes in the ΛCDM simulation. This is shown in Fig. 5.12,

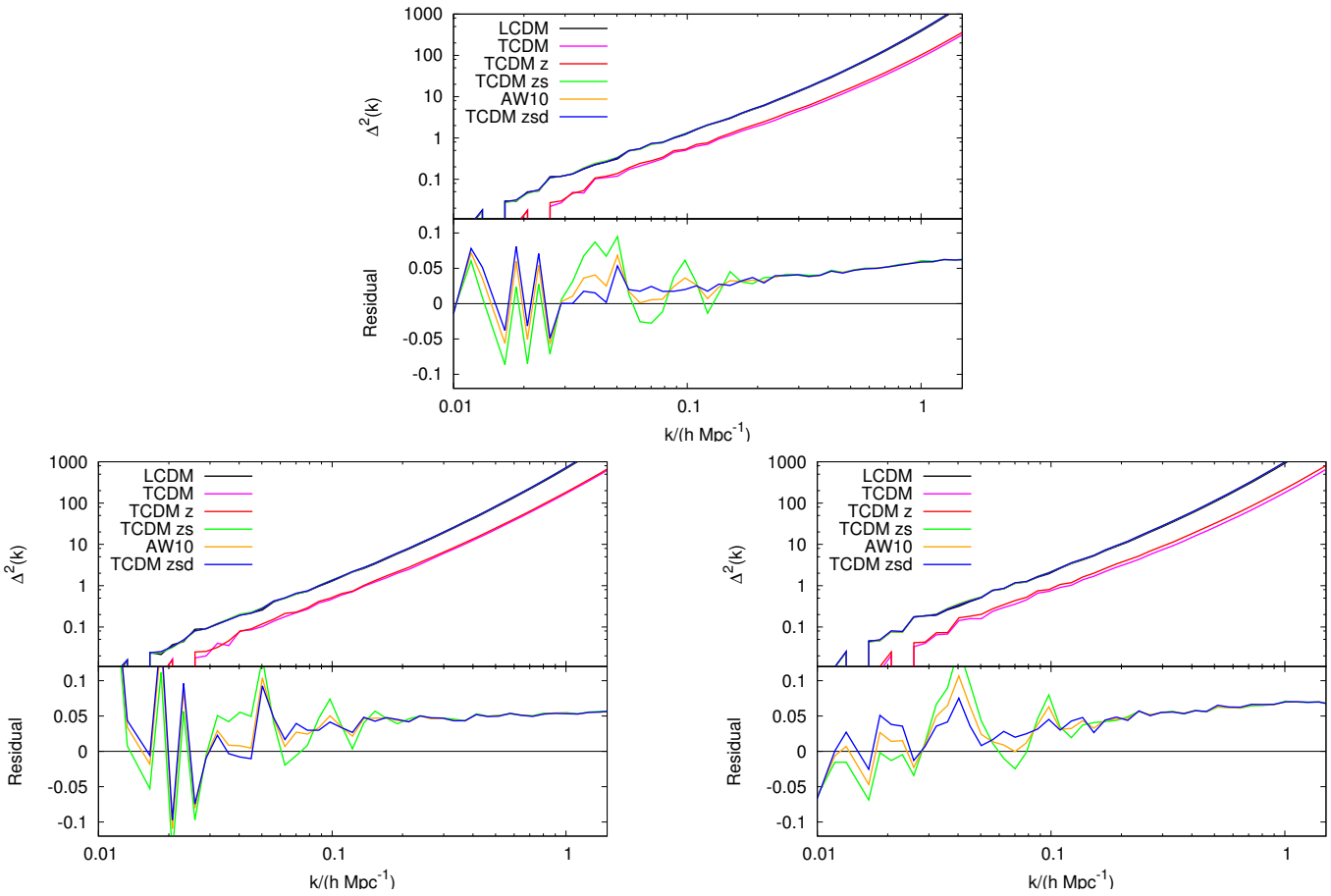

Figure 5.11: The power spectrum of haloes at each stage of the rescaling procedure. The target ΛCDM spectrum of haloes is shown (black) and the original halo catalogue at each stage of the scaling process, the original catalogue at $z = 0$ (pink), the redshift scaled τCDM (red), τCDM with both box size relabelled and redshift changed (green) and finally the result of also then modifying the halo positions according to the ZA. This is done in two distinct ways: applying the same differential displacement field to all haloes (AW10; orange), and giving different haloes a biased version of this displacement according to mass (blue). The upper panel shows the number weighted spectrum of haloes above $2.6\times10^{13}\,h^{-1}\,\mathrm{M}_\odot$ while the lower panel shows that of haloes below (left) and above (right) $5\times10^{13}\,h^{-1}\,\mathrm{M}_\odot$. In all cases, one can see that the universal displacement leaves a residual that reflects the BAO signal, whereas the mass-dependent displacement alleviates this problem to some degree, leaving agreement in both spectra at the level of 5% or better except at the largest scales shown where the match is degraded slightly. The slant in the power towards small scales is consistant with shot noise due to the differing number of haloes in the target and rescaled catalogues

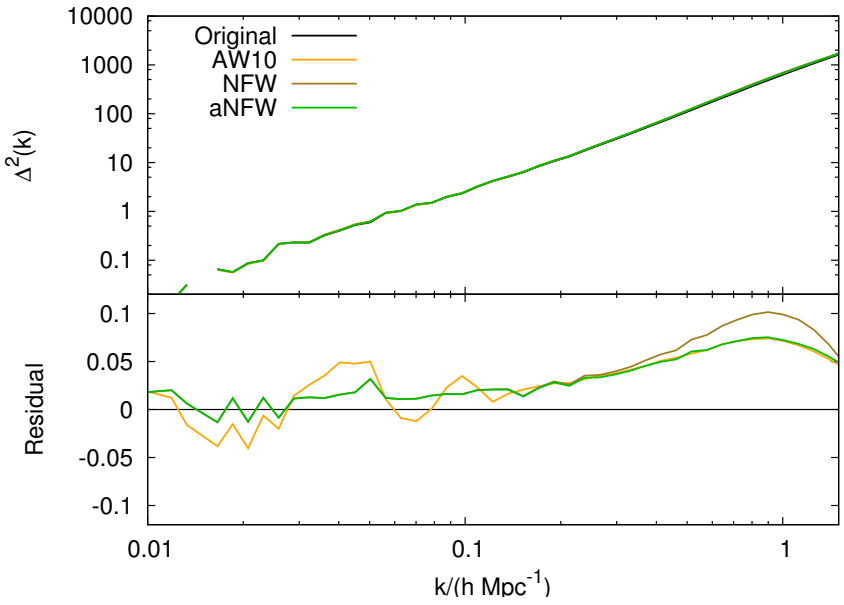

Figure 5.12: The power spectrum of only particles residing in haloes. Shown are spectra of the particles in the original haloes in the target simulation (black) together with particles in haloes reconstituted from the original catalogue that are spherical (brown), aspherical (green). Also shown is the result of using the original AW10 method with aspherical reconstituted haloes (orange), which contains a residual BAO signal due to the incorrect treatment of bias. Haloes are dressed with NFW profiles with concentration relations described in the text. There is a clear improvement gained by using a bias dependent displacement field and by using aspherical haloes over spherical haloes. The maximum error here does not exceed 6%.

which again displays good agreement (the spectra agree to 5% across the range of scales shown) by using the full scaling algorithm. Clearly there is an improvement on small scales gained by using a bias dependent displacement and by using aspherical haloes over spherical ones.

Finally the regurgitation method is looked at in which, after the original AW10 scaling method has been applied to particle data, the haloes are located with FOF, removed and then replaced by reconstituted haloes with corrected mass-concentration relations. The results of this were shown above in the form of the power spectrum in Fig. 5.10, where one can see that the agreement between the original and target cosmologies is much improved by this method at scales above $k = 0.1\,h\,\mathrm{Mpc}^{-1}$ due to modifications of the haloes' internal structure. Thus the final fully rescaled power spectra agrees at a sub percent level to $k = 0.1\,h\,\mathrm{Mpc}^{-1}$ and to a 5% level out to $k = 1\,h\,\mathrm{Mpc}^{-1}$ if one reconstitutes the haloes in their entirety. Here there is a clear improvement over the original AW10 algorithm, gained by manipulating the properties of individual haloes. Additionally the effect of restructuring the haloes is shown although the improvement gained from doing this is less than from regurgitating them, this is somewhat surprising. However, this situation is reversed in redshift space.

5.7 Redshift space

In order to connect with real observables, it is necessary to investigate how the rescaling method performs in redshift space. In a real cosmological survey galaxies are measured in terms of their angular position on the sky and (possibly an approximate) redshift. As discussed in Section 1.12.3; the redshift position coordinate is affected by the peculiar velocity of the galaxy in question and thus there is not a one-to-one mapping between redshift and position and this needs to be taken into account in any analysis. Importantly the degree of linear redshift-space distortion depends on how fast perturbations are growing and so provides an important source of information about the growth rate, which can be used to distinguish various dark energy and modified gravity scenarios from more conventional ΛCDM.

In Fig. 5.13 the redshift-space monopole power spectrum is shown. Once again the BAO feature can be seen to be efficiently removed by modifying the displacement field as per the original AW10 method. The eventual match at the level of the redshift space monopole is at the 1% level up to $k = 0.1\,h\,\mathrm{Mpc}^{-1}$, but deviations are seen at smaller scales due to the lack of treatment of halo internal structure. Improvements are therefore gained by modifying the internal structure of haloes either by restructuring haloes or removing them and regurgitating theoretical haloes with modified internal structure and velocity dispersions. In contrast to the case of real space, shown in Fig. 5.10, restructuring the haloes performs better in redshift space compared to regurgitation. Looking at the full redshift space power information, shown in Fig. 5.14 one can see that regurgitation performs better for perpendicular modes that are unaffected by distortions in redshift space, but that restructuring performs slightly better across the entire redshift space and this accounts for the slighly better overall prediction for the monopole. The eventual monopole in the restructured case is good to 3% up to $k = 1\,h\,\mathrm{Mpc}^{-1}$, whereas the regurgitated monopole is good to 5%.

In Fig. 5.15 the redshift-space monopole power of rescaled haloes is shown for all haloes and for haloes binned into an (approximate) high and low mass sample. Rescaling in redshift space, compared to real space, additionally involves both a gross shift in halo velocities according to equation (5.23) and then also a more minor velocity shift to take account of the changing linear power spectrum, shown in equation (5.25). Again one can see that the original AW10 method fails to completely remove the residual BAO feature and only when halo positions are moved, taking into account their biased displacements, is the BAO residual removed. The original AW10 method performs better in redshift space, compared to its performance in real space, because it is only the displacement field of haloes that is biased, not the velocity field due to the equivilence principle. However, using a biased displacement field is still obviously the correct way to rescale. The agreement in the monopole power is better than 3% for the full halo sample out to $k = 1\,h\,\mathrm{Mpc}^{-1}$ except at the largest scales shown where discrepancies are seen. These seem to be worse for the low mass halo sample as can be seen at large scales in the bottom left panel and the reasons for this are unknown. For the low mass sample the improvement over the original AW10 method is less marked because low mass haloes are less biased.

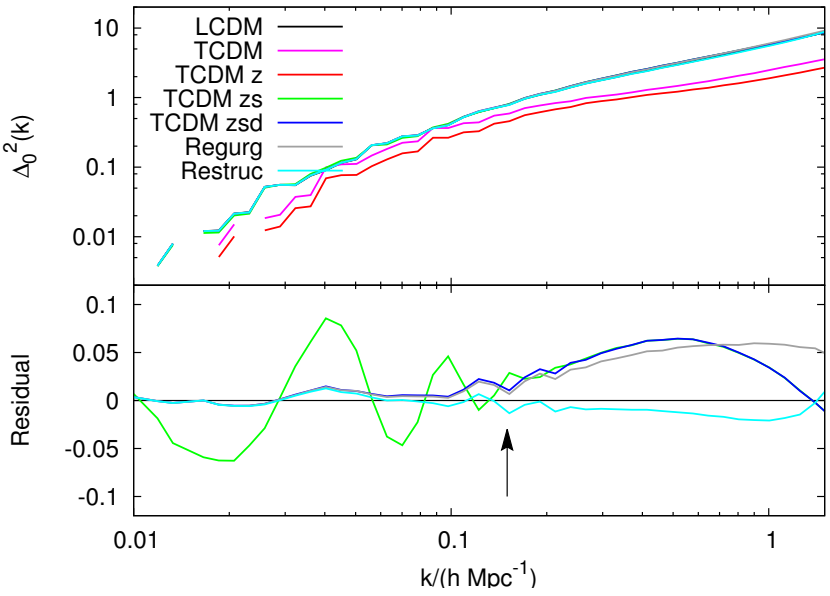

Figure 5.13: The redshift-space monopole power spectra measured in the simulations at various stages of the method scaling between the τCDM and ΛCDM simulations. The black line is the target ΛCDM power spectrum whereas the other lines show the various stages of the method, original τCDM simulation (pink), scaling in redshift (red), scaling in redshift and size (green), full AW10 scaling including position modifications using the displacement fields (blue) and finally power spectra in which haloes have been removed from the scaled simulation and replaced with aspherical haloes of the correct concentrations for this cosmology (regurgitation, gray) and in which halo particles have been restructured (cyan) rather than being replaced entirely. One can see that adjusting particle positions using the ZA almost completely removes the residual BAO feature in the power spectrum, leaving the agreement between simulations at the level of 1% up to the nonlinear scale (black arrow, equation 5.4). Replacing haloes entirely with theoretical haloes of the correct concentrations and dispersions (regurgitation) improves the match to the target simulation at small scales leaving the agreement at the level of 5% up to $k = 1\,h\,\mathrm{Mpc}^{-1}$ but one can see that reshaping the haloes works better than replacing them, where the match is good to 3%. This is in contrast to real space. In both of these cases theoretical Gaussian velocity dispersions have been assigned. Note that this is the original AW10 applied to particles with no biased displacements This plot is the redshift-space monopole version of Fig. 5.10.

In Fig. 5.16 the redshift-space monopole power of particles in reconstituted haloes is shown when compared to the power in particles in haloes in the target cosmology. One can see that the agreement is good at linear scales once a biased displacement field has been used. At non-linear scales the agreement is less good if one uses the theoretical dispersion relation in equation (5.26) compared to using a rescaled version of the catalogued halo velocity dispersion; the evetual agreement is at the 3% level here across all scales shown. The lower panel shows residuals in the full 2D redshift space plane for the case of using biased displacements together with theoretical dispersions (left) and rescaled catalogued dispersions (right). Here one can see that errors in the catalogued dispersion case are concentrated at high k, high μ, which

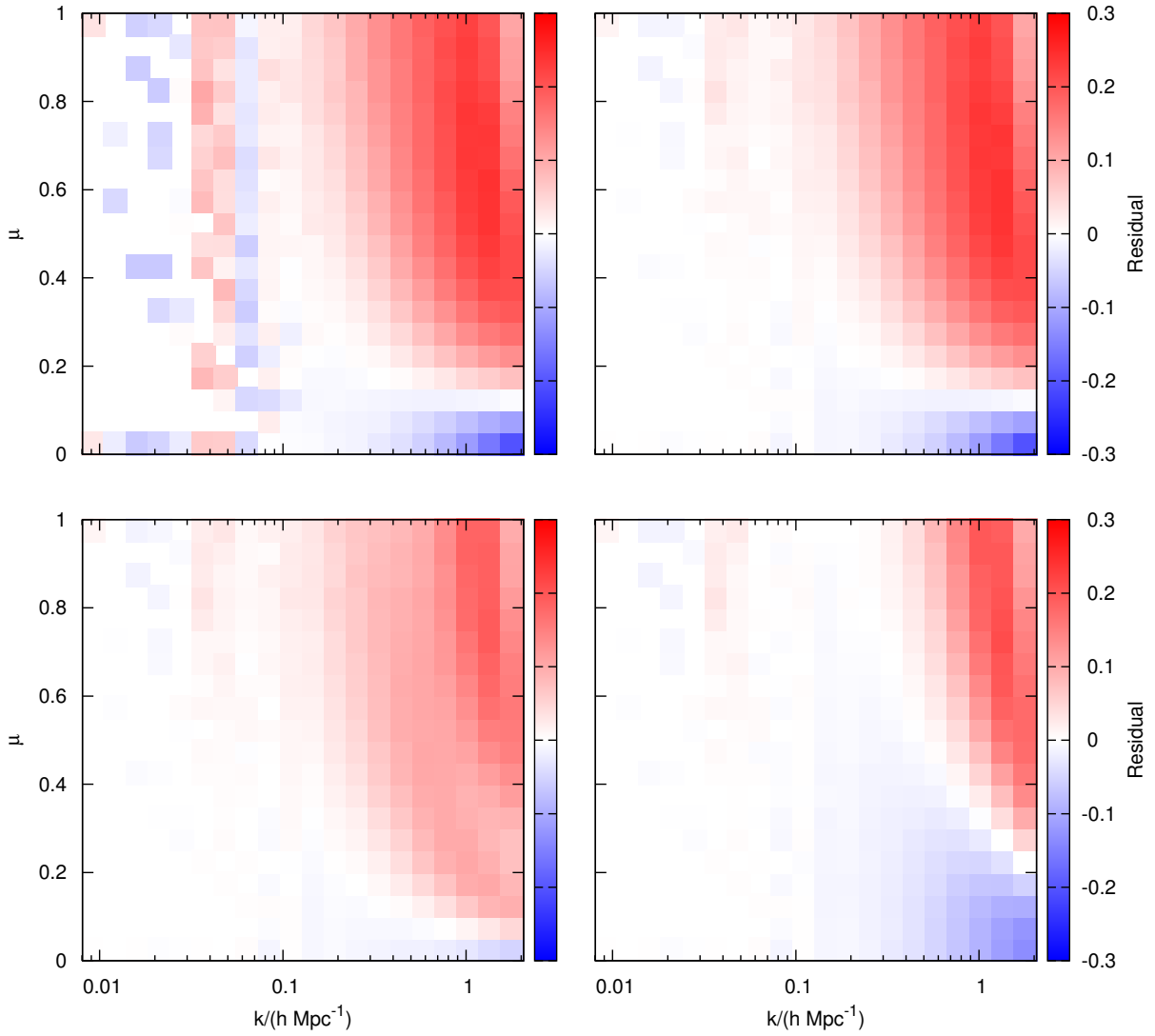

Figure 5.14: The residuals for the full redshift-space power spectrum shown as a function of k and μ. Residuals are shown at each stage of the rescaling process when comparing the rescaling to the target ΛCDM simulation. The top left panel shows the scaling in redshift and size. The top right panel shows the addition of the displacement field step where the residual BAO can be seen to be efficiently removed, although this is slightly better at low μ. The bottom left panel then shows the effect of regurgitating reconstituted haloes with theoretical dispersions back into the parent particle distribution; the bottom right panel shows the effect of restructuring haloes. Restructuring the haloes performs better across the entirety of redshift space but regurgiation is better for $\mu = 0$. One can also see that the good agreement of the restructuring monopole in Fig. 5.13 is partially due to cancellations of errors across the full redshift-space plane. This plot is the full redshift-space version of Fig. 5.10 and Fig. 5.13.

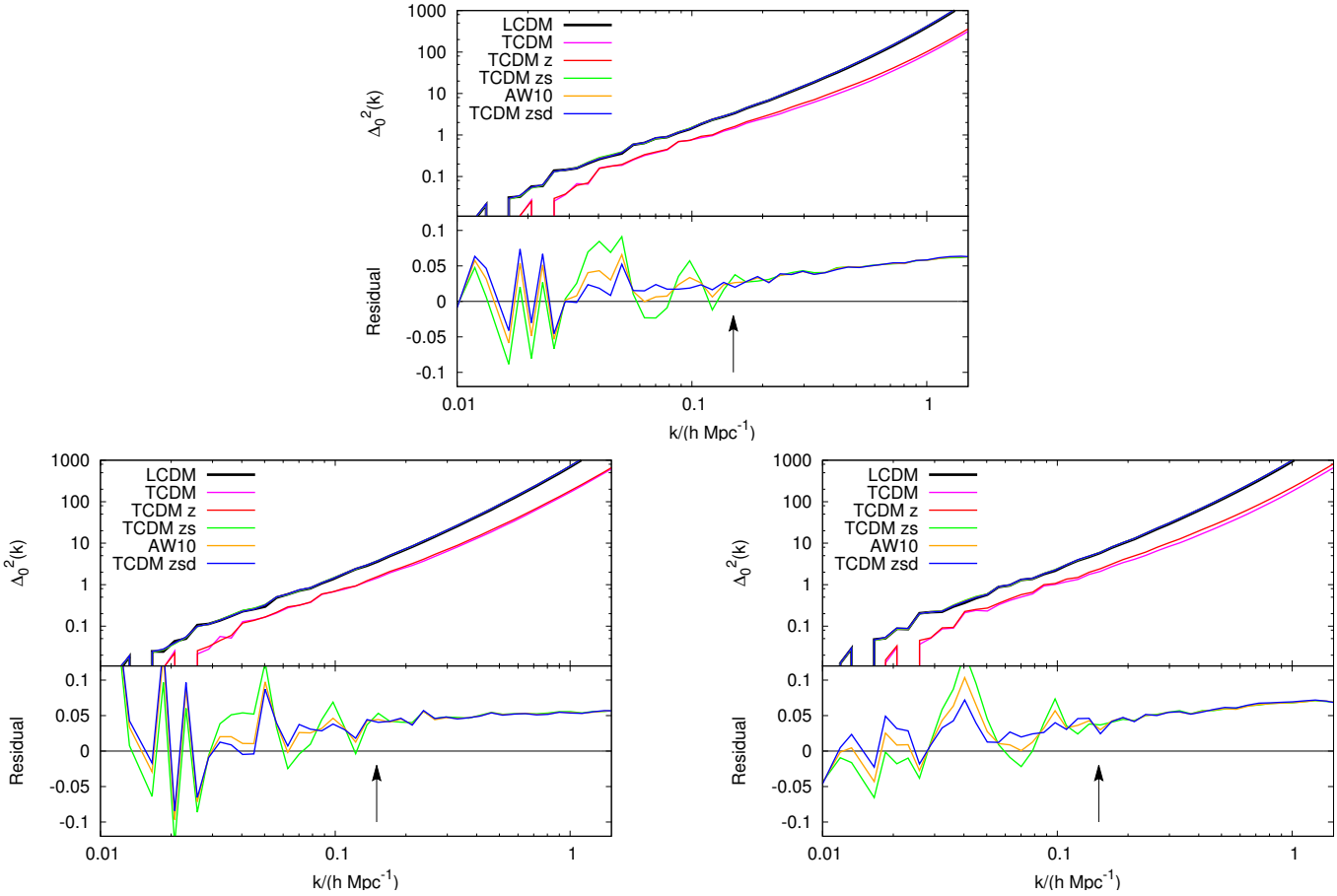

Figure 5.15: The top panel shows the redshift-space monopole power spectrum of haloes above $2.6 \times 10^{13}\,h^{-1}\,\mathrm{M}_\odot$ at each stage of the rescaling process, whereas the bottom two panels show the sample split into a low mass (left) and high mass (right) sample about $5 \times 10^{13}\,h^{-1}\,\mathrm{M}_\odot$. The target ΛCDM spectrum of haloes is shown (black) and the original halo catalogue at each stage of the scaling process, the original catalogue at $z = 0$ (pink), the redshift scaled τCDM (red), τCDM with both box size relabelled and redshift changed (green) and finally the result of also then modifying the halo positions according to the ZA. This is done in two distinct ways: applying the same differential displacement field to all haloes (AW10; orange), and giving different haloes a biased version of this displacement according to mass (blue). One can see that the universal displacement leaves a residual that reflects the BAO signal, whereas the mass-dependent displacement alleviates the problem, leaving agreement in both spectra at the level of 5% or better up to $k = 1\,h\,\mathrm{Mpc}^{-1}$ for the full halo population, except at the largest scales shown where the match is degraded slightly. The slant in the spectra is due to shot noise from different halo numbers in each case that arises due to the imperfect match of the mass function. The match is noisier for the split samples, but still good to a few %. The improvement gained by using biased displacements is less marked than in real space because redshift space mixes in velocity field information, which is unbiased with respect to the mass. The reason for the degredation of the match at the largest scales shown, particularly for the low mass sample, is not known. This plot is the redshift-space monopole version of Fig. 5.11.

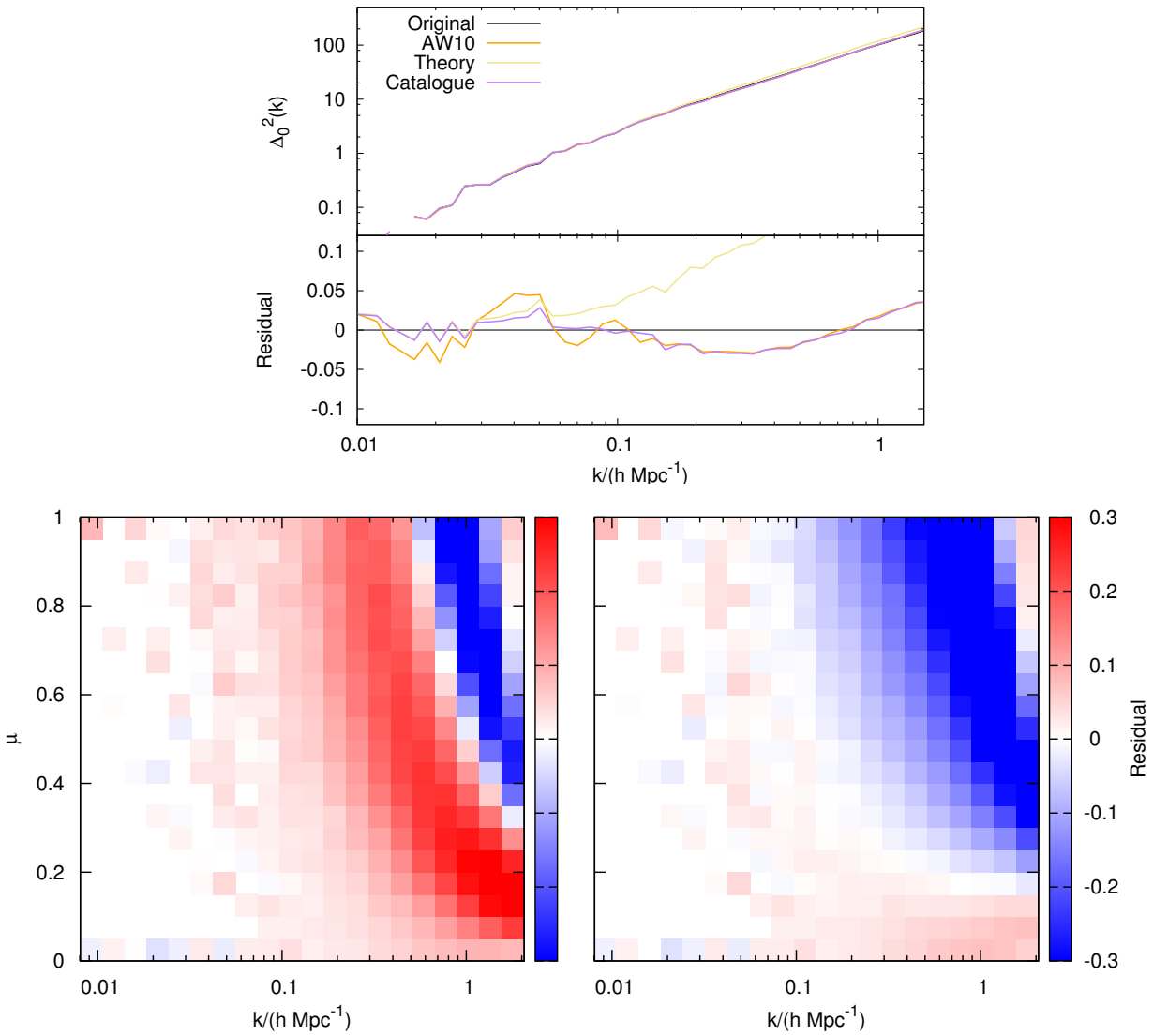

Figure 5.16: The redshift-space monopole power spectrum of reconstituted particles residing in rescaled haloes is shown in the top panel. The AW10 method (unbiased displacements; orange) with haloes with catalogued dispersions; the full method with biased displacements with haloes with theoretical dispersions (yellow) and biased displacements with haloes with rescaled catalogued dispersions (purple) compared to the target ΛCDM (black). The bottom panels show the full redshift space residuals from using theoretical velocity dispersions (left) and rescaled catalogued dispersions (right). The monopole of the original AW10 rescaling shows a residual BAO due to incorrect treatment displacements. Using rescaled, catalogued dispersions is much more accurate at the level of the monopole than using theoretical dispersions but this is partly due to positive and negative cancellations of errors, which can be seen in the bottom two panels. For the monopole if one uses biased displacements and rescales catalogued velocity dispersions the agreement is good at the 3% level up to $k = 1\,h\,\mathrm{Mpc}^{-1}$. This figure is the redshift-space monopole version of Fig. 5.12.

contributes less to the monopole because the full power is damped here and the monopole is a simple average. The theoretical dispersions perform worse across the entirety of redshift space, even at surprisingly large scales. This plot, combined with the tests in Fig. 5.8 gives hope that the theoretical dispersion relation can be modified slightly to produce better results. Direct comparisons between theoretical and catalogued dispersions reveal a scatter, but also show that the theoretical value is low by a factor of 1.07. Increasing the dispersion by this amount increases the non-linear supression in the monopole and brings the theoretical curve in line with the catalogued curve. This all brings hope that the growth rate can be accurately extracted from rescaled simulations; discussed in the next section.

5.8 Recovery of the growth rate

A realistic goal of forthcoming galaxy reshift surveys will be to measure the growth rate of cosmic structure at $\sim 1\%$ accuracy (*e.g. Euclid*). With this in mind it is reasonable to see to what level the growth rate can be recovered from simulations that have undergone rescaling. Any galaxy catalogues eventually generated from a rescaled halo catalogue need to have the correct underlying growth rate in order to calibrate a survey analysis. In Fig. 5.17 the recovered $G(k) = \Delta_2^2(k)/\Delta_0^2(k)$ values are shown for: the full particle distribution; the halo distribution; the distribution of particles in haloes reconstitued from halo catalogues. In all cases the value of $G(k)$ present in the original simulation is recovered by the method at scales around $k = 0.1\,h\,\mathrm{Mpc}^{-1}$ but degredations are seen at more non-linear scales, and at very large scales when haloes have been used in the rescaling process. The match shown is good enough that in each case $G(k)$ can be said to be recovered at the 3% level for linear scales. Again this is impressive because the original simulation is $\Omega_\mathrm{m} = 1$ and thus $f_\mathrm{g} = 1$ so that the linear shift in G is quite broad. However, this match is degraded at non-linear scales in the case of the particles being reconstituted

In each plot the linear theory G_lin is also shown

$$G_\mathrm{lin} = \frac{1 + \frac{2}{3}\beta + \frac{1}{5}\beta^2}{\frac{4}{3}\beta + \frac{4}{7}\beta^2} \ , \tag{5.28}$$

for the full matter distribution $b = 1$ and $\beta = f_\mathrm{g}$, where $f_\mathrm{g} \approx 0.47$ for the cosmology in question, so that $G = 0.55$. In the case of the halo fields the tracer bias must be taken into account: for the haloes themselves this is simply the number weighted 'effective' bias discussed in the text, in this case $b = 1.57$, $\beta = 0.30$ and $G = 0.37$. In the case of the halo particles this halo bias is instead mass weighted so that $b = 2.09$, $\beta = 0.22$ and which results in a slightly different theoretical expectation value $G = 0.28$. Fig. 5.17 shows that if one were to attempt to recover the growth rate of linear perturbations from a rescaled simulation the answer should be unbiased, although in the case of haloes a less noisy simulation containing larger scales (thus more linear modes) would help to support this conclusion. In practice in a survey analysis one would maginalise over velocity dispersion nuisance parameters; in this regard it is good to

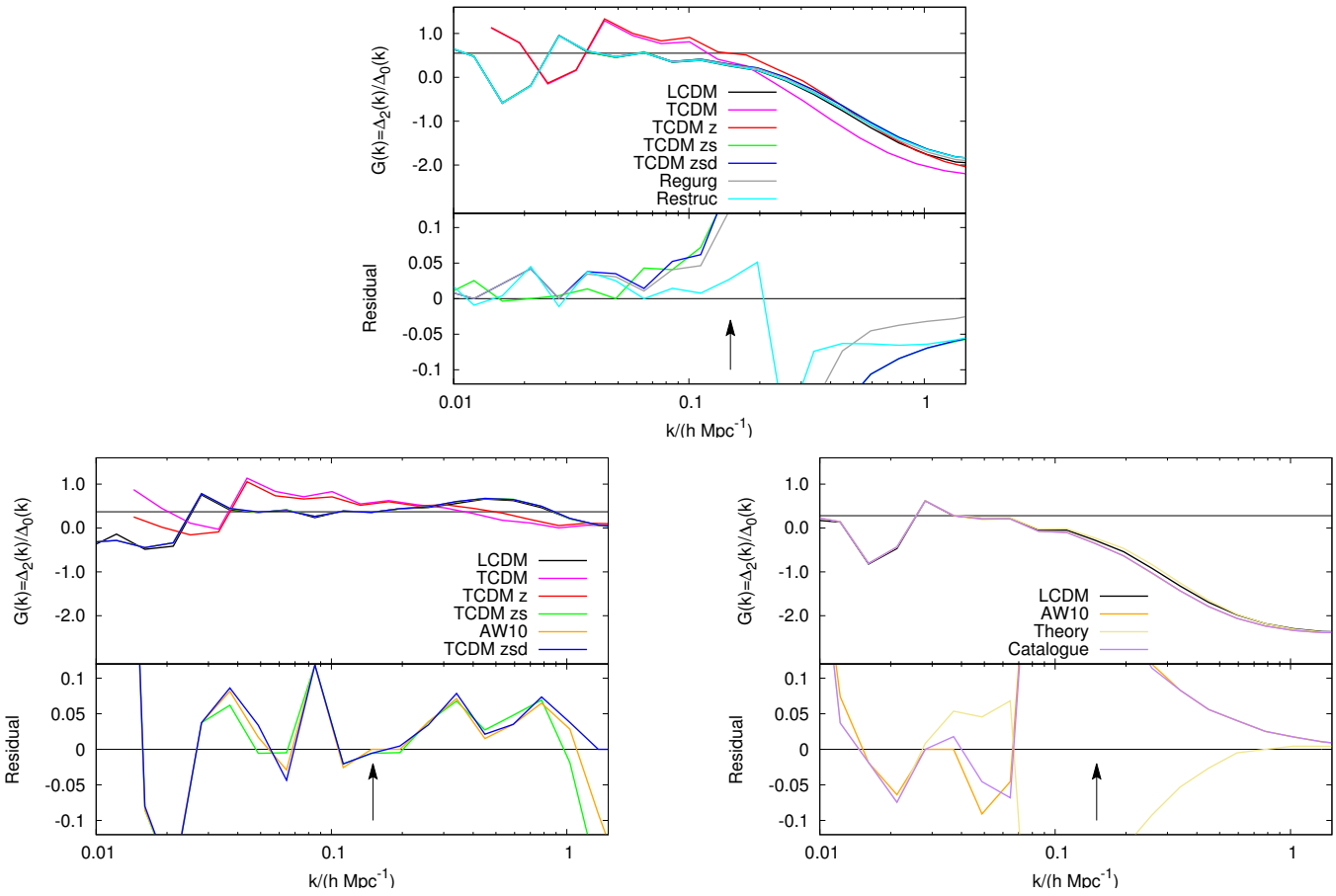

Figure 5.17: The value of $G(k) = \Delta_2^2(k)/\Delta_0^2(k)$ recovered from the simulations before and after scaling. The arrow shows the non-linear scale. The top panel shows the case of the full particle distribution where methods of regurgitation and restructuring have been used to alter halo interiors. Here the residual difference is small across the full range of scales shown and particularly the non-linear tail is quite well reproduced. The bottom panels show the case of haloes, with the left panel being the haloes themselves whereas the right panel shows the case of reconstituted halo particles with both theoretical and catalogued velocity dispersions used in the reconstitution, in both cases a comparison is made with the original AW10 method, which performs well here because the residual BAO is effectively divided out. The error blows up around the non-linear scale as the quadrupole changes sign. After restructuring the haloes G is matched at the 5% level upto the non-linear scalesm, surprisingly the ZA step of the method degrades the match at linear scales slightly. For haloes the value of $G(k)$ is noisy, and reproduced at the 10% level across all scales shown, the ZA step of the method seems to improve things only marginally. For the reconstituted particles it is less good where the imperfect redshift space power as a function of μ, shown in Fig. 5.16, is having an effect. In each case the linear theory prediction for G is shown. Large deviations from this are seen at the largest scales, due to cosmic variance, meaning that the simulations themsevles are not probing enough linear scales to generate good measurements of f_g.

see that the rescaled distributions reproduce the non-linear regime quite well; although there is certainly room for improvement in the case of reconstituted halo particles. The non-linear portion of G for haloes is particularly well matched and this is related to the fact that they lack a strongly non-linear FOG; it is plausible for future surveys to target just halo central galaxies in order to mitigate the effect of FOG, or to use other weighting schemes (Seljak et al. 2009).

5.9 Discussion

In this chapter it has been demonstrated that the rescaling method of Angulo & White (2010) may be modified so as to apply directly to halo catalogues. AW10 rescalings of length, mass, and redshift were made as well as using the halo positions themselves to compute the displacement fields (by debiasing the halo over-density fields), in order to correct the linear clustering in the simulation, using the Zel'dovich approximation. This method enables rapid scaling of a halo catalogue to a different cosmology, and is entirely self-contained, being based only on the halo catalogue. One should note that this provides a dramatic increase in speed when using the halo catalogue alone due to the smaller halo catalogue being read into memory more quickly. Computational effort is only expended when reading the catalogue into memory and when computing the Fourier Transforms for the displacement field correction. In this work the halo catalogue was small, containing only $\approx 70,000$ haloes, and a Fourier mesh of 75^3 was all that was required to resolve the linear components of the displacement field. This resulted in a total run time for the rescaling of only a few seconds on a standard desktop computer. This would increase for larger halo catalogues that span a larger cosmological volume, because more mesh cells would be required to resolve the linear fields, and for catalogues containing more haloes because of the increased time taken to read them in and out of memory. However, in any case it is obviously many orders of magnitude faster than running a new simulation.

Working with haloes has the advantage of speed, but also allows two improvements on the original AW10 method. The first of these concerns the internal structure of haloes, which depends on cosmology. This can be allowed for by reconstituting the halo internal density distribution using analytical profiles and scaling relations appropriate for the target cosmology. If a catalogue of halo particles is available, it is also possible to restructure haloes without replacing them entirely. Additionally reconstituted haloes can be regurgitated back into the parent particle distribution if desired.

The other issue applies on large scales. The AW10 method applies an additional displacement in order to ensure that the large-scale linear clustering is as desired in the target cosmology. But applying this extra displacement to all haloes, independent of their mass, will not yield the correct mass-dependent bias, $b(M)$. Better results were found to be obtained by scaling the extra displacement in a mass-dependent way. Clearly this is a minor issue if the original and target cosmologies are close to each other, but it may be important in spanning a large parameter space. Clear residual BAO signal can be seen in the cases where a biased displacement

field was *not* applied.

The method has been tested by rescaling a halo catalogue generated from a matter-only τCDM simulation into that of a more standard ΛCDM model. This represents a radical shift in cosmology, especially considering that the initial simulation contains no dark energy. At the level of the particle distribution the matter power spectrum is predicted correctly after the rescaling to the level of 1% to $k = 0.1\,h\,\mathrm{Mpc}^{-1}$ in excellent agreement with the original AW10 results and provides independent confirmation of the accuracy of their scaling algoirthm. A match of 5% to $k = 1\,h\,\mathrm{Mpc}^{-1}$ is possible if haloes are replaced by those appropriate for the new cosmology. For the haloes themselves the rescaled power spectra are noisier, but are still predicted correctly at the level of 5% up to $k = 1\,h\,\mathrm{Mpc}^{-1}$ with no obvious biases.

The mass function of dark-matter haloes was reproduced at only the 5% level despite the cosmologies being designed to have exactly the same $\sigma(R)$. Disagreements seen must reflect the non-universality of the mass function. In future work it may therefore be preferable to work with non-universal prescriptions for the mass function such as Reed et al. (2007) or Tinker et al. (2008).

In redshift space the method was shown to work well at the level of the monopole, as in the original AW10 case. For the full particle distribution the redshift space monopole was recovered at the 1% level up to $k = 0.1\,h\,\mathrm{Mpc}^{-1}$ and to 3% to smaller scales if halo internal properties are also manipulated. The method also worked well when applied to haloes in redshift space, although the improvements gained from using a biased displacement field as less marked because redshift space mixes in the unbiased velocity field. The monopole agrees at the few % level out to $k = 1\,h\,\mathrm{Mpc}^{-1}$ with the exception of large deviations at the largest scales investigaged, the reasons for these deviations are not known. For reconstituted haloes; the monopole power spectrum was recovered at the 1% level upto $k = 0.1\,h\,\mathrm{Mpc}^{-1}$ if a biased displacement field is used and the agreement is at the 3% level up to $k = 1\,h\,\mathrm{Mpc}^{-1}$ if catalogued dispersions are also rescaled.

The recovery of the ratio of quadrupole to monopole ratio was also investigated. This is a quantity of interest because in the linear regime it can be used to infer the growth rate of cosmic structure. The form of $G(k)$ in the target simulation was well recovered in the case of particles, haloes and reconstituted haloes; but the quantity itself, even in the target simulation, quite poorly approximates the linear theory expectation. In reality a large cosmological survey, with many linear modes, is required to accurately measure G and this is the goal of forthcoming surveys – the simulations used here probably do not probe linear scales to the requisite degree. Measurements of G can be biased by a lack of understanding of the linear to non-linear transition, which is due to FOG. It is good to see that this transition is comparatively well modelled by the rescaling method, although some deviation is seen in the case of the reconstituted haloes; this could plausibly be improved by a better modelling of the velocity distribution in halo interiors.

Chapter 6

Applications to modified gravity theories

6.1 Preamble

This chapter aims to apply the methods of the calibrated halo model and simulation rescaling, developed in the previous two chapters, to modified gravity models. In doing this an attempt is made to keep the methods as general as possible, so that they may plausibly be applied to a wide range of modified theories. However, at this stage tests are restricted to the subclass of Hu & Sawicki (2007a) (hereafter HS07) $f(R)$ models, discussed briefly in Section 1.8. HS07 models have a scale dependent linear growth rate and a screening mechanism to shield some regions from enhanced gravitational forces; such features are fairly generic amongst modified gravity theories. In $f(R)$ theories the screening mechanism at play is called the chameleon mechanism, and it screens haloes in a way which depends on their mass and environment. This adds the complication of strong non-locality, because the properties of haloes can vary quite strongly depending upon their environment. The aim of this chapter is to make an attempt to incorporate some of these effects into the work of the previous two chapters.

6.2 f(R) gravity

A short introduction to general modified gravity theories was given in the introductory chapter in Section 1.8. Here the main results relevant to chameleon $f(R)$ theories are repeated for convenience. A substantial review of $f(R)$ models can be found in Sotiriou & Faraoni (2010).

Equations of motion for $f(R)$ models are derived from an action principle, starting from the action

$$S = \int \mathrm{d}^4x \sqrt{|g|} \left(\frac{R + f(R)}{16\pi G} + \mathcal{L}_\mathrm{m}(\psi_i, g_{ab}) \right) , \tag{6.1}$$

and minimising with respect to g_{ab}. The HS07 $f(R)$ model is given by the broken power law ansatz

$$f(R) = -R_0 \frac{c_1 (R/R_0)^n}{c_2 (R/R_0)^n + 1} , \tag{6.2}$$

which has free dimensionless parameters c_1, c_2 and n. R_0 is the current value of the background curvature and could be incorporated into c_1 or c_2 if desired (there are only three truly free parameters in the model). This function can be expanded in the high curvature, $R/R_0 \gg 1$, limit as

$$f(R) \approx -R_0 \frac{c_1}{c_2} + R_0 \frac{c_1}{c_2^2} \left(\frac{R_0}{R} \right)^n , \tag{6.3}$$

which has the form of a cosmological constant ($2\Lambda = R_0 c_1/c_2$) together with an inverse power-law term in R

$$f(R) = -2\Lambda - R_0 \frac{f_{R0}}{n} \left(\frac{R_0}{R} \right)^n , \tag{6.4}$$

the derivative of $f(R)$ can be interpreted as a new field, f_R, which modifies gravity depending on the local value of the curvature:

$$f'(R) \equiv f_R = f_{R0} \left(\frac{R_0}{R} \right)^{n+1} . \tag{6.5}$$

Thus, in this limit, the theory is specified via three parameters; Λ, f_{R0} and n. The full equation of motion for f_R derives from the trace of the $f(R)$ field equation, and is given by

$$\Box f_R = \frac{1}{3}[R + 2f(R) - R f_R - 8\pi G T] . \tag{6.6}$$

If $f_{R0} \ll 1$ then this theory produces an expansion history that is indistinguishable from ΛCDM. This is the limit in which this chapter uses $f(R)$ theories and a background ΛCDM limit is assumed throughout the rest of this work. In this limit, $\bar{R}$ can be calculated as in standard ΛCDM as $\bar{R} - 4\Lambda = 8\pi G \bar{\rho}_\mathrm{m}$, therefore:

$$\bar{R}(a) = 3H_0^2 \left(\Omega_\mathrm{m} a^{-3} + 4\Omega_\Lambda \right) \tag{6.7}$$

so that the background $\bar{f}_R$ varies with time as

$$\bar{f}_R(a) = f_{R0} \left(\frac{1 + 4\Omega_\Lambda/\Omega_\mathrm{m}}{a^{-3} + 4\Omega_\Lambda/\Omega_\mathrm{m}} \right)^{n+1} \tag{6.8}$$

Interesting features of HS07 models come from modifications to the Poisson equation that are generated via gradients in f_R from the weak-field, quasi-static version of equation (6.6). The weak field metric is

$$\mathrm{d}s^2 = (1 + 2\Psi)\,\mathrm{d}t^2 - a^2(t)(1 - 2\Phi)\,\mathrm{d}\mathbf{x}^2 , \tag{6.9}$$

from which the equation for the time-gravitational potential, Ψ, can be derived:

$$\nabla^2 \Psi = \frac{16\pi G}{3} \bar{\rho}_\mathrm{m} \delta - \frac{1}{6} \delta R , \tag{6.10}$$

and a similar equation for the space-gravitational potential, Φ:

$$\nabla^2\Phi = \frac{8\pi G}{3}\bar{\rho}_{\rm m}\delta + \frac{1}{6}\delta R \ . \tag{6.11}$$

Non-relativistic particles are accelerated by the time potential, $\ddot{\mathbf{x}} = -\nabla\Psi$, but lensing is governed by the lensing potential $\Phi_{\rm L}$, which is the sum of space and time potentials:

$$\nabla^2\Phi_{\rm L} = \frac{1}{2}\nabla^2(\Psi + \Phi) = 4\pi G\bar{\rho}_{\rm m}\delta \ , \tag{6.12}$$

which is the same as the standard gravity result. Lensing is therefore not sensitive to the modification whereas non-relativistic particles are, via the Ψ Poisson equation (6.11), which means that dynamical mass and lensing mass estimates will be different for $f(R)$ models (Schmidt et al. 2009). The quasi-static f_R equation can be derived from equation (6.6), subtracting the background $\bar{f}_R$:

$$\nabla^2\delta f_R = \frac{1}{3}\delta R - \frac{8\pi G}{3}\bar{\rho}_{\rm m}\delta \ , \tag{6.13}$$

since the value of f_R can change depending on environment, modifications to gravity that depend on environment are possible via the Poission equation (6.11). Note that in standard gravity $\delta R = 8\pi G\bar{\rho}_{\rm m}\delta$ and therefore $\Phi = \Psi$, but in HS07 models this is not true because the δR–$\delta\rho$ relation depends on f_R gradients.

6.2.1 Perturbation theory

If δR is small compared to the average background $\bar{R}$ at a particular epoch, it can be approximated as

$$\delta f_R \approx \left.\frac{{\rm d}f_R}{{\rm d}R}\right|_{\bar{R}} \delta R \equiv \frac{1}{3}\lambda^2\delta R \ . \tag{6.14}$$

In the case of the HS07 model

$$\lambda^2 = -3(n+1)\frac{f_{R0}}{R_0}\left(\frac{R_0}{\bar{R}}\right)^{n+2} \ , \tag{6.15}$$

where λ is known as the Compton wavelength. This is because equation (6.6) can be interpreted as a Klein-Gordon type equation

$$\Box\phi = V'(\phi) \tag{6.16}$$

with the mass being given by $V''(\phi) \sim m^2$ when evaluated about a stationary point. The Compton wavelength is then $\lambda = 1/m$ and gives the approximate scale over which effects of the scalar are felt. Note that in such theories $f_{R0} < 0$ so that $\lambda > 0$ and that $\bar{R}$ depends on time according to equation (6.7). With this relation between δR and δf_R, equations (6.10) and (6.13) can be used to eliminate δR and δf_R in (comoving) Fourier space. The resulting equation for Ψ_k is

$$-\frac{k^2}{a^2}\Psi_k = 4\pi G\bar{\rho}_{\rm m}\delta_k\left[\frac{4}{3} - \frac{1}{3}\left(\frac{1}{1+\lambda^2k^2/a^2}\right)\right] \ . \tag{6.17}$$

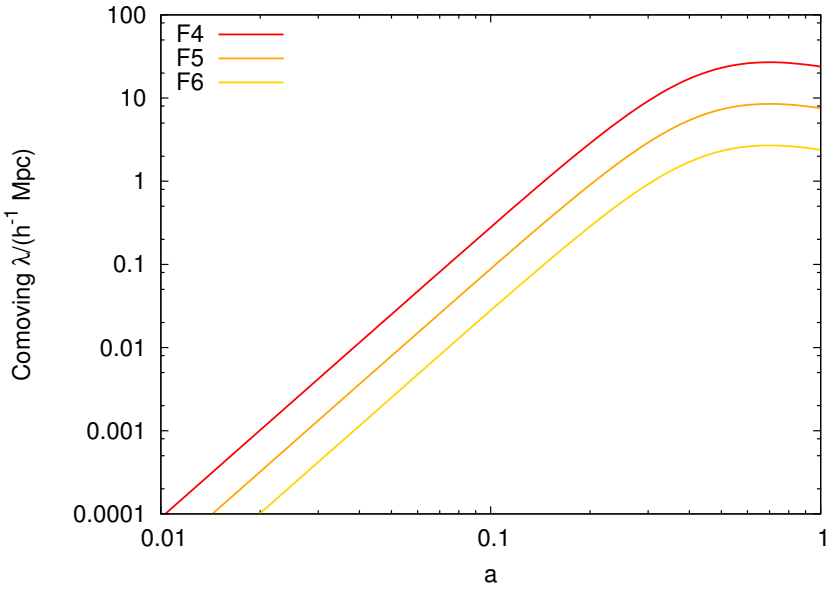

Figure 6.1: The comoving Compton wavelength in a standard ($\Omega_{\rm m} = 0.3$, $\Omega_\Lambda = 0.7$) ΛCDM background as a function of scale factor for models F4 ($f_{R0} = -10^{-4}$, $n = 1$), F5 ($f_{R0} = -10^{-5}$, $n = 1$) and F6 ($f_{R0} = -10^{-6}$, $n = 1$) from equation (6.15). The Compton wavelength governs the scale below which gravity is enhanced in the linear regime by the factor 4/3. As the strength of the modification increases larger scales are affected by the enhancement. While $\Omega_{\rm m}(a) \sim 1$ the wavelength scales like $\lambda \propto a^{3(n+2)/2}$. As $\Omega_{\rm m} \to 0$ the scale can be seen to begin to decrease, which is due to the modification becoming less important as matter becomes more dilute.

The perturbation equation is sourced by the Ψ Poisson equation (6.11), so the growth of perturbations is scale dependent:

$$\ddot{\delta}_k + 2H\dot{\delta}_k = \frac{3}{2}H^2\Omega_{\rm m}(a)\delta_k\left[\frac{4}{3} - \frac{1}{3}\left(\frac{1}{1+\lambda^2k^2/a^2}\right)\right] \ ; \tag{6.18}$$

on large scales $\lambda k/a \ll 1$, the term in brackets is approximately equal to 1, and the perturbation equation is identical to that in ΛCDM . However on scales smaller than the comoving Compton wavelength $\lambda k/a \gg 1$, gravity is then enhanced by the factor 4/3. For an $\Omega_{\rm m} = 1$ model, at large scales, the growth is $\delta \propto t^{2/3} \propto a$ as usual but at small scales growth is enhanced and this becomes $\delta \propto t^{(\sqrt{33}-1)/6} \propto t^{\sim 0.791} \propto a^{\sim 1.19}$. The comoving Compton wavelength is plotted for various f_{R0} values in Fig. 6.1.

The only part of the linear theory calculation that depends on the specific form of $f(R)$, as long as $f'(R)$ is small, is how λ relates to parameters in the specific function $f(R)$. It is generally true that any $f(R)$ theory with a ΛCDM background expansion and $f'(R) \ll 1$ can produce at maximum a 4/3 enhancement in the strength of gravity. All that changes is λ, the scale at which the modification becomes important, the general expression for which is

$$\lambda^2 = 3\left.\frac{{\rm d}^2 f(R)}{{\rm d}R^2}\right|_{\bar{R}} \ . \tag{6.19}$$

In Fig. 6.2 the numerical solution for the linear growth factor as a function of k is shown for small perturbations at various different redshifts, and a series of different f_R models, all with $n = 1$ and $f_{R0} = -10^{-4},\ -10^{-5}$ and -10^{-6}. These three models are used throughout this chapter. In Fig. 6.3 the same information is shown but the linear growth factor is normalised relative to standard gravity at $z = 0$ at all scales, rather than to the $z = 0$ case of the specific model in question. This allows the enhanced growth, relative to standard gravity, to be seen more and clearly this quantity is more relevant if models are considered to have the same initial conditions, which corresponds to them all having the same primordial CMB. In Fig. 6.4 the logarithmic growth rate of small perturbations is shown where enhancements compared to the ΛCDM prediction can be seen at small scales. Although bear in mind that the growth rate is suppressed from 1 as Λ comes to dominate anyway, so really these plots show that less suppression is being seen at small scales in the HS07 than ΛCDM would predict.

6.2.2 The Chameleon Mechanism

A remarkable feature of HS07 models is that they have the potential to 'chameleon screen' the effect of the modification in dense regions. This was first discussed for general scalar field models by Khoury & Weltman (2004). Screening potentially allows stringent tests of gravity within the Solar System to remain satisfied, while modifying gravity on larger scales and still retaining effective ΛCDM expansion on the largest scales. As shown in the previous section $f(R)$ theories with $f_R \ll 1$ have a Compton wavelength; for scales smaller than this gravity is enhanced by a factor of 4/3. Clearly this applies at the smallest scales and thus $f(R)$ models could enhance gravitational forces within the Solar System at a level that could have been already detected. Although note that the value set for G is that measured in the Solar System, so that one would really be looking for a 3/4 diminishment in gravity on cosmological scales. However, clearly the Solar System is far removed from the perturbative regime so one needs to explore exactly how an $f(R)$ model behaves in dense environments in order to say what deviations from standard gravity they might predict within the Solar System. The equations for Ψ and δf_R are

$$\nabla^2\Psi = \frac{16\pi G}{3}\bar{\rho}_{\rm m}\delta - \frac{1}{6}\delta R\ , \tag{6.20}$$

$$\nabla^2\delta f_R = \frac{1}{3}\delta R - \frac{8\pi G}{3}\bar{\rho}_{\rm m}\delta\ . \tag{6.21}$$

In regions where $\nabla^2\delta f_R = 0$, *i.e.* minima of the effective potential, then

$$\frac{1}{3}\delta R = \frac{8\pi G}{3}\bar{\rho}_{\rm m}\delta\ . \tag{6.22}$$

Using this to eliminate δR from the Ψ field equation means that

$$\nabla^2\Psi = 4\pi G\bar{\rho}_{\rm m}\delta\ , \tag{6.23}$$

and thus gravitational forces are restored to the standard.

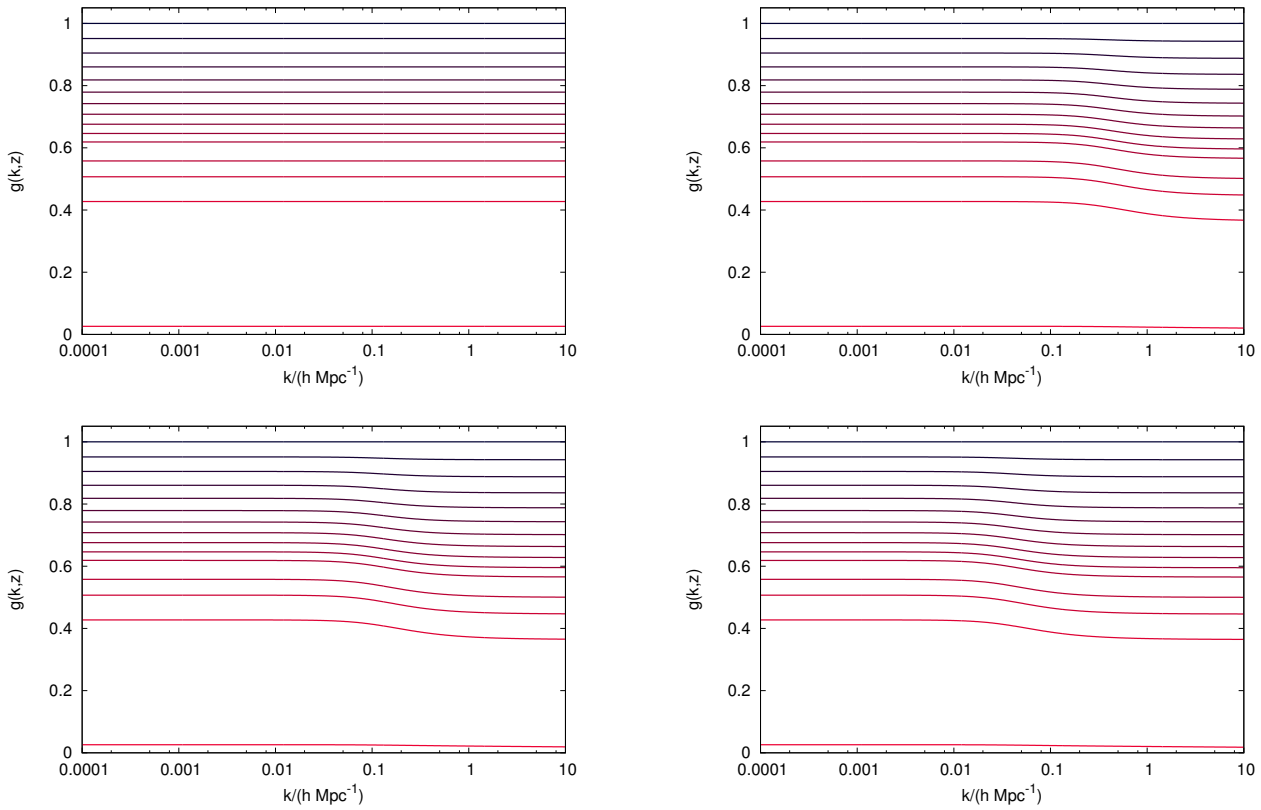

Figure 6.2: Linear growth factors in the quasi-static limit for standard ΛCDM (top left), F6 (top right), F5 (bottom left) and F4 (bottom right) all defined such that $g(k, 0) = 1$. Curves are for redshifts from $z = 0.0$ (top, black) 0.1, 0.2, ..., 0.9, 1, 1.25, 1.5, 2, 49 (bottom, red) in each panel. That the growth rate is normalised at $z = 0$ means that perturbations can be seen to be evolving faster at small scales in the modified models, this is seen as a *suppression* in their growth factors at small scales. Perturbation growth is clearly altered most for the F4 model, which is that most different from standard gravity. The lowest curve is completely flat because the modification to gravity is irrelevant at such high redshift.

For a given model it is then necessary to discover in which environments this condition is satisfied and thus which environments are screened. This is non-trivial given that the problem in necessarily non-linear. The combined equations must be solved for a given density distribution from the external cosmological value all the way into the internal structure of the density distribution in question. This can either be solved in a cosmological context by simulations (*e.g.* Li et al. 2012; Puchwein et al. 2013) or by direct calculations (*e.g.* Hu & Sawicki 2007a; Lombriser et al. 2012a) in situations of symmetry. The result of calculations and simulations is that the modification to gravity is able to be screened in dense environments for certain HS07 parameter values. For $n = 1$ models the transition of the field from the cosmological regime into the Solar System can be used to place limits of $|f_{R0}| < 10^{-5}$ (Hu & Sawicki 2007a). Alternatively limits can be placed by looking at environments that should be unscreened, even

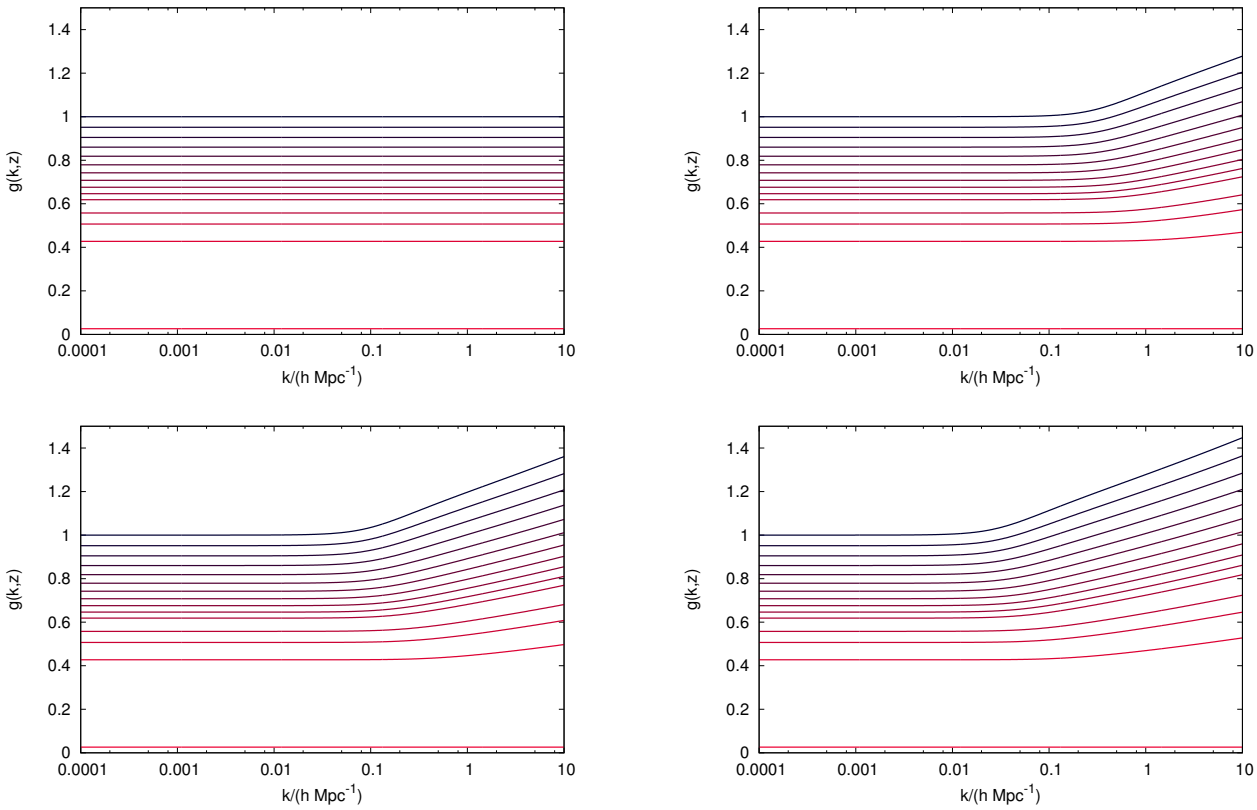

Figure 6.3: The linear growth factors in the quasi-static limit for standard gravity ΛCDM (top left) and models F6 (top right), F5 (bottom left) and F4 (bottom right) all relative to the standard gravity ΛCDM case at $z = 0$. Curves are for redshifts from $z = 0.0$ (top, black) 0.1, 0.2, ..., 0.9, 1, 1.25, 1.5, 2, 49 (bottom, red) in each panel. The enhancement of growth in the HS07 models relative to ΛCDM can clearly be seen at small scales. Perturbation growth is most enhanced for the F4 model, which is that most different from standard gravity. The lowest curve is completely flat because the modification to gravity is irrelevant at such high redshift.

when the Solar System is screened, such as dwarf galaxies (Jain et al. 2013) and much the same level of constraint is obtained. Independent constraints can be placed from large-scale structure measurements, particularly from the abundance of clusters, which increases in HS07 models, owing to the enhanced σ_8 for set initial conditions (*i.e.* the same primordial CMB). Constraints from clusters yield $|f_{R0}| < 10^{-4}$ (Schmidt et al. 2009; Lombriser et al. 2012b; Ferraro et al. 2011; Lombriser et al. 2012c). Note that it is theoretically feasible that the modification to gravity couples only to dark matter (if the HS07 model is thought of in terms of a scalar field; Lombriser 2014), and that this would invalidate Solar System and Galactic constraints on HS07 parameters, potentially meaning that it could only be constrained on cluster or cosmological scales. It should also be noted that $f(R)$ models exhibit chameleon screening fairly naturally, without it having to be introduced 'by hand', and so even if one is tempted to disagree with the specifics of the HS07, it serves as an example of the type of changes that are plausible with

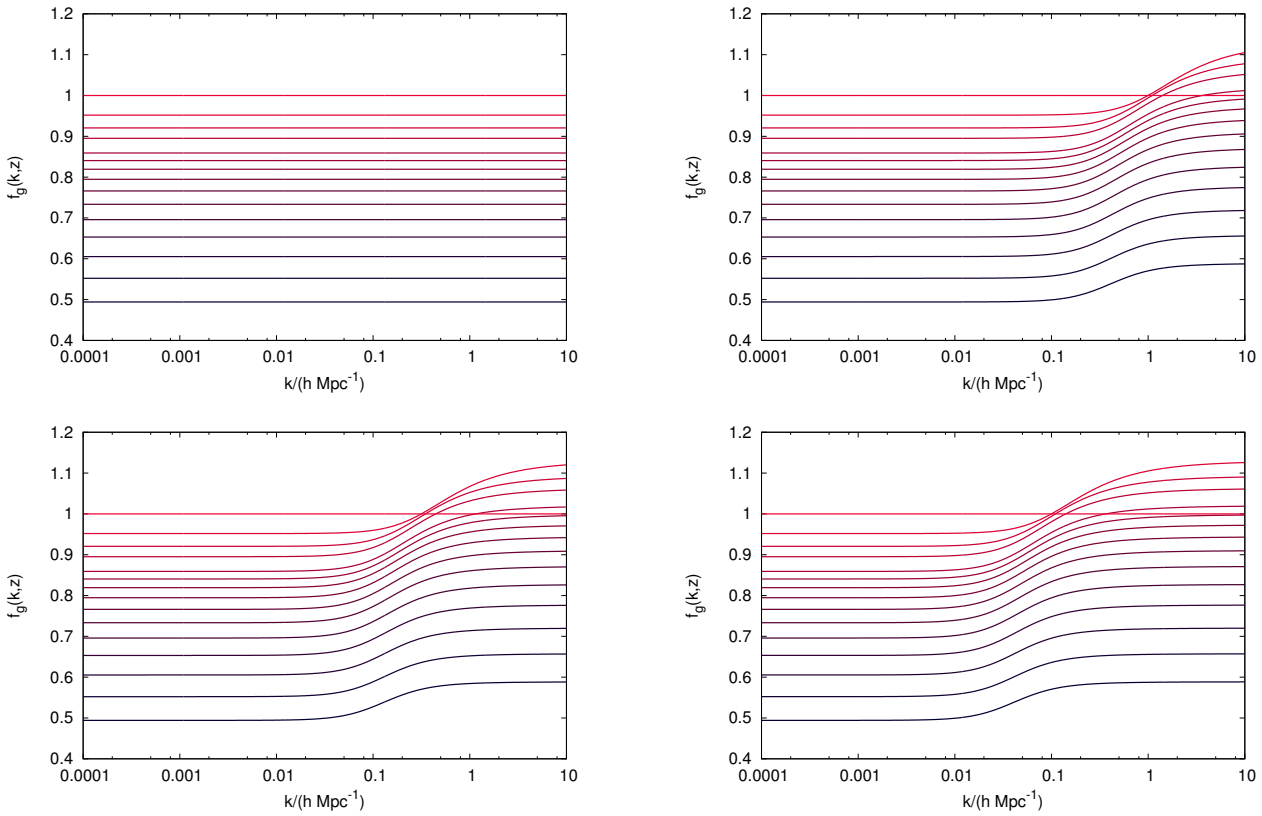

Figure 6.4: The linear logarithmic growth rates in the quasi-static limit for standard ΛCDM gravity (top left) and models F6 (top right), F5 (bottom left) and F6 (bottom right) all relative to the standard gravity case at $z = 0$. Curves are for redshifts from $z = 0.0$ (bottom, black) 0.1, 0.2, ..., 0.9, 1, 1.25, 1.5, 2, 49 (top, red) in each panel. The differing growth rates in the HS07 models relative to ΛCDM can clearly be seen at small scales. The $z = 49$ curve is flat in each case because the Compton wavelength is very small in this case (see Fig. 6.1). Perturbation growth is clearly enhanced more for the F4 model, which is that most different from standard gravity. The ΛCDM result, which should apply on large scales, is $f_g \approx \Omega_{\rm m}^{0.55}(a)$. At small scales for the most amount of modification possible for a $\Omega_{\rm m} = 1$ HS07 model is $g \propto a^{\sim 1.19}$ so the curves should never exceed $f_{\rm g} = 1.19$. The $z = 49$ curve is completely flat because the modification to gravity is irrelevant at such high redshift.

relatively simple gravitational modifications.

6.3 Simulations

An N-body simulation must calculate the gravitational forces on all particles and evolve their positions over time according to these forces. This is complicated in $f(R)$ models, even with a standard background expansion, because it is also necessary to solve the field equation for f_R, gradients in which provide an extra force on the particles. However, recently codes have been developed to do just this (PM only methods – Oyaizu 2008; Oyaizu et al. 2008; `ECOSMOG` – Li

et al. 2012; MG-GADGET – Puchwein et al. 2013). A simulation will solve equations for Ψ and f_R (equations 6.11 and 6.13) together in the quasi-static limit.

In practice, the required perturbations from the background, $\delta R = R - \bar{R}$, can be expressed using the definition of R in terms of f_R (equation 6.5),

$$R = R_0 \left(\frac{f_R}{f_{R0}} \right)^{1/(n+1)} , \tag{6.24}$$

so that

$$\delta R = R_0 \left(\frac{f_R}{f_{R0}} \right)^{1/(n+1)} - 3H_0^2 \left(\Omega_{\rm m} a^{-3} + \Omega_\Lambda \right) , \tag{6.25}$$

where the second term is $\bar{R}$ defined in equation (6.7). δf_R will be known (stored in cells) so can be used to compute δR. Particle positions, and the δf_R field, can then be updated using equations (6.11) and (6.13). Initial perturbations in the f_R field can be set via the linear perturbation result between δf_R, the matter perturbation δ using the linear result $\delta f_R = \lambda^2 \delta R/3$. Together with the Poisson equation for f_R this is

$$-\frac{k^2}{a^2} \delta f_{R,\mathbf{k}} = \frac{\delta f_{R,\mathbf{k}}}{\lambda^2} - \frac{8\pi G}{3} \bar{\rho}_{\rm m} \delta_{\mathbf{k}} , \tag{6.26}$$

so that perturbations in f_R can be matched with perturbations in δ in Fourier Space via

$$\delta f_{R,\mathbf{k}} = \frac{H^2 \Omega_{\rm m}(a) \lambda^2}{1 + \lambda^2 k^2 / a^2} \delta_{\mathbf{k}} . \tag{6.27}$$

At small scales $\delta f_{R,\mathbf{k}}$ is suppressed relative to $\delta_{\mathbf{k}}$ due to the inverse k^2 term and so the linear δf_R field will be less featured on small scales than the linear overdensity.

Simulation data for this chapter were kindly provided by Baojiu Li, and were run using the ECOSMOG code of Li et al. (2012), which is based on the N-body code RAMSES (Teyssier 2002).This N-body code uses adaptive meshes to solve the coupled Ψ and f_R Poisson equations, and does not use a particle-particle or tree algorithm to calculate short range forces, so the resolution of these simulations is different than GADGET-2 runs discussed elsewhere in this thesis. ECOSMOG runs in the approximation that the background expansion is exactly ΛCDM and so the modification due to gravity is only present via the δf_R field in equation in (6.13). This covers f_{R0} values that are interesting observationally but will break down as the limit $|f_{R0}| \ll 1$ ceases to be true.

This chapter analyses data from simulations of standard gravity and some HS07 models. These all start from the same initial conditions with 512^3 particles run from grid initial conditions in a box with $L = 512\,h^{-1}\,{\rm Mpc}$ and are summarised in Table 6.1. The cosmological parameters are $h = 0.697$, $\Omega_{\rm m} = 0.281$, $\Omega_{\rm b} = 0.046$, $\Omega_\Lambda = 0.719$, $n_{\rm s} = 0.971$, $\sigma_8 = 0.82$. An initial power spectrum was generated using the MPGRAPHIC code (Prunet & Pichon 2013) with the standard values of the CMB temperature $T_{\rm CMB} = 2.7255$ K, effective number of neutrinos $n_{\rm eff} = 3$, and Helium mass fraction $Y_{\rm He} = 0.24$. The particle mass in each case is $\simeq 7.80 \times 10^{10}\,h^{-1}\,{\rm M}_\odot$. Each simulation has exactly the same power spectrum at $z_{\rm i} = 49$, the same cosmological parameters and therefore background expansion rate, which means that

Simulation	n	f_{R0}	True σ_8
GR	-	-	0.820
F6	1	-10^{-6}	0.834
F5	1	-10^{-5}	0.875
F4	1	-10^{-4}	0.940

Table 6.1: Simulations of standard gravity and HS07 models run for the work in this chapter. All models have $n = 1$ but differing values of f_{R0} (see equation 6.4). All simulations start at $z_\mathrm{i} = 49$ in a cube of length $512\,h^{-1}\,\mathrm{Mpc}$ from exactly the same initial conditions file. It follows that σ_8 at $z = 0$ will be different in each case due to the different linear growth in the HS07 models, this is shown in the table. Note that the F4 model has a very different σ_8 from GR despite having the same initial conditions, whereas the F6 case is very similar to GR.

observers in each case will see exactly the same CMB sky, with the possible exception of foreground effects such as the integrated Sachs-Wolfe (ISW) effect. The σ_8 value quoted is that in the standard gravity model: since it is defined as an integral over the linear power spectrum grown to $z = 0$ this means that the true σ_8 will be larger in the modified gravity models due to the enhanced growth at small scales; the true σ_8 for the modified models is given in Table 6.1. The linear growth factors for this set of cosmological parameters are shown in Fig. 6.3 and the rates in Fig. 6.4. To get the true σ_8 values in the HS07 models, the linear power must be multiplied by the scale-dependent growth factor and then the variance computed in an $8\,h^{-1}\,\mathrm{Mpc}$ sphere in the standard way (equation 1.100). The $z = 0$ linear power spectra for each model is shown in Fig. 6.5 together with the non-linear spectrum measured in each simulation at $z = 0$. These enhancements agree well with similar results for simulated matter power shown in Li et al. (2012) and Lombriser et al. (2013a) amongst others. The non-linear enhancement in power is less strong than the linear enhancement, partly due to the chameleon effect but also partly due to the different non-linear velocity fields and this effect can also be found in simulations with scalar fields with no screening mechanism (Li et al. 2013).

6.4 The calibrated halo model

As discussed above, modifications to gravity produced by the HS07 models can be thought of as a modified linear growth rate combined with a chameleon mechanism that can return gravity to the standard form in some haloes, depending upon their mass and environment. The obvious way of incorporating this into the framework of the calibrated halo model (see chapters 3 and 4) is to change the 2-halo term so that it uses the correct linear power for the HS07 model with scale-dependent growth:

$$\Delta^2_{\mathrm{2H}}(k,z) = g^2(k,z)\Delta^2(k,0)e^{-k^2\sigma_\mathrm{v}^2}\,, \tag{6.28}$$

where the exponential term accounts for the damping of the BAO (see equation 4.4).

The 1-halo term will be modified by the relation between ν and M because δ_c is a function

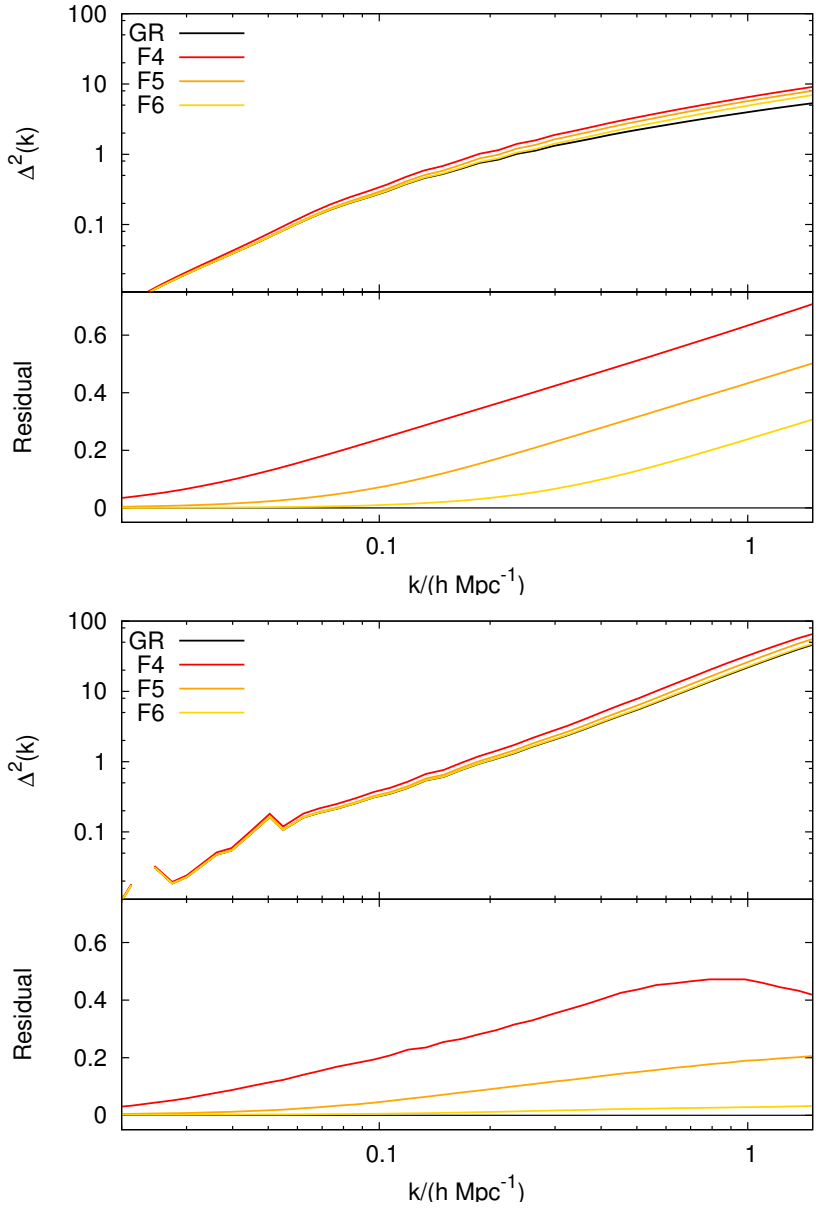

Figure 6.5: The $z = 0$ linear theory power spectrum (upper panel) and measured non-linear power (lower panel) for each of the HS07 models together with that of a standard gravity (GR) model and residuals to this. The models are identical but for the modification to gravity by the parameter f_{R0}. An enhancement in power at small scales can be seen in each model with the enhancement being most pronounced in the F4 case. At large scales all the models agree exactly because they share exactly the same power spectrum at high z and the growth factor is equal in all models at large scales (Fig. 6.3). One can see that the relative enhancement of power in the linear regime for each HS07 model is diminished in the full non-linear simulation, which is due to chameleon screening. This is seen at its most extreme in the F6 case where the full non-linear spectrum only deviates from GR at the few % level at $k = 1\,h\,\mathrm{Mpc}^{-1}$ compared to the $\simeq 20\%$ deviations seen in the linear spectrum.

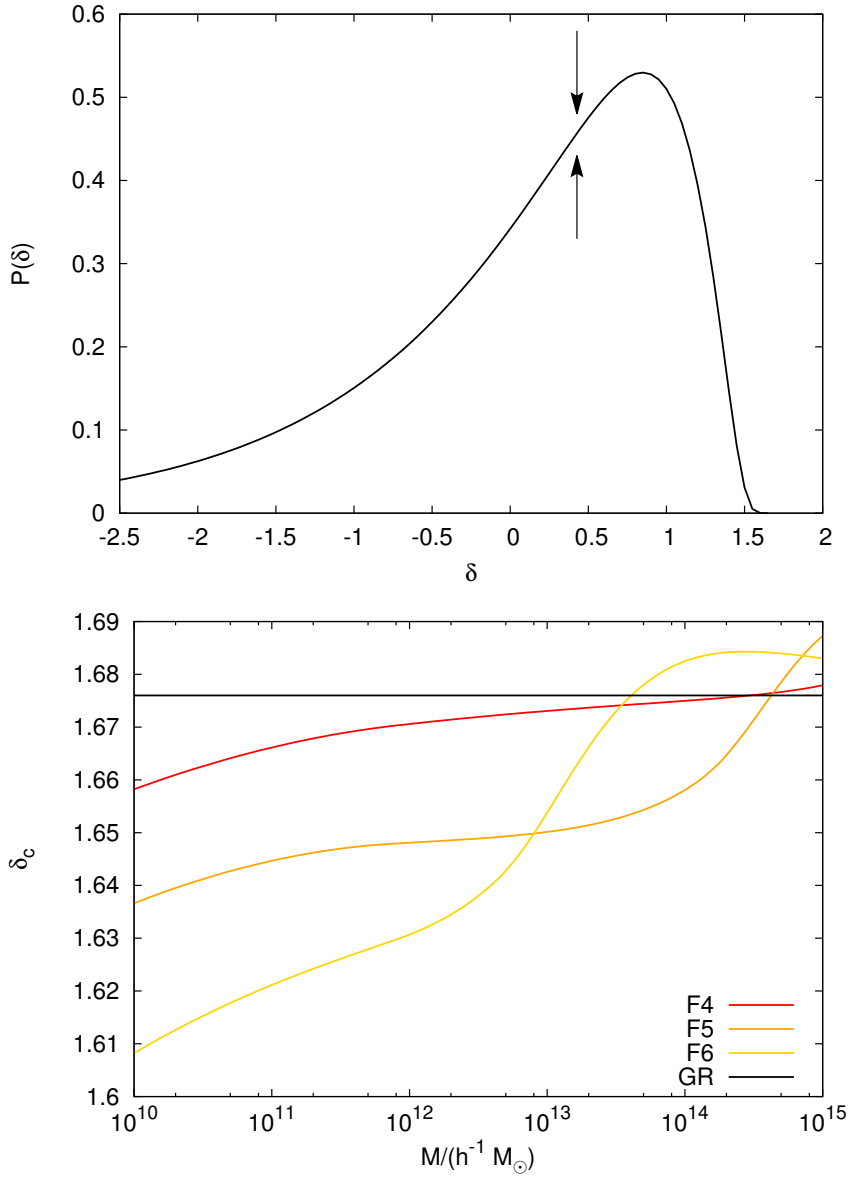

Figure 6.6: The upper panel shows the probability distribution of environments, defined with a filter of width $5\,h^{-1}\,$Mpc, parametrised by δ. For the calculations of $\delta_{\rm c}$ shown in the lower panel the mean environment is taken, which is shown by the arrows in this figure at $\delta_{\rm env} \simeq 0.43$. $\delta_{\rm c}$ shown here is such that when divided by the true $\sigma(M)$ for the cosmology in question it gives the correct value of ν. The flat black line is the GR prediction of $\delta_{\rm c} = 1.676$ for the ΛCDM cosmology in question. Haloes are screened in all models with this screening being most pronounced in the F6 case where the largest deviations are observed. That the curves rise above the GR line at high masses is due to them being scaled with the weak field version of σ, which does not contain any information about screening (see Fig. 6 of Brax & Valageas 2013). In Schmidt et al. (2009) it was shown that for maximum gravity enhancement $\delta_{\rm c} \simeq 1.692$ in HS07 models.

of M in these models to account for screening and because $\sigma(M)$ is computed via an integral over the linear matter power spectrum, which is different in each case. In this way this work follows the approach of Lombriser et al. (2013b) to model the halo mass function. For the models discussed here $\delta_{\rm c}(M)$, which is the result of a spherical model calculation (Lombriser et al. 2013b), is plotted in the lower panel in Fig. 6.6. The result of the spherical model calculation will depend on environment in which the halo resides as this determines the local background value of f_R. The probability distribution of environment can be calculated via an excursion set approach (Parfrey et al. 2011; Li et al. 2012). The distribution of environments for the cosmology in question is shown in the upper panel of Fig. 6.6 and it is from this that an approximate average halo environment of $\delta_{\rm env} \simeq 0.43$ is taken. Taking an average should be appropriate for the power spectrum given that the halo model prediction effectively averages over all haloes of each mass. With this in mind it makes sense to modify $\sigma(M)$ in the halo model to use the correct linear power spectrum for each model and also to modify $\delta_{\rm c} = 1.525$ (the value set in the calibration in Chapter 4) by the ratio of the theoretical prediction for the HS07 models to that of ΛCDM :

$$\delta_{\rm c}(M) = 1.525\frac{\delta_{\rm c}(M)}{1.676} \ , \tag{6.29}$$

where 1.676 is the ΛCDM prediction for the simulated cosmology.

The 1-halo term should also change because halo virial radii will change via $\Delta_{\rm v}$ in the spherical model, and also because the concentration-mass relation should be different given that haloes form at different times depending upon the model and also due to the different gravity law and velocity structure (*e.g.* Lombriser et al. 2012a). However, the simulations discussed in Section 6.3 have different resolution effects compared to those discussed elsewhere in this thesis. This is due to the adaptive mesh techniques employed by `ECOSMOG`; it is not certain how the mesh refinement criteria, combined with a finite number of particles, affect the eventual matter distribution on small scales. Therefore as a first step towards testing the power of the halo model, only the linear power and $\delta_{\rm c}$ are modified. Since $\delta_{\rm c}$ is the parameter that affects the halo model prediction for the power at the largest scales (Fig. 4.4) it makes sense to investigate shifts in this parameter first.

A halo model calculation based on an altered linear power spectrum and $\nu(M)$ relation is shown in Fig. 6.7. Here one can see that the halo model calculation is $\sim 10\%$ low compared to the simulations in all cases, across the range of k where the simulated power is not noisy, even in the standard gravity case. This is plausibly due to resolution issues with the simulations themselves because they have different convergence properties compared to `GADGET-2` runs due to adaptive mesh techniques being employed. Fig. 4.1 shows how power is damped at high k in simulations of finite resolution although there is no obvious way to equate the resolution of `ECOSMOG` with a finite mesh refinement level, to that of `GADGET-2` with a finite force softening. Additionally only a single realisation of each model is being considered (see the scatter in Fig. 4.1) and this can introduce considerable scatter, even at non-linear scales, due to mode coupling. Recall that in Chapter 4 the power spectrum measured in simulations was fixed to account for

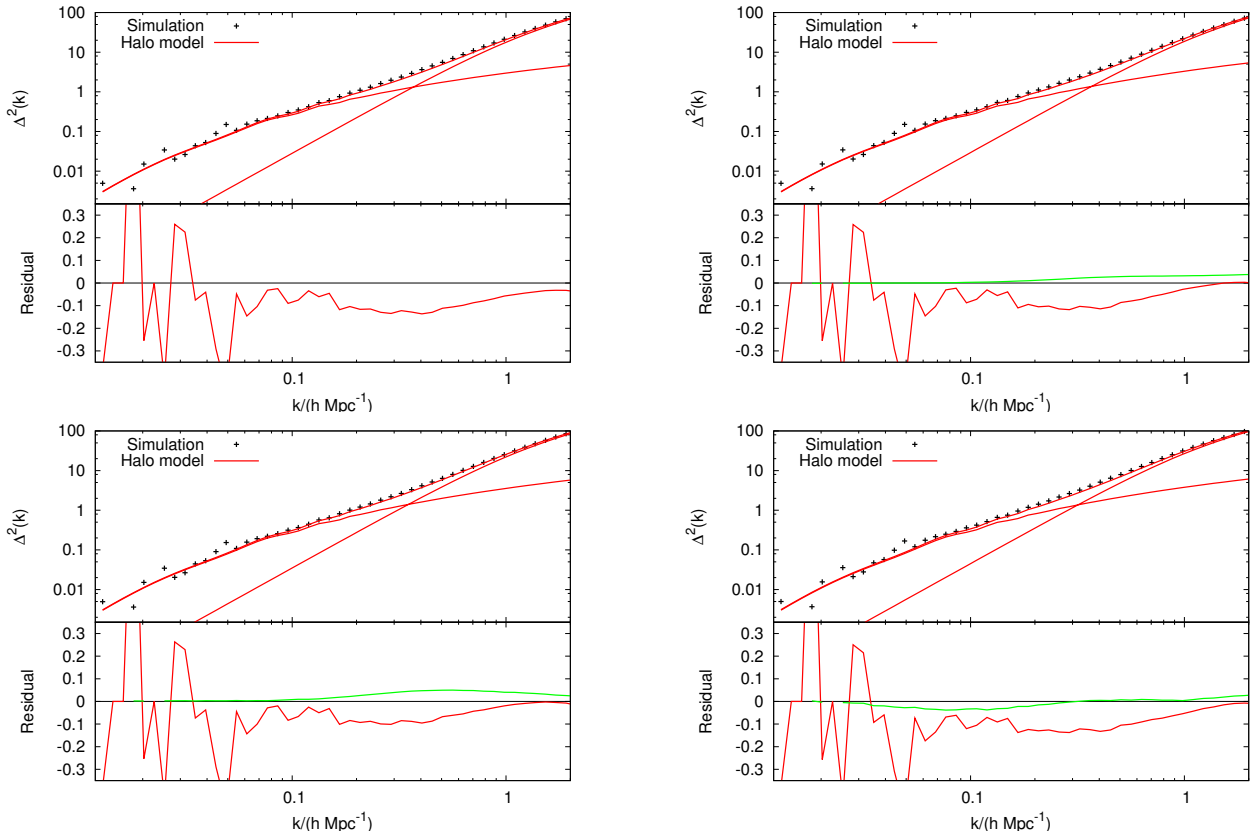

Figure 6.7: The power spectrum from the calibrated halo model compared to that in simulations: GR (top left) and models F6 (top right), F5 (bottom left) and F4 (bottom right). One can see that although the prediction is universally low by $\sim 10\%$ the form of the full power spectrum is matched well in each case. If one instead takes the halo model prediction for standard gravity to be true, and corrects the simulated power in each of the HS07 models using this power ratio, then the agreement is good for all models at the 5% level (green residual curve) but better than this across most scales.

the finite resolution, which has not been done here. The halo model used here was accurately calibrated to standard gravity simulations in Chapter 4, so one would not expect it to be so wrong for a simple ΛCDM model. This conclusion is bolstered if one compares the halo model prediction for the cosmology in question to that predicted by the Coyote emulator of Heitmann et al. (2014), shown in Fig. 6.8, where disagreements are only seen at a maximum 5% level around $k = 0.3\,h\,\mathrm{Mpc}^{-1}$, being much better both below and above this scale. With this in mind it is reasonable to take the halo model ΛCDM prediction as true and then force the ΛCDM simulation power to agree with this, the same factor can then be adopted as a first estimate of the correction to be applied to the HS07 simulations. If one then compares the halo model prediction to these fixed simulations the result is the green curve in the residual panels in Fig. 6.7, where the halo model prediction is good to the 5% level across the range of scales shown. If one is uncomfortable with considering the ΛCDM halo model prediction to be 'true' in this

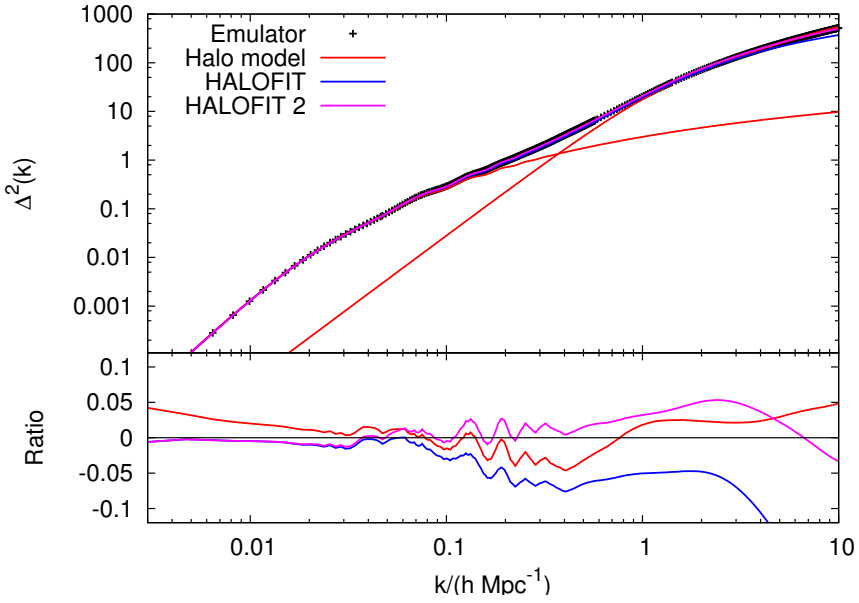

Figure 6.8: A comparison of the calibrated halo model prediction for the matter power spectrum to that of the Coyote Emulator of Heitmann et al. (2014). The Coyote prediction can be considered to be the 'truth' here (at the 3% level) because the authors went to great length to assure simulations had converged over the scales that they give emulator predictions. This shows that the halo model prediction is good to the 5% level across the range of scales shown; with the most severe excursion being the low prediction around the 1- to 2-halo transition scale around $k = 0.3\,h\,\mathrm{Mpc}^{-1}$. The poor performace of the halo model at very large scales is due to the unphysical shot noise contribution of the 1-halo term at these scales. The predictions here can be compared to the halo model prediction shown in Fig. 6.7 with the inevitable conclusion being that the particular realisation of the `ECOSMOG` prediction is low across the range in the standard gravity case.

case (given the 5% disagreement seen in Fig. 6.8) one can consider these green curves to show a residual of the comparisons of the ratio of halo model predictions to the ratio of simulated predictions. In any case, it is remarkable that such a good match to the data is possible without any additional tuning of the calibrated halo model. This can be compared with the results for `HALOFIT` shown in Li & Hu (2011) and Li et al. (2013) and results for an uncalibrated halo model shown in Schmidt et al. (2009) or Lombriser et al. (2013a), where it can be inferred that the calibrated model performs better than either of these two approaches.

6.5 Rescaling

In this section the rescaling algorithm, developed in Chapter 5, is applied to modified gravity theories. In doing so an attempt is made to keep the theory as general as possible, within the confines of theories with scale dependent growth, screening mechanism and a ΛCDM background expansion. However, tests are restricted to HS07 models at this stage.

Scale dependent growth requires the rescaling method to be modified, or clarified, slightly. In computing the best fit scaling between simulations, the original AW10 procedure minimises the differences in variance between the two models across a range of scales. As noted, it is unclear if this is the best course of action given that the aim of this is to match the mass function, which one might assume would be better matched by minimising the difference in $\nu = \delta_{\rm c}/\sigma(R)$, where the change in $\delta_{\rm c}(M)$ can potentially take into account the spherical model in the chameleon screened theory (or even a theory with Vainshtein screening *e.g.* Galileon models: Nicolis et al. 2009). However it has been shown by Schmidt (2008) and Li & Hu (2011) that the Sheth et al. (2001) mass function works well in HS07 models if one computes the variance using the true linear power spectrum with the correct scale-dependent growth:

$$\sigma^2(R) = \int_0^\infty g(k,z)\Delta^2(k,0)W^2(kR)\,{\rm d}\ln k \ . \tag{6.30}$$

Note that this means that σ no longer scales trivially with the growth factor, as it does in standard gravity. To test this Fig. 6.9 shows the mass function measured in simulations together with predictions from the ST mass function, in one case taking $\delta_{\rm c}$ fixed and in the other case using $\delta_{\rm c}$ varying as a function of mass as per the chameleon screening calculation shown in Fig. 6.6. In both cases σ is computed as per equation (6.30). One can see that across the range of mass shown, which corresponds to the masses probed by the simulations, there is very little difference in using either prescription for the mass function. This relates to the fact that $\delta_{\rm c}$ only differs from the ΛCDM result by a few % for the range of masses shown. Therefore, in this chapter rescaling parameters s and z are chosen exactly as before by simply minimising the difference in σ, rather than ν, even though it is acknowledged that a ν minimisation may be preferable in general. This might be more important if one is dealing with a simulation that resolves smaller haloes where the chameleon screening alters the collapse threshold more (see the low mass part of Fig. 6.6).

In the displacement field step of AW10 one must also take account of scale dependent growth when correcting the displacement field on a mode-by-mode basis (equation 5.8). The obviously correct thing to do here is to use the true $\Delta^2_{\rm lin}(k,z)$ for the modified gravity models. Slightly less obviously, the original method described in Chapter 5 reassigned bulk velocities via

$$\mathbf{v} \to \mathbf{v}' = s\frac{a'H'f'_{\rm g}}{aHf_{\rm g}}\mathbf{v} \ ; \tag{6.31}$$

but since there is no universal growth rate in these models (it is scale dependent) for modified models this approach cannot be followed. Instead one can use $f_{\rm g}(k_{\rm box},z)$, where $k_{\rm box} = 2\pi/L$, since the bulk velocity of the box is that which is being scaled. Note that for the type of cosmological volumes usually simulated the modification to gravity at the scale of the box will be negligible, so the growth rate used here will be almost exactly the ΛCDM one. Velocities are then also corrected on a mode-by-mode basis (equation 5.25) and the scale-dependent growth rate can be included explicitly in this step.

In this section the results of rescaling a standard ΛCDM simulation to the various HS07 models discussed earlier are shown. To do this it was necessary to run a ΛCDM simulation

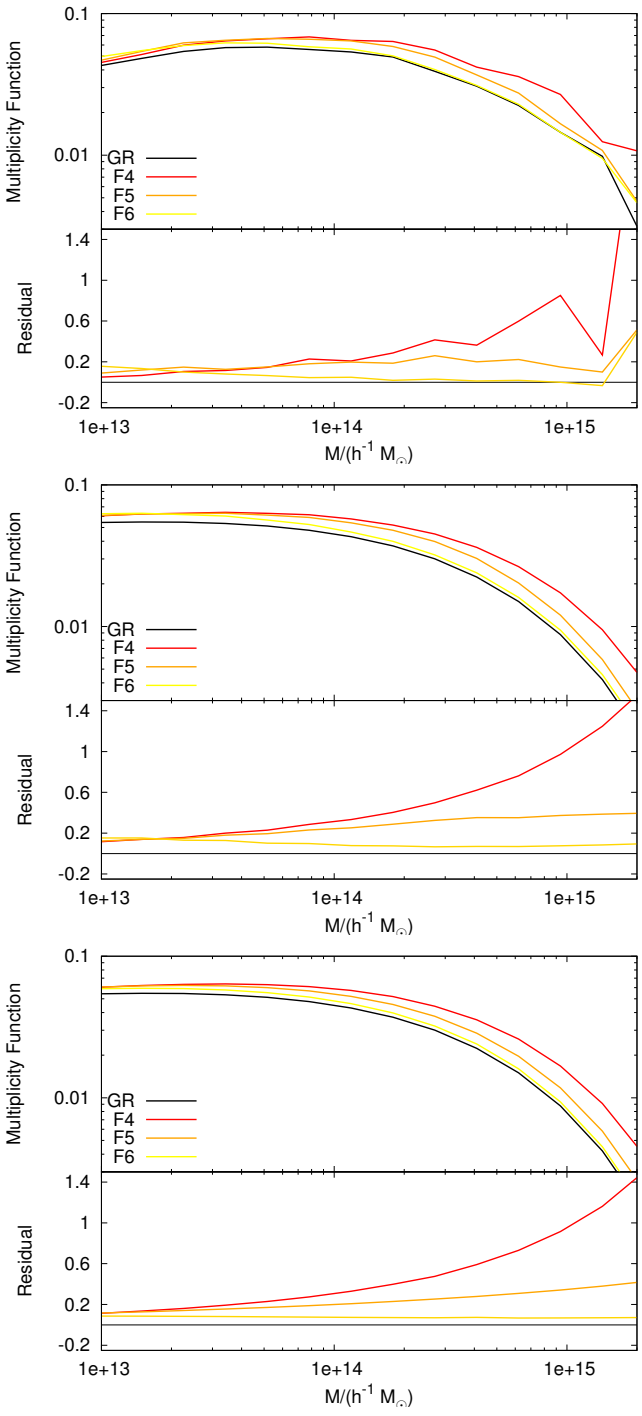

Figure 6.9: The mass function measured in the simulations listed in Table 6.1. The top panel shows the measured mass function while the lower two panels show theoretical predictions; the middle panel being ST using $\delta_c(M)$ shown in Fig. 6.6 while the lowest panel shows the same mass function with fixed $\delta_c = 1.686$. In both cases $\sigma(R)$ has been calculated using the modified growth rates for the HS07 models. Although the matches are similar it should be noted that they are perhaps slightly better at the low mass end if one uses the $\delta_c(M)$ prescription, particularly for the F6 case.

Original	Target	s	z	$k_{\rm NL}$
ΛCDM	F6	0.85	0.47	0.164
ΛCDM	F5	0.85	0.38	0.151
ΛCDM	F4	0.85	0.25	0.136

Table 6.2: Best fit scaling parameters between the high σ_8 ΛCDM cosmology discussed in the text and the various HS07 models. $s = 0.85$ was chosen as being a good value for all 3 scalings and then the corresponding z was determined for each model with $s = 0.85$ fixed. This allows scalings to all the HS07 models to be made from a single parent simulation.

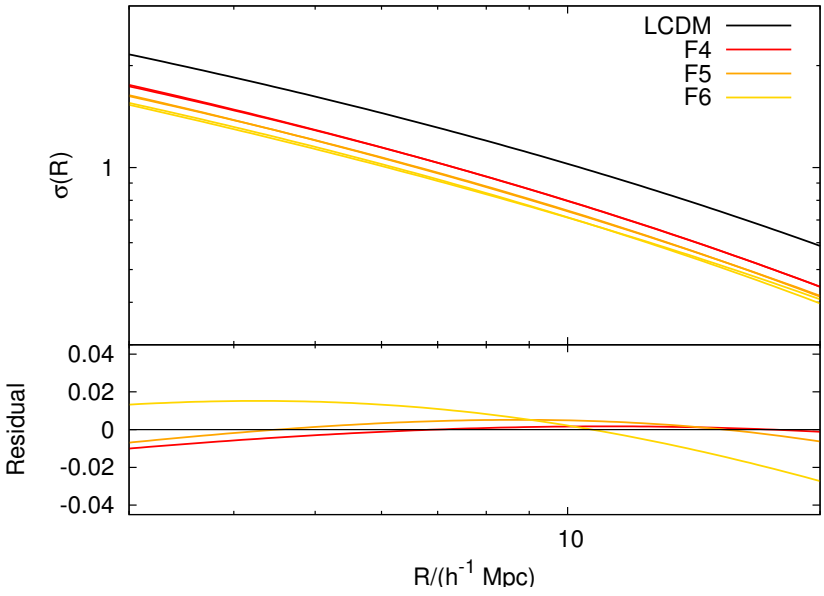

Figure 6.10: Theoretical fractional residuals of $\sigma(R)$ for the modified gravity models compared to ΛCDM after scaling in size and redshift by values given in Table 6.2. In the upper panel two coloured curves are shown for each model, one being the simulation and the other the rescaling, although they cannot be distinguished and so the residual differences are shown in the lower panel. Note that the $F6$ model matches slightly less well than the other two models but that the agreement is good to 2% for all models across the range of scales shown, which correspond to the mass range probed by the simulations.

with a high σ_8 value in order to cover the required range of fluctuation amplitudes (see Chapter 5). A standard gravity simulation was run using the same code as for the HS07 simulations discussed in Section 6.3. Specifically the transfer function was again computed using `MPGRAPHIC` with cosmological parameters $h = 0.7$, $\Omega_{\rm m} = 0.3$, $\Omega_{\rm b} = 0.045$, $\Omega_\Lambda = 0.7$, $n_{\rm s} = 0.97$, $\sigma_8 = 1.2$ and standard values of the CMB temperature $T_{\rm CMB} = 2.7255$ K, effective number of neutrinos $n_{\rm eff} = 3$ and Helium mass fraction $Y_{\rm He} = 0.24$. The box size of this simulation was chosen to match the best fit scaling value of $s = 0.85$ which implies $L = 602\,h^{-1}\,$Mpc. These simulation parameters imply a particle mass in the parent simulation of $\sim 1.35 \times 10^{11}\,h^{-1}\,{\rm M}_\odot$. It was

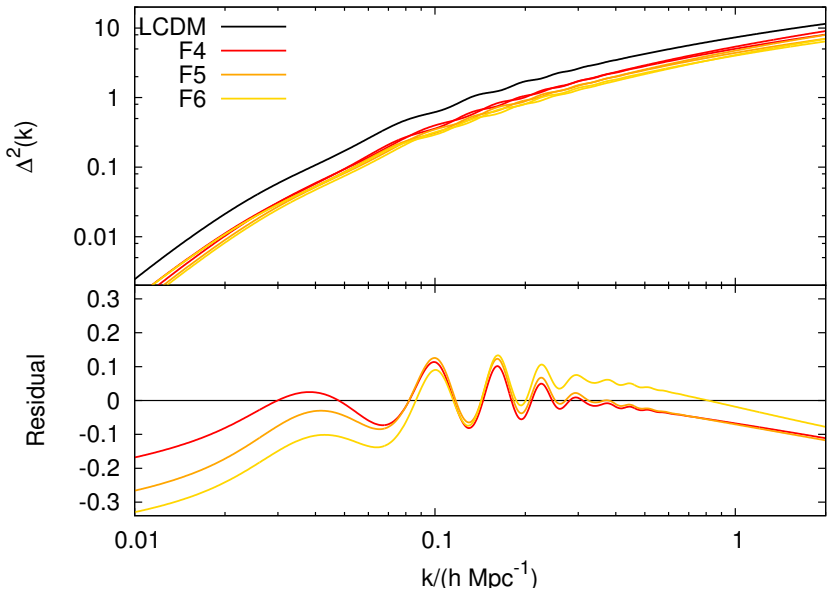

Figure 6.11: Residuals of the theoretical linear power spectrum for the modified gravity models compared to ΛCDM after scaling in size and redshift by values given in Table 6.2. In the upper panel two coloured curves are shown for each model, one being the simulation and the other the rescaling, the residual differences are shown in the lower panel which match at the 10% level around $k = 0.1\,h\,\mathrm{Mpc}^{-1}$ where a residual BAO can clearly be seen. Note the comparatively large disagreements at large scales and the fact that the $F6$ model matches in $\sigma(R)$ less well than the other two models. These differences in linear power are exactly what are corrected for by the displacement field step of the method.

decided to only run a single parent ΛCDM simulation and to see how effective it was to scale to each of the HS07 simulations from this. The value of $s = 0.85$ was chosen because the resulting $\sigma(R)$ was a good fit to each of the three HS07 models at the redshifts listed in Table 6.2 as shown in Fig. 6.10 where the match can be seen to be at the 2% level across the range of scales that correspond to halo masses in the simulations. The fractional residual linear power spectrum differences are shown in Fig. 6.11 where it can be seen that the spectra match at the 10% level around $k = 0.1\,h\,\mathrm{Mpc}^{-1}$ but residual BAO features are visible. The match degrades at the largest scales, particularly for the $F6$ model, which is different to the τCDM scaling case considered in Chapter 5.

The halo mass functions at each stage of the rescaling process are shown in Fig. 6.12, together with the residuals after both the size and redshift scaling have been applied. Surprisingly the mass function is better matched here than it was in the scaling from $\Omega_\mathrm{m} = 1$ case analysed in Chapter 5 with the match being at the 5% level. The larger deviations at the largest masses shown are probably due to the noise in these bins due to them containing few haloes. In general in HS07 models one would expect the mass function to exhibit strong environmental dependence and this has not been checked at this stage. However, it is comforting to know that the gross mass function is recovered well by the rescaling. This also supports the conclusion that the

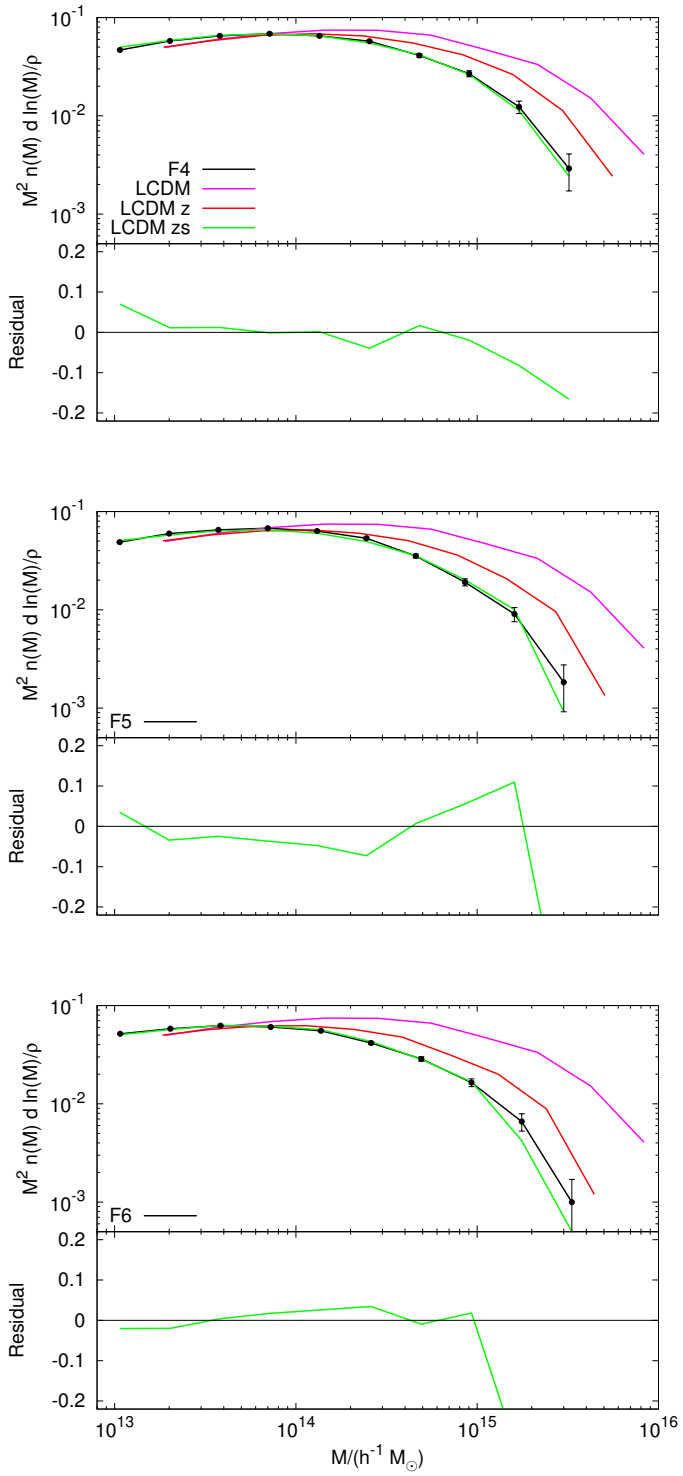

Figure 6.12: The mass functions, computed in 10 bins, of the ΛCDM simulations at each stage of the rescaling process to models F4 (top), F5 (middle) and F6(bottom). The target HS07 model is shown in black, with Poisson errors due to finite halo numbers, while the pink curve shows the ΛCDM simulation curve at $z = 0$, the red curve shows the result of scaling in redshift (LCDM z) and the green curve shows additionally scaling the box size (LCDM zs). The mass functions are matched well (mainly at the 5% level) across the entire range for each model which is due to $\sigma(R)$ being matched well across the range.

mass function can be well modelled for HS07 models using a Sheth et al. (2001) type argument with the correct $\sigma(R)$ value used; at the level investigated here nothing more complicated needs to be done.

The results of rescaling the particles according to the original AW10 prescription are shown in Fig. 6.13 where the rescaled matter and monopole power spectra are shown and in Fig. 6.14, where the full redshift space residuals are shown. The matter power spectrum of particles can be seen to match the HS07 simulations at the 5% level across the range of scales shown for all models. Importantly no large deviations are seen at the largest scales shown are observed which is good given that the linear spectra disagree at up to the 30% for the F6 model at large scales, so the ZA correction is quite severe here. The F4 model seems to be best matched across all scales which is probably because the chameleon effect is relatively unimportant in this model and it behaves simply as a ΛCDM model with an enhanced growth rate. Larger deviations are seen at small scales in the F5 and F6 cases which is plausibly due to the chameleon mechanism operating in these models and the fact that this has not been accounted for at this stage of the rescaling. Studies have found that halo concentration varies very little when comparing HS07 models to ΛCDM (Schmidt et al. 2009; Lombriser et al. 2013b) and this is plausibly the reason for a relatively good match in real space at non-linear scales, without manipulating halo properties. At the level of the monopole one can see that the spectrum is recovered well up to the non-linear scale (arrow) but with small biases at the largest scales shown, which may be due to the linear power being very different at these scales. However, large differences can be seen at non-linear scales, particularly for the F4 case (15% at $k = 1\,h\,\mathrm{Mpc}^{-1}$; not shown in plot) in which gravity is probably universally enhanced by 4/3 for all haloes. Based on the good match for the matter power in this model for non-linear scales one would expect the halo profiles to be very similar in both the target and rescaled case – the difference must therefore be due to the incorrect FOG in the rescaled case, caused by the enhanced halo velocity dispersion in the $F4$ case. This can be seen to be the case in the 2D plot in Fig. 6.14, where the power in all non-transverse modes are strongly over-predicted by the scaling in the F4 and F5 cases.

One might therefore hope that better results could be obtained by manually altering halo velocity dispersions once scaling had been completed. A naive calculation for the dispersion would be

$$\sigma_{\mathrm{v}}^2 \propto \frac{GM}{r_{\mathrm{v}}} \,, \tag{6.32}$$

given that the halo masses should be identical due to the scaling (see the match in the mass function in Fig. 6.12), and that the virial radii should be similar due to $b = 0.2$ being used to define haloes, means that σ_{v} should be enhanced by $\sqrt{4/3}$ due to the enhancement in G. Halo velocity dispersions are shown in Fig. 6.15 in both the rescaled and target simulations together with the effect of enhancing this dispersion in the rescaled case by the factor $\sqrt{4/3}$. In the F4 and F5 cases this can be seen to bring the dispersions in line with the targets, reflecting that chameleon screening is less important in these models, at least on average, for the range of masses shown. In the F6 case the initially correct dispersions are too high after being

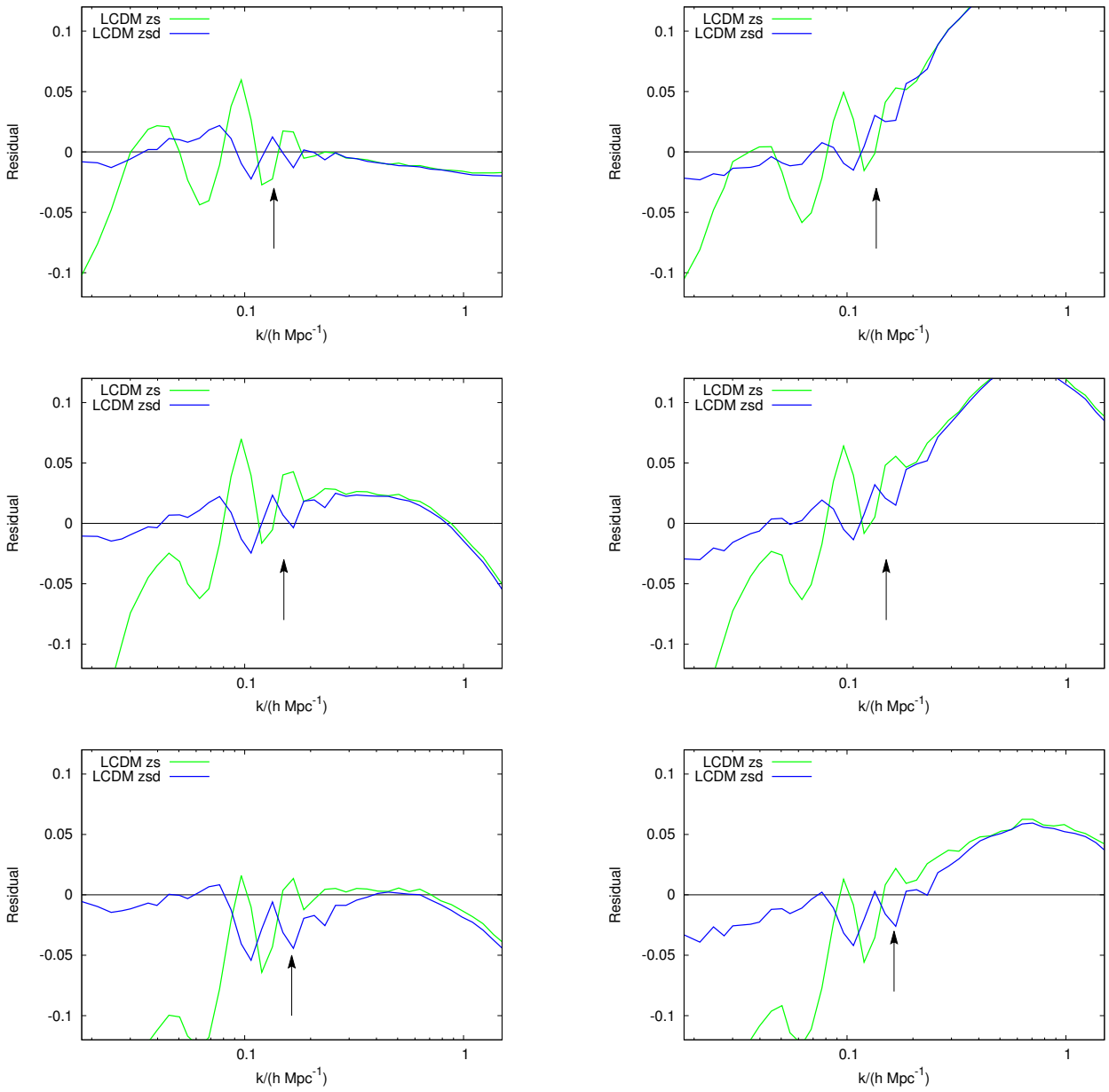

Figure 6.13: The matter power spectra (left column) and redshift-space monopole (right column) from scaling the full ΛCDM particle distribution to F4 (top), F5 (middle) and F6 (bottom). In each case the green curve shows the scaling in size and redshift while the blue curve shows the result of applying the additional extra displacements. The black arrow shows the non-linear scale which is slightly different for each model. The matter power spectrum is matched at the 3% level but least well in the F6 case (dip around BAO) and this could plausibly be due to the fact that the chameleon mechanism has not been incorporated at this stage. Note the large errors for the monopole at small scales, the equivalent error for the τCDM to ΛCDM scaling was 5%, which is only comparable to the F6 case. That the non-linear redshift space error is much more severe here in the F4 and F5 cases reflects the very different halo velocity dispersion in these HS07 models with least screening (see Fig. 6.15).

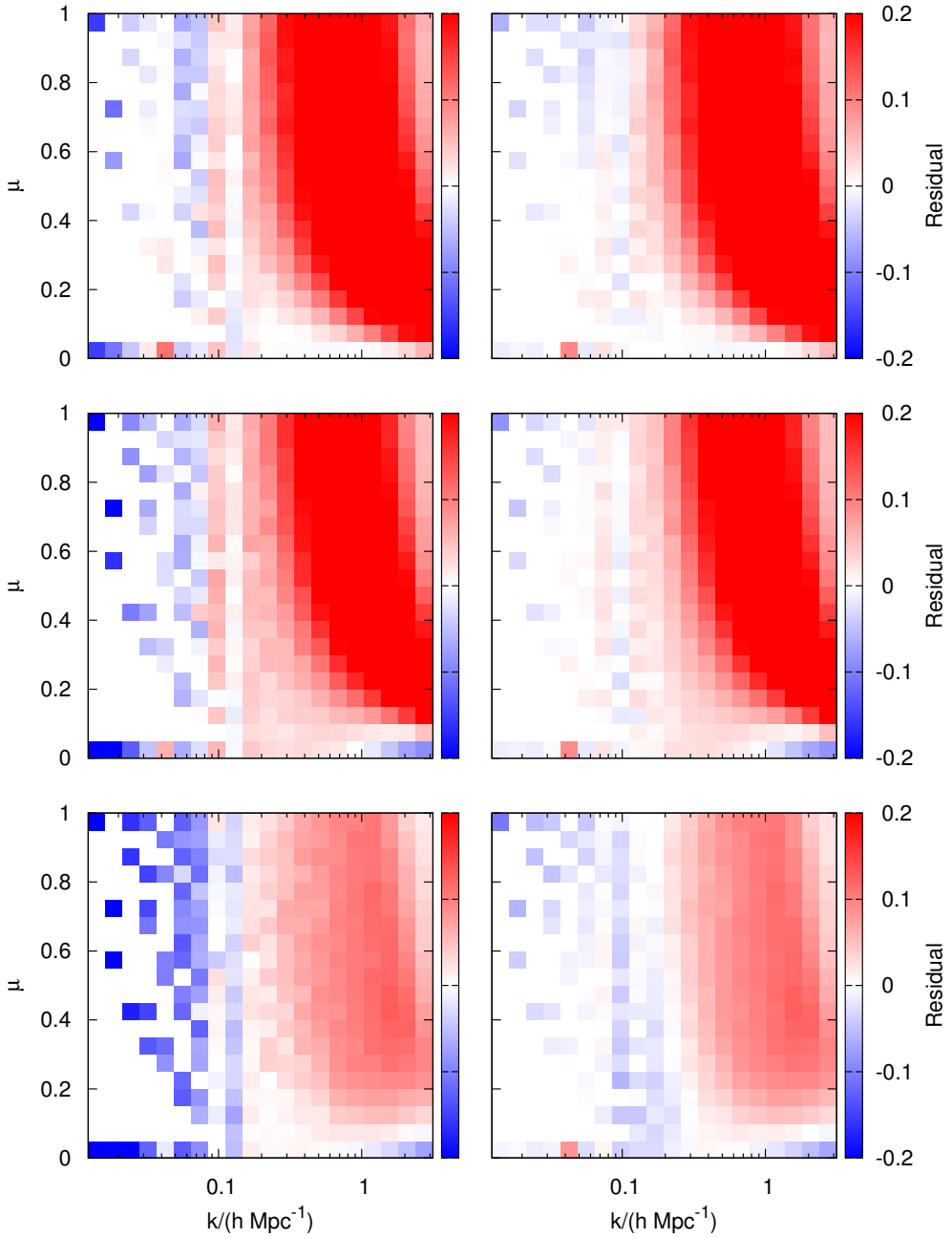

Figure 6.14: The residuals in 2D redshift space for the F4 (top row), F5 (middle row) and F6 (bottom row) modes when just the size and redshift parts of the rescaling method have been applied (left column) and when additionally modifying the displacement field (right column). This is the original AW10 method but applied to modified gravity simulations. The residual BAO seen noisily across all μ at large scales can be seen to be efficiently removed by the rescaling procedure (left to right column). Residual differences are then mainly concentrated at high μ values at small scales and thus must be due to incorrect FOG features after the rescaling. Only minor differences are seen for $\mu = 0$ transverse modes which indicate that halo structure is similar in both cases. The coluor bar is saturated in the top two panels, the maximum error reaches 33% in the F4 case and 34% in the F5 case.

boosted by $\sqrt{4/3}$, which reflects the action of the chameleon mechanism here. The enhanced halo velocity dispersion is consistent with that seen in simulations (*e.g.* Lombriser et al. 2012a; Arnold et al. 2013). Although note that in general this enhancement should depend on both mass and environment for each HS07 model (*e.g.* Lombriser et al. 2013b) and this has not been investigated here at this stage.

The result of applying the rescaling algorithm directly to halo catalogues, developed in Chapter 5, is shown in Fig. 6.16. This rescaling includes the use of a biased displacement field for haloes, discussed in Section 5.4.1. The bias is calculated using the appropriate $\sigma(R)$ for each model and this has been shown (Schmidt et al. 2009) to provide a good match to halo bias seen in simulations. One can see that the halo power is matched at the 5% level across most of the scales shown in both the F4 and F5 case, with biggest deviation at the largest scales in line with what was seen previously. The F6 model is the least well recovered at the level of the halo power spectrum and this is plausibly because the chameleon mechanism is most strong in this model and this has not been taken into account at this stage. However, it is unclear what effect screening might have on the distribution of haloes and the poorer performance in the F6 may be because it is the case in which the displacement field correction is largest (see Fig. 6.11). However, it is good to see that other scales match well, particularly quite non-linear scales. Large excursions from the match are not seen at non-linear scales in the monopole, in contrast to the particle case, because the halo power is insensitive to FOG.

6.6 Discussion

It has been shown that the calibrated halo model and rescaling algorithm are easily adapted to take into account some of the complexity in modified gravity models. In each case the scale dependence of the growth rate can be naturally implemented into the pre-existing framework of both approaches. Non-linear features, such as differences in the mass function, can also be taken into account.

The end result for the calibrated halo model is that few % level predictions are possible for the matter power spectrum up to $k = 1\,h\,\mathrm{Mpc}^{-1}$. In order to test the calibrated halo model against HS07 simulations it was necessary to artificially correct the power to account for cosmic variance and finite resolution artificially suppressing power. In order to test the method more fully it would be necessary to have a suite of simulations for HS07 models (akin to that in Heitmann et al. 2009) that had been thoroughly checked for convergence. Due to the increased computer time necessary for solving the f_R field equation in these models this seems to be an unlikely prospect in the near future, particularly given that there are many modified gravity scenarios other than HS07 to test. In light of this the method of fixing a calibrated ΛCDM power spectrum, such as that from Cosmic Emu, by a ratio of the same realisation of a modified model to a ΛCDM model seems to be the most economic way forward. Recent work by Baldi et al. (2014) showed that this approach works rather well even in simulations of combined

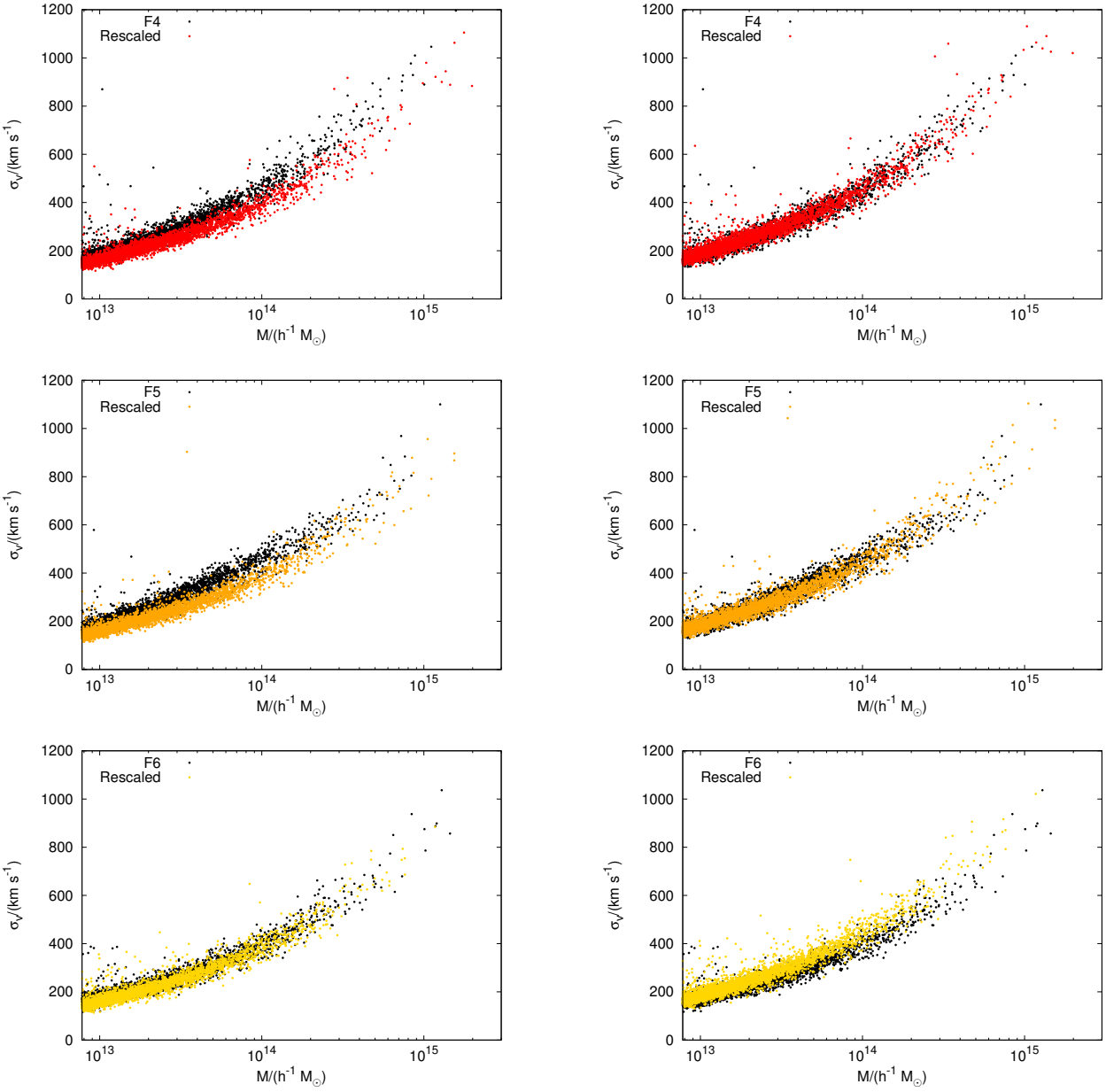

Figure 6.15: Halo velocity dispersions for 5% of haloes in the target simulation (black dots) compared haloes built from the rescaled particle distribution in the F4 (red; top), F5 (orange; middle) and F6 (yellow; bottom) cases (left column). One can see that dispersions are higher in the F4 and F5 cases, which is probably a reflection of the enhanced gravitational forces on small scales that remain unscreened in this model, if the rescaled halo dispersions are multiplied by a factor of $\sqrt{4/3}$, to account for the enhanced gravitational forces in these models, then the dispersions line up almost perfectly with the target (right column). In the F6 case one can see that halo dispersions agree without the scaling, this is due to the chameleon screening in this model. The mass dependence of this $\sqrt{4/3}$ correction as a function of model has yet to be investigated.

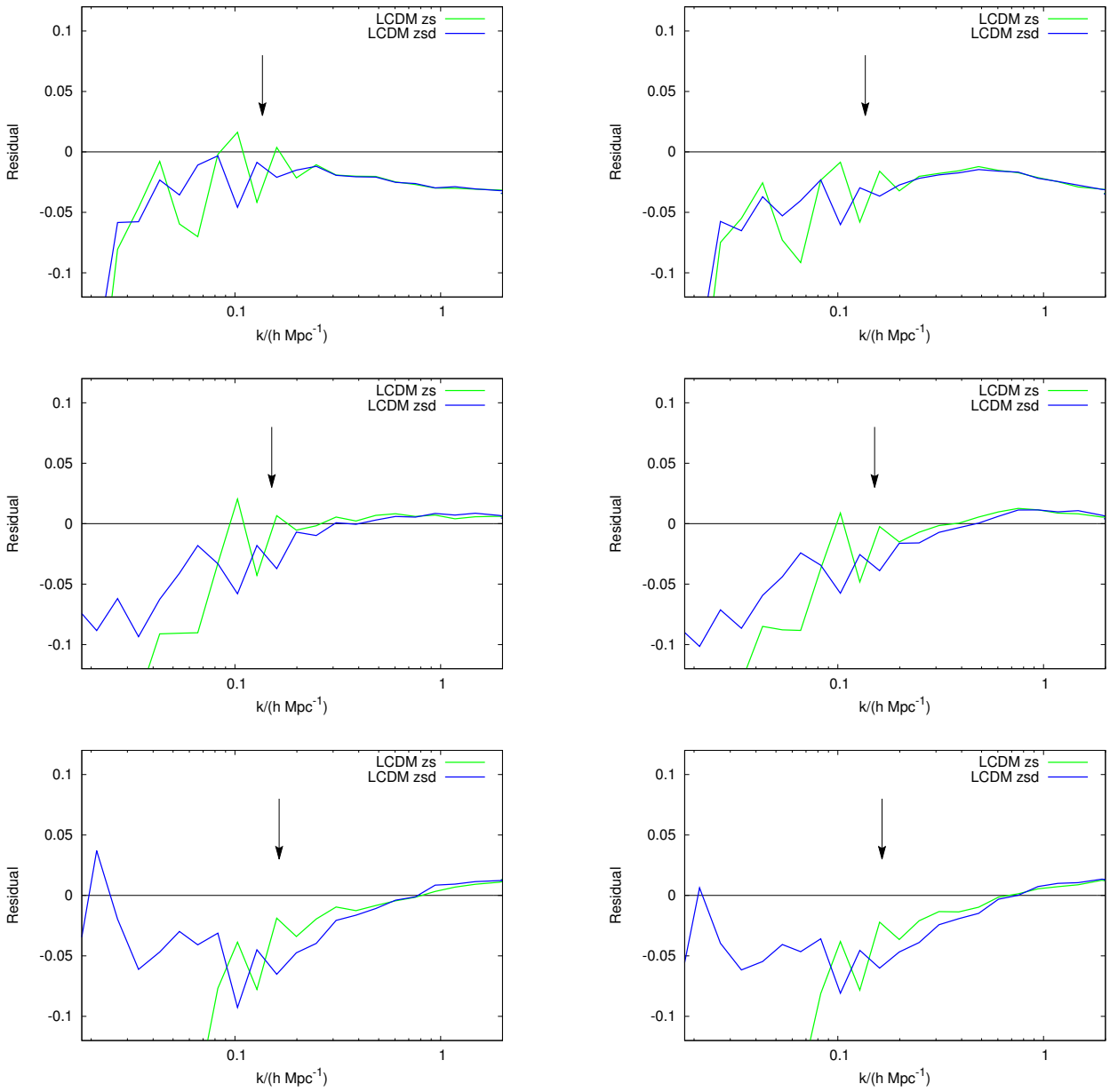

Figure 6.16: The power spectrum of haloes from scaling the full ΛCDM halo catalogue to F4 (top), F5 (middle) and F6 (bottom). The left column shows real space while the right column shows the redshift-space monopole. In each case the green curve shows the scaling in size and redshift (LCDM zs) while the blue curve shows the result of applying the additional extra displacements (LCDM zsd). After the full scaling the halo power is mainly matched at the 5% level for most of the scales shown, but larger discrepancies are seen at largest scales with the F6 model is the least well recovered across all scales, possibly because the chameleon mechanism has been ignored. The black arrow shows the non-linear scale which is slightly different for each model.

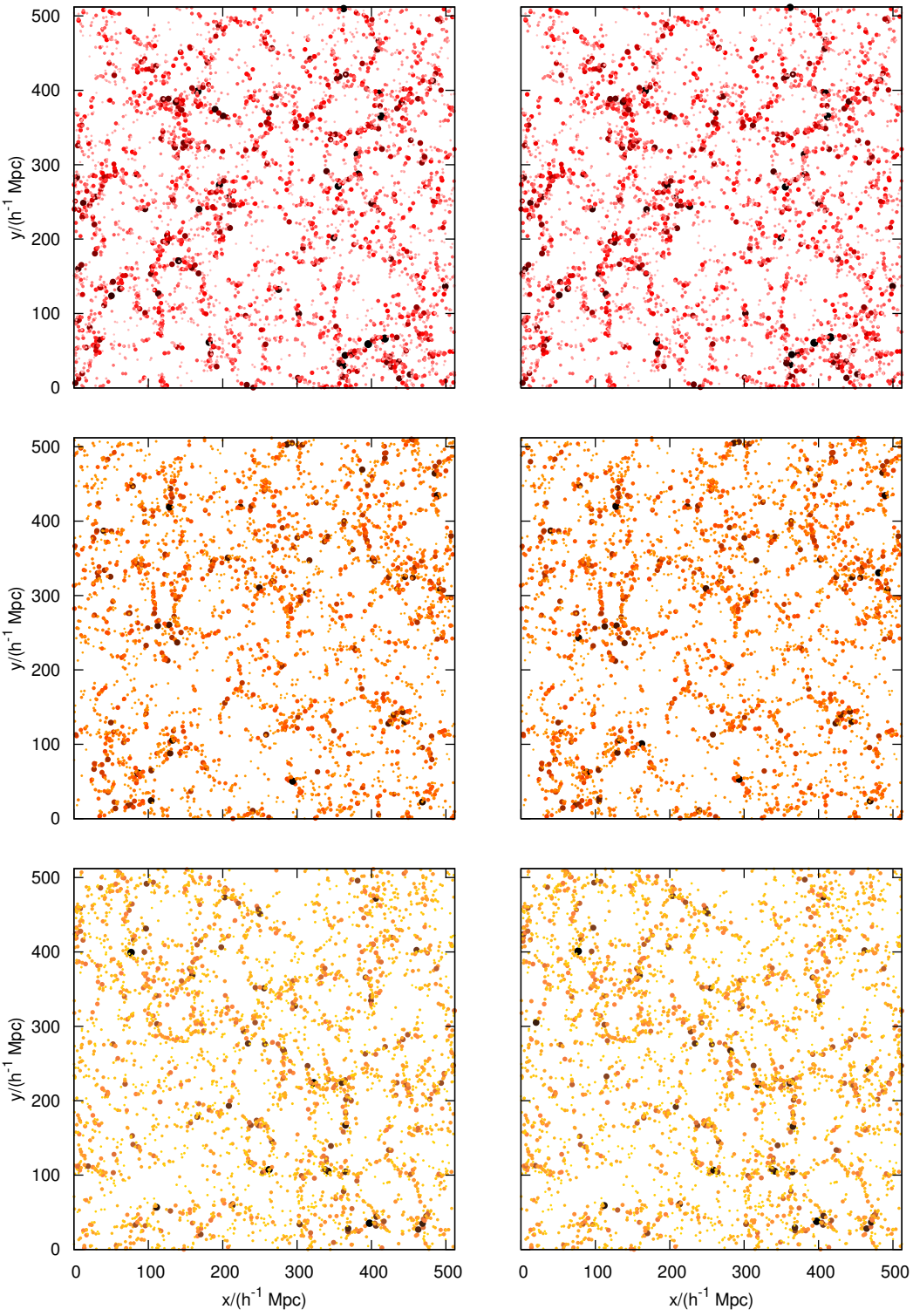

Figure 6.17: A visual summary of the rescaling of halo catalogues, shown as 25 h^{-1} Mpc slices through the simulation volume for the F4 (top), F5 (middle) and F6 (bottom) cases. The left column shows fully rescaled catalogues, using a size and redshift relabelling and a biased displacement field correction, while the right column shows real HS07 catalogues. In each case the same realisation of the initial conditions has been used. Differences are difficult to identify visually.

massive neutrinos and modified gravity where the effects of each seem to add quite linearly, even quite far into the non-linear regime of structure formation.

It would be useful to check the matter power spectrum calculation to smaller scales ($\simeq 10\,h\,\mathrm{Mpc}^{-1}$), but this would require more accurate simulations than those presented here. This is plausibly possible with the latest generation of modified gravity simulations if they are run in small enough boxes. This would also reveal more of the non-linear effects associated with chameleon screening in the models and may necessitate changing the mass-concentration relation or halo virial radius to reflect this. Recently Zhao (2013) recalibrated a version of `HALOFIT` to include HS07 parameters, the author claims this is accurate to 6% for large scales $k \leq 1\,h\,\mathrm{Mpc}^{-1}$ and 12% up to $k = 10\,h\,\mathrm{Mpc}^{-1}$. Zhao (2013) chose to fit `HALOFIT` to the ratio of power from the HS07 simulations to ΛCDM simulations in order to eliminate sample variance. Clearly testing the calibrated model presented here against this fitting formula, and both against higher resolution simulations, is a necessary next step.

By rescaling it was shown that accurate mock HS07 particle distributions and halo catalogues can be created from a pre-existing ΛCDM simulation or catalogue, in a way that their properties closely mimic those seen in HS07 simulations. Specifically the mass function is reproduced at the 5% level, with discrepancies likely to be caused by noise rather than biases, and power in both real and redshift space can be reproduced at the 3% level out to $k = 0.1\,h\,\mathrm{Mpc}^{-1}$. While the non-linear tail of power looks reasonable for the matter power spectrum, plausibly because HS07 models do not make large alterations to halo structure, the non-linear tail in redshift space is in error. It was shown that this error is due to incorrect velocity dispersions post scaling because the non-linear effect of an enhanced G has not been taken into account. Artificially increasing the velocity dispersion of haloes would cure this problem. In choosing rescaling parameters s and z it was chosen to use $\sigma(R)$ calculated from just linear theory, so in effect the chameleon mechanism has been ignored. Smaller volume simulations, particularly of the $F6$ model, would serve to highlight differences introduced by screening. It may then prove necessary to investigate if rescaling would be better achieved using a mass function with $\delta_{\mathrm{c}}(M)$ respected, and if the biased displacement field used to move haloes requires the use of a screened $b(M)$ relation.

The rescaling algorithm has been tested on both the particle and halo distribution, but it has yet to be tested on reconstituted haloes (or mock galaxy catalogues) that may plausibly be generated from the halo catalogues. Clearly the first step of such a prescription has been outlined but it will be necessary to investigate the effect of changing halo structure, both in real and velocity space has on the eventual reconstituted halo distribution. Clearly increasing the halo dispersion in the F4 and F5 cases will be a necessary first step.

So far environmental dependence has been ignored in rescaling; there is evidence of strong environment dependence in modified gravity models for quantities such as the halo mass function (*e.g.* Lombriser et al. 2013b) because spherical model calculations depend on the local value of background f_R field. If the rescaled halo catalogues and particle distributions respect this

dependence is yet to be seen, even in the case of standard gravity rescaling. Investigating this would be interesting given that rescaling only allows one to scale box quantities in a gross way, and there is no obvious way of including an environmental dependence in this. However, it is plausible that one might be able to introduce additional scalings, once the gross rescaling has taken place, to account for environmental effects.

Finally, it should be pointed out that the reason for focussing on HS07 models in this work was purely because of the availability of simulations. There are no features of most other modified gravity models that obviously make them unsuitable for the type of methods used in this chapter, although attempts to apply halo model type arguments to Galileon cosmological models (Barreira et al. 2014) have been more difficult than in the HS07 case.

Chapter 7

Summary and conclusions

7.1 Overview

Throughout this thesis theoretical techniques have been developed which should enable a more accurate, or more thorough, analysis of current and future large-scale structure data sets. Essentially the work in this thesis can be decomposed into two quite distinct pieces; the calibrated halo model, presented in Chapter 4 and the simulation rescaling algorithm, presented in Chapter 5, with Chapter 6 of this thesis applying both techniques to the modified gravity realm. The calibrated halo model was designed to produce accurate matter power spectra as a function of cosmological parameters in the non-linear regime. This is important for gravitational lensing analyses, which measure a version of the matter power spectrum integrated along the line of sight and therefore mixes small and large k modes; one is therefore not able to make a clean cut in k to remove problematic (not understood) scales in weak lensing. The halo rescaling algorithm, developed in Chapter 5, provides the basis for the quick generation of mock galaxy catalogues as a function of cosmology. These are necessary to test survey analysis methods and to generate covariance matrices. Current survey analysis is all conducted with suites of simulations of a specific cosmological model, while purporting to constrain many different cosmological models. Therefore being able to analyse a survey with cosmology dependent mock data lends weight to any conclusions that may be drawn from it. Cosmological surveys measure galaxies in redshift space, rather than the underlying matter power spectrum directly, and therefore the motion of galaxies within haloes are important, as is the bias of a galaxy population: haloes below a certain mass will not be populated and high mass haloes will be multiply populated. Clearly being able to produce accurate matter and halo distributions, with the correct velocity

field, as a function of cosmology is an important step in being able to produce accurate galaxy catalogues. Although there is considerable overlap in these two pieces of work conclusions will be discussed separately.

7.2 Calibrated halo models

7.2.1 Summary

It has been shown that the halo model can accurately reproduce power spectra that are measured from N-body simulations, even at small scales ($k \simeq 10\,h\,\mathrm{Mpc}^{-1}$), provided one is willing to introduce a small number of empirical modifications of its ingredients – in particular the parameters describing halo virialisation and concentration. Initially the halo model was calibrated using the power spectra of the Millennium Simulation at redshifts between 0 and 2. It was then shown that this calibrated halo model is able to accurately reproduce the small-scale power spectra in a range of different cosmologies without further adjustment. This success reflects the fact that the halo model is built on well-posed theoretical ingredients, which naturally adapt to changes in cosmology in a robust fashion.

This above comes with the caveat that it has only been tested on a limited range of plausibly interesting cosmologies. In particular, it was only tested in cases where the linear power spectra of the simulations had similar spectral shape to that of standard ΛCDM; this should not be a restriction for practical applications given that the general shape of the power spectrum is well constrained by current data and viable models have to reproduce this shape.

It is clear from Figs. 4.8, 4.9 and 4.10 that the calibrated halo model would not be the tool of choice if one is interested in the most accurate possible predictions of the matter power spectrum across all scales. Unfortunately as this work was being completed Takahashi et al. (2012) released an updated version of `HALOFIT` that updates the fit to more modern, high resolution, simulations and Heitmann et al. (2014) released an updated emulator that covers a larger cosmological parameter range and extends the emulator prediction to $k = 10\,h\,\mathrm{Mpc}^{-1}$. The calibrated halo model is clearly more accurate than the original `HALOFIT` prediction but unfortunately compares slightly unfavourably with the Takahashi et al. (2012) prediction, particularly in the quasi-linear regime. Worse, the Heitmann et al. (2014) prediction will be as accurate as simulations (or almost, the authors claim to 1%) for any cosmology within its parameter range due to its nature as an interpolator. Both of these facts mean that the halo model would not be the tool of choice for the use in the weak lensing analysis of current and future surveys. However, it is still useful as a way of producing accurate power spectra of models that are yet to be simulated and as a way of interpreting the measured power spectra of simulated models.

The halo model approach performs less well in the transition region between the 1-halo and 2-halo terms (which is around $k = 0.3\,h\,\mathrm{Mpc}^{-1}$ at $z = 0$) and also performs less well at higher

redshifts. Unfortunately a simple parametrisation of this behaviour was not found, and this remains an unsolved problem.

The halo model is a physical model and, even in its calibrated state, physical terms such as halo profiles and mass functions can still be identified. The difference in having a fitting formula with such physical objects in it, compared to fitting formula (*e.g.* Takahashi et al. 2012; Zhao 2013) or emulators (*e.g.* Heitmann et al. 2014) cannot be overstated. The approach can readily be extended to take account of new physical processes and changes in the cosmological paradigm in a way that other methods of predicting the matter spectrum simply cannot do. This means that extensions to the standard cosmological paradigm can readily be incorporated, as has been seen in Chapter 6 where accurate results were obtained for the power spectrum for various Hu & Sawicki (2007a) type $f(R)$ models with no additional parameter fitting. This contrasts with the modified gravity `HALOFIT` approach of Zhao (2013) or the massive neutrino approach of Bird et al. (2012) in which all of the parameters of the original Smith et al. (2003) `HALOFIT` had to be recalibrated to a new suite of simulations. Such a recalibration requires many new simulations that cover the new parameter space and refitting introduces the possibility of changing the original `HALOFIT` predictions in regions of parameter space where they are already accurate. In the halo model approach shown in Chapter 6 one simply needs to know the new linear growth factor and new $\delta_{\rm c}(M)$ in order to produce accurate results and this is true generally; one only need to know linear theory together with a small number of halo parameters that can be predicted theoretically, or calibrated against a simulation, in order to predict the matter power spectrum accurately.

7.2.2 Further work

Clearly the largest problems exist in the quasi-linear regime, which in the halo model is the transition between 1- and 2-halo terms. If this transition could be fixed then the accuracy of the halo model could potentially be improved. The reason for this is that the 1-halo power goes as k^3 shot noise at large scales, with an amplitude fixed by $\delta_{\rm c}$ and the simple recipe of $\Delta^2_{\rm lin} + Ak^3$ is insufficient to capture the complexities of the quasi-linear regime as a function of cosmology or z. Progress could potentially be made by using an alternative prescription for the 2-halo term because clearly the breakdown of the power into 'linear + haloes' fails to capture the finer detail of the quasi-linear regime. A suitable alternative maybe something like 'ZA + haloes' or 'Perturbation theory + haloes'. The ZA prediction for the power (*e.g.* White 2014) is different from linear theory and captures more elements of quasi-linear evolution (*e.g.* Schneider & Bartelmann 1995; Taylor & Hamilton 1996) which may make it better suited as a 2-halo term than the linear power spectrum. Using higher order perturbation theory for a 2-halo term is also possible, and since perturbation theory breaks down after shell crossing (*e.g.* Crocce & Scoccimarro 2006) there is no danger double counting power in both the 1- and 2-halo terms because perturbation theory cannot deal with virialised structures. However, some perturbative approaches produce nonsensical answers at small scales, outside their regime of

validity; for example power tending to either zero or to absurdly high values. These adverse effects would need to be dealt with to produce a manageable 2-halo term. As an aside; it would also be useful to quench the 1-halo term at very large scales to prevent it from artificially over-taking linear theory around $k = 0.0001\,h\,\mathrm{Mpc}^{-1}$.

As discussed in the previous section, one might optimistically expect that many different extensions to the cosmological paradigm could be incorporated, even in tandem (*e.g.* Baldi et al. 2014), with a minimum of calibratory simulations. Such scenarios are beginning to be looked at in high resolution simulations and so tests of the accuracy of the halo model will be possible in the near future. Example extensions include:

Non-Gaussianity at levels not already ruled out on cosmological scales plausibly only affects the halo mass function. Gaussianity is one of the assumptions in deriving theoretical mass functions such as Press & Schechter (1974) and it is therefore possible that good halo-model results may be obtained by multiplying the Sheth et al. (2001) mass function that appears in the current halo model calculation by a ratio of non-Gaussian to Gaussian theoretical Press & Schechter (1974) mass functions (*e.g.* Dalal et al. 2008; Achitouv & Corasaniti 2012).

Massive neutrinos have already been incorporated into a `HALOFIT` type fitting formula by Bird et al. (2012) and into an emulator type construction by Agarwal et al. (2013). The effect of neutrinos on the linear power spectrum is known and incorporated into tools such as `CAMB` and simulations have shown that good estimates of the mass function are possible in these models as long as one calculates $\sigma(M)$ for CDM only, ignoring the ν contribution (Villaescusa-Navarro et al. 2013; Costanzi et al. 2013; Castorina et al. 2014; Baldi et al. 2014).

Warm dark matter has effects on the linear power spectrum that are well understood in that it introduces a damping in power below a scale that depends on the particle mass (Fig. 1.10), clearly such a suppression can be included via the 2-halo term. Although it should be noted that damping of the 2-halo term may make the quasi-linear transition regime more problematic. It has also been shown (Angulo et al. 2013c) that WDM models introduce a cut in the halo mass function and numbers of haloes below a critical mass (that depends on the particle mass) are highly suppressed compared to their CDM counterparts. This could clearly be included in the halo model calculation via an appropriate cut in the mass function that forms part of the 1-halo term.

Dark energy has already been tested in some regards, given that varying a varies the relative contribution of Ω_Λ to the universe. However, during testing, simulations were not available where $w \neq -1$ and clearly it would be necessary to test the halo model for such models. The main effects of dark energy are to cause haloes to collapse at different epochs compared to the $w = -1$ case, which alters the concentration-mass relation via the formation redshift, and also alters how the linear power and fluctuation amplitude vary

with time. All of these ingredients are already captured in the halo model calculation so that the current model should extend naturally to dark energy models without major modification.

Modified gravity has been tested in Chapter 6 on the subset of Hu & Sawicki (2007a) models and excellent results were obtained with some minimal, theoretically motivated, changes and no additional parameter tunings. In light of these good results it would be interesting to test to smaller scales and against simulations for different models. Simulations of modified gravity are in their infancy and those discussed in Chapter 6 almost represent the current state of the art. Resolution is limited by the fact that an extra equation for the additional field(s) must be solved in tandem with that of the gravitational potential and that these two quantities are coupled. However, in the future simulations will be pushed to smaller scales and testing the halo model calculation here – where the internal structure of haloes is well resolved, will certainly be important. That the simulations shown here probe scales of $k = 10\,h\,\mathrm{Mpc}^{-1}$ and lensing in *Euclid* will be sensitive to scales of $k = 15\,h\,\mathrm{Mpc}^{-1}$ clearly shows that there is much to be done in terms of improving resolution. Additionally testing the halo model calculation against different modified gravity models will be important; increasingly simulations for these are becoming available (*e.g.* Galileons Barreira et al. 2014). Given the plethora of models perhaps having some unified framework for models, that includes the non-linear regime (similar to Hu & Sawicki 2007b; Baker et al. 2013), would be beneficial. For example, at some level it is possible that any reasonable modified gravity model can be specified via a scale dependent enhancement to gravity and by a screening mass for haloes.

Baryons are not strictly an extension to the standard paradigm but the effect of baryons on the matter distribution is certainly something that can be important and that is often ignored. Some work has been done on the inclusion of baryons in simulations, with various recipes compared in van Daalen et al. (2012). Work has also been done in including baryons in halo model type calculations (*e.g.* Fedeli 2014) and at a minimum it is probably fair to say that the deviations between theory and dark-matter simulations seen here at $k \sim 10\,h\,\mathrm{Mpc}^{-1}$ are becoming within the range of uncertainty introduced by baryonic effects. Nevertheless, in principle the halo model method may help remedy the problem, by using extra physically motivated ingredients. Baryons should only alter the internal structure of haloes, and are not thought to alter the linear power or the halo mass function significantly (van Daalen et al. 2013) and this should be easily captured in the halo model calculation by altering the concentration of haloes in a way that takes account of baryon cooling, feedback and galaxy formation and evolution.

Being able to produce *accurate* power spectra in each of these extensions to the standard paradigm will be important in order to distinguish standard and nonstandard cosmological models. Particularly, for weak lensing constraints, the power spectrum as a function of cos-

mology needs to be accurate well into the non-linear regime in order not to bias parameter constraints. Moreover, exploration of a large parameter space of models will inevitably be necessary, and there will therefore be a strong motivation to explore rapid means of generating non-linear power spectra. Extensions of the halo model such as the one explored here have the potential to be an invaluable tool in such studies.

7.3 Simulation rescaling

7.3.1 Summary

In Chapter 5 it has been demonstrated that the rescaling method of Angulo & White (2010) may be modified so as to apply directly to halo catalogues. AW10 rescalings of length, mass, and redshift were made as well as using the halo positions themselves to compute the displacement fields (by debiasing the halo over-density fields), in order to correct the linear clustering in the simulation using the Zel'dovich approximation. This method enables rapid scaling of a halo catalogue to a different cosmology, and is entirely self-contained, being based only on the halo catalogue.

Working with haloes has the advantage of speed, but also allows two improvements on the original AW10 method. The first of these concerns the internal structure of haloes, which depends on cosmology. This can be allowed for by reconstituting the halo internal density distribution using analytical profiles and scaling relations appropriate for the target cosmology. If the catalogue of halo particles is available, it is also possible to restructure haloes without replacing or regenerating them entirely. Additionally reconstituted haloes can be regurgitated back into the parent particle distribution if desired. All of these approaches were shown to improve upon the initial AW10 method in terms of the accuracy of the recovered power.

The second issue applies on large scales. The AW10 method applies an additional displacement in order to ensure that the large-scale linear clustering is as desired in the target cosmology. But applying this extra displacement to all haloes, independent of their mass, will not yield the correct mass-dependent bias, $b(M)$. Better results were found to be obtained by scaling the extra displacement in a mass-dependent way. A clear residual BAO was seen if one did not apply the bias dependent displacement field, particularly in reconstituted haloes, and the only explanation for this is that an incorrect $b(M)$ relation is otherwise produced by the original AW10 method. Although $b(M)$ was not checked explicitly it would be easy enough to do so.

The method has been tested by rescaling a halo catalogue generated from a matter-only τCDM simulation into that of a more standard ΛCDM model and also on some HS07 modified gravity models. Both cases represent a radical shift in cosmology, in the τCDM case especially considering that the initial simulation contains no dark energy and in the HS07 case because the original simulation contained no scalar field. For τCDM at the level of the particle distribution

the matter power spectrum is predicted correctly after the rescaling to the level of 1% to $k = 0.1\,h\,\mathrm{Mpc}^{-1}$ and to 5% to $k = 1\,h\,\mathrm{Mpc}^{-1}$ if one also manipulates halo properties post scaling. This is in excellent agreement with the original AW10 results and provides independent confirmation of the accuracy of the scaling algorithm. For the haloes the power spectra are noisier, but are still predicted correctly at the level of a few % up to $k = 0.1\,h\,\mathrm{Mpc}^{-1}$ with no obvious biases. In redshift space the method was shown to work well, as in the original AW10 case, but improvements were made by reconstituting or restructuring the haloes so that they had the correct velocity dispersion and mass-concentration relations. Across the entire redshift-space plane the redshift-space power spectrum was recovered at the $\sim 30\%$ level for all orientations of modes up to $k = 1\,h\,\mathrm{Mpc}^{-1}$. The monopole power spectrum is particularly well recovered in the case of restructuring haloes where the match is 2% up to $k = 1\,h\,\mathrm{Mpc}^{-1}$. The quadrupole to monopole ratio was also computed to see if the growth rate might be recovered post scaling; no obvious biases were seen although the measurement itself was noisy due to the relatively small simulation volume available.

In Chapter 6 rescaling was also tested for HS07 modified gravity models, where it was shown to produce accurate particle and halo distributions. Power spectra in real and redshift space were recovered at similar accuracy to the τCDM to ΛCDM transition seen in Chapter 5 and surprisingly the mass function was better recovered in the HS07 models than in the τCDM to ΛCDM case. It is yet to be fully investigated how the method works at producing reconstituted haloes but it was demonstrated that this could be quite simple in principle because the major differences seen in the residuals after scaling were to do with halo velocity dispersion, which is enhanced by a factor of $\sqrt{4/3}$ in the modified models resulting in a much higher FOG suppression than in ΛCDM. A clear next step is to implement this in a halo reconstitution algorithm, possibly together with minor shifts in halo concentration relations and respecting the mass dependence of the screening mechanism. A simplistic view is that low mass haloes are unscreened whereas high mass haloes are fully screened and this transition can be calculated fairly easily; what is more complicated is that such screening will depend on environment (Lombriser et al. 2013b) and if the scaled simulations respect this environmental dependence remains to be investigated.

However, these are minor issues, and it is particularly worthy of note that power spectra in both real and redshift space, as well as mass functions, were almost perfectly recovered in HS07 models, despite the increased complexity in these models. Therefore the current method already seems well suited for the application of rapid generation of mock galaxy catalogues covering a wide range of cosmologies. This could potentially be complementary to approaches for rapidly running simulations to generate clustering statistics (Tassev et al. 2013; White et al. 2014; Winther & Ferreira 2014) to enable many different realisations to be created, and with approaches, such as de la Torre & Peacock (2012) and Angulo et al. (2013a), to generate low mass haloes below the resolution limit of existing simulations.

7.3.2 Further work

There are a number of ways the rescaling algorithm developed here could be improved and furthered. It would be of value to test to see whether the power spectra could be better reproduced using different displacement field reconstruction techniques. For example, the peculiar velocity field relates more directly to the displacement field (no derivatives) and reconstruction of the displacement field was only tested using the overdensity field. Particularly for haloes it might be possible to simply use their velocity as a proxy for the displacement field at their location, given that bulk halo motion ought to be fairly linear (*e.g.* Doumler et al. 2013).

It would also be advantageous to test the algorithm for the recovery of statistics other than the power spectrum and halo mass function, such as halo bias, correlation functions or higher order statistics such as the bispectrum. Although theoretically the correlation function is the simple Fourier Transform of the power spectrum, it mixes modes so that at large r part of the correlation function does not consist of entirely small k modes; therefore how well correlation functions are reproduced is not entirely obvious. Clearly tests over a broad range of cosmologies would also be desirable given that only a single transition between τCDM and ΛCDM and some HS07 modified gravity models has been tested.

Although the linear portion of the power spectrum was reproduced almost perfectly in rescaling, the non-linear portion was less perfect. It may be possible to produce improved results in both real and redshift space by using different ways of rescaling the internals of haloes, for example using different mass-concentration relations or velocity dispersion relations or even fitting these to improve results for the non-linear portions. This is particularly important in unscreened HS07 haloes where the increased velocity dispersion could clearly be seen in the residual power spectra and this leads to a large error.

The work here investigated matching simulations at the level of the mass function, parameterised by $\sigma(R)$. It has been shown that the mass function can only be considered to be universal at the level of $\simeq 10\%$ (Lukić et al. 2007; Tinker et al. 2008, indeed the failure of the method to reproduce the exact mass function, despite being tuned to have exactly the same $\sigma(R)$, is *proof* that the mass function is not universal) but rescaling is possible by choosing to match to *any* mass function. Therefore one could test with different non-universal prescriptions for the mass function and see if better results were obtained.

The eventual aim of the rescaling algorithm is to be able to generate realistic mock galaxy populations as a function of cosmology. Getting the correct matter distribution and halo distribution is clearly a necessary first step but a next step would be to test the ability of the algorithm to reproduce HOD catalogues directly, because this is the important final product and the only thing that would then be tested against observations directly.

Many extensions to the standard cosmological paradigm have been proposed that the rescaling algorithm ought to be able to be extended for use in each case, without running a large suite of simulations. For example:

Non-Gaussianity will affect the halo mass function and bias relation (Dalal et al. 2008;

Wagner et al. 2010). However, this can be taken into account when choosing rescaling parameters by minimising the difference in halo mass function directly, rather than just $\sigma(R)$, given that $\sigma(R)$ could be identical in two models with different non-Gaussianity. Fits to mass functions in non-Gaussian scenarios are available in the literature (Lo Verde et al. 2008; Smith & Markovic 2011) and stem from theoretical PS type arguments. The non-Gaussian prediction for scale dependet bias could also be respected in displacing haloes.

Massive neutrinos damp the linear power spectrum in a way that has been incorporated into `CAMB`, and linear evolution is well understood theoretically (Lesgourgues & Pastor 2006). The non-linear spectrum will be effected as the matter distribution is smoothed by the neutrinos and this will then have an impact on halo properties. Villaescusa-Navarro et al. (2013) and Castorina et al. (2014) have shown that reasonable halo mass functions and bias may be obtained if one considers standard Sheth et al. (2001) prescriptions but calculate $\sigma(R)$ using the CDM matter spectrum only, ignoring the smooth neutrino component. Clearly this can be easily incorporated into choosing the s and z parameters in the initial minimisation part of the method.

Warm dark matter affects the linear spectrum by damping power at small scales in a way that is well understood and can therefore be included when the displacement field is created mode-by-mode. Additionally WDM has been shown to heavily suppress halo formation below a certain mass scale that depends on the WDM particle mass. Obviously this can be included in halo rescaling; for example simply be removing all haloes below a certain mass.

Dark energy is a particularly simple case because conceptually there is very little difference between these models and the τCDM to ΛCDM transition covered in Chapter 5 where it was seen that dark energy could be effectively generated by rescaling. Linear perturbation theory for dark energy models is also simple and was outlined in Chapter 1. The effect on the mass function and halo profiles should then feed through the halo model apparatus from linear theory.

Modified gravity rescaling has already been tested for HS07 models in Chapter 6. As discussed in that chapter, modified gravity alters both the linear growth rate of perturbations, but also has the potential to screen haloes from the effects of the modification. As seen, these effects can be incorporated into rescaling fairly easily and good results are obtained for the power spectrum in both real and redshift space. Clearly testing against different modified gravity models is necessary, where the linear growth and screening can be different, as well as considering environmental dependence of modified gravity effects in more detail.

Baryons Despite galaxies being composed of baryons, the effect of baryons on the *distribution* of galaxies should be small, beyond perhaps altering halo profiles in a way that potentially

changes halo mass and alters the distribution of satellite galaxies within a halo (van Daalen et al. 2013). For example in HOD prescriptions galaxies are located either exactly at the centre of a halo, or satellites that stochastically trace the extended halo mass distribution and a baryon dependent $c(M)$ relation could capture this.

7.4 Speculation

The material presented in this thesis has the potential to be used in the analysis of cosmological data sets with the eventual aim of constraining parameters to greater accuracy, or ruling in and out new parameters. To end, the author concludes this thesis with a few sentences of his thoughts on the future of cosmology:

I believe that the next big discovery in large-scale structure cosmology will be measurements of the neutrino mass from large-scale structure surveys. Personally I believe that Λ *is here to stay and that no deviations from* $w = -1$ *will ever be observed, also that no deviation from a flat* $\Omega_{\rm m} = 0.3$*,* $\Omega_\Lambda = 0.7$*,* $h = 0.7$ *model will be seen, except for the fine % level details. Ever tighter constraints will be placed on modified gravity models, and new models will be created in the gaps left by observations, but none of them will ever be shown to be a more correct description of our Univese than* Λ*. As to whether or not the magnitude of the vacuum energy will ever be able to be altered to account for the tiny cosmological constant I am not so sure. Possibly anthropic arguments will be given more weight if the inflation models, allowed by the latest CMB measurements, would tend to produce a multiverse and maybe there will be theoretical research done into whether or not cosmological parameters and fundamental constants might vary across a multiverse. It is often said that anthropic arguments are untestable, but I do not believe this to be the case, although they are certainly difficult to test. As an example, one might investigate the development of structure in universes with high values of* Λ *to see what density of star formation is produced and this could then be multiplied by a weighting, accounting for how large, and how frequent, a universe with that set of parameters is. It is certainly conceivable that we live in a Universe with parameters close to those that happen to maximise the number of stars formed across the multiverse.*

It will be amusing to see how wrong the author is about these points in coming decades.

Bibliography

Achitouv I. E., Corasaniti P. S., 2012, JCAP , 2, 2

Agarwal S., Abdalla F. B., Feldman H. A., Lahav O., Thomas S. A., 2012, MNRAS, 424, 1409

Agarwal S., Abdalla F. B., Feldman H. A., Lahav O., Thomas S. A., 2013, ArXiv e-prints

Agarwal S., Feldman H. A., 2011, MNRAS, 410, 1647

Ahmad Q. R. et al., 2001, Physical Review Letters, 87, 071301

Alcock C. et al., 1996, ApJ, 471, 774

Anderson L. et al., 2014, MNRAS, 439, 83

Angulo R. E., Baugh C. M., Frenk C. S., Lacey C. G., 2013a, ArXiv e-prints

Angulo R. E., Hahn O., Abel T., 2013b, MNRAS, 434, 1756

Angulo R. E., Hahn O., Abel T., 2013c, MNRAS, 434, 3337

Angulo R. E., White S. D. M., 2010, MNRAS, 405, 143

Arnold C., Puchwein E., Springel V., 2013, ArXiv e-prints

Baker T., Ferreira P. G., Skordis C., 2013, Phys. Rev. D, 87, 024015

Baldi M., Villaescusa-Navarro F., Viel M., Puchwein E., Springel V., Moscardini L., 2014, MNRAS

Barreira A., Li B., Hellwing W. A., Lombriser L., Baugh C. M., Pascoli S., 2014, ArXiv e-prints

Bartelmann M., Schneider P., 2001, Phys. Rep., 340, 291

Bartolo N., Matarrese S., Riotto A., 2005, JCAP , 10, 10

Baugh C. M., 2006, Reports on Progress in Physics, 69, 3101

Baugh C. M., Gaztanaga E., Efstathiou G., 1995, MNRAS, 274, 1049

Ben-Dayan I., Durrer R., Marozzi G., Schwarz D. J., 2014, ArXiv e-prints

Benson A. J., 2012, New Astronomy, 17, 175

Bernardeau F., Colombi S., Gaztañaga E., Scoccimarro R., 2002, Physics Reports, 367, 1

Beutler F. et al., 2011, MNRAS, 416, 3017

Beutler F. et al., 2014, ArXiv e-prints

Bhattacharya S., Heitmann K., White M., Lukić Z., Wagner C., Habib S., 2011, ApJ, 732, 122

BICEP2 Collaboration et al., 2014, ArXiv e-prints

Binney J., Tremaine S., 2008, Galactic Dynamics, 2nd edn.

Bird S., Viel M., Haehnelt M. G., 2012, MNRAS, 420, 2551

Blake C. et al., 2011, MNRAS, 418, 1707

Böhmer C. G., Harko T., Lobo F. S. N., 2008, Astroparticle Physics, 29, 386

Bond J. R., Cole S., Efstathiou G., Kaiser N., 1991, ApJ, 379, 440

Brax P., Valageas P., 2013, Phys. Rev. D, 88, 023527

Bryan G. L., Norman M. L., 1998, ApJ, 495, 80

Bullock J. S., Kolatt T. S., Sigad Y., Somerville R. S., Kravtsov A. V., Klypin A. A., Primack J. R., Dekel A., 2001, MNRAS, 321, 559

Burles S., Nollett K. M., Turner M. S., 2001, Phys. Rev. D, 63, 063512

Busha M. T., Evrard A. E., Adams F. C., 2007, ApJ, 665, 1

Carroll S. M., de Felice A., Duvvuri V., Easson D. A., Trodden M., Turner M. S., 2005, Phys. Rev. D, 71, 063513

Carroll S. M., Press W. H., Turner E. L., 1992, Annual Review of Astronomy and Astrophysics, 30, 499

Castorina E., Sefusatti E., Sheth R. K., Villaescusa-Navarro F., Viel M., 2014, JCAP , 2, 49

Chevallier M., Polarski D., 2001, International Journal of Modern Physics D, 10, 213

Clifton T., Ferreira P. G., Padilla A., Skordis C., 2012, Phys. Rep., 513, 1

Cole S., 1997, MNRAS, 286, 38

Cole S., Fisher K. B., Weinberg D. H., 1994, MNRAS, 267, 785

Cole S., Kaiser N., 1989, MNRAS, 237, 1127

Cole S. et al., 2005, MNRAS, 362, 505

Coles P., Lucchin F., 1995, Chichester: Wiley

Colombi S., Dodelson S., Widrow L. M., 1996, ApJ, 458, 1

Cooray A., Sheth R., 2002, Physics Reports, 372, 1

Costanzi M., Villaescusa-Navarro F., Viel M., Xia J.-Q., Borgani S., Castorina E., Sefusatti E., 2013, JCAP , 12, 12

Crocce M., Scoccimarro R., 2006, Phys. Rev. D, 73, 063520

Dalal N., Doré O., Huterer D., Shirokov A., 2008, Phys. Rev. D, 77, 123514

Davis M., Efstathiou G., Frenk C. S., White S. D. M., 1985, ApJ, 292, 371

de la Torre S., Guzzo L., 2012, MNRAS, 427, 327

de la Torre S. et al., 2013, ArXiv: 1303.2622

de la Torre S., Peacock J. A., 2012, ArXiv: 1212.3615

Dhar B. K., Williams L. L. R., 2010, MNRAS, 405, 340

Doumler T., Gottlöber S., Hoffman Y., Courtois H., 2013, MNRAS, 430, 912

Durrer R., Maartens R., 2008, ArXiv e-prints

Efstathiou G., 1995, MNRAS, 274, L73

Efstathiou G., Davis M., White S. D. M., Frenk C. S., 1985, ApJS, 57, 241

Einstein A., 1916, 354, 769

Eisenstein D. J., Hu W., 1998, ApJ, 496, 605

Eisenstein D. J., Seo H.-J., Sirko E., Spergel D. N., 2007, APJ, 664, 675

Eke V. R., Cole S., Frenk C. S., 1996, MNRAS

Eke V. R., Navarro J. F., Steinmetz M., 2001, ApJ, 554, 114

Esposito-Farèse G., Polarski D., 2001, Phys. Rev. D, 63, 063504

Feast M. W., Laney C. D., Kinman T. D., van Leeuwen F., Whitelock P. A., 2008, MNRAS, 386, 2115

Fedeli C., 2014, ArXiv e-prints

Ferraro S., Schmidt F., Hu W., 2011, Phys. Rev. D, 83, 063503

Frampton P. H., Kawasaki M., Takahashi F., Yanagida T. T., 2010, JCAP , 4, 23

Governato F., Moore B., Cen R., Stadel J., Lake G., Quinn T., 1997, New Astronomy, 2, 91

Griest K., 1991, ApJ, 366, 412

Guo Q., White S., Angulo R. E., Henriques B., Lemson G., Boylan-Kolchin M., Thomas P., Short C., 2013, MNRAS, 428, 1351

Guth A. H., 1981, Phys. Rev. D, 23, 347

Guzzo L. et al., 2013, ArXiv e-prints

Harker G., Cole S., Jenkins A., 2007, MNRAS, 382, 1503

Hawking S. W., 1982, Physics Letters B, 115, 295

Hawkins M. R. S., 2011, MNRAS, 415, 2744

Heitmann K., Higdon D., White M., Habib S., Williams B. J., Lawrence E., Wagner C., 2009, ApJ, 705, 156

Heitmann K., Lawrence E., Kwan J., Habib S., Higdon D., 2014, ApJ, 780, 111

Heitmann K., White M., Wagner C., Habib S., Higdon D., 2010, ApJ, 715, 104

Hernquist L., 1990, ApJ, 356, 359

Herrnstein J. R. et al., 1999, Nature, 400, 539

Heymans C. et al., 2012, MNRAS, 427, 146

Higgs P. W., 1964, Phys. Rev. Lett., 13, 508

Hilbert S., Hartlap J., White S. D. M., Schneider P., 2009, AA, 499, 31

Hu W., Sawicki I., 2007a, Phys. Rev. D, 76, 064004

Hu W., Sawicki I., 2007b, Phys. Rev. D, 76, 104043

Hubble E., 1929, Proceedings of the National Academy of Science, 15, 168

Huterer D., Takada M., 2005, Astroparticle Physics, 23, 369

Jain B., Vikram V., Sakstein J., 2013, ApJ, 779, 39

Jenkins A. et al., 1998, ApJ, 499, 20

Jenkins A., Frenk C. S., White S. D. M., Colberg J. M., Cole S., Evrard A. E., Couchman H. M. P., Yoshida N., 2001, MNRAS, 321, 372

Jennings E., Baugh C. M., Angulo R. E., Pascoli S., 2010, MNRAS, 401, 2181

Ji S. et al., 2013, ApJ, 773, 136

Jing Y. P., 2005, ApJ, 620, 559

Joachimi B., Semboloni E., Bett P. E., Hartlap J., Hilbert S., Hoekstra H., Schneider P., Schrabback T., 2013a, MNRAS, 431, 477

Joachimi B., Semboloni E., Hilbert S., Bett P. E., Hartlap J., Hoekstra H., Schneider P., 2013b, MNRAS, 436, 819

Kaiser N., 1987, MNRAS, 227, 1

Karachentsev I. D., Kashibadze O. G., Makarov D. I., Tully R. B., 2009, MNRAS, 393, 1265

Khoury J., Weltman A., 2004, Phys. Rev. D, 69, 044026

Kiessling A., Heavens A. F., Taylor A. N., Joachimi B., 2011, MNRAS, 414, 2235

Kirshner R. P., Oemler, Jr. A., Schechter P. L., Shectman S. A., 1981, ApJ, 248, L57

Klypin A., Holtzman J., 1997, ArXiv Astrophysics e-prints

Knebe A. et al., 2011, MNRAS, 415, 2293

Koksma J. F., Prokopec T., 2011, ArXiv e-prints

Komatsu E. et al., 2011, ApJS, 192, 18

Kwan J., Bhattacharya S., Heitmann K., Habib S., 2013, ApJ, 768, 123

Lacey C., Cole S., 1993, MNRAS, 262, 627

Lawrence E., Heitmann K., White M., Higdon D., Wagner C., Habib S., Williams B., 2010, ApJ, 713, 1322

Lesgourgues J., Pastor S., 2006, Phys. Rep., 429, 307

Lewis A., Challinor A., Lasenby A., 2000, ApJ, 538, 473

Li B., Hellwing W. A., Koyama K., Zhao G.-B., Jennings E., Baugh C. M., 2013, MNRAS, 428, 743

Li B., Zhao G.-B., Teyssier R., Koyama K., 2012, JCAP , 1, 51

Li Y., Hu W., 2011, Phys. Rev. D, 84, 084033

Linde A. D., 1983, Physics Letters B, 132, 317

Linde A. D., 1986, Physics Letters B, 175, 395

Linder E. V., 2003, Physical Review Letters, 90, 091301

Linder E. V., 2005, Phys. Rev. D, 72, 043529

Linder E. V., Cahn R. N., 2007, Astroparticle Physics, 28, 481

Lo Verde M., Miller A., Shandera S., Verde L., 2008, JCAP , 4, 14

Lombriser L., 2014, ArXiv e-prints

Lombriser L., Koyama K., Li B., 2013a, ArXiv e-prints

Lombriser L., Koyama K., Zhao G.-B., Li B., 2012a, Phys. Rev. D, 85, 124054

Lombriser L., Li B., Koyama K., Zhao G.-B., 2013b, Phys. Rev. D, 87, 123511

Lombriser L., Schmidt F., Baldauf T., Mandelbaum R., Seljak U., Smith R. E., 2012b, Phys. Rev. D, 85, 102001

Lombriser L., Slosar A., Seljak U., Hu W., 2012c, Phys. Rev. D, 85, 124038

Lovell M. R. et al., 2012, MNRAS, 420, 2318

Lovell M. R., Frenk C. S., Eke V. R., Jenkins A., Gao L., Theuns T., 2013, ArXiv e-prints

Lovelock D., 1971, J.Math.Phys., 12, 498

Lukić Z., Heitmann K., Habib S., Bashinsky S., Ricker P. M., 2007, ApJ, 671, 1160

Lynden-Bell D., 1967, MNRAS, 136, 101

Lyth D. H., Liddle A. R., 2009, The Primordial Density Perturbation, 1st edn. Cambridge University Press

Macciò A. V., Governato F., Horellou C., 2005, MNRAS, 359, 941

MacFarland T., Couchman H. M. P., Pearce F. R., Pichlmeier J., 1998, NA, 3, 687

Maddox S. J., Efstathiou G., Sutherland W. J., Loveday J., 1990, MNRAS, 243, 692

Majaess D., Turner D., Lane D., 2009, Acta Astronomica, 59, 403

Manera M. et al., 2013, MNRAS, 428, 1036

Manera M., Sheth R. K., Scoccimarro R., 2010, MNRAS, 402, 589

Martel H., Shapiro P. R., Weinberg S., 1998, ApJ, 492, 29

Mead A. J., Peacock J. A., 2014, MNRAS

Meszaros P., 1974, A&A, 37, 225

Mo H. J., White S. D. M., 1996, MNRAS, 282, 347

Monaco P., Theuns T., Taffoni G., 2002, MNRAS, 331, 587

Moore B., Quinn T., Governato F., Stadel J., Lake G., 1999, MNRAS, 310, 1147

More S., Kravtsov A. V., Dalal N., Gottlöber S., 2011, ApJS, 195, 4

Mukhanov V. F., Chibisov G. V., 1981, Soviet Journal of Experimental and Theoretical Physics Letters, 33, 532

Navarro J. F., Frenk C. S., White S. D. M., 1997, ApJ, 490, 493

Neto A. F. et al., 2007, MNRAS, 381, 1450

Nicolis A., Rattazzi R., Trincherini E., 2009, Phys. Rev. D, 79, 064036

Oyaizu H., 2008, Phys. Rev. D, 78, 123523

Oyaizu H., Lima M., Hu W., 2008, Phys. Rev. D, 78, 123524

Padmanabhan N., Xu X., Eisenstein D. J., Scalzo R., Cuesta A. J., Mehta K. T., Kazin E., 2012, MNRAS, 427, 2132

Panagia N., 1998, Mem. Soc. Astron. Italiana, 69, 225

Parfrey K., Hui L., Sheth R. K., 2011, Phys. Rev. D, 83, 063511

Peacock J. A., 1999, Cosmological Physics

Peacock J. A., 2007, MNRAS, 379, 1067

Peacock J. A., Dodds S. J., 1994, MNRAS, 267, 1020

Peacock J. A., Heavens A. F., 1990, MNRAS, 243, 133

Peacock J. A., Smith R. E., 2000, MNRAS, 318, 1144

Peccei R. D., Quinn H. R., 1977, Physical Review Letters, 38, 1440

Peebles P. J. E., 1980, The Large Scale Structure of the Universe, 1st edn. Princeton University Press

Penrose R., 1989, Annals of the New York Academy of Sciences, 571, 249

Penzias A. A., Wilson R. W., 1965, ApJ, 142, 419

Percival W. J., 2005, A&A, 443, 819

Perlmutter S. et al., 1999, APJ, 517, 565

Phillips M. M., Wells L. A., Suntzeff N. B., Hamuy M., Leibundgut B., Kirshner R. P., Foltz C. B., 1992, AJ, 103, 1632

Planck Collaboration et al., 2013a, ArXiv e-prints

Planck Collaboration et al., 2013b, ArXiv e-prints

Power C., Knebe A., 2006, MNRAS, 370, 691

Press W. H., Schechter P., 1974, ApJ, 187, 425

Prunet S., Pichon C., 2013, MPgrafic: A parallel MPI version of Grafic-1. Astrophysics Source Code Library

Puchwein E., Baldi M., Springel V., 2013, MNRAS, 436, 348

Rajantie A., 2012, Royal Society of London Philosophical Transactions Series A, 370, 5705

Rasera Y., Alimi J.-M., Courtin J., Roy F., Corasaniti P.-S., Füzfa A., Boucher V., 2010, in American Institute of Physics Conference Series, Vol. 1241, American Institute of Physics Conference Series, Alimi J.-M., Fuözfa A., eds., pp. 1134–1139

Reed D. S., Bower R., Frenk C. S., Jenkins A., Theuns T., 2007, MNRAS, 374, 2

Reid B. A. et al., 2010, MNRAS, 404, 60

Reid B. A. et al., 2012, MNRAS, 426, 2719

Riemer-Sørensen S., Parkinson D., Davis T. M., 2013a, ArXiv e-prints

Riemer-Sørensen S., Parkinson D., Davis T. M., Blake C., 2013b, ApJ, 763, 89

Roos M., 2010, ArXiv e-prints

Ruiz A. N., Padilla N. D., Domínguez M. J., Cora S. A., 2011, MNRAS, 418, 2422

Schmidt B. P. et al., 1998, APJ, 507, 46

Schmidt F., 2008, Phys. Rev. D, 78, 043002

Schmidt F., Vikhlinin A., Hu W., 2009, Phys. Rev. D, 80, 083505

Schneider P., Bartelmann M., 1995, MNRAS, 273, 475

Schrabback T. et al., 2010, Astronomy and Astrophysics, 516, A63

Scoccimarro R., 2004, Phys. Rev. D, 70, 083007

Seljak U., 2000, MNRAS, 318, 203

Seljak U., Hamaus N., Desjacques V., 2009, Physical Review Letters, 103, 091303

Seljak U., Sugiyama N., White M., Zaldarriaga M., 2003, PRD, 68, 083507

Seljak U., Zaldarriaga M., 1996, ApJ, 469, 437

Semboloni E., Hoekstra H., Schaye J., van Daalen M. P., McCarthy I. G., 2011, MNRAS, 417, 2020

Seo H.-J., Eisenstein D. J., 2003, ApJ, 598, 720

Sheth R. K., Mo H. J., Tormen G., 2001, MNRAS, 323, 1

Sheth R. K., Tormen G., 1999, MNRAS, 308, 119

Simha V., Cole S., 2013, ArXiv e-prints

Slipher V. M., 1917, The Observatory, 40, 304

Smith R. E., Markovic K., 2011, eprint arXiv:1103.2134

Smith R. E. et al., 2003, MNRAS, 341, 1311

Sotiriou T. P., Faraoni V., 2010, Reviews of Modern Physics, 82, 451

Spergel D. N. et al., 2003, ApJs, 148, 175

Springel V., 2005, MNRAS, 364, 1105

Springel V. et al., 2005, Nature, 435, 629

Starobinsky A. A., 1980, Physics Letters B, 91, 99

Suzuki N. et al., 2012, ApJ, 746, 85

Takahashi R., Sato M., Nishimichi T., Taruya A., Oguri M., 2012, ApJ, 761, 152

Taruya A., Nishimichi T., Saito S., 2010, Phys. Rev. D, 82, 063522

Tassev S., Zaldarriaga M., Eisenstein D., 2013, ArXiv: 1301.0322

Taylor A., Joachimi B., Kitching T., 2013, MNRAS, 432, 1928

Taylor A. N., Hamilton A. J. S., 1996, MNRAS, 282, 767

Teyssier R., 2002, A&A, 385, 337

Tinker J., Kravtsov A. V., Klypin A., Abazajian K., Warren M., Yepes G., Gottlöber S., Holz D. E., 2008, ApJ, 688, 709

Tinker J. L., Robertson B. E., Kravtsov A. V., Klypin A., Warren M. S., Yepes G., Gottlöber S., 2010, ApJ, 724, 878

Tinker J. L., Weinberg D. H., Zheng Z., Zehavi I., 2005, ApJ, 631, 41

Trenti M., Hut P., 2008, eprint arXiv:0806.3950

van Daalen M. P., Angulo R. E., White S. D. M., 2012, MNRAS, 424, 2954

van Daalen M. P., Schaye J., McCarthy I. G., Booth C. M., Dalla Vecchia C., 2013, ArXiv e-prints

Villaescusa-Navarro F., Marulli F., Viel M., Branchini E., Castorina E., Sefusatti E., Saito S., 2013, ArXiv e-prints

Wagner C., Verde L., Boubekeur L., 2010, JCAP , 10, 22

Wang J., Hui L., Khoury J., 2012, Physical Review Letters, 109, 241301

Warren M. S., Abazajian K., Holz D. E., Teodoro L., 2006, APJ, 646, 881

Weinberg S., 1987, Physical Review Letters, 59, 2607

Weinberg S., 1989, Reviews of Modern Physics, 61, 1

White M., 2014, MNRAS

White M., Gelmini G., Silk J., 1995, PRD, 51, 2669

White M., Tinker J. L., McBride C. K., 2014, MNRAS, 437, 2594

White M., Vale C., 2004, Astroparticle Physics, 22, 19

White S. D. M., Rees M. J., 1978, MNRAS, 183, 341

Winther H. A., Ferreira P. G., 2014, ArXiv e-prints

Woodard R., 2007, in Lecture Notes in Physics, Berlin Springer Verlag, Vol. 720, The Invisible Universe: Dark Matter and Dark Energy, Papantonopoulos L., ed., p. 403

Zel'dovich Y. B., 1970, AAP, 5, 84

Zhao G.-B., 2013, ArXiv e-prints

Zheng Z. et al., 2005, ApJ, 633, 791